NON–LINEAR FINITE ELEMENT ANALYSIS OF CONTINUA WITH EMPHASIS ON HYPERELASTICITY

Gray Farias Moita

A thesis submitted for the degree of Doctor of Philosophy
of the University of London and for the
Diploma of Membership of Imperial College

Department of Aeronautics
Imperial College of Science, Technology and Medicine
London, SW7 2BY

1994

Abstract

The development of finite element formulations for the study of continua is investigated in this thesis. The objective is to devise new robust and efficient techniques firstly for problems with geometric non-linearities but small strains and later for large-strain analysis and in particular hyperelasticity.

As an introduction to non-linear problems, membrane elements are considered. The elements are developed for application in hyperelastic structures and utilise the concept of the total Lagrangian approach.

The effort is then focussed on continuum mechanics and the development of a plane-strain element. The element deserves special attention because, in order to examine the large-strain hyperelastic behaviour, the incompressibility issue, characteristic inherent of any hyperelastic material, has to be addressed. The conventional linear lower-order plane-strain element tends to behave poorly when $\nu \rightarrow 0.5$. Consequently, the elements applied here are enhanced by incorporating into their linear formulation the so-called incompatible displacement modes. It is shown that this allows the element to accurately treat problems involving both bending and incompressibility. Subsequently, the element is upgraded to a non-linear formulation using again the total Lagrangian technique. The new formulation generally performs well but presents some problems of convergence when applied to large-strain analysis.

To overcome the problem with the non-linear incompatible modes element, a procedure is developed based upon the co-rotational formulation in which linear finite elements are embedded within a co-rotating local frame while the geometric non-linearities are accounted for via the rotation of this local system. In this manner the rigid body motions are kept separated from the actual deformation of the element. The resulting formulation can easily handle large displacements and large rotations. The formulation is derived consistently and can incorporate any linear element, including the linear incompatible modes element. Unconventionally, the method is extended so as to also handle large-strains. The technique is used in both two- and three-dimensional problems.

A wide range of numerical examples is presented in support of the different proposed theories. The elements were implemented within the research version of a large scale finite element package.

To Maria Lúcia and my parents

Acknowledgements

I would like to express my sincere gratitude to my supervisor Mike Crisfield for his most important guidance and encouragement. Mike has helped me to keep the enthusiasm even during the darkest period of this research.

I would also like to thank the following:

My friends who shared with me the noise room 363A during the last 4 years, especially Xiaohong, Jun, Hans, Gordan, Ugo and Mohammad, for the pleasant atmosphere and their help to make it possible to complete this work.

Mike, Júlio, Nicholas, Qing and all the people that made my stay at Imperial enjoyable and somehow collaborated towards the success of this work.

All the staff in the Department of Aeronautics for their friendly attitude and their support.

FEA Ltd. and its staff for providing the software and for the helpful discussions.

CNPq – Brazilian Council for Scientific and Technological Development for the financial support throughout the development of this work.

Finally, I express my deepest thanks to Maria Lúcia for her support and patience during the entire period of this Ph.D..

Contents

List of Figures 8

List of Tables 10

1 Introduction 11
- 1.1 Motivation and aim of the study . . . 11
- 1.2 A brief literature survey . . . 12
- 1.3 General layout of this thesis . . . 16

2 Hyperelasticity: Basic Concepts and Models Definitions 18
- 2.1 Introduction . . . 18
- 2.2 General kinematic relations . . . 19
- 2.3 Hyperelastic material models . . . 23

3 Membrane Finite Elements for Hyperelastic Materials Analysis 28
- 3.1 Introduction . . . 28
- 3.2 Axisymmetric membrane element for hyperelastic materials analysis . . 29
  - 3.2.1 Finite element development . . . 29
  - 3.2.2 Displacement-dependent pressure load . . . 33
  - 3.2.3 Hyperelasticity . . . 36
- 3.3 General three-dimensional non-linear membrane element . . . 40
  - 3.3.1 Finite element development . . . 40
  - 3.3.2 Load vector and stiffness matrix for a follower pressure load . . . 44
  - 3.3.3 Hyperelasticity . . . 46
- 3.4 Numerical tests . . . 48
  - 3.4.1 Cylinder under internal pressure . . . 48
  - 3.4.2 Inflation of a balloon . . . 52
  - 3.4.3 Inflation of a shallow spherical cap . . . 54
  - 3.4.4 Homogeneous deformation tests . . . 57
  - 3.4.5 Stretching of a square sheet with a central circular hole . . . 60
- 3.5 Final remarks . . . 61

4 Plane–stress/Plane–strain Analysis - The use of Non–linear Incompatible Elements **63**
- 4.1 Introduction . . . 63
- 4.2 Development . . . 64
  - 4.2.1 Linear elastic element . . . 64

4.2.2 Geometrical non-linearity using incompatible modes 71
4.3 Displacement-dependent (follower) pressure load 75
4.4 Incompatible elements with hyperelastic materials 77
4.4.1 Plane stress 77
4.4.2 Plane strain 77
4.5 Numerical tests 80
4.5.1 Linear elasticity 80
4.5.2 Non-Linear Elasticity 83
4.5.3 Hyperelasticity 89
4.6 Final remarks 92

5 Co-rotational Formulation for Two-dimensional Continua 96
5.1 Introduction 96
5.2 Development 97
5.2.1 Usual co-rotational procedure 97
5.2.2 Co-rotational formulation for continua 99
5.3 Numerical tests 110
5.3.1 Convergence tests 110
5.3.2 Cantilever beam subject to large deflections 111
5.3.3 Shallow arch under central load 113
5.4 Final remarks 113

6 Co-rotational Formulation for Three-dimensional Continua 117
6.1 Introduction 117
6.2 Development 118
6.2.1 Conventional linear three-dimensional element 118
6.2.2 Non-linear formulation 119
6.2.3 Adding the incompatible modes 129
6.3 Numerical tests 130
6.3.1 Large deflection and rotation analysis of a cantilever beam . . . 130
6.3.2 Three-dimensional curvilinear beam 131
6.3.3 Hinged cylindrical shell subject to a point load 131
6.4 Final remarks 133

7 Co-rotational Formulation for Hyperelasticity 140
7.1 Introduction 140
7.2 Plane-strain analysis 141
7.3 Three-dimensional analysis 146
7.4 Numerical tests 148
7.4.1 Hyperelastic shear deformation of a rectangular block 149
7.4.2 Thick-walled cylinder with internal pressure 151
7.4.3 Indentation problem 153
7.4.4 Cracked rectangular bar 157
7.4.5 Suspension ring 157
7.4.6 Thick-cylinder analysed with the three-dimensional element . . . 159
7.4.7 Rubber block under compression 160
7.5 Final remarks 164

8 Final Remarks and Conclusions **167**
8.1 General conclusions 167
8.2 Future works 169

A Arc-Length Method with a Displacement-Dependent Load **171**

B Pressure as a Separated Variable **173**

C Problems with Rank Deficiency **176**

References **178**

List of Figures

3.1 Axisymmetric membrane element 30
3.2 Original and final configurations of the element 34
3.3 three-dimensional membrane element 41
3.4 Cylinder under internal pressure 50
3.5 Cylinder - deformed configuration 50
3.6 Cylinder - internal pressure versus upper radial displacement 51
3.7 Rubber balloon - pressure p^* versus stretch λ 53
3.8 Inflation of a Shallow Spherical Cap 54
3.9 Shallow spherical cap - pressure versus mid-point displacement 55
3.10 Shallow Spherical Cap - Deformed Configurations 56
3.11 Simple tension 57
3.12 Equibiaxial tension 58
3.13 Pure shear 59
3.14 Sheet with a circular hole - force versus displacement 60
3.15 Original and deformed meshes 61

4.1 Isoparametric bi-linear element 65
4.2 Pure bending problem 67
4.3 Incompressible element - original and deformed configuration 68
4.4 Incompatible displacement modes 69
4.5 Displacement-dependent load pressure 76
4.6 Mesh sensitivity to distortion 81
4.7 Thick-walled cylinder 82
4.8 Large deflection of a cantilever beam 84
4.9 Deformation of the beam 85
4.10 Shallow arch subject to a concentrated load 85
4.11 Load-deflection curve for the shallow arch problem 86
4.12 Shallow arch - original and deformed configuration 87
4.13 Cook's membrane problem 87
4.14 Cook's Membrane - Contour for σ_{xx} stress 88
4.15 Cook's membrane - Neo-Hookean model 90
4.16 Cook's membrane - original undeformed and final deformed meshes . . . 91
4.17 Mooney-Rivlin cylinder - load vs. displacement curve 92
4.18 Cylinder under internal pressure 93
4.19 Dimensionless non-follower pressure vs. displacement 94
4.20 Dimensionless follower pressure vs. displacement 95

5.1 Element local triad 97
5.2 Initial and final element configuration 100
5.3 Determination of γ 102
5.4 Large strain patch test 103
5.5 Cantilever Beam - $\nu = 0.3$ 111
5.6 Cantilever Beam (irregular mesh) - $\nu = 0.3$ 112
5.7 Cantilever Beam - $\nu = 0.49$ 113
5.8 Cantilever beam under large deflection 114
5.9 Load-deflection curve for the plane-stress analysis 115
5.10 Load-deflection curve for the plane-strain analysis ($\nu = 0.49$) 116

6.1 Eight-noded brick element 119
6.2 Initial and final configurations – rotation followed by stretch 121
6.3 Polar decomposition – stretching preceding the rotation 121
6.4 Pseudo-vector $\boldsymbol{\theta}$ - Order-dependence of the rotations 125
6.5 Three-dimensional cantilever beam under end shear 131
6.6 Large deflection and rotation of a cantilever beam 132
6.7 Three-dimensional curve cantilever beam 133
6.8 Three-dimensional curvilinear beam 134
6.9 Non-dimensional tip deflection vs. load factor ($\nu = 0.$) 135
6.10 Non-dimensional tip deflection vs. load factor ($\nu = 0.49$) 136
6.11 Cylindrical shell under a point load 137
6.12 Load vs. displacement curve (thickness $t = 12.7mm$) 138
6.13 Load vs. displacement curve (thickness $t = 6.35mm$) 139

7.1 Shear deformation of a rectangular block 149
7.2 Normalised stress vs. displacement e: ($\triangle$) and ($\bigcirc$) are the analytical solutions for $\tau_{11} = -\tau_{22}$ and τ_{12}, respectively 152
7.3 Cylinder under Internal Pressure - Load vs. Displacement 153
7.4 Cylinder under Internal Pressure - Load vs. Displacement (Different Materials) 154
7.5 Indentation problem 155
7.6 Indentation problem - Deformed mesh for Co-rotational formulation . . 156
7.7 Indentation problem - Deformed mesh for Co-rotational formulation ($k = 100$) 156
7.8 Cracked rectangular bar 158
7.9 Cracked bar - Original and deformed mesh and σ_{22} contour 159
7.10 Suspension ring 160
7.11 Undeformed and deformed configuration 161
7.12 Contour for y-y stress 162
7.13 Cylinder analysed with three-dimensional elements - dimensionless pressure vs. displacement 163
7.14 Block under compression - total force vs. vertical displacement 164
7.15 Block under compression - horizontal displacement vs. vertical displacement 165
7.16 Undeformed and deformed meshes at 13.6% compression 166

C.1 Test problem - block under compression 177

List of Tables

3.1 Convergence rate for the Newton-Raphson method 49
3.2 Convergence rate for the Newton-Raphson method 52

4.1 Thick cylinder 82
4.2 Displacement at points A and B for Cook's membrane 84

5.1 Euclidean residual norm as a percentage of total reactions 115

Notation

The notation presented here represents the main notation used throughout this thesis. When the same notation is used for different quantities, the non-usual notation is explained and referred to the section or equation where it is applied. We use the basic vector and matrix notation, i.e., their symbols are written in bold.

Scalars

λ_i	=	principal stretches
V	=	virtual work
J	=	determinant of $\mathbf{F}$
φ	=	strain-energy function
W	=	work done by a force on a body
Q	=	heat flow
T	=	kinetic energy
V_o	=	initial volume
C_1,C_2	=	Mooney-Rivlin model constants
k	=	bulk modulus
I_1,I_2,I_3	=	strain invariants
μ_p,α_p	=	Ogden's model constants
μ	=	ground state of the shear modulus
α	=	length of the element (Section 3.2.1)
E	=	Young's modulus
ν	=	Poisson's ratio
t	=	thickness
p^*	=	applied pressure load (see equation (3.20))
A,a	=	original and current areas
λ	=	vector loading multiplier (see equation (3.29))
p	=	pressure term (see equations (3.45) and (3.46))
ξ,η,ζ	=	non-dimensional (natural) co-ordinates
Ω_l	=	local spin
a,b,c	=	scalars obtained from $\Omega_l = 0$
θ	=	angle to define local co-rotating frame
e	=	shear strain (see equation (7.32))

Vectors and matrices or tensors

$\mathbf{E}$	=	Green's strain
$\mathbf{F}$	=	deformation gradient
$\mathbf{X}$	=	vector of original co-ordinates

$\mathbf{x}$	=	vector of updated co-ordinates ($\mathbf{x} = \mathbf{X} + \mathbf{u}$)
$\mathbf{u}$,$\mathbf{v}$,$\mathbf{w}$	=	displacement vector (collectively called $\mathbf{p}$)
$\mathbf{D}$	=	displacement derivative matrix (see equations (2.2), (2.3), (4.47) and (4.48))
$\mathbf{I}$	=	identity matrix
$\mathbf{C}$	=	right Cauchy-Green stretch tensor
$\mathbf{Q}$	=	matrix containing the principal direction vectors
$\mathbf{N}_i$	=	principal direction vectors in the Lagrangian triad
$\mathbf{n}_i$	=	principal direction vectors in the Eulerian triad
$\mathbf{S}$	=	second Piola-Kirchhoff stress
$\boldsymbol{\sigma}$	=	Cauchy stress
$\boldsymbol{\epsilon}$	=	engineering strain
$\boldsymbol{\tau}$	=	Kirchhoff stress
$\mathbf{D}$	=	tangent modular matrix
$\mathbf{U}$	=	stretch matrix
$\boldsymbol{\sigma}_b$	=	Biot stress
$\mathbf{E}_b$	=	Biot strain
$\mathbf{b}$	=	strain-displacement vector
$\mathbf{q}_i$	=	nodal internal force vector
$\mathbf{q}_e$	=	nodal external force vector
$\mathbf{g}$	=	out-of-balance force vector
$\mathbf{B}$	=	strain-displacement matrix
$\mathbf{K}_{t1}$,$\mathbf{K}_{tg}$	=	tangent stiffness matrix
$\mathbf{K}_{\sigma t}$	=	initial stress or geometric stiffness matrix
$\mathbf{K}_p$	=	stiffness matrix due to follower pressure load
$\mathbf{K}_T$	=	total stiffness matrix
$\mathbf{H}$	=	shape functions matrix (Section 3.2.2)
$\mathbf{t}_i$	=	element local triad
$\mathbf{L}$	=	shape functions matrix for general 3-noded membrane element
$\boldsymbol{\theta}$	=	vectorised form of the displacement derivative matrix
$\mathbf{G}$	=	matrix connecting $\boldsymbol{\theta}$ to $\mathbf{p}$
$\mathbf{T}$	=	transformation matrix
$\hat{\mathbf{S}}$	=	matrix containing second Piola-Kirchhoff stresses
$\mathbf{x}_{ij}$	=	$\mathbf{x}_i - \mathbf{x}_j$
$\mathbf{S}^L$	=	second Piola-Kirchhoff stress vector related to the Lagrangian triad
$\mathbf{E}^L$	=	Green's strain related to the Lagrangian triad
$\mathbf{R}$	=	rotation matrix
$\mathbf{h}$	=	shape functions vector
$\mathbf{h}_\xi$,$\mathbf{h}_\eta$	=	differential of $\mathbf{h}$ w.r.t. ξ and η, respectively
$\mathbf{J}$	=	Jacobian matrix
$\mathbf{h}^*$	=	shape functions vector for the incompatible modes
$\mathbf{u}^*$,$\mathbf{v}^*$	=	incompatible displacements (collectively called $\mathbf{p}^*$)
$\mathbf{B}^*$	=	strain-displacement matrix for the incompatible modes
$\boldsymbol{\theta}^*$	=	vectorised form of the displacement derivative matrix for the incompatible modes
$\mathbf{K}_{ll}$	=	conventional small-strain linear tangent stiffness matrix

$\mathbf{e}_1$,$\mathbf{e}_2$	=	co-rotating base vectors
$\mathbf{i}_1$,$\mathbf{i}_2$	=	global base vectors
$\mathbf{\Omega}_l$	=	pseudo-vector of local spin
$\mathbf{A}_l$	=	vector (or matrix) connecting ω_l (or $\mathbf{\Omega}_l$) to $\mathbf{p}$
$\mathbf{c}$	=	vector connecting a and $\mathbf{x}_g$ (see equation (5.25))
$\mathbf{d}$	=	vector connecting b and $\mathbf{x}_g$ (see equation (5.26))
$\mathbf{v}$	=	vector (or matrix) connecting $\delta\theta$ (or $\delta\boldsymbol{\theta}$) to $\delta\mathbf{p}$
$\bar{\mathbf{x}}_l$	=	special vector (see equation (5.46))
$\mathbf{E}$	=	matrix containing local frame $\mathbf{e}_1$,$\mathbf{e}_2$
$\mathbf{T}^j$	=	vector containing the jth column of $\mathbf{T}^T$
$\mathbf{G}^i$	=	special matrix (see equations (5.56) and (5.58))
$\boldsymbol{\theta}$	=	pseudo-vector with terms θ_1, θ_2 and θ_3 (see equation (6.23))
$\mathbf{S}$	=	skew-symmetric matrix (see equation (6.24))
$\mathbf{z}$	=	column matrix (see equation (6.34))
$\bar{\mathbf{q}}^j_{i,l}$	=	vector $\mathbf{R}\mathbf{q}^j_{il}$ for node j
$\mathbf{B}$	=	left Cauchy-Green tensor (see equation (7.2))
$\mathbf{a}_i$	=	principal direction vectors obtained from the local engineering strains
$\boldsymbol{\sigma}_l$	=	local stresses (Section 7.2)
$\mathbf{h}_p$	=	shape functions for the pressure term (Appendix B)
$\mathbf{P}$	=	pressure-displacement connectivity part of the stiffness matrix (Appendix B)
$\mathbf{H}$	=	pressure term stiffness matrix (Appendix B)

Chapter 1

Introduction

1.1 Motivation and aim of the study

From the beginning, the development of engineering tools for the analysis of complex problems has been an ultimate goal of researchers. Earlier workers had to rely on simple and relatively inaccurate techniques when tackling those complex problems. Without something that would enable them to perform difficult calculations, these engineers could only produce results that, although accurate enough for those days, could not be used in large and more complicated structures. With the introduction of digital computers, the engineering research stepped into a new phase of rapid development. An important product of this new technology is the Finite Element method and the possibility of studying problems of such a complexity that could hardly be imagined by previous engineers. This research focusses attention on the part of the Finite Element method that deals with non-linearity of structures, especially of those capable of undergoing large strains and deformation. The group of materials that will be considered is known as *Hyperelastic* and more details will be presented in the following chapter of this thesis.

In hyperelastic analysis the principal materials to be studied are the rubber-like ones. Rubbers present a relevant engineering importance due to their ability to support large elastic strains. Moreover, some special manufactured rubbers can actually replace traditional materials in a vast number of applications in structural engineering. Their employment in engineering, although not as widespread as steel, concrete or aluminium, for example, is very important since these materials act in critical parts of certain structural components. Consequently the engineer or designer should be able to understand and to apply the properties of rubbers or rubber compounds to supersede or to com-

plement the use of other materials. It is important to be aware of the advantages and disadvantages associated with the use of rubbers in order to assess their potential in relation to the field of application. Examples like shock absorbers that avoid damage in the interface between concrete and steel in a structure; rubber joints to seal parts in submerged tunnels and supports devices in bridges indicate clearly that a failure occurring in these complicated connections can cause serious damage to the structure or even its total collapse. There are numerous others applications for rubber-like materials including those in offshore engineering and the aerospace industry.

The aim of this work is to investigate new possibilities of utilising the Finite Element method to devise robust element formulations to analyse problems involving large displacements and large rotations. Additionally, the elements designed should be able to treat incompressibility or *near*-incompressibility and large-strains deformations, characteristics inherent of any hyperelastic structure. In the procedure used, there exists the commitment to avoid incorporating unnecessary complexities into the formulation of the different elements to be developed, without, however, compromising the excellent performance achieved here. One significant step towards this end is the application of lower order elements, in which the obvious advantages associated to their simplicity are apparent, in conjunction with approaches to improve the performance of these lower order elements and to enable them to be used in a non-linear environment.

1.2 A brief literature survey

The general study of mechanical structural behaviour of different materials is an old concern among researchers. Different behaviour means different forms of treatment for each type of material and each type of analysis. As discussed previously, in the present work we focus our attention on the non-linear geometric and physical analysis of continua with special emphasis on a class of materials known as hyperelastic. For this study special finite elements will be employed, including axisymmetric and three-dimensional membranes, plane-stress and plain-strain elements with incompatible displacement modes, two-dimensional and three-dimensional co-rotational elements and others. The formulation for these elements will be described in detail in this thesis.

The theoretical analysis of hyperelastic or rubberlike materials has been investigated by many authors since the first half of this century (see Treloar [91] and Mullins and Thomas [56] for an overview on the pioneering works in the field). The first considerations were based on experimental work and on the molecular structure of the

material. The major breakthrough in the study of the material came with the work of Mooney [55], that developed a general theory applicable to large deformations, and the subsequent studies of Rivlin [73]. Using continuum theory, a general way of achieving reliable analytical and numerical solutions for rubberlike materials is the application of the concept of a strain energy function [23, 91]. The Mooney-Rivlin approximation for the strain energy function is based on strain invariants and in the original developments the material is assumed to be isotropic and incompressible. However, the view of expressing the strain energy function in term of invariants is not always sufficiently accurate for large strain type analysis. Therefore, there was a need for a more flexible and effective way of dealing with hyperelasticity. Another important hypothesis is due to Valanis and Landel [92]. In their representation, the strain energy function is presented in a separable form in which the separate functions of the principal stretches are identical. Ogden in his paper of 1972 [61] proposed a new strain energy function which, in his own words, "*provides an adequate representation of the mechanical response of rubberlike solids and is simple enough to be amenable to mathematical analysis*". This function is a linear combination of power forms of the principal stretches and it has been broadly used in hyperelastic material analysis. It is noteworthy that at the beginning all the distinct propositions for the strain energy function were based in the assumption that rubberlike materials were perfectly incompressible. This affirmation is not completely true since some of the rubberlike materials exhibit a slight compressibility that should be taken into consideration, whence the strain energy functions have been modified, making feasible their use with *near-* or *quasi-*incompressible materials.

In relation to finite element approximations, some applications made in the late 1960s [60] are regarded as the first approaches applying the method. The strain energy function of Ogden is extensively employed although some of the works with finite elements also use a simpler Mooney-Rivlin model [13, 30, 37, 84]. Recently, several works have been published and major steps have been taken towards a fully comprehensive finite element formulation for hyperelasticity (see, for example, references [12, 33, 36, 49, 98]). A rather mathematical approach for the study of hyperelastic materials have been given by Dobrowolski [25].

An important factor in the study of large deformation and/or large strains is the special attention to be given when a pressure load is applied in such an analysis. It is known that pressure acts normal to the surface to which it has been applied. To allow the applied pressure to be maintain normal to the surface, a displacement-dependent pressure or "follower" load should be used [5, 39, 75]. This will bring into account a

new stiffness that should be added to the standard stiffness matrix.

With respect to the use of hyperelasticity, various applications can be found in the literature. They comprise the use of rubber-like materials in different fields like supports for bridges, piers and fenders, earthquake protection, aircraft engineering, shock and vibration isolation, offshore engineering among others [29, 83]. In addition, the theory of hyperelasticity can be applied as the basis for the study of large-strain plasticity problems (see, for example, [28, 70, 80, 22]).

As mentioned earlier, the Finite Element method plays an important role in the whole analysis of a non-linear structure. The reference books of Zienkiewicz and Taylor [101], Crisfield [18], Hughes [44] and Cook [15] in spite of presenting only a linear formulation, give the basic steps for the understanding of the method. The more advanced works in non-linear finite element can be found in the books of Bathe [6], Zienkiewicz and Taylor [102] , Crisfield [20] and Hinton [40].

With a view to developing finite elements capable of dealing with large deformations and incompressibility or *near*-incompressibility, a number of elements have arisen. Among them are the so-called mixed and hybrid elements which are a powerful class of element suitable for this kind of problem. In addition to the elements above, incompatible modes elements are also important in this study. Incompatible modes elements were first proposed by Wilson *et al.* [96] in 1973. The idea was to improve the performance of low-order elements in bending deformations. It also aimed to improve the accuracy for course meshes and with near incompressible and non-linear materials. One of the main problems of Wilson's element was that it could not cope with very distorted meshes. Taylor *et al.* [86] presented a way of correcting the problem by enforcing the satisfaction of the *patch test* [87]. More recent works [97, 46, 48] have been using incompatible modes based elements and successful results have been obtained. Other works (Simo *et al.* in [76] and [79], Andelfinger and Ramm [2] and Li [51]) have also been closely related to the original incompatible modes, even although the term "enhanced strain mixed method" is more generally used in these papers.

Another very usual way of tackling the problem of incompressibility is to separate the deviatoric part of the constitutive model from its volumetric part [15, 26, 44] [§]. The idea has been used by many authors [13, 27, 84] and excellent results have been obtained. This approximation is regard by many authors as a mixed and sometimes as a hybrid formulation.

The co-rotational finite element formulation is also an attractive technique for the

[§]This approach is also known as the **u-p** formulation

non-linear analysis. It has been used as an alternative strategy to analyse problems exhibiting large rotations during large deformation processes. The pioneering work in the field is due to Argyris *et al.* [3] and Wempner [95] in the sixties. The methodology implied the decomposition of the motion of the element into a rigid body motion followed by a deformation, or vice-versa, i.e., a deformation followed by a rigid body motion. This is the framework of the co-rotational technique in which the standard linear formulations can be used with respect to the rotating co-ordinate system and the non-linearities are incorporated via the rotation of this system. Argyris *et al.* [4], in a rather long paper, introduced their "natural method" that states that the rigid body modes may be large while the natural modes remain small. This approach is closely related to the co-rotational technique described above. Belytschko and co-workers [8, 9] applied the formulation to transient dynamic analysis of large-displacement and small-strain problems. In dealing with dynamic analysis using an explicit formulation the derivation of a tangent stiffness matrix is not treated, although Belytschko [9] showed that it was possible to generate a consistent tangent stiffness matrix using the co-rotational approach. He also outlined that the motion of the rigid-convected co-ordinate or co-rotational description leads to a simpler strain-displacement and force-stress relationships, resulting in a more efficient computational analysis. The work of Oran [65, 66, 67] also uses two-dimensional and three-dimensional co-rotational procedures to analyse the behaviour of beam-columns in a non-linear environment. However, his work for space frame [66] was limited to small increments. Later, Belytschko and Glaum [10] extended the dynamic formulation to a higher order co-rotational formulation which accounts for initial curvature and moderate variations of rigid body rotation within the element. In this work, shallow arches were loaded with point loads and the formulation converges more rapidly than the lower order one. Further work in the field was done by Hsiao and co-workers [41, 42, 43] for problems involving in-plane frames, flat triangular shells elements and spatial beam structures.

The argument that a non-linear analysis could be simply achieved by dissociating rotations from deformations, introducing the non-linearity into the transformation between the element frame and the global frame led some authors to simply derive the stiffness matrix by rotating it, via the transformation matrices, to the global co-ordinate system. However, this idea is not entirely true because it does not take into account the variation of the transformation matrices mentioned above. To extend the formulation towards a consistent derivation of the second contribution of the stiffness matrix, it is necessary to consistently differentiate the transformation matrices. Approaches such as

those by Crisfield [19], Cole [14], Peng and Crisfield [69] and Nygård [58] embody this differentiation, producing consistent co-rotational formulations for beams and shells.

As far as the application of co-rotational procedures for continua is concerned, the work of Jetteur and Cescotto [50] appears to have been the only proposition. In their paper, they described an incremental co-rotational formulation with the element formulation being developed for elastoplasticity with large-strains. However, their development did not consider the inclusion of the consistent derivation of the tangent stiffness matrix.

1.3 General layout of this thesis

This section briefly describes the contents of each part of the work with the thesis being organised as follows.

Chapter 2 contains a general overview into the subject of hyperelasticity. Some essential kinematics concepts are presented and some basic definitions of continuum mechanics are also reviewed. The chapter also describes some of the important work on hyperelasticity, especially presenting a review of the strain-energy functions used in hyperelastic simulations.

Chapter 3 concentrates on the development of two finite elements for hyperelastic membranes: an axisymmetric and a general three-dimensional approach. Both elements are evaluated using a total Lagrangian approach. The elements can take into account loads that are displacement-dependent in a consistent way. The hyperelastic model is introduced using first a Mooney-Rivlin material and subsequently employing an Ogden model. Various test cases are shown and compared against analytical and numerical results.

In Chapter 4 a plane-stress and plane-strain element is introduced. The element incorporates incompatible displacement modes that is improved to include non-linear capabilities into the element. Again the formulation is based on a total Lagrangian approach and follower loads are also studied. The hyperelasticity approximations are performed using an Ogden-type model. The chapter also contains numerical tests with the element and some problems with convergence are displayed.

Largely as a result of the problems faced by the element of the previous chapter, attention was turned towards a co-rotational formulation. Chapter 5 discusses a two-dimensional co-rotational approach for plane-stress and plane-strain conditions. The formulation is based on the idea of analysing the element in a linear way with respect

to a co-ordinate system attached to the element. The non-linearity is introduced by the rotation of this co-ordinate system. The linear element also comprises the incompatible modes defined in Chapter 4 in a linear manner. The tangent stiffness matrix is computed consistently producing a very robust formulation. The chapter is completed by a series of tests demonstrating the accuracy of the formulation.

Chapter 6 considers a full three-dimensional element. The theory for this element is again based on the co-rotational formulation. The technique utilises the polar decomposition theorem to treat effects arising from a rigid body rotation independently from the effects originating from the 'real' stretches. The element also includes incompatible displacement modes. The final tangent stiffness matrix is consistent and the desirable quadratic rate of convergence for the Newton-Raphson method is obtained. Numerical results are also presented at the end of the chapter.

Chapter 7 deals with hyperelastic applications for the two- and three-dimensional co-rotational elements of Chapters 5 and 6. A "Biot-type" formulation is adopted and applied with the Ogden model. The stress tensors and constitutive matrices are evaluated and several results are shown in order to assure the accuracy of the predictions.

The final chapter gives a summary of the conclusions and also some suggestions for future research.

Chapter 2

Hyperelasticity: Basic Concepts and Models Definitions

2.1 Introduction

A definition for hyperelasticity or more precisely for hyperelastic materials can be given as a group of materials which are able to recover their original undeformed state after being submitted to any large deformation pattern. The term hyperelasticity, therefore, merely defines a material capable of undergoing higher-order elastic deformation, fully recovering the strains when the imposing forces are released.

The best example of hyperelastic material is rubber. The term rubber was originally given to the material obtained from the tree *Hevea brasiliensis* [29, 91]. As far as the chemical composition is concerned, rubber is classified as lying within a group of materials named 'polymers'. This study, however, is not concerned with the microscopic aspects but concentrates its attention into the macroscopic elastic behaviour of the rubberlike or hyperelastic materials. A good review about the micro composition of rubber is given by Gent in [34].

Another way of defining hyperelasticity, in this case in a rather mathematical manner, is to associate it to the existence of a strain-energy function φ, that is, the strain energy per unit volume under deformation. A hyperelastic material is included among the so-called 'Green Elastic Material Models' [20, 23]. Different strain-energy functions can be used and have been proposed to describe the properties of a given hyperelastic material. Some of them are shown in this chapter. The derivation of the mechanical properties for hyperelasticity is also reviewed below.

2.2 General kinematic relations

The starting point to understand the mechanical behaviour of any elastic and hyperelastic material is the comprehension of its properties and physical response when the material is submitted to a certain deformation. The approach to be followed is phenomenological, based on the theory of elasticity and the mathematical formulation of the (macroscopic) properties of such a theory [63, 62].

The hyperelastic model is expressed in terms of a strain-energy function φ that can be formulated using either the strain invariants of the right Cauchy-Green tensor $\mathbf{C}$ or the principal stretches ratios $\lambda_1, \lambda_2, \lambda_3$. However, before moving to a typical representation of a strain-energy function it is worth reviewing some basic but fundamental definitions in the study of continuum mechanics.

In continuum mechanics, a number of different strain measures can be used. When the deflections are large (in hyperelasticity, besides the deflections the strains are also large), it is often convenient to use the 'Green-Lagrange' or simply 'Green' strain tensor, $\mathbf{E}$. In conjunction with finite element procedures this approach involves the *total Lagrangian formulation.* Later in this chapter another strain tensor will be described which can be applied with the so-called *co-rotational technique.*

The Green strain tensor can be written as [20]

$$\mathbf{E} = \frac{1}{2}[\mathbf{F}^T\mathbf{F} - \mathbf{I}] \tag{2.1}$$

where $\mathbf{F}$ is the deformation gradient.

$$\mathbf{F} = \frac{\partial \mathbf{x}}{\partial \mathbf{X}} = \mathbf{I} + \mathbf{D} \tag{2.2}$$

The matrix $\mathbf{D}$ above is the displacement-derivative or the displacement-gradient matrix and is given by

$$\mathbf{D} = \frac{\partial \mathbf{u}}{\partial \mathbf{X}} \tag{2.3}$$

In equation (2.1) defined above, the term $\mathbf{F}^T\mathbf{F}$ is known as the right Cauchy-Green tensor $\mathbf{C}$. Using polar decomposition (see references [54, 82, 45, 20] for details) it can be shown that the eigenvalues of $\mathbf{C}$ are the squares of the principal stretches λ_i and the eigenvectors are the principal directions, which define the Lagrangian (or material) triad, i.e., we can write

$$\mathbf{C} = \mathbf{Q}(\mathbf{N})[\mathbf{diag}(\lambda_i^2)]\mathbf{Q}^T(\mathbf{N}) \tag{2.4}$$

where $\mathbf{Q(N)} = [\mathbf{N_1 N_2 N_3}]$ is the matrix containing the principal directions vectors $\mathbf{N}_1$, $\mathbf{N_2}$ and $\mathbf{N_3}$ and $[\mathbf{diag}(\lambda_i^2)]$ is the 3×3 diagonal matrix containing the λ_i^2 values. The above definitions are very important for the future development of the formulation.

Having defined $\mathbf{C}$, we also need to obtain the invariants of $\mathbf{C}$ which will be utilised in some of the hyperelastic constitutive models to be formulated later. The invariants, in terms of the components of $\mathbf{C}$ and in terms of principal stretches, are

$$\begin{aligned} I_1 &= \mathrm{tr}(\mathbf{C}) = C_{11} + C_{22} + C_{33} = \lambda_1^2 + \lambda_2^2 + \lambda_3^2 \\ I_2 &= \text{cofactor of } C_{ii} \\ &= C_{11}C_{22} + C_{22}C_{33} + C_{33}C_{11} - C_{12}C_{21} - C_{23}C_{32} - C_{13}C_{31} \\ &= \lambda_2^2\lambda_3^2 + \lambda_3^2\lambda_1^2 + \lambda_1^2\lambda_2^2 \\ I_3 &= \det\mathbf{C} = C_{11}C_{22}C_{33} + 2C_{12}C_{23}C_{13} - C_{11}C_{23}C_{32} - C_{22}C_{13}C_{31} - C_{33}C_{12}C_{21} \\ &= \lambda_1^2\lambda_2^2\lambda_3^2 \end{aligned} \tag{2.5}$$

The stress measure used in conjunction with the Green's strain tensor of equation (2.1) is the second Piola-Kirchhoff stress tensor, here called $\mathbf{S}$. This stress measure is work-conjugate with $\mathbf{E}$, i.e., the virtual work expression is given by

$$V = V_i - V_e = \int_{V_o} \mathbf{S} : \delta\mathbf{E}_v dV_o - V_e \tag{2.6}$$

where V_i and V_e are the internal and external virtual works, respectively.

Note that the measures defined for stress and strain are given in terms of tensors. They can also be represented as vectors and for many of the subsequent finite element developments we will use the latter configuration. Although the symbols will be the same for both tensors and vectors, the context will make the difference clear .

Another relevant stress measure that should be mentioned here is the Cauchy or true stress. The use of Cauchy stress $\boldsymbol{\sigma}$ instead of the second Piola-Kirchhoff stress, $\mathbf{S}$, eases the interpretation of the final results. The former relates the forces to the final area where they have been applied whereas the latter relates them to the original area and to the original configuration.

The Cauchy stress is work-conjugate to $\delta\boldsymbol{\varepsilon}_v$ [§] and is related to the Second Piola-

[§]This strain measure can be regarded as a form of engineering strain increment but related to the current configuration [20] and can be written as

$$\delta\boldsymbol{\varepsilon}_v = \frac{1}{2}[\frac{\partial\delta\mathbf{u}_v}{\partial\mathbf{x}} + \frac{\partial\delta\mathbf{u}_v}{\partial\mathbf{x}}^T]$$

Kirchhoff stress via

$$\boldsymbol{\sigma} = \frac{1}{J}\mathbf{F}\mathbf{S}\mathbf{F}^T \tag{2.7}$$

with $J = \det\mathbf{F}$ or $J = I_3^{\frac{1}{2}} = \lambda_1\lambda_2\lambda_3$.

We can define an equivalent stress measure to the Cauchy stress but related to the original volume. It is known as the Kirchhoff stress and is given by

$$\boldsymbol{\tau} = J\,\boldsymbol{\sigma} \tag{2.8}$$

The question at this stage is how to obtain the stresses for a hyperelastic material from a strain-energy function? If the strain-energy function φ is the strain energy per unit initial volume under deformation, the change of φ is expressed as

$$\delta\varphi = \mathbf{S} : \delta\mathbf{E} \tag{2.9}$$

Hence,

$$\mathbf{S} = \frac{\partial\varphi}{\partial\mathbf{E}} \tag{2.10}$$

The previous relation can be called the Green elastic constitutive law and can be obtained as follows: using the first law of thermodynamics, i.e., "The work of the external forces done on a body plus the heat that flows into the system is equal to the increase of kinetic energy plus the increase in internal strain-energy" or

$$\delta W_{ext} + \delta Q = \delta T + \delta\varphi \tag{2.11}$$

From the principle of conservation of energy, the total work performed by the forces applied in a body (internal and external) is equal to the variation of the kinetic energy, hence

$$\delta W_{ext} + \delta W_{int} = \delta T \tag{2.12}$$

If we have no heat flow, using equations (2.11) and (2.12), we obtain

$$\delta W_{int} = -\delta\varphi, \tag{2.13}$$

so that the variation of the work done by the internal forces is equal to minus the variation of the strain-energy. If there is no variation of kinetic energy, (2.12) and (2.13) lead to

$$\delta W_{ext} = \delta \varphi \tag{2.14}$$

At this point we write the change of external work as

$$\delta W_{ext} = \int_V F_i \delta u_i dV + \int_A \sigma_{ij} n_i \delta u_i dA \tag{2.15}$$

where: F_i are the external body forces applied in each direction;

u_i are the displacement components;

σ_{ij} are the surface (Cauchy) stresses;

n_i are the direction cosines normal to the surface A.

Following Desai and Siriwardane [23], it can be shown from virtual work that equation (2.15) above leads to

$$\delta W_{ext} = \int_{V_o} S_{ij} \delta E_{ij} dV_o \tag{2.16}$$

Now, from (2.14), we can write

$$\delta \varphi = \int_{V_o} S_{ij} \delta E_{ij} dV_o \tag{2.17}$$

and then,

$$\delta \varphi = \int_{V_o} \delta \varphi_o dV_o \tag{2.18}$$

From (2.17) and (2.18), dropping the subscript o for initial, we reach (2.9), hence (2.10).

From (2.10), a second variation with respect to the strain yields the necessary tangent relationship, i.e., $\mathbf{D}$.

$$\delta \mathbf{S} = \mathbf{D} : \delta \mathbf{E} \tag{2.19}$$

and

$$\mathbf{D} = \frac{\partial^2 \varphi}{\partial \mathbf{E}^2} \tag{2.20}$$

Equation (2.20) clearly illustrates that the tangent tensor $\mathbf{D}$ is not constant for hyperelastic materials but rather is dependent upon the current strains.

If, instead of using a total Lagrangian approach, we decide to make use of the co-rotational formulation (details will be given in Chapter 6 and 7), a different strain tensor can be applied. The most convenient strain tensor turns out to be the so-called *Biot*

strain tensor, represented by $\mathbf{E}_b$. It comes from the concept of co-rotated engineering strain,i.e., $\epsilon = \lambda - 1$. Using the definitions given by Crisfield [20, 21] (see also [54, 82, 45]) and the polar decomposition theorem,

$$\begin{aligned} \mathbf{E}_b &= \mathbf{Q}(\mathbf{N})[\mathbf{diag}(\lambda_i - 1)]\mathbf{Q}^T(\mathbf{N}) = \mathbf{Q}(\mathbf{N})[\mathbf{diag}(\lambda_i)]\mathbf{Q}^T(\mathbf{N}) - \mathbf{Q}(\mathbf{N})\mathbf{Q}^T(\mathbf{N}) \\ &= \mathbf{U} - \mathbf{I} \end{aligned} \tag{2.21}$$

where $\mathbf{Q}(\mathbf{N})$ is the same as in (2.4) and $[\mathbf{diag}(\lambda_i - 1)]$ is the diagonal matrix containing the $\lambda_i - 1$ values.

We have to consider the stress measure that is work-conjugate to the Biot strain. This stress is known as *Biot stress* and using (2.6) the virtual work is given by [21]

$$V_i = \int_{V_o} \mathbf{S} : \delta\mathbf{E}_v \, dV_o = \int_{V_o} \boldsymbol{\sigma}_b : \delta\mathbf{E}_{bv} \, dV_o = \int_{V_o} \boldsymbol{\sigma}_b : \delta\mathbf{U}_v \, dV_o \tag{2.22}$$

Thus, equations (2.9) and (2.10) are re-defined as

$$\delta\varphi = \boldsymbol{\sigma}_b : \delta\mathbf{E}_b \tag{2.23}$$

and

$$\boldsymbol{\sigma}_b = \frac{\partial\varphi}{\partial\mathbf{E}_b} \tag{2.24}$$

2.3 Hyperelastic material models

Various attempts have been made to represent the mechanical behaviour of hyperelastic materials, especially the rubber-like ones, in terms of a strain-energy function. Some of these works are described in this review although as far as the finite elements simulations are concerned, we will concentrate this study mainly on the strain-energy function proposed by Ogden [61]. Ogden's model has been widely used to treat the properties of rubberlike structures in engineering design and the results produced are very accurate. Moreover, this model can still represent two other models, also extensively used by researchers and designers, the neo-Hookean and the Mooney-Rivlin models.

As mentioned before the approach described and employed in this work is phenomenological and no attention is given to the molecular structure of the material. One could divide the several representations of the strain-energy functions into two major groups: the first in which constitutive relations are described in terms of the invariants of the right Cauchy-Green tensor $\mathbf{C}$ and the second where the relations are defined via the principal stretches (or extension ratios), λ_i. We shall start with the former.

Among the strain-energy functions developed, the one proposed by Mooney [55] and later modified by Rivlin [73] is one of the most known. Mooney developed a theory based in two assumptions that (i) rubber is incompressible and isotropic in the undeformed state and (ii) Hooke's law is obeyed in simple shear. His theory yields a strain-energy function of the form:

$$\varphi = C_1(\lambda_1^2 + \lambda_2^2 + \lambda_3^2 - 3) + C_2(\lambda_1^{-2} + \lambda_2^{-2} + \lambda_3^{-2} - 3) \tag{2.25}$$

Equation (2.25) represents quite accurately simple extensions but can give serious problems when other kinds of strain are imposed [90]. In a subsequent work, Rivlin amended Mooney's theory and the strain-energy is then expressed in terms of invariants of **C**. This new function takes the invariants I_1 and I_2 to be the two independent variables from which the state of strain is defined. So, the series

$$\varphi = \sum_{i=1;j=1}^{\infty} C_{ij}(I_1 - 3)^i(I_2 - 3)^j \tag{2.26}$$

represents the most general form of the strain-energy. The first order approximation of (2.26) is the expression for the Mooney-Rivlin model that is one of the most utilised in rubber elasticity analysis, that is,

$$\varphi = C_1(I_1 - 3) + C_2(I_2 - 3) \tag{2.27}$$

From the expression above another particular strain-energy function can be derived by setting $C_2 = 0$. This leads to the neo-Hookean form of the strain-energy function, i.e.,

$$\varphi = C_1(I_1 - 3) \tag{2.28}$$

It should be noted that the equations above are valid for incompressible materials for which $J = 1$. In other words, equations (2.27) and (2.28) represent only the deviatoric part of the strain-energy function since the volumetric part does not change. This strict incompressibility is not always true for a hyperelastic material and a small compressibility may be allowed, especially in problems involving plane-strain and three-dimensional analysis. Therefore, a term involving the bulk modulus k can be added to the strain-energy expressions. The volumetric part of φ may be written as

$$\varphi_b = \frac{1}{2}k(J-1)^2 \qquad \text{or} \qquad \varphi_b = \frac{1}{2}k(lnJ)^2 \tag{2.29}$$

and the fully incompressible state must be recovered if k tends to infinity. φ_b is zero for the undeformed initial configuration where $J = 1$.

Following the work of Crisfield [21], we can produce expressions for the strain-energy function of (2.27) and (2.28) for a compressible hyperelastic material. The neo-Hookean compressible form can be given by

$$\varphi = C_1'(I_1 - 3I_3^{1/3}) + \varphi_b \tag{2.30}$$

whereas the Mooney-Rivlin form would be (see also [31])

$$\varphi = C_1'(I_1 - 3I_3^{1/3}) + C_2'(I_2 - 3I_3^{2/3}) + \varphi_b \tag{2.31}$$

Here, a strictly separation between the deviatoric and the volumetric parts of the strain-energy functions is opportune. This is so due to the appropriateness of such a split when one examines and predicts the behaviour of hyperelastic materials, making easier the validation of each part by experimental tests. Thus, we can define new modified invariants, so that

$$\bar{I}_1 = I_1 I_3^{-1/3} \tag{2.32}$$

$$\bar{I}_2 = I_2 I_3^{-2/3} \tag{2.33}$$

that come from the new modified stretches,

$$\bar{\lambda}_i = J^{-1/3}\lambda_i \tag{2.34}$$

Note that $\bar{J} = \bar{\lambda}_1\bar{\lambda}_2\bar{\lambda}_3 = 1$, that is, the $\bar{\lambda}_i$ are as such as there is no change in the volume.

Hence, from (2.32) and (2.33) we get the strictly separated strain-energy function for a neo-Hookean and a Mooney-Rivlin materials (equations (2.30) and (2.31)), respectively, as

$$\varphi = C_1(\bar{I}_1 - 3) + \frac{1}{2}k(J-1)^2 \tag{2.35}$$

and

$$\varphi = C_1(\bar{I}_1 - 3) + C_2(\bar{I}_2 - 3) + \frac{1}{2}k(J-1)^2 \tag{2.36}$$

Other strain-energy functions have also been formulated based on the invariants of **C** but they are not shown here. They include the contributions of Blatz and Ko [11] and Fried and Johnson [31].

Before continuing the development, it is worth emphasizing that rubber-like materials are regarded as isotropic. This condition implies that their principal directions of stress and strain coincide. This characteristic will be used throughout this work.

The second group of strain-energy functions that can be used is that described by the principal stretches. The principal stretches can be determined from the square root of the eigenvalues of the right Cauchy-Green tensor **C**, i.e., the squares of the principal stretches are the main diagonal of the matrix **C** when this matrix is rotated to the principal axes. Hence, in the principal directions $\mathbf{N}_1$–$\mathbf{N}_3$ (see (2.4)),

$$\mathbf{C} = \begin{bmatrix} \lambda_1^2 & 0 & 0 \\ 0 & \lambda_2^2 & 0 \\ 0 & 0 & \lambda_3^2 \end{bmatrix} \tag{2.37}$$

Several proposals have been given to represent, in a more general way, the mechanical properties of a hyperelastic material via the principal stretches. From them the proposition of Valanis and Landel [92] and the work of Ogden [61] are selected and shown here. Details of other representations can be found in Treloar [90] among others.

Valanis and Landel have formulated a strain-energy function for an incompressible isotropic hyperelastic material that can be expressed as the sum of symmetrical functions of the principal stretches λ_i, as shown below.

$$\varphi = \phi(\lambda_1) + \phi(\lambda_2) + \phi(\lambda_3) \tag{2.38}$$

where the three functions $\phi(\lambda_i)$ are identical.

It has been demonstrated that the hypothesis of Valanis and Landel produces results which are in close agreement with experimental observations [90].

Ogden [61], still assuming incompressibility for hyperelasticity, proposed a strain-energy function able to predict accurately the mechanical behaviour of a material under very large strain that is expressible as

$$\varphi = \sum_p \frac{\mu_p}{\alpha_p}[\lambda_1^{\alpha_p} + \lambda_2^{\alpha_p} + \lambda_3^{\alpha_p} - 3] \tag{2.39}$$

in which μ_p and α_p are the model constants. Furthermore, these constants have to satisfy

$$2\mu = \sum_p \mu_p \alpha_p \tag{2.40}$$

(μ is the ground state of the shear modulus) in order to guarantee the compatibility with an analysis which involves small deformations (the classical Hooke's law). This expression recovers the ground-state of the shear modulus [61].

This formulation incorporates some of the previous propositions, including those based on the invariants. The incompressible neo-Hookean is recovered by using $p = 1$ and $\alpha_1 = 2$, whereas the incompressible Mooney-Rivlin can be derived by setting $p = 2$ and $\alpha_1 = 2$, $\alpha_2 = -2$. The constants C_1 and C_2 are retrieved by taking $C_1 = \frac{\mu_1}{2}$ and $C_2 = \frac{\mu_2}{2}$.

By including different number of terms in (2.39), it is possible to express different stress-strain relations with the desired degree of accuracy.

As for the compressible approximation for the Ogden model, again a compressible term (or volumetric term) φ_b, equation (2.29), should be added to the deviatoric term of the modified function φ_d. This modified function, separated into a deviatoric and a volumetric parts, can be found adopting the same approach applied for the invariant-based strain-energy functions, that is, replacing λ_i of (2.39) by (2.34), so that we have

$$\varphi = \sum_p \frac{\mu_p}{\alpha_p}[\bar{\lambda}_1^{\alpha_p} + \bar{\lambda}_2^{\alpha_p} + \bar{\lambda}_3^{\alpha_p} - 3] + \frac{1}{2}k(J-1)^2 \tag{2.41}$$

and, again, the modified stretches are volume constant. Therefore, (2.41) is to be used in plane-strain and solid analysis as in Chapters 4 and 7.

Chapter 3

Membrane Finite Elements for Hyperelastic Materials Analysis

3.1 Introduction

The idea in this chapter is to produce a finite element for a membrane, in this first place axisymmetrical, which is able to support large displacements and strains and therefore to study structures designed with hyperelastic (rubberlike) materials. It is intended to begin the investigation into the area of large strains using these simple elements. The work will be expanded subsequently in later chapters to applications with other more complex kinds of element.

In this work, first the formulation for a geometrically non-linear axisymmetric membrane is discussed. In the second part, a general tridimensional membrane is analysed. For both cases, the procedures to establish the out-of-balance force vectors and the tangent the stiffness matrices are shown. Afterwards, an extension for a displacement-dependent load vector is introduced. This new vector will produce a non-symmetric element stiffness matrix which can end up, after the assembly procedure, in either a symmetric or a non-symmetric matrix at the total structure level. This will depend on the class of problem that is being studied.

The modifications to handle rubberlike materials are then introduced. They are basically to calculate new strains and stresses values and to define a non-linear constitutive matrix. Thus, the procedure to obtain the new tangent stiffness matrix is the same as previously used.

This work follows the developments made by Crisfield [20] for a truss element and is applied to introduce the concept of hyperelasticity. The work of Wriggers and Taylor

[98] and Gruttmann and Taylor [36] are also used as references, although the latter was not available when the formulation was first derived.

Several examples are presented to depict the accuracy and efficiency of the formulation. Furthermore, the present element produces a very good quadratic rate of convergence which ensures the consistency of the formulation.

3.2 Axisymmetric membrane element for hyperelastic materials analysis

3.2.1 Finite element development

In the introduction of this thesis, the importance of materials with hyperelastic behaviour for certain kinds of structures was stressed. A first step to begin the study of such materials is to develop a membrane element (axisymmetric) that is able to perform non-linear analysis of large strain, particularly working with rubberlike materials. The total Lagrangian approach is applied and it is shown that, even for this sort of analysis, it produces very accurate results.

To begin the development of the element it is necessary to define the shape functions by using isoparametric approximations. Hence, the R co-ordinate and the displacements (figure 3.1) are interpolated through

$$u = 1/2 \left\{ \begin{array}{c} 1-\xi \\ 1+\xi \end{array} \right\}^T \left\{ \begin{array}{c} u_1 \\ u_2 \end{array} \right\}$$

$$w = 1/2 \left\{ \begin{array}{c} 1-\xi \\ 1+\xi \end{array} \right\}^T \left\{ \begin{array}{c} w_1 \\ w_2 \end{array} \right\} \qquad (3.1)$$

$$R = 1/2 \left\{ \begin{array}{c} 1-\xi \\ 1+\xi \end{array} \right\}^T \left\{ \begin{array}{c} R_1 \\ R_2 \end{array} \right\}$$

$$\mathbf{p}^T = \left(\begin{array}{cccc} u_1 & w_1 & u_2 & w_2 \end{array} \right) \qquad (3.2)$$

Because this is an axisymmetric membrane, the strains to be computed are the axial (along the membrane, in its meridional direction) and the hoop strains. These values, here called E_1 and E_2, respectively, are Green's strains. The first one can be written in exactly the same way as in a truss element [20], i.e.,

$$E_1 = \frac{l_n^2 - l_o^2}{2l_o^2} = \mathbf{b}_1^T \mathbf{p} + \frac{1}{2\alpha_o^2} \mathbf{p}^T \bar{\mathbf{A}} \mathbf{p} \tag{3.3}$$

$$\mathbf{b}_1^T = \tfrac{1}{4\alpha_o^2} \begin{pmatrix} -R_{21} & -Z_{21} & R_{21} & Z_{21} \end{pmatrix} \tag{3.4}$$

where, for example,

$$R_{21} = R_2 - R_1,$$

$$\bar{\mathbf{A}} = \frac{1}{4} \begin{bmatrix} 1 & 0 & -1 & 0 \\ 0 & 1 & 0 & -1 \\ -1 & 0 & 1 & 0 \\ 0 & -1 & 0 & 1 \end{bmatrix}, \tag{3.5}$$

l_n is the final length of the element and $l_o = 2\alpha$ is the original length.

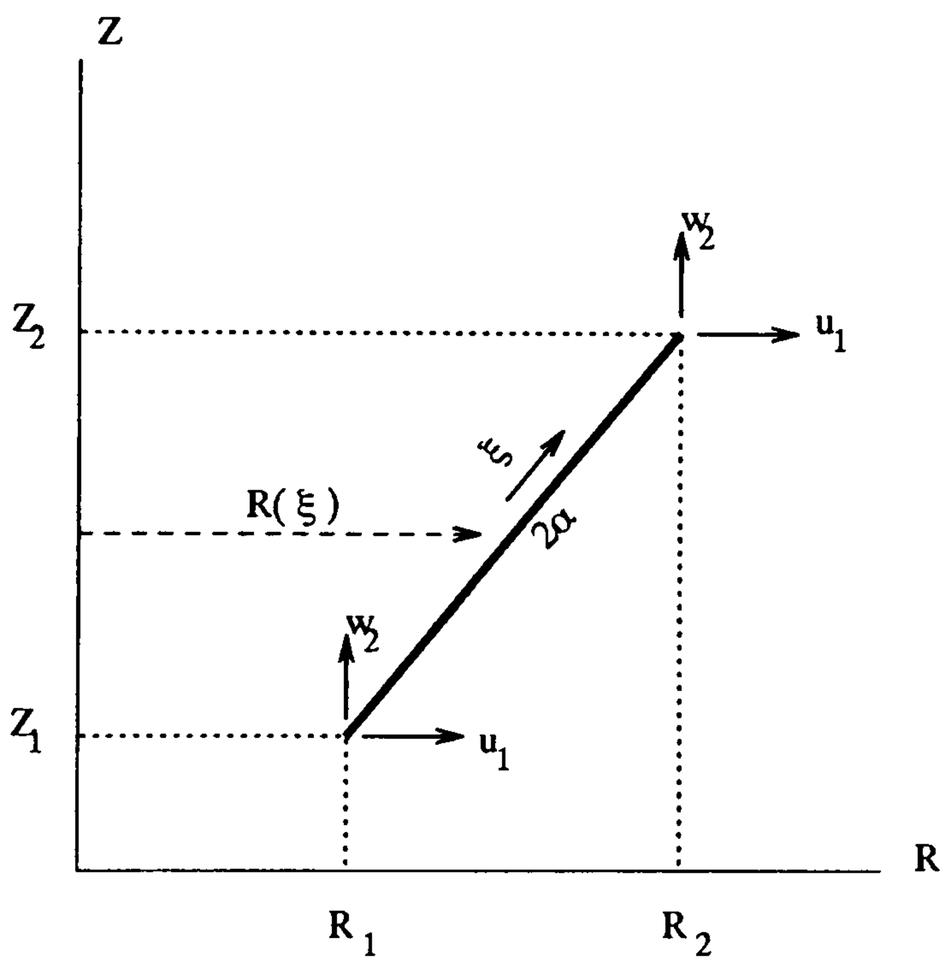


Figure 3.1: Axisymmetric membrane element

The change in E_1, after some calculations, results in

$$\begin{aligned} \delta E_1 &= \frac{1}{4\alpha_o^2} \begin{bmatrix} -(R_{21} + u_{21}) & -(Z_{21} + w_{21}) & (R_{21} + u_{21}) & (Z_{21} + w_{21}) \end{bmatrix} \delta \mathbf{p} \\ &= (\mathbf{b}_1^T + \mathbf{b}_2^T)\, \delta \mathbf{p} = \mathbf{b}_{nl}^T\, \delta \mathbf{p} \end{aligned} \tag{3.6}$$

where

$$\mathbf{b}_2^T = \frac{1}{4\alpha_o^2}\begin{pmatrix} -u_{21} & -w_{21} & u_{21} & w_{21} \end{pmatrix} \tag{3.7}$$

$$u_{21} = u_2 - u_1$$

and the value $\mathbf{b}_1$ has already been established in (3.4).

With C_o and C_n as the old and new circumferences, the hoop strain E_2 can be define as

$$E_2 = \frac{C_n^2 - C_o^2}{2C_o^2} = \frac{u}{R} + \frac{1}{2}(\frac{u}{R})^2 = E_{2l} + \frac{1}{2}E_{2l}^2 \tag{3.8}$$

$$E_{2l} = \frac{u}{R(\xi)} = \mathbf{d}^T\mathbf{p} = \frac{1}{2R(\xi)}\begin{pmatrix} 1-\xi & 0 & 1+\xi & 0 \end{pmatrix}^T\mathbf{p} = \frac{(h_1u_1 + h_2u_2)}{R(\xi)} \tag{3.9}$$

It could be worth emphasizing that, unlike the axial strain, the circumferential strain is not constant within the element and therefore it must be evaluated at the Gauss point level in the integration process, hence the application of shape function in the definition above.

From (3.8), the change in E_2 is given by

$$\delta E_2 = (1+E_{2l})\delta E_{2l} = (1+E_{2l})\mathbf{d}^T\delta\mathbf{p} = \frac{(1+E_{2l})}{R(\xi)}\begin{pmatrix} h_1 & 0 & h_2 & 0 \end{pmatrix}\delta\mathbf{p} \tag{3.10}$$

Now, by placing both changes of strain in a matrix form, one can obtain

$$\delta E = \begin{Bmatrix} \delta E_1 \\ \delta E_2 \end{Bmatrix} = \begin{bmatrix} \mathbf{b}_{nl}(\mathbf{p})^T \\ (1+E_{2l})\mathbf{d}^T \end{bmatrix}\delta\mathbf{p}$$

$$= \begin{bmatrix} -\frac{1}{4\alpha_o^2}(R_{21}+u_{21}) & -\frac{1}{4\alpha_o^2}(Z_{21}+w_{21}) & \frac{1}{4\alpha_o^2}(R_{21}+u_{21}) & \frac{1}{4\alpha_o^2}(Z_{21}+w_{21}) \\ \frac{1+E_{2l}}{R(\xi)}h_1 & 0 & \frac{1+E_{2l}}{R(\xi)}h_2 & 0 \end{bmatrix}\delta\mathbf{p} \tag{3.11}$$

$$= \mathbf{B}_{nl}\,\delta\mathbf{p}$$

The internal force vector, calculated using virtual work [20], is written as

$$\mathbf{q}_i = \int_{V_o} \mathbf{B}_{nl}^T\,\mathbf{S}\,dV_o \tag{3.12}$$

The stress vector $\mathbf{S}$ shown above contains the second Piola-Kirchhoff stresses. These stresses are derived straight from Green's strains, being computed as

$$\mathbf{S} = \mathbf{D}\,\mathbf{E} \qquad \text{or} \qquad \left\{ \begin{array}{c} S_1 \\ S_2 \end{array} \right\} = \mathbf{D} \left\{ \begin{array}{c} E_1 \\ E_2 \end{array} \right\} \tag{3.13}$$

It is important to highlight that in the current development all the strains and stresses measures are in principal directions which do not change.

The **D** matrix in equation (3.13) is the constitutive or modular matrix which relates stresses and strains. For the case of small strain analysis, this matrix is only a function of Young's modulus and Poisson's ratio and it does not change during a non-linear analysis, i.e.,

$$\mathbf{D} = \frac{E}{1-\nu^2} \left[\begin{array}{cc} 1 & \nu \\ \nu & 1 \end{array} \right] \tag{3.14}$$

On the other hand, as will be shown later, in an analysis of rubberlike materials, involving large strains, this **D** matrix should be updated at every iteration during the non-linear process.

Carrying on from this point, it is necessary to compute the out-of-balance force vector g as follow:

$$\mathbf{g} = \mathbf{q}_i - \mathbf{q}_e \tag{3.15}$$

where $\mathbf{q}_i$ and $\mathbf{q}_e$ are the internal and external nodal force vectors, respectively.

It should be noted that for a first analysis only the internal force vector $\mathbf{q}_i$ is displacement- dependent, whereas the applied load (external force vector $\mathbf{q}_e$) is constant. Thus the differentiation of the out-of-balance force vector, that yields the stiffness matrix, is actually the differentiation of $\mathbf{q}_i$ for this case. Using this, the change of $\mathbf{q}_i$ is given by

$$\delta\mathbf{q}_i = \int_{V_o} (\mathbf{B}_{nl}^T\,\delta\mathbf{S} + \delta\mathbf{B}_{nl}^T\,\mathbf{S})\,dV_o \tag{3.16}$$

The tangent stiffness matrix is composed of two parts: the first portion, here called $\mathbf{K}_{t1}$, is the standard stiffness matrix obtained from the first term of (3.16); the second one, $\mathbf{K}_{\sigma g}$, is the geometric or initial stress stiffness matrix, derived from the second term in the same expression (3.16).

$$\mathbf{K}_{t1} = \int_{V_o} \mathbf{B}_{nl}^T\,\mathbf{D}\,\mathbf{B}_{nl}\,dV_o \tag{3.17}$$

$$\mathbf{K}_{\sigma g} = \int_{V_o} \frac{1}{\alpha_o^2}\,S_1\,\bar{\mathbf{A}}\,dV_o + \int_{V_o} S_2\,\mathbf{d}\,\mathbf{d}^T\,dV_o \tag{3.18}$$

where $\bar{\mathbf{A}}$ have been defined in (3.5) and $\mathbf{d}$ have been defined in (3.10). S_1 and S_2 are the two principal components of $\mathbf{S}$.

Note that

$$dV_o = 2\pi\, t_o\, R(\xi)\, \alpha_o\, d\xi \tag{3.19}$$

3.2.2 Displacement-dependent pressure load

Since the purpose here is to use the axisymmetric element to study rubberlike materials, before defining the quantities related to such analysis (strains, stresses, constitutive matrix etc), it is relevant to have in mind the modifications in the external force vector when a pressure load is applied. In this case, where very large strains and displacements are involved, this vector will be dependent on the current configuration rather than on the original one [75, 5, 39]. So, the external force vector should be updated at each step of the non-linear procedure. Hence, from virtual work

$$\delta \mathbf{p}_v^T \mathbf{q}_e = \int_a p^* \delta e'_v da \tag{3.20}$$

where: $\delta \mathbf{p}_v$ are the virtual displacements;

$\mathbf{q}_e$ is the external load vector;

p^* is the applied pressure (here assumed constant);

$\delta e'_v$ is the change of displacement in the direction of the normal to the surface on each area da.

Observe that the lower case characters used in the notation mean that these quantities are related to the current configuration of the structure.

From figure 3.2 comes

$$\begin{aligned} r_1 &= R_1 + u_1 \qquad & z_1 &= Z_1 + w_1 \\ r_2 &= R_2 + u_2 \qquad & z_2 &= Z_2 + w_2 \end{aligned} \tag{3.21}$$

$$r_{21} = R_{21} + u_{21} \qquad z_{21} = Z_{21} + w_{21}$$

where $r_{21} = r_2 - r_1$ and $u_{21} = u_2 - u_1$, for example.

To calculate $\delta e'_v$, firstly it is necessary to define the tangent and the normal vectors of the element. Thus,

$$\mathbf{t}_n = \frac{1}{2\alpha_n} \begin{Bmatrix} r_{21} \\ z_{21} \end{Bmatrix} \tag{3.22}$$

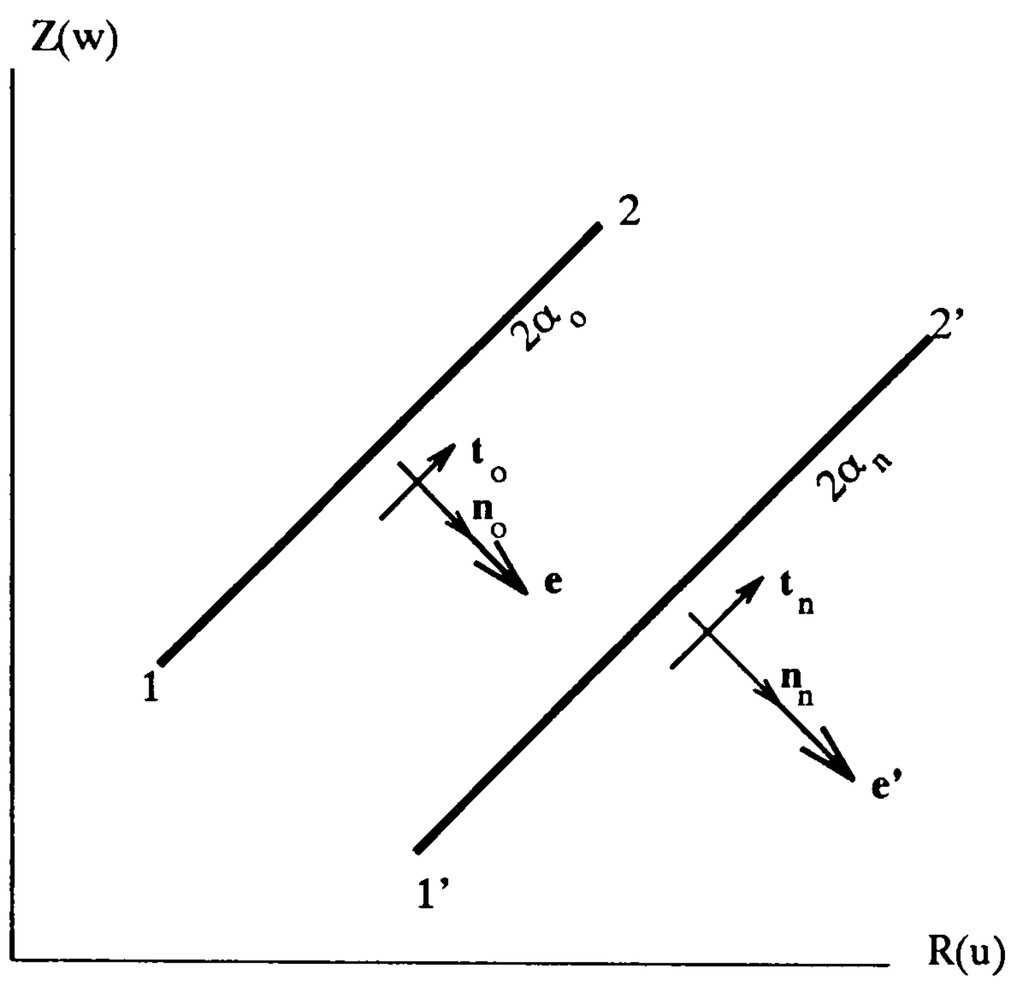


Figure 3.2: Original and final configurations of the element

and then

$$\mathbf{n}_n = \frac{1}{2\alpha_n} \begin{Bmatrix} z_{21} \\ -r_{21} \end{Bmatrix} \tag{3.23}$$

Following the development, $\delta e'_v$ is determined as

$$\delta e'_v = \delta \mathbf{u}_v^T \, \mathbf{n}_n = \delta \mathbf{p}_v^T \, \mathbf{H}^T \, \mathbf{n}_n \tag{3.24}$$

with

$$\delta \mathbf{u}_v = \frac{1}{2} \begin{bmatrix} 1-\xi & 0 & 1+\xi & 0 \\ 0 & 1-\xi & 0 & 1+\xi \end{bmatrix} \delta \mathbf{p}_v = \mathbf{H} \, \delta \mathbf{p}_v \tag{3.25}$$

In equation (3.20), da is defined as

$$da = 2\pi \, r(\xi) \, \alpha_n \, d\xi \tag{3.26}$$

with $r(\xi)$ as in (3.1) but now using the current co-ordinates instead of the original ones.

Applying (3.24) and (3.26) in (3.20), we have

$$\delta \mathbf{p}_v^T \, \mathbf{q}_e = \int_{-1}^{1} p^* \, \delta \mathbf{p}_v^T \, \mathbf{H}^T \, \mathbf{n}_n \, 2\pi \, r(\xi) \, \alpha_n \, d\xi \tag{3.27}$$

Equation (3.27) must apply for any $\mathbf{p}_v$. So that,

$$\mathbf{q}_e = \frac{p^*\pi}{3}\begin{Bmatrix} z_{21}(2r_1 + r_2) \\ z_{21}(r_1 + 2r_2) \\ -r_{21}(2r_1 + r_2) \\ -r_{21}(r_1 + 2r_2) \end{Bmatrix} \tag{3.28}$$

After obtaining the displacement-dependent $\mathbf{q}_e$ vector, the new part of the stiffness matrix, produced from this new $\mathbf{q}_e$, must be computed and added to that originally defined in (3.17) and (3.18). Re-writing equation (3.15) using the new $\mathbf{q}_e$ which relates to a fixed pressure p^*, it becomes

$$\mathbf{g} = \mathbf{q}_i(\mathbf{p}) - \lambda \mathbf{q}_e(\mathbf{p}) \tag{3.29}$$

The term λ is a vector loading multiplier which multiplies the fixed pressure p^*. For load control, during the Newton-Raphson iterations, this factor is kept fixed for each increment. The parameter can be made variable when some other techniques (arc-length, for example) are employed, as will be seen later in this chapter.

From the derivative of (3.29) with relation to the displacements, it follows that

$$\mathbf{K}_t = \frac{\partial \mathbf{g}}{\partial \mathbf{p}} = \frac{\partial \mathbf{q}_i(\mathbf{p})}{\partial \mathbf{p}} - \lambda \frac{\partial \mathbf{q}_e(\mathbf{p})}{\partial \mathbf{p}} \tag{3.30}$$

In the above, the first term $\frac{\partial \mathbf{q}_i(\mathbf{p})}{\partial \mathbf{p}}$ has been previously described and can be seen in (3.17) and (3.18). The second derivative that involves $\mathbf{q}_e$ is computed directly from (3.28) and can be expressed as

$$\mathbf{K}_p = \frac{\partial \mathbf{q}_e(\mathbf{p})}{\partial \mathbf{p}} = \frac{p^*\pi}{3}\begin{bmatrix} 2z_{21} & -(2r_1 + r_2) & z_{21} & 2r_1 + r_2 \\ 4r_1 - r_2 & 0 & -(r_1 + 2r_2) & 0 \\ z_{21} & -(r_1 + 2r_2) & 2z_{21} & r_1 + 2r_2 \\ 2r_1 + r_2 & 0 & r_1 - 4r_2 & 0 \end{bmatrix} \tag{3.31}$$

This matrix is clearly non-symmetric and an appropriate solver should be used in a general case. However, when dealing with conservative systems, despite the fact that this matrix is non-symmetric, after the process of assembling each element into the total matrix for the structure, the resulting stiffness matrix is symmetric [75] and then a standard symmetric solver is better applied. Some examples that confirm this affirmation are shown at the end of this chapter.

The final stiffness matrix for one element is re-expressed as

$$\mathbf{K}_T = (\mathbf{K}_t + \mathbf{K}_{\sigma g}) - \lambda \mathbf{K}_p \tag{3.32}$$

with $\mathbf{K}_t$, $\mathbf{K}_{\sigma g}$ and $\mathbf{K}_p$ from (3.18), (3.19) and (3.32), respectively.

3.2.3 Hyperelasticity

The aim now is to define the stresses and strains and the constitutive matrix for applications to hyperelastic materials. Two different material definitions for rubberlike materials will be used. In the first place, the material to be studied is the Mooney-Rivlin material [55, 73]. Its strain-energy function is given in terms of principal stretches, as in (2.25), by

$$\varphi = C_1(\lambda_1^2 + \lambda_2^2 + \lambda_3^2 - 3) + C_2(\lambda_1^{-2} + \lambda_2^{-2} + \lambda_3^{-2} - 3) \tag{3.33}$$

The constants C_1 and C_2 are determined through experiments. The principal stretches λ_i can be obtained from the Green's strains defined earlier in this context, i.e.,

$$\begin{gathered} E_1 = \frac{l_n^2 - l_o^2}{2l_o^2} = 1/2\lambda_1^2 - 1/2 = 1/2(\lambda_1^2 - 1) \rightarrow \lambda_1^2 = 2E_1 + 1 \\ E_2 = \frac{C_n^2 - C_o^2}{2C_o^2} = 1/2(\lambda_2^2 - 1) \rightarrow \lambda_2^2 = 2E_2 + 1 \end{gathered} \tag{3.34}$$

Hence,

$$\lambda_i^2 = 2E_i + 1 \tag{3.35}$$

Applying the incompressibility condition

$$\lambda_1 \lambda_2 \lambda_3 = 1 \tag{3.36}$$

into expression (3.33) gives

$$\bar{\varphi} = C_1(\lambda_1^2 + \lambda_2^2 + \lambda_1^{-2}\lambda_2^{-2} - 3) + C_2(\lambda_1^{-2} + \lambda_2^{-2} + \lambda_1^2\lambda_2^2 - 3) \tag{3.37}$$

Using $\bar{\varphi}$ above, the Cauchy stresses can be written as [63]

$$\sigma_i = \lambda_i \frac{\partial \bar{\varphi}}{\partial \lambda_i} \tag{3.38}$$

which results in

$$\sigma_i = 2C_1(\lambda_i^2 - \lambda_1^{-2}\lambda_2^{-2}) - 2C_2(\lambda_i^{-2} - \lambda_1^2\lambda_2^2) \tag{3.39}$$

From this point, it is necessary to replace the Cauchy stresses by the second Piola-Kirchhoff stresses, which are work conjugate to the Green's strains.

The relationship between the Cauchy stresses and the second Piola-Kirchhoff stresses is given by (see (2.7))

$$\mathbf{S} = \frac{1}{J}\mathbf{F}^{-1}\,\boldsymbol{\sigma}\,\mathbf{F}^{-T} \tag{3.40}$$

where $\mathbf{F}$ is the deformation-gradient matrix of (2.2), i.e., $\mathbf{F} = \frac{\partial \mathbf{x}}{\partial \mathbf{X}}$. In terms of principal values (see equation (2.37)),

$$\mathbf{F} = \begin{bmatrix} \lambda_1 & 0 & 0 \\ 0 & \lambda_2 & 0 \\ 0 & 0 & \lambda_3 \end{bmatrix} \tag{3.41}$$

Because for incompressibility $J = det\mathbf{F} = 1$, equation (3.40) yields

$$S_i = \frac{1}{\lambda_i^2}\sigma_i = \frac{1}{\lambda_i}\frac{\partial \bar{\varphi}}{\partial \lambda_i} \tag{3.42}$$

which represents the new second Piola-Kirchhoff stresses for the material, considering it as a Mooney-Rivlin material.

There is an alternative and more straightforward way to calculate the second Piola-Kirchhoff stresses. Now the stresses are computed directly for the change of the strain energy function in relation to each strain. Using incompressibility in the Mooney-Rivlin strain function (3.37), the principal stresses become

$$S_1 = \frac{\partial \bar{\varphi}}{\partial E_1} = \frac{\partial \bar{\varphi}}{\partial \lambda_1}\frac{\partial \lambda_1}{\partial E_1} = 2C_1(1 - \lambda_1^{-4}\lambda_2^{-2}) + 2C_2(-\lambda_1^{-4} + \lambda_2^2) \tag{3.43}$$

$$S_2 = \frac{\partial \bar{\varphi}}{\partial E_2} = 2C_1(1 - \lambda_1^{-2}\lambda_2^{-4}) + 2C_2(-\lambda_2^{-4} + \lambda_1^2) \tag{3.44}$$

From this point the development is precisely the same as that already given.

The Mooney-Rivlin function of (3.33) and other *deviatoric* energy functions, normally only define the deviatoric stresses and it leaves an undefined pressure term. Strictly, this pressure term should have been considered, but it will be shown that, for the present problem, the results are the same as those just given. To achieve this, initially all three stretches $(\lambda_1, \lambda_2, \lambda_3)$ are kept and working from the energy function of (3.33) (rather than (3.37)), the Cauchy stresses are derived as

$$\sigma_i = \lambda_i \frac{\partial \varphi}{\partial \lambda_i} - p = \lambda_i (2C_1 \lambda_i - 2C_2 \lambda_i^{-3}) - p \tag{3.45}$$

where p is the pressure (positive for compression).

For a plane stress case in a membrane, the condition $\sigma_3 = 0$ is valid, so that

$$\lambda_3 (2C_1 \lambda_3 - 2C_2 \lambda_3^{-3}) = p \tag{3.46}$$

which allows the elimination of p.

Substituting (3.46) into (3.45) we obtain σ_1 and σ_2. To eliminate λ_3, the incompressibility condition of (3.36) is used. This process finally leads to (3.39) above.

As a last step for fulfilling the requirements of an analysis of a rubberlike material, it is necessary to define the new tangential modular matrix, **D**. This matrix is required for the change of the internal force vector of (3.12).

Hence,

$$\delta S_i = D_{ij}\, \delta E_j \tag{3.47}$$

but, from (3.35)

$$\delta E_i = \lambda_i\, \delta \lambda_i \tag{3.48}$$

and finally (see (3.43), (3.44) and (3.48)),

$$\begin{Bmatrix} \delta S_1 \\ \delta S_2 \end{Bmatrix} = \begin{bmatrix} \frac{1}{\lambda_1}\frac{\partial S_1}{\partial \lambda_1} & \frac{1}{\lambda_2}\frac{\partial S_1}{\partial \lambda_2} \\ \frac{1}{\lambda_1}\frac{\partial S_2}{\partial \lambda_1} & \frac{1}{\lambda_2}\frac{\partial S_2}{\partial \lambda_2} \end{bmatrix} \begin{Bmatrix} \delta E_1 \\ \delta E_2 \end{Bmatrix} \tag{3.49}$$

So that, (3.49) leads to

$$\begin{Bmatrix} \delta S_1 \\ \delta S_2 \end{Bmatrix} = \begin{bmatrix} 8\lambda_1^{-6}(C_1\lambda_2^{-2} + C_2) & 4[C_1(\lambda_1\lambda_2)^{-4} + C_2] \\ \text{Sym.} & 8\lambda_2^{-6}(C_1\lambda_1^{-2} + C_2) \end{bmatrix} \begin{Bmatrix} \delta E_1 \\ \delta E_2 \end{Bmatrix} \tag{3.50}$$

This matrix **D** replaces (3.14) and, as mentioned before, depends upon the current configuration of the membrane, therefore it should be updated for the calculation of (3.17).

After having defined all the parameters to work with a Mooney-Rivlin material, we can use similar steps to study an Ogden material [63]. The strain-energy function for this material, as in (2.39), becomes

$$\varphi = \sum_p \frac{\mu_p}{\alpha_p} [\lambda_1^{\alpha_p} + \lambda_2^{\alpha_p} + \lambda_3^{\alpha_p} - 3] \tag{3.51}$$

Henceforth, the procedure follows exactly the same steps that have been used for Mooney-Rivlin. The Cauchy stresses, from (3.38), are

$$\sigma_i = \sum_p \mu_p [\lambda_i^{\alpha_p} - (\lambda_1 \lambda_2)^{-\alpha_p}] \tag{3.52}$$

and then, with the help of (3.42), it is easy to find the second Piola-Kirchhoff stresses.

The modular matrix for an Ogden material should also be established, i.e.,

$$\mathbf{D} = \begin{bmatrix} D_{11} & D_{12} \\ D_{21} & D_{22} \end{bmatrix} \tag{3.53}$$

with

$$\begin{aligned} D_{11} &= \frac{1}{\lambda_1^4} \sum_p \mu_p [(\alpha_p - 2)\lambda_1^{\alpha_p} + (\alpha_p + 2)(\lambda_1 \lambda_2)^{-\alpha_p}] \\ D_{12} &= D_{21} = \frac{1}{\lambda_1^2 \lambda_2^2} \sum_p \mu_p \alpha_p (\lambda_1 \lambda_2)^{-\alpha_p} \\ D_{22} &= \frac{1}{\lambda_2^4} \sum_p \mu_p [(\alpha_p - 2)\lambda_2^{\alpha_p} + (\alpha_p + 2)(\lambda_1 \lambda_2)^{-\alpha_p}] \end{aligned} \tag{3.54}$$

In an Ogden type material, the second Piola-Kirchhoff stresses can also be determined by applying the same derivation of $\bar{\varphi}$ in relation to the strains as before (see (3.43) and (3.44)) and will yield a similar expression for $\mathbf{S}$.

$$S_i = \sum_p \frac{\mu_p}{\lambda_i^2} [\lambda_i^{\alpha_p} - (\lambda_1 \lambda_2)^{-\alpha_p}] \tag{3.55}$$

The solution of problems that exhibit large deformation, such as those with rubber-like materials now being studied, is very likely to present limit and bifurcation points. To enable solutions that overcome these limit-points and the snap-throughs and snap-backs that eventually occur, one needs procedures to be able to follow these post-limit paths and then to determine accurately the total behaviour of the structure. A very powerful way to examine these problems is to use the arc-length method in addition to the Newton-Raphson method [17, 20]. The combination of these methods results in an efficient tool which makes it possible to achieve accurate solution for the problem and, in addition, it produces a desirable quadratic convergence rate for the numerical algorithm. A brief comment on the arc-length method, laying emphasis on the current element and the displacement-dependent load, is given in appendix A of this thesis.

3.3 General three-dimensional non-linear membrane element

3.3.1 Finite element development

In the second part of this chapter, we work to develop an element for non-linear analysis of thin membrane structures with arbitrary shape. The extension of the axisymmetric membrane element to a general membrane element is an inevitable step since an axisymmetric element is only able to handle very limited kinds of problems. It is essential to cover a broader class of problems, hence the need of a new and more powerful element.

In this development, we use an Ogden type material (it was shown before that this material is attractive since its formulation covers, as special cases, the so-called Mooney-Rivlin and Neo-Hookean materials) and, consequently, the material strain-energy function is given with respect to the principal directions. Again we derive the finite element equations for the element using a total Lagrangian formulation.

One of the major difficulties of the general membrane is that, unlike the axisymmetric membrane stress state, the principal directions of the stretches, required by the formulation, do not coincide with the axes of the natural coordinates system. These principal stretches are computed from the right Cauchy-Green tensor $\mathbf{C}$ defined in Chapter 2. The tensor $\mathbf{C}$ is written in terms of the deformation-gradient matrix $\mathbf{F}$ as $\mathbf{C} = \mathbf{F}^T\mathbf{F}$. During the computations, the incompressibility condition for rubberlike materials must also be satisfied.

As a first step to develop a three-dimensional continuum membrane finite element, we need to define an initial local orthogonal system. The element developed here is the simplest triangular membrane element with corner nodes only. From figure 3.3, the local co-ordinate system is defined as

$$\mathbf{t}_1 = \frac{\mathbf{X}_{21}}{S_{21}}$$

$$\bar{\mathbf{t}}_2 = \frac{\mathbf{X}_{31}}{S_{31}} \tag{3.56}$$

$$\mathbf{t}_3 = \mathbf{t}_1 \times \bar{\mathbf{t}}_2 = \frac{\mathbf{X}_{21} - \mathbf{X}_{31}}{2a}$$

$$\mathbf{t}_2 = \mathbf{t}_3 \times \mathbf{t}_1$$

where $\mathbf{X}_{21} = \mathbf{X}_2 - \mathbf{X}_1$, $\mathbf{X}_{31} = \mathbf{X}_3 - \mathbf{X}_1$, S_{21} = length of $\mathbf{X}_{21}$ and S_{31} = length of $\mathbf{X}_{31}$.

By using area coordinates [101] the shape functions for the displacements can be

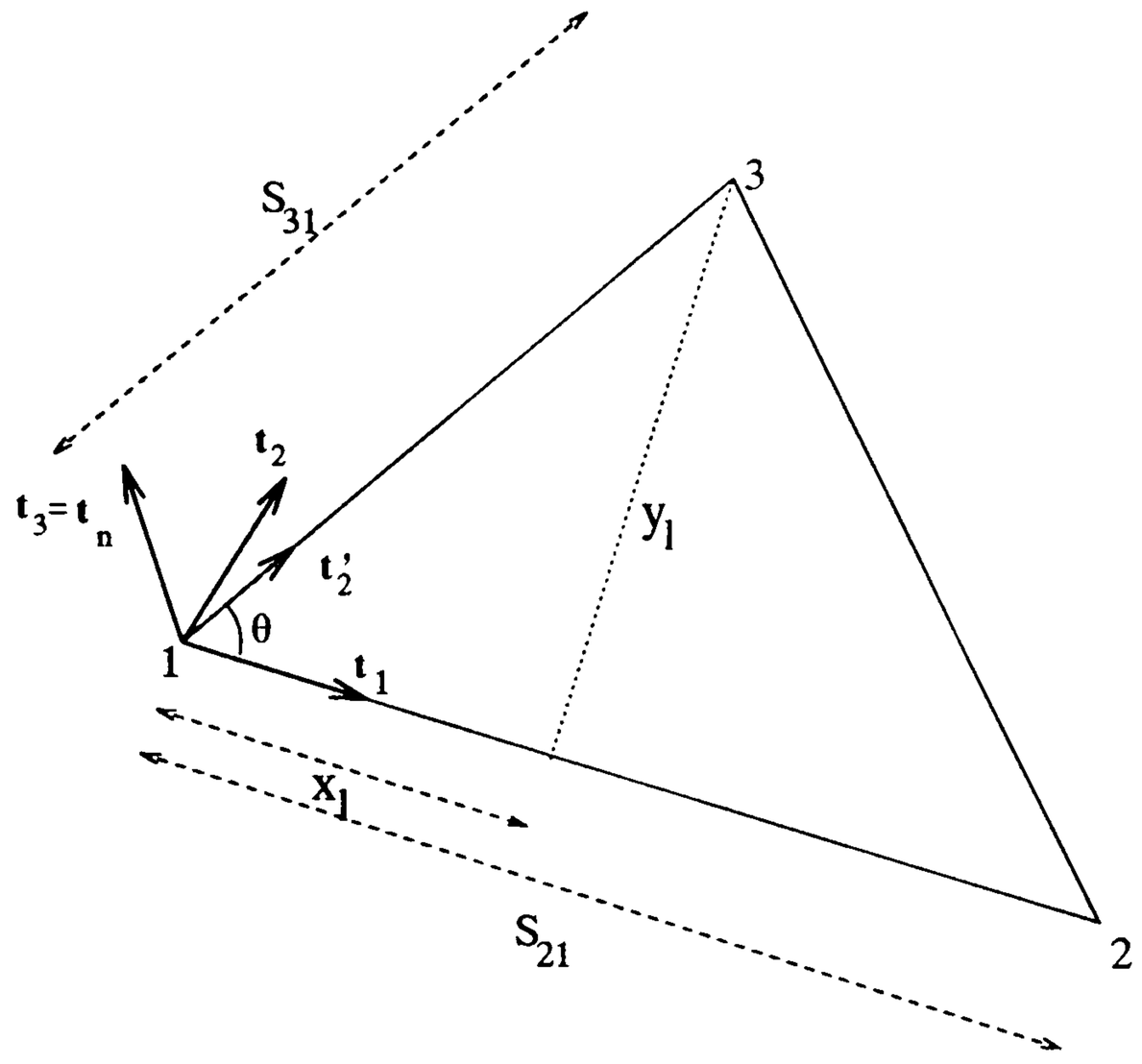


Figure 3.3: three-dimensional membrane element

found. Hence, the local displacements u_l, v_l and w_l and the nodal values are related by

$$\begin{Bmatrix} u_l \\ v_l \\ w_l \end{Bmatrix} = \begin{bmatrix} L_1 & 0 & 0 & L_2 & 0 & 0 & L_3 & 0 & 0 \\ 0 & L_1 & 0 & 0 & L_2 & 0 & 0 & L_3 & 0 \\ 0 & 0 & L_1 & 0 & 0 & L_2 & 0 & 0 & L_3 \end{bmatrix} \begin{Bmatrix} u_1 \\ v_1 \\ w_1 \\ u_2 \\ v_2 \\ w_2 \\ u_3 \\ v_3 \\ w_3 \end{Bmatrix}_l = \mathbf{L}\,\mathbf{p}_l \qquad (3.57)$$

where

$$L_i = \frac{a_i + b_i X_l + c_i Y_l}{2A}$$

and $a_1 = X_2Y_3 - X_3Y_2$; $b_1 = Y_2 - Y_3$ and $c_1 = X_3 - X_2$, for example.

From the above, the Jacobian follows as

$$\begin{Bmatrix} \frac{\partial}{\partial X_l} \\ \frac{\partial}{\partial Y_l} \end{Bmatrix} = \begin{bmatrix} \frac{\partial L_1}{\partial X_l} & \frac{\partial L_2}{\partial X_l} & \frac{\partial L_3}{\partial X_l} \\ \frac{\partial L_1}{\partial Y_l} & \frac{\partial L_2}{\partial Y_l} & \frac{\partial L_3}{\partial Y_l} \end{bmatrix} \begin{Bmatrix} \frac{\partial}{\partial L_1} \\ \frac{\partial}{\partial L_2} \\ \frac{\partial}{\partial L_3} \end{Bmatrix}$$

$$= \frac{1}{2A} \begin{bmatrix} b_1 & b_2 & b_3 \\ c_1 & c_2 & c_3 \end{bmatrix} \begin{Bmatrix} \frac{\partial}{\partial L_1} \\ \frac{\partial}{\partial L_2} \\ \frac{\partial}{\partial L_3} \end{Bmatrix} \tag{3.58}$$

Equation (3.58) yields the vectorised form of the local displacement derivative tensor, here represented by $\boldsymbol{\theta}_l$, as

$$\boldsymbol{\theta}_l = \begin{Bmatrix} \frac{\partial u_l}{\partial X_l} \\ \frac{\partial v_l}{\partial X_l} \\ \frac{\partial w_l}{\partial X_l} \\ \frac{\partial u_l}{\partial Y_l} \\ \frac{\partial v_l}{\partial Y_l} \\ \frac{\partial w_l}{\partial Y_l} \end{Bmatrix} = \frac{1}{2A} \begin{bmatrix} b_1 & 0 & 0 & b_2 & 0 & 0 & b_3 & 0 & 0 \\ 0 & b_1 & 0 & 0 & b_2 & 0 & 0 & b_3 & 0 \\ 0 & 0 & b_1 & 0 & 0 & b_2 & 0 & 0 & b_3 \\ c_1 & 0 & 0 & c_2 & 0 & 0 & c_3 & 0 & 0 \\ 0 & c_1 & 0 & 0 & c_2 & 0 & 0 & c_3 & 0 \\ 0 & 0 & c_1 & 0 & 0 & c_2 & 0 & 0 & c_3 \end{bmatrix} \mathbf{p}_l = \mathbf{G}_l \, \mathbf{p}_l \tag{3.59}$$

where $\mathbf{p}_l$ above contains the local nodal displacements.

Following the same steps as in [20], we proceed to the determination of the local (initial) Green's strains that can be written in the expression

$$\mathbf{E}_l = \begin{Bmatrix} \frac{\partial u_l}{\partial X_l} \\ \frac{\partial v_l}{\partial Y_l} \\ \frac{\partial u_l}{\partial Y_l} + \frac{\partial v_l}{\partial X_l} \end{Bmatrix} + \frac{1}{2} \begin{bmatrix} \frac{\partial u_l}{\partial X_l} & 0 & \frac{\partial v_l}{\partial X_l} & 0 & \frac{\partial w_l}{\partial X_l} & 0 \\ 0 & \frac{\partial u_l}{\partial Y_l} & 0 & \frac{\partial v_l}{\partial Y_l} & 0 & \frac{\partial w_l}{\partial Y_l} \\ \frac{\partial u_l}{\partial Y_l} & \frac{\partial u_l}{\partial X_l} & \frac{\partial v_l}{\partial Y_l} & \frac{\partial v_l}{\partial X_l} & \frac{\partial w_l}{\partial Y_l} & \frac{\partial w_l}{\partial X_l} \end{bmatrix} \boldsymbol{\theta}_l \tag{3.60}$$

From the above,

$$\mathbf{E}_l = \left[\mathbf{H} + \frac{1}{2} \mathbf{A}_l(\boldsymbol{\theta}_l) \right] \boldsymbol{\theta}_l \tag{3.61}$$

where,

$$\mathbf{H} = \begin{bmatrix} 1 & 0 & 0 & 0 & 0 & 0 \\ 0 & 0 & 0 & 1 & 0 & 0 \\ 0 & 1 & 1 & 0 & 0 & 0 \end{bmatrix} \tag{3.62}$$

At this stage, we have to use the transformation matrix to relate local to global displacements, therefore the local strains can be obtained straight from the (total) global

displacements. The transformation matrix comes from the initial triad established in equations (3.56)[§]. Then the local displacements can be expressed, for each node, by

$$\left\{ \begin{array}{c} u_l \\ v_l \\ w_l \end{array} \right\}_i = \underbrace{\left[\begin{array}{c} \mathbf{t}_1^T \\ \mathbf{t}_2^T \\ \mathbf{t}_3^T \end{array} \right]}_{\mathbf{T}_i} \left\{ \begin{array}{c} u_g \\ v_g \\ w_g \end{array} \right\}_i \tag{3.63}$$

or,

$$\mathbf{p}_l = \mathbf{T}\,\mathbf{p}_g \tag{3.64}$$

with

$$\mathbf{T} = [\mathbf{diag}\ \mathbf{T}_i] \tag{3.65}$$

From (3.59) and (3.64), we obtain

$$\boldsymbol{\theta}_l = \mathbf{G}_l \mathbf{T}\,\mathbf{p}_g = \mathbf{G}_{lg}\,\mathbf{p}_g \tag{3.66}$$

Equation (3.61) can be re-written as

$$\mathbf{E}_l = \left[\mathbf{H} + \frac{1}{2}\mathbf{A}_l(\boldsymbol{\theta}_l)\right] \mathbf{G}_{lg}\,\mathbf{p}_g \tag{3.67}$$

The change in Green's strain is given by

$$\delta\mathbf{E}_l = [\mathbf{H}\mathbf{G}_{lg} + \mathbf{A}_l(\boldsymbol{\theta}_l)\mathbf{G}_{lg}]\ \delta\mathbf{p}_g = [\mathbf{B}_L + \mathbf{B}_{NL}]\ \delta\mathbf{p}_g = \mathbf{B}\,\delta\mathbf{p}_g \tag{3.68}$$

Observe that in the equation above higher order terms have been neglected. The subscripts L and NL mean linear and non-linear, respectively.

For small virtual displacements, (3.68) is written

$$\delta\mathbf{E}_{l_v} = \mathbf{B}\,\delta\mathbf{p}_{g_v} \tag{3.69}$$

From virtual work [20], we can calculate the out-of-balance force as

$$\mathbf{g} = \mathbf{q}_{i_g} - \mathbf{q}_{e_g} = \int_{V_o} \mathbf{B}^T\,\mathbf{S}_l\,dV_o - \mathbf{q}_{e_g} = \int_{V_o} \mathbf{G}_{lg}^T[\mathbf{H} + \mathbf{A}_l]^T\mathbf{S}_l\,dV_o - \mathbf{q}_{e_g} \tag{3.70}$$

where $\mathbf{q}_{i_g}$ and $\mathbf{q}_{e_g}$ are the internal and external global force vectors, respectively.

The stresses $\mathbf{S}_l$ shown in (3.70) are the (local) second Piola-Kirchhoff stresses which for small strains analysis are computed direct from the (local) Green's strains via a fixed modular matrix $\mathbf{D}$.

[§]In the following the transformation matrix $\mathbf{T}$ is fixed. A different approach will be presented in the later chapters which describe the co-rotational formulation.

Differentiating the $\mathbf{g}$ vector (3.70), we obtain the tangent stiffness matrix $\mathbf{K}_t$ for the membrane.

$$\delta\mathbf{g} = \delta\mathbf{q}_{i_g} - \delta\mathbf{q}_{e_g} = \int_{V_o} (\mathbf{B}^T\,\delta\mathbf{S} + \delta\mathbf{B}^T\,\mathbf{S})\,dV_o + 0 \tag{3.71}$$

$$\mathbf{K}_t = \int_{V_o} \left[\mathbf{B}^T\,\mathbf{D}\,\mathbf{B} + \mathbf{G}^T\,\hat{\mathbf{S}}_l\,\mathbf{G}\right] dV_o \tag{3.72}$$

where $\hat{\mathbf{S}}_l$ is given by

$$\hat{\mathbf{S}}_l = \begin{bmatrix} \begin{bmatrix} S_{11} & S_{12} \\ S_{12} & S_{22} \end{bmatrix} & \mathbf{0} & \mathbf{0} \\ \mathbf{0} & \begin{bmatrix} S_{11} & S_{12} \\ S_{12} & S_{22} \end{bmatrix} & \mathbf{0} \\ \mathbf{0} & \mathbf{0} & \begin{bmatrix} S_{11} & S_{12} \\ S_{12} & S_{22} \end{bmatrix} \end{bmatrix}_l \tag{3.73}$$

3.3.2 Load vector and stiffness matrix for a follower pressure load

As already mentioned, for large displacement and/or large strain analysis we must compute a new load vector, updated throughout the process, as well as a new portion of the stiffness matrix which is displacement-dependent.

We begin with the definition of the load vector. Figure 3.3 represents the element we are studying.

Let a be the current area of the element, defined as

$$a = |\mathbf{x}_{21} \times \mathbf{x}_{31}| = \{(\mathbf{x}_{21} \times \mathbf{x}_{31})^T(\mathbf{x}_{21} \times \mathbf{x}_{31})\}^{\frac{1}{2}} \tag{3.74}$$

where $\mathbf{x}_{21}$ is the vector $\mathbf{x}_2 - \mathbf{x}_1$ and $\mathbf{x}_{31}$ is the vector $\mathbf{x}_3 - \mathbf{x}_1$. The use of low case characters in these vectors means that these vectors are related to the current (updated) configuration ($\mathbf{x} = \mathbf{X} + \mathbf{u}$). The same local element trial $\mathbf{t}_1$, $\mathbf{t}_2$, $\mathbf{t}_3$ of (3.56) is used but now with current instead of initial co-ordinates being applied.

Using virtual work, it follows that

$$\delta\mathbf{p}_v^T\,\mathbf{q}_e = \int_A p^*\,\delta e'_v\,da \tag{3.75}$$

with p^* being the applied pressure.

To calculate $\delta e'_v$ (the change of the displacement in the normal direction of da) of (3.75), we take

$$\delta e'_v = \delta \mathbf{u}_v^T \, \mathbf{t}_3 = \delta \mathbf{p}_v^T \, \mathbf{L}^T \, \mathbf{t}_3 \tag{3.76}$$

with L from (3.57).

Knowing that

$$\int_A L_i \, da = \frac{a}{3}$$

and after some calculations, we finally obtain the new external force vector or the new load vector, so that

$$\mathbf{q}_e = \frac{p^* \, a}{3} \bar{\mathbf{H}}^T \, \mathbf{t}_3 \tag{3.77}$$

where,

$$\bar{\mathbf{H}} = \begin{bmatrix} 1 & 0 & 0 & 1 & 0 & 0 & 1 & 0 & 0 \\ 0 & 1 & 0 & 0 & 1 & 0 & 0 & 1 & 0 \\ 0 & 0 & 1 & 0 & 0 & 1 & 0 & 0 & 1 \end{bmatrix} \tag{3.78}$$

Now the $\mathbf{q}_e$ vector is dependent on the current configuration of the structure,i.e., $\mathbf{q}_e(\mathbf{p})$, therefore the variation the expression for the out-of-balance force vector (3.70) will produce a stiffness matrix with an extra term due to this new $\mathbf{q}_e$. The new portion to be added in the previous stiffness matrix established in (3.72) is

$$\mathbf{K}_p = \tfrac{p^*}{6} \bar{\mathbf{H}}^T \, \bar{\mathbf{E}} \tag{3.79}$$

$$= \frac{p^*}{6} \begin{bmatrix} 0 & e_{12}+f_{12} & e_{13}+f_{13} & 0 & -e_{12} & -e_{13} & 0 & -f_{12} & -f_{13} \\ -(e_{12}+f_{12}) & 0 & e_{23}+f_{23} & e_{12} & 0 & -e_{23} & f_{12} & 0 & -f_{23} \\ -(e_{13}+f_{13}) & -(e_{23}+f_{23}) & 0 & e_{13} & e_{23} & 0 & f_{13} & f_{23} & 0 \\ 0 & e_{12}+f_{12} & e_{13}+f_{13} & 0 & -e_{12} & -e_{13} & 0 & -f_{12} & -f_{13} \\ -(e_{12}+f_{12}) & 0 & e_{23}+f_{23} & e_{12} & 0 & -e_{23} & f_{12} & 0 & -f_{23} \\ -(e_{13}+f_{13}) & -(e_{23}+f_{23}) & 0 & e_{13} & e_{23} & 0 & f_{13} & f_{23} & 0 \\ 0 & e_{12}+f_{12} & e_{13}+f_{13} & 0 & -e_{12} & -e_{13} & 0 & -f_{12} & -f_{13} \\ -(e_{12}+f_{12}) & 0 & e_{23}+f_{23} & e_{12} & 0 & -e_{23} & f_{12} & 0 & -f_{23} \\ -(e_{13}+f_{13}) & -(e_{23}+f_{23}) & 0 & e_{13} & e_{23} & 0 & f_{13} & f_{23} & 0 \end{bmatrix}$$

with

$$e_{12} = -[x_l(t_2^{(1)}t_3^{(2)} - t_3^{(1)}t_2^{(2)}) - y_l(t_1^{(1)}t_3^{(2)} - t_3^{(1)}t_1^{(2)})]$$

$$e_{13} = -[x_l(t_2^{(1)}t_3^{(3)} - t_3^{(1)}t_2^{(3)}) - y_l(t_1^{(1)}t_3^{(3)} - t_3^{(1)}t_1^{(3)})]$$

$$e_{23} = -[x_l(t_2^{(2)}t_3^{(3)} - t_3^{(2)}t_2^{(3)}) - y_l(t_1^{(2)}t_3^{(3)} - t_3^{(2)}t_1^{(3)})] \tag{3.80}$$

$$f_{12} = -S_{21}(t_3^{(1)}t_2^{(2)} - t_2^{(1)}t_3^{(2)})$$

$$f_{13} = -S_{21}(t_3^{(1)}t_2^{(3)} - t_2^{(1)}t_3^{(3)})$$

$$f_{23} = -S_{21}(t_3^{(2)}t_2^{(3)} - t_2^{(2)}t_3^{(3)})$$

and (see figure 3.3)

$$x_l = S_{31}\cos\theta$$

$$y_l = S_{31}\sin\theta \tag{3.81}$$

Again, the new part of the stiffness matrix is not symmetric at the element level, but for energy conservative problems (with no loss of energy) the final stiffness matrix for the structure will be symmetric and a symmetric solver can be used. Nevertheless, in a more general case, the membrane element should be able to cope with this non-symmetry in the stiffness matrix and a suitable solver should be used.

3.3.3 Hyperelasticity

The equations presented above are related to the usual geometric non-linear formulation. To include also the material non-linearity that is due to the hyperelastic (rubberlike) materials, hereafter we will apply all the previous steps to an Ogden model [61]. Firstly, we need to obtain the principal stretches necessary for the development. These stretches could be define from the displacement-derivative matrix (or displacement gradient matrix), as will be shown for the plane-stress/plane-strain element in the next chapter. Here, however, we use a more standard and appropriate way of obtaining the principal stretches by applying Mohr's circle [88] to get the principal strains and the principal direction from $\mathbf{E}_l$, equations (3.60) or (3.61), and using the relationship

$$E_{li} = \frac{1}{2}(\lambda_i^2 - 1) \tag{3.82}$$

for the Green's strains.

Now we apply Ogden's strain energy function (3.51) for incompressibility to get the stresses.

$$\varphi = \sum_p \frac{\mu_p}{\alpha_p} [\lambda_1^{\alpha_p} + \lambda_2^{\alpha_p} + (\lambda_1 \lambda_2)^{-\alpha_p} - 3] \tag{3.83}$$

The principal second Piola-Kirchhoff stresses in local coordinates are

$$S_{li} = \frac{\partial \varphi}{\partial E_{li}} = \frac{\partial \varphi}{\partial \lambda_i} \frac{\partial \lambda_i}{\partial E_{li}} \tag{3.84}$$

With the principal stresses acting in the $\mathbf{N}_1$, $\mathbf{N}_2$ system (principal directions given by the Mohr's circle), the local stresses are

$$\mathbf{S}_l = \mathbf{Q}(\mathbf{N})[\mathbf{diag}\, S_{li}]\mathbf{Q}^T(\mathbf{N}) \tag{3.85}$$

where $\mathbf{Q}(\mathbf{N})$ is the matrix containing the principal directions vectors $\mathbf{N}_1$ and $\mathbf{N}_2$, i.e., $\mathbf{Q}(\mathbf{N}) = [\mathbf{N}_1, \mathbf{N}_2]$ and $[\mathbf{diag}\, S_{li}]$ is the diagonal matrix formed by the S_{li} stresses.

The remaining problem is the computation of the constitutive or modular matrix, $\mathbf{D}$. First we have

$$\delta \mathbf{S}_l^L = \mathbf{D}\, \delta \mathbf{E}_l^L \tag{3.86}$$

where $\delta \mathbf{S}_l^L$ and $\delta \mathbf{E}_l^L$ are the variations of the stress and strain in the 'Lagrangian triad' or 'material axes', respectively (see reference [20]).

The constitutive matrix $\mathbf{D}$ can be evaluated in the Lagrangian frame as

$$\delta \mathbf{S}_l^L = \begin{bmatrix} \begin{bmatrix} \frac{\partial S_{l1}}{\partial E_{l1}} & \frac{\partial S_{l1}}{\partial E_{l2}} \\ \frac{\partial S_{l2}}{\partial E_{l1}} & \frac{\partial S_{l2}}{\partial E_{l2}} \end{bmatrix} & \begin{matrix} 0 \\ 0 \end{matrix} \\ \begin{matrix} 0 & 0 \end{matrix} & \frac{(S_{l1} - S_{l2})}{2(E_{l1} - E_{l2})} \end{bmatrix} \delta \mathbf{E}_l^L \tag{3.87}$$

where,

$$\delta \mathbf{S}_l^L = \mathbf{Q}^T(\mathbf{N})\, \delta \mathbf{S}_l\, \mathbf{Q}(\mathbf{N})$$

$$\delta \mathbf{E}_l^L = \mathbf{Q}^T(\mathbf{N})\, \delta \mathbf{E}_l\, \mathbf{Q}(\mathbf{N}) \tag{3.88}$$

The shear component D_{33} is obtained for isotropy, that means that the principal directions of stress and strain coincide [21].

Note that the sub-matrix shown in (3.87) is the same as that obtained for the axisymmetric element from the previous section. However, the **D** matrix above is related to the $\mathbf{N}_1$, $\mathbf{N}_2$ directions. To place this matrix back into the original directions, we must rotate it, as it follows:

$$\delta \mathbf{S}_l = \underbrace{\mathbf{R}^T \mathbf{D} \mathbf{R}}_{\mathbf{D}_t} \delta \mathbf{E}_l \tag{3.89}$$

with,

$$\mathbf{R} = \begin{bmatrix} c^2 & s^2 & sc \\ s^2 & c^2 & -sc \\ -2sc & 2sc & (c^2 - s^2) \end{bmatrix} \tag{3.90}$$

where $s = sin\theta$ and $c = cos\theta$. θ is the angle between the principal and the (fixed) local directions.

In equation (3.87), it is important to stress that to overcome the problem that appears when $E_{l1} = E_{l2}$, following references [36, 21], the limit

$$\lim_{E_{l1} \to E_{l2}} \frac{(S_{l1} - S_{l2})}{2(E_{l1} - E_{l2})} = \frac{1}{2}\left(\frac{\partial S_{l1}}{\partial E_{l1}} - \frac{\partial S_{l2}}{\partial E_{l1}}\right) = \mu = \frac{1}{2}\sum_p \mu_p \alpha_p \tag{3.91}$$

i.e., the ground state of the shear modulus, is applied.

3.4 Numerical tests

Now some examples that confirm the effectiveness and the accuracy of the results from the elements just developed are shown. The finite element computations are implemented in the general purpose finite element program LUSAS [53]. A workstation IBM RS6000 is used to perform the calculations. The examples are compared with previous works in the area and show very good agreement in the solutions.

3.4.1 Cylinder under internal pressure

The first example deals with the inflation of the cylinder of figure 3.4. The cylinder is fixed in both directions at the lower end and is restrained to move in the axial direction at the top end to simulate the symmetry. Ten axisymmetric membrane elements are used to model half of the cylinder. The geometrical and material data for the structure is given below. This hyperelastic problem is analysed using a three-term constitutive model chosen by Ogden [61] to simulate the incompressible behaviour.
Geometry: radius $R = 10.$, total height $H = 40.$, thickness $t_o = 0.1$

Material: $\mu_1 = 6.3$ $\alpha_1 = 1.3$
$\mu_2 = 0.012$ $\alpha_2 = 5.0$
$\mu_3 = -0.1$ $\alpha_3 = -2.0$

The cylinder constitutes a conservative system, i.e., it is closed and no energy is lost during the inflation. Therefore, when we use a displacement-dependent pressure load the final tangent stiffness matrix is symmetric despite the fact that it has been assembled from non-symmetric element stiffness matrices, even for the boundary condition simulating symmetry. This fact has already been mentioned in the theoretical development and it is now confirmed for a numerical example.

The cylinder is loaded by an internal constant pressure which is initially of $p_i = \frac{0.2}{\pi}$. In addition to the large strain behaviour exhibited in this example, it also presents large rotations.

The deformed configuration for the first load step is shown in figure 3.5. The convergence rate of the Newton-Raphson method is quadratic which confirms the consistency of the formulation (table 3.1). The load-displacement curve is plotted in figure 3.6. In order to be able to follow the deformation path and the snap-through presented in the curve, a combination of the standard Newton-Raphson method with the arc-length procedure is used. The results are compared with those produced by Gruttmann and Taylor [36] and present a good agreement.

Iteration	*Convergence Factor*
0	2.01×10^{0}
1	1.81×10^{1}
2	7.08×10^{0}
3	2.59×10^{0}
4	6.55×10^{-1}
5	9.39×10^{-2}
6	1.35×10^{-2}
7	4.57×10^{-5}
8	8.39×10^{-10}
9	3.64×10^{-15}

Table 3.1: Convergence rate for the Newton-Raphson method

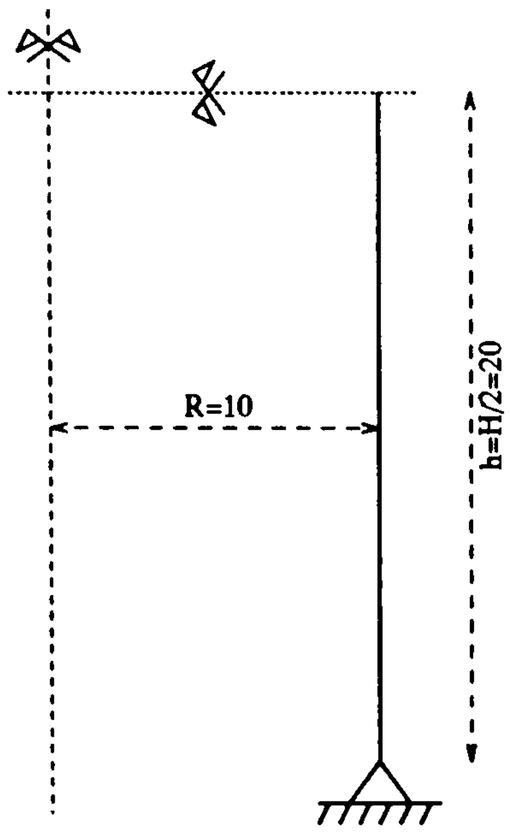


Figure 3.4: Cylinder under internal pressure

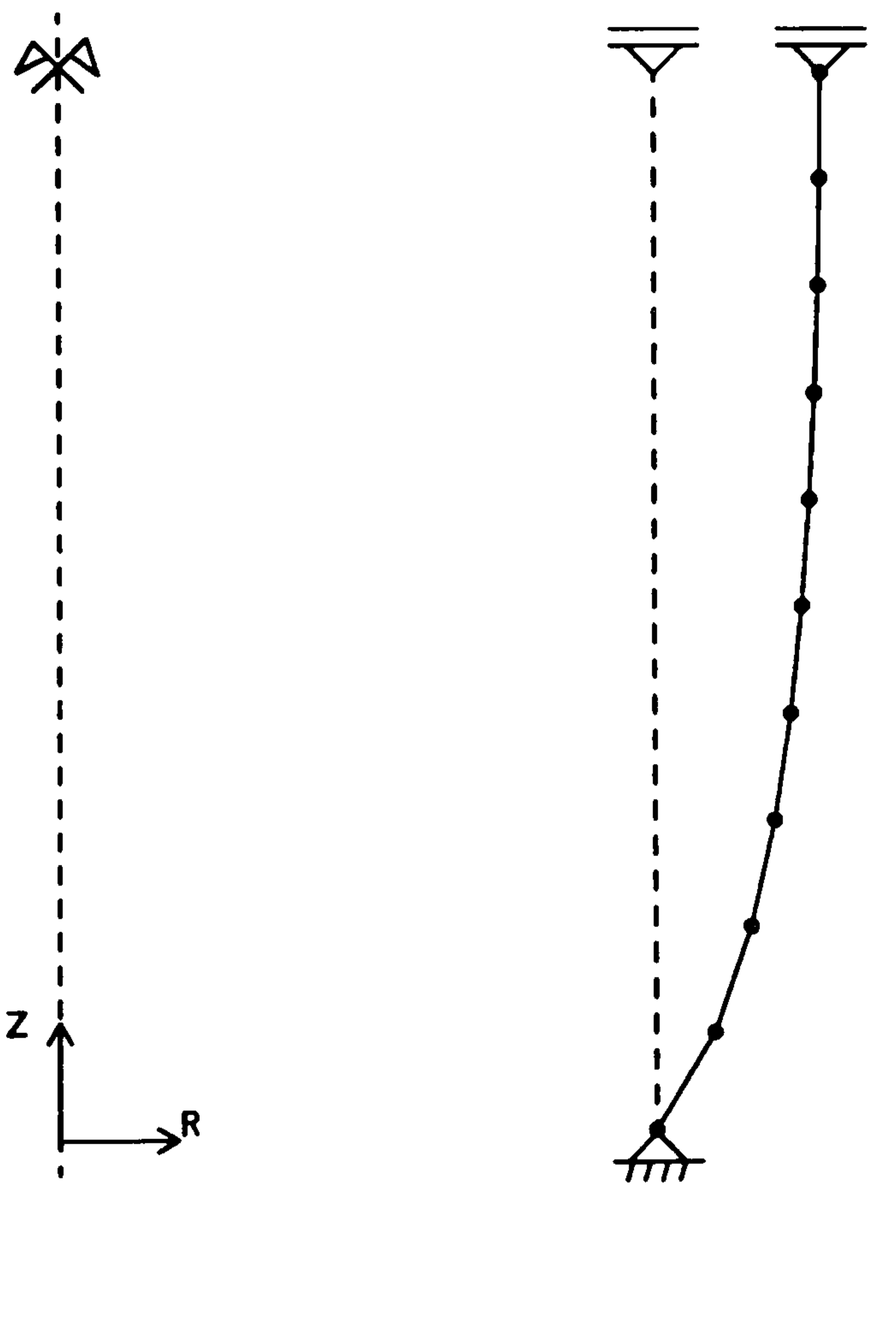


Figure 3.5: Cylinder - deformed configuration

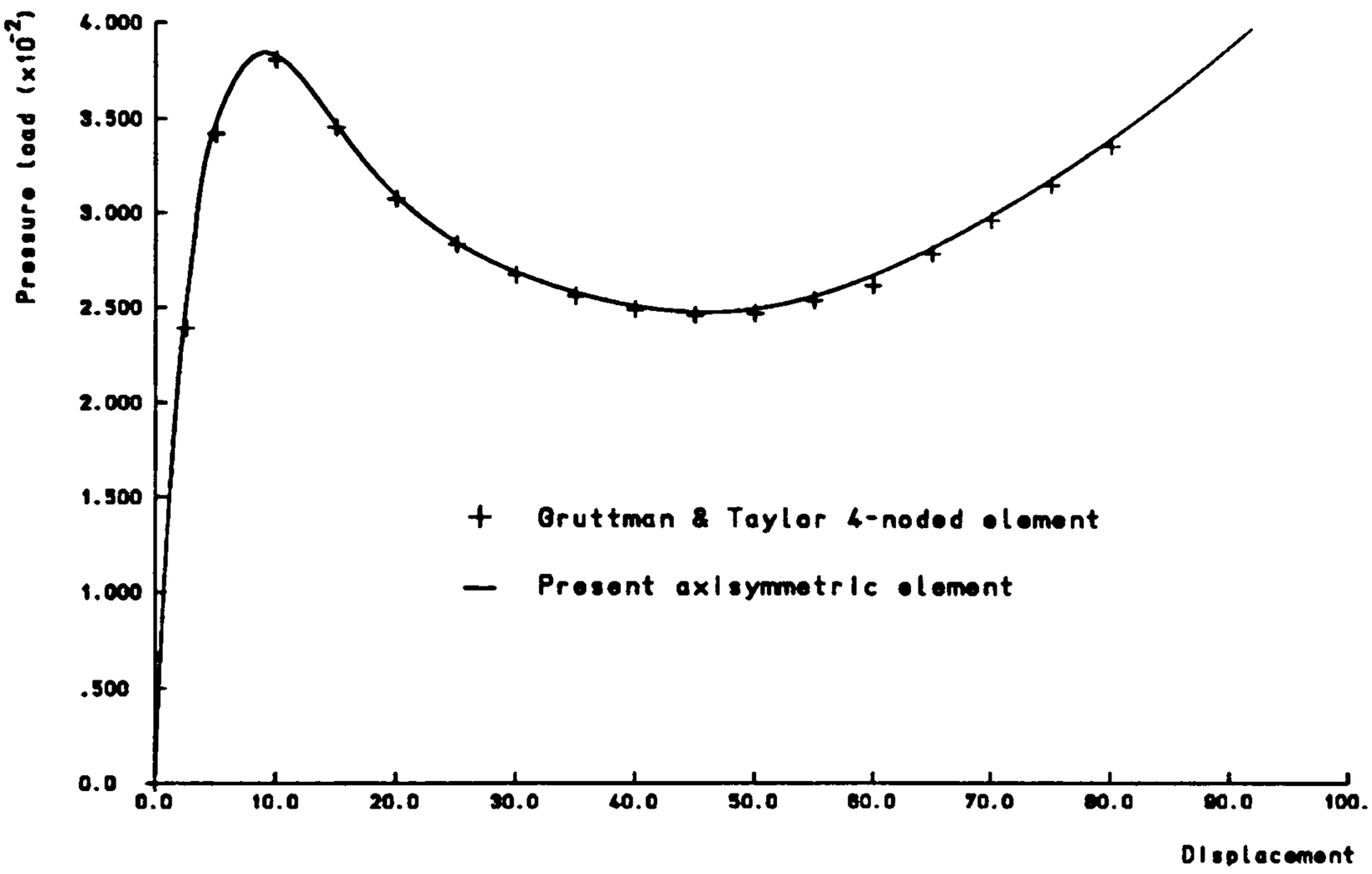


Figure 3.6: Cylinder - internal pressure versus upper radial displacement

3.4.2 Inflation of a balloon

In this example, the inflation of a rubber balloon, as considered by Needleman [57], is analysed. This problem is largely studied and solutions can also be found in [36, 49, 98]. Once more the example involves a conservative system and, as previously quoted, the final matrix obtained is symmetric. The mesh designed is formed by ten elements to model half of the balloon. This is loaded by a internal pressure p. The results of this analysis can be represented as a plot of the pressure (p^* below is dimensionless)

$$P = \frac{p^*}{2\frac{t_o}{R}\sum_r \mu_r \alpha_r} \tag{3.92}$$

against the deflection in the centre of the balloon (figure 3.7). The convergence behaviour is also quadratic in each step of the iterative process as shown in table 3.2 for the first increment ($\lambda = 1.076$), for example. This problem also exhibits a Snap-through and to pass this limit-point an arc-length procedure has been applied in addition to the full Newton-Raphson method to determine the complete solution path.

The material used is the same Three-Term Ogden Model employed in the first example and the geometry is the following:

Radius $= R = 30.$ e *thickness* $= t_o = 0.6$

The final results are compared with those produced by Needleman (Ritz Galerkin approach) [57] and the axisymmetric finite element of Wriggers and Taylor [98].

Iteration	*Convergence Factor*
0	2.81×10^{1}
1	3.56×10^{0}
2	1.13×10^{0}
3	7.93×10^{-3}
4	1.04×10^{-5}
5	8.43×10^{-13}

Table 3.2: Convergence rate for the Newton-Raphson method

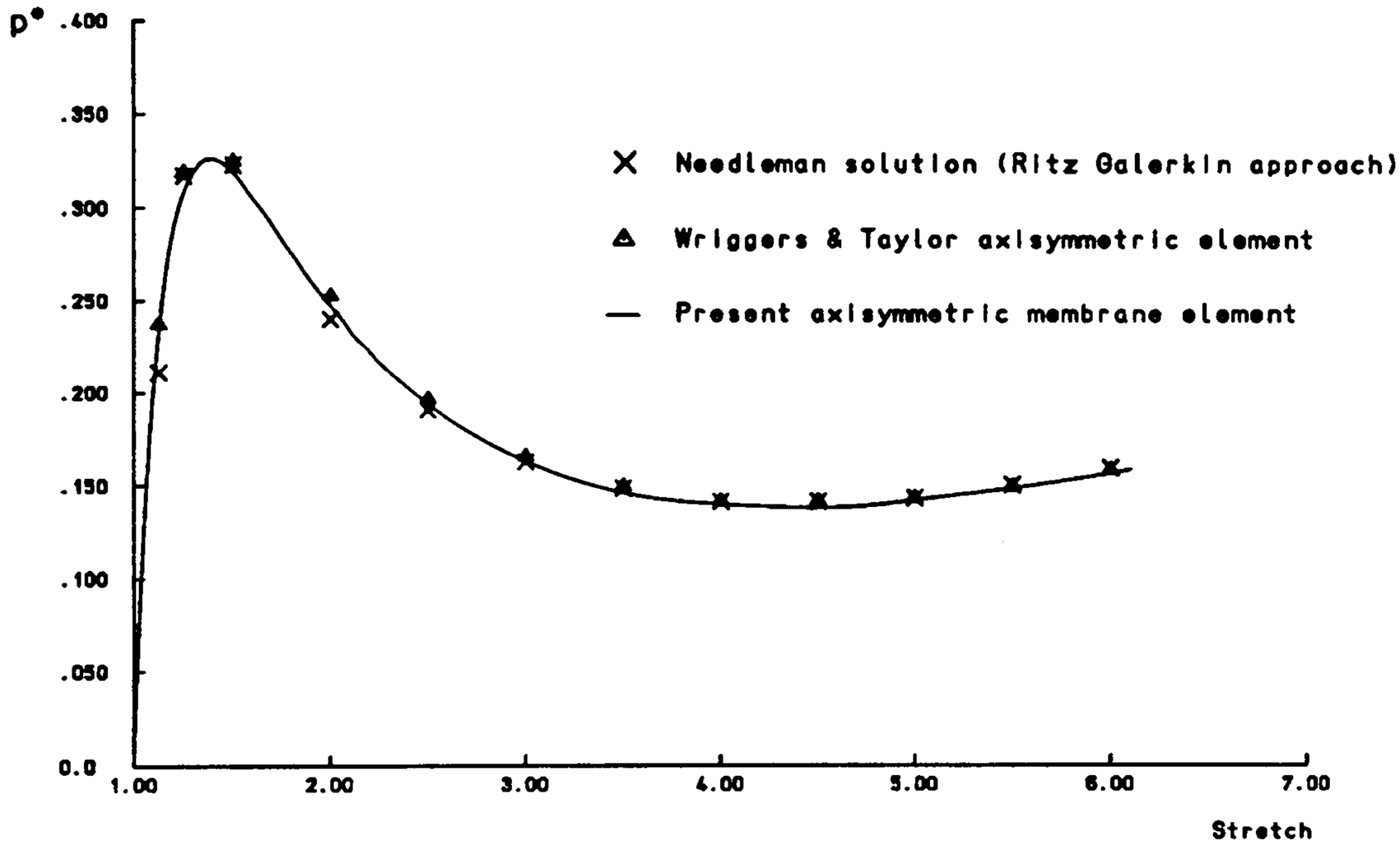


Figure 3.7: Rubber balloon (radius=30 and t=0.6) - pressure p^* versus stretch λ

3.4.3 Inflation of a shallow spherical cap

Again the three-term Ogden material with data given in the first example is used to study this structure. Now the inflation of a shallow spherical cap is considered (figure 3.8). Twenty elements are used to idealise the cap. The initial radius of the cap is $R = 10.$ and the thickness is $t_o = 0.1$.

An very small initial deformation in the geometry of the cap is imposed in order to prevent numerical problems caused by the initial null stiffness of the flat structure. The arc-length method is also used because of the snap-through present in the example.

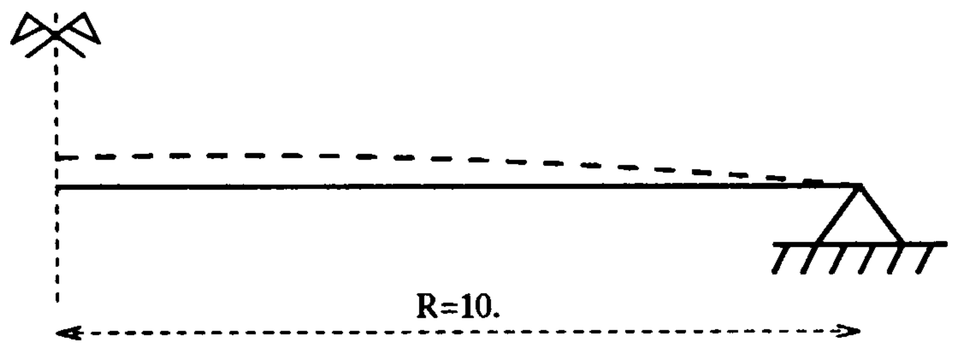


Figure 3.8: Inflation of a Shallow Spherical Cap

Figure 3.9 depicts a graphic of the load parameter λ against the mid surface displacements where one can see the good approach achieved, whereas in figure 3.10 the deformed membrane is shown for different load steps. The results agree with the solution with 4-noded membrane elements shown by Gruttmann and Taylor [36].

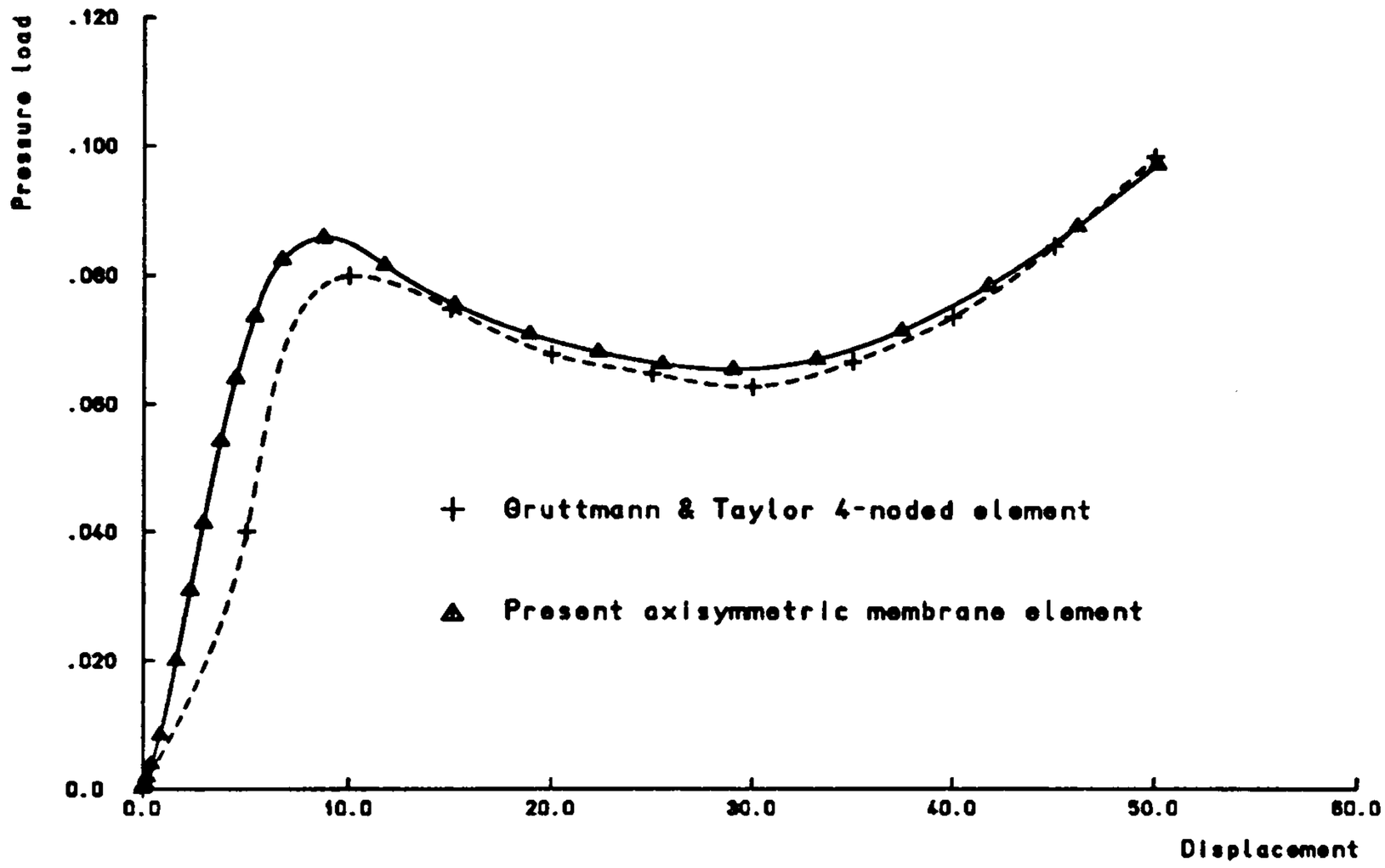


Figure 3.9: Shallow spherical cap - pressure versus mid-point displacement

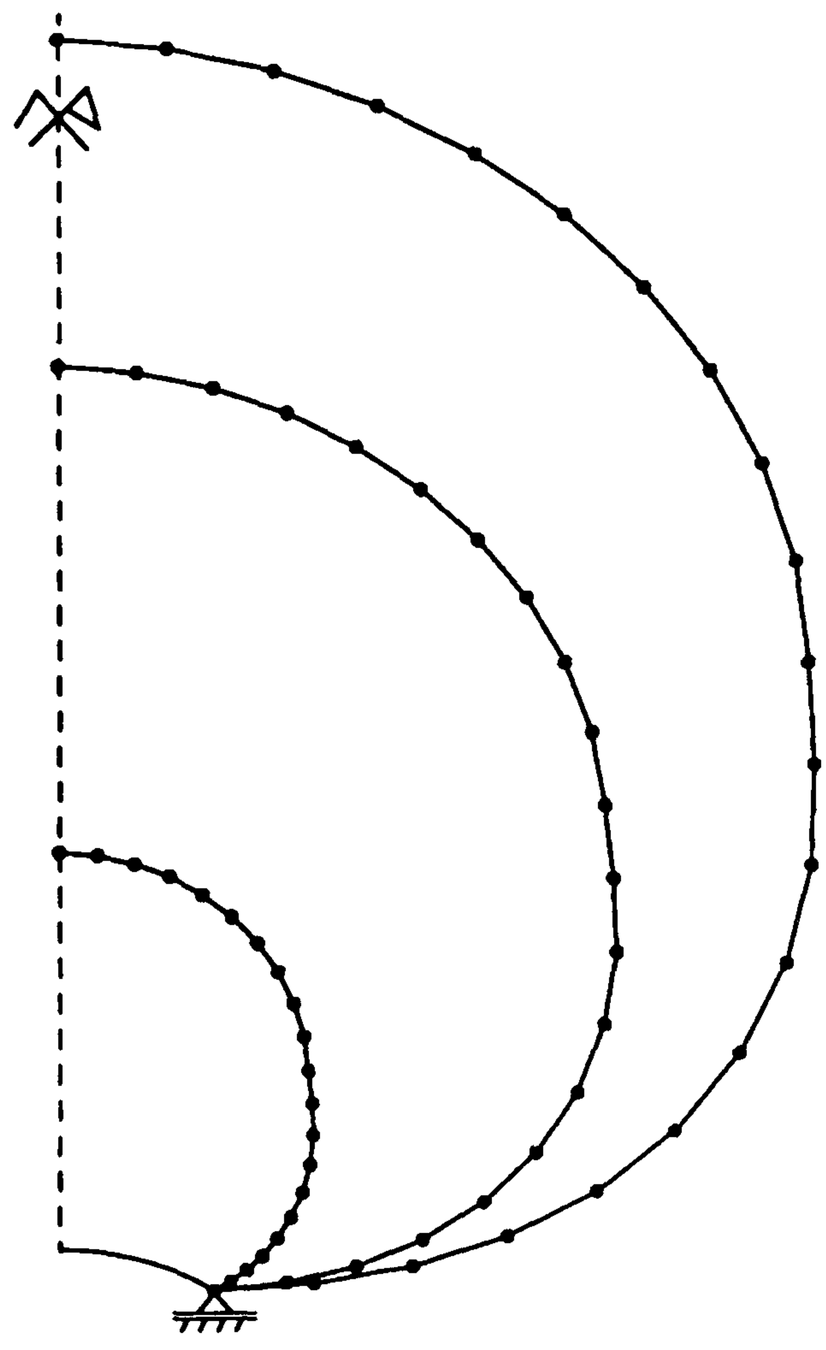


Figure 3.10: Shallow Spherical Cap - Deformed Configurations

3.4.4 Homogeneous deformation tests

In the first set of tests for the general three-dimensional membrane three examples for homogeneous stress states are considered and compared with the analytical exact solutions given in the literature. The comparison illustrates the agreement between results obtained by the present finite element and those from the theory. We use an Ogden constitutive model in principal stretches with three terms given in section 3.4.1 as the material properties for the examples.

The model data give an excellent fit to experimental data on rubber reported by Treloar [89]. Three plane stress states (simple tension, equibiaxial tension and pure shear) are considered and analysed with the membrane finite element and the comparison with the exact theoretical solution given by Ogden [63] shows an exact agreement. Figures 3.11, 3.12 and 3.13 depict these results.

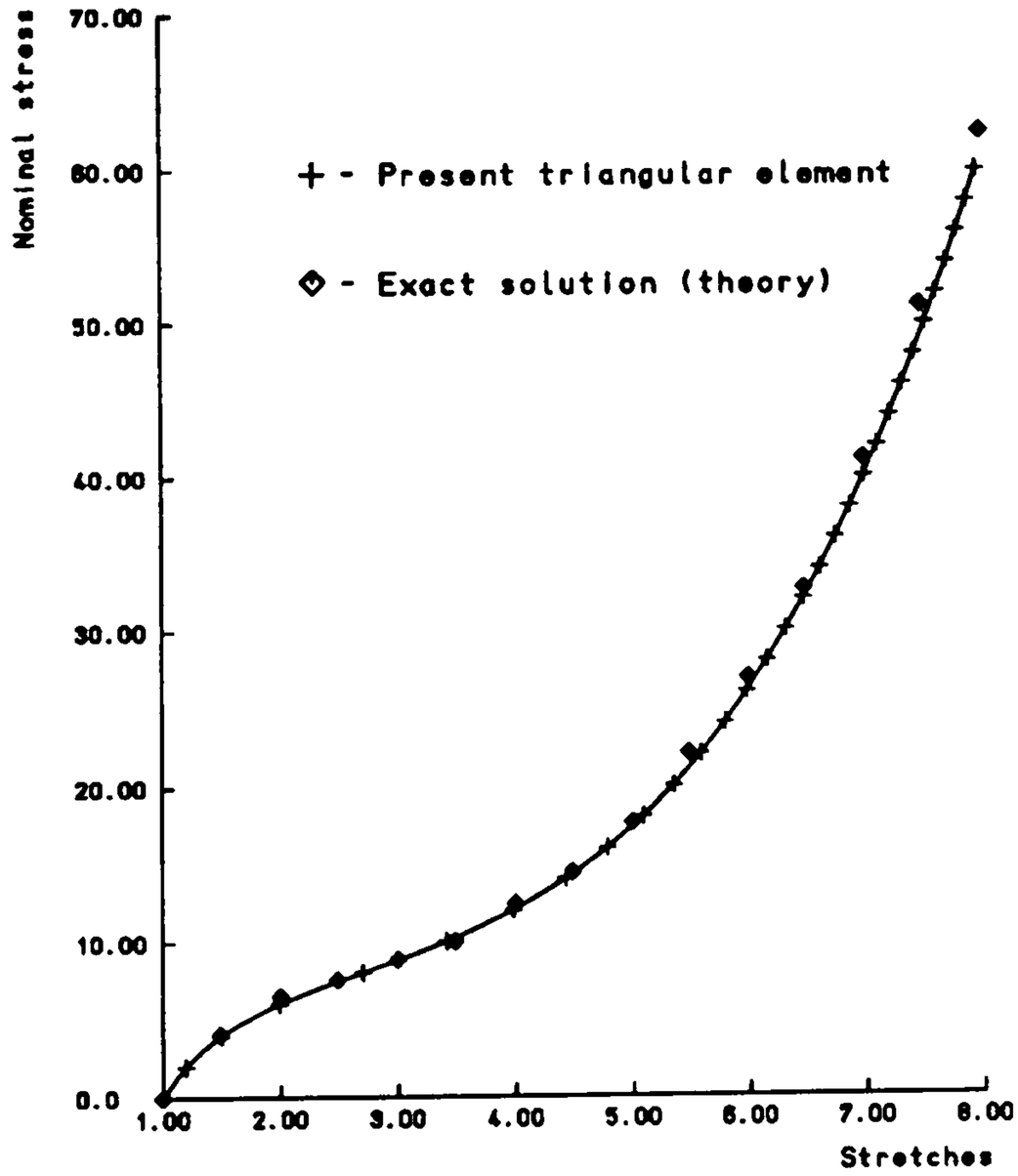


Figure 3.11: Simple tension

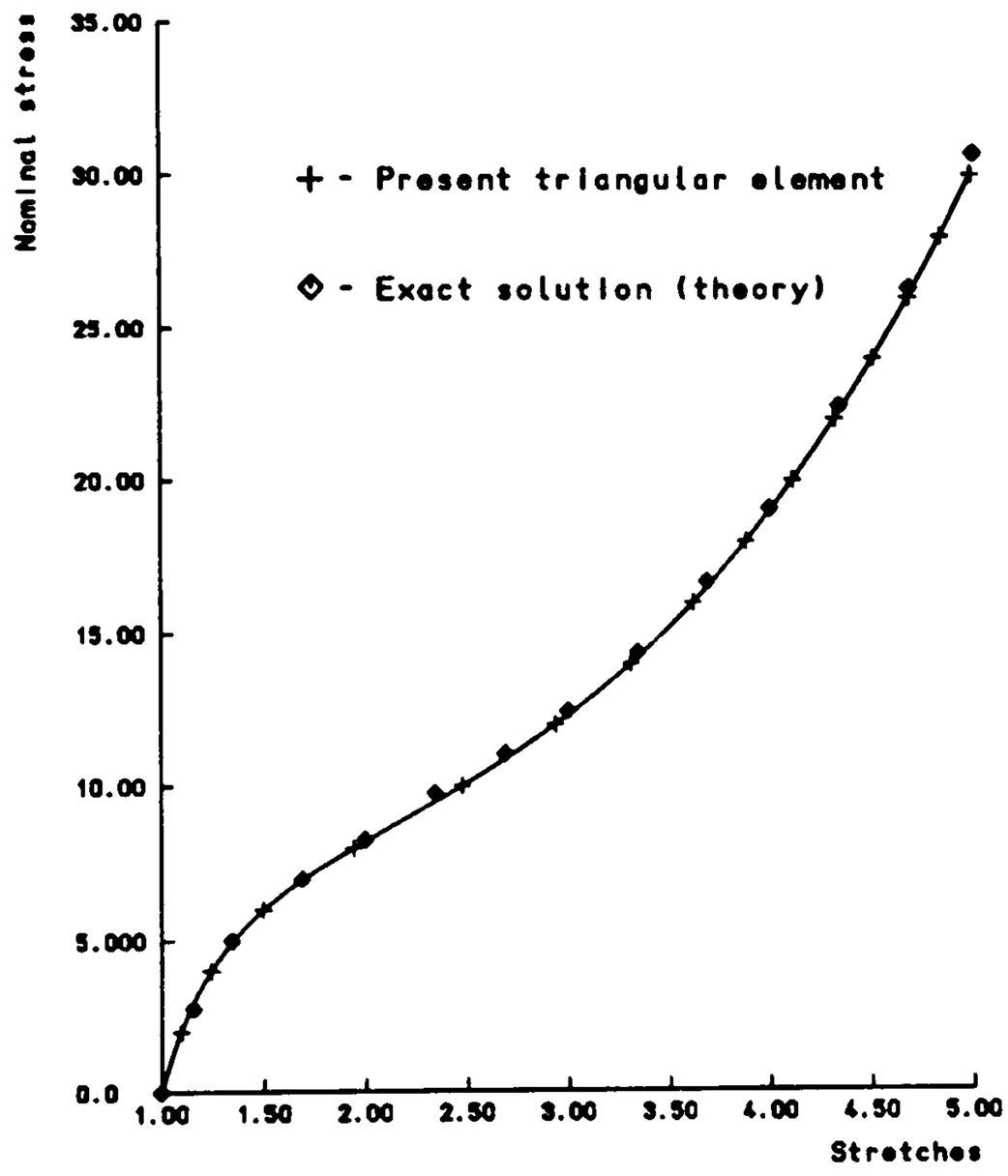


Figure 3.12: Equibiaxial tension

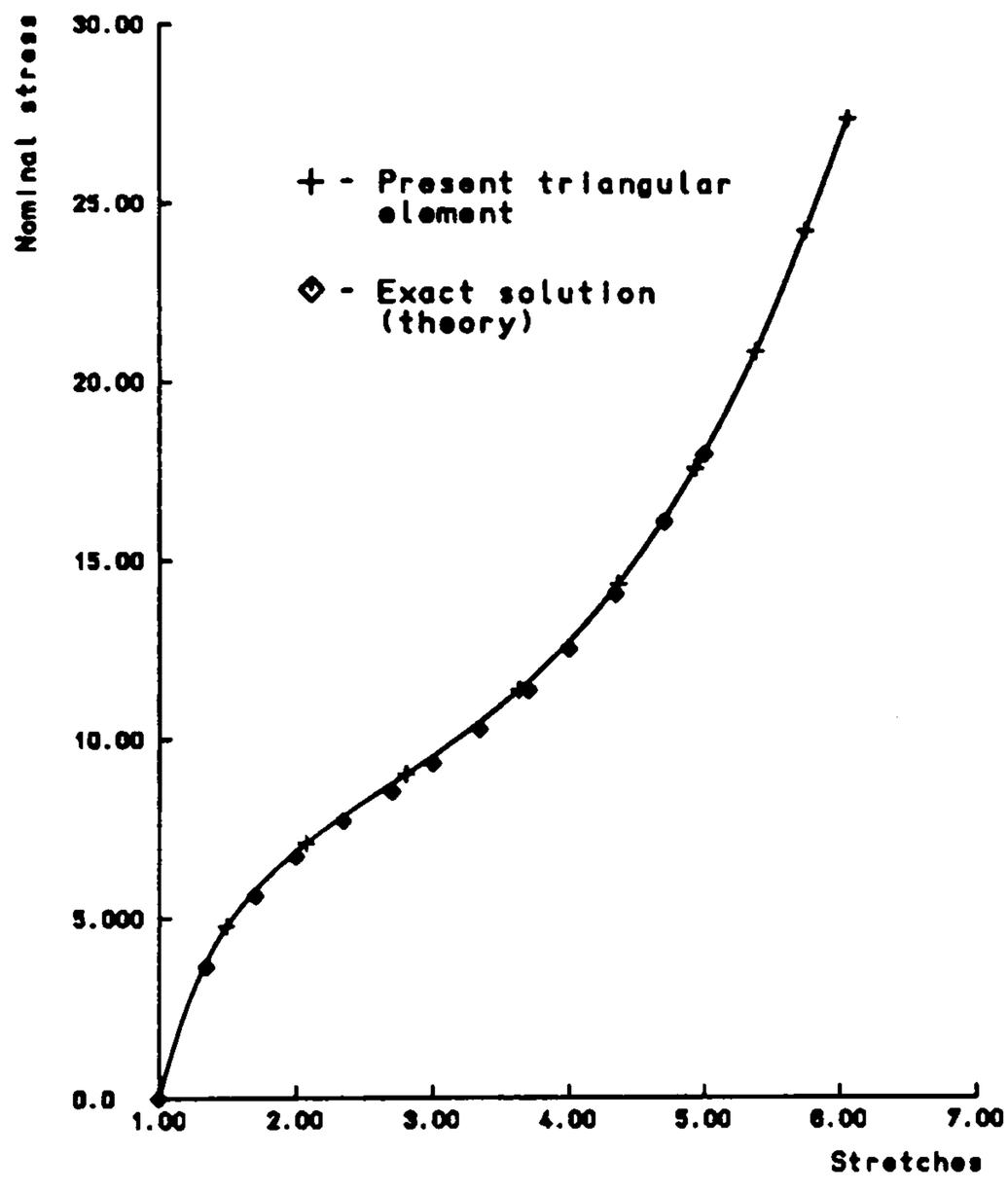


Figure 3.13: Pure shear

3.4.5 Stretching of a square sheet with a central circular hole

This example illustrates the stretching of a square sheet with a circular hole. The same problem has been studied in [68] and [36]. The length of the side is $2L = 20..$ The radius of the central hole is $r = 3.$ and the sheet has a thickness of $t = 0.1$. The edge at $x = \pm 20.$ is fixed in both directions. This problem is analysed using a Mooney-Rivlin material with the constants $C_1 = 25.0$ and $C_2 = -7.0$.

The finite element mesh is designed to model only a quarter of the structure because of the symmetry. We use 48 elements to model the sheet. Figure 3.14 shows the applied load (Force F) plotted against the strain $\frac{u}{L}$ whereas in figure 3.15 we can see the final deformed shapes at two different load steps (total force of 96 and 168, respectively). This example also presents very good agreement with the previous studies, for example with Parish's shell element [68].

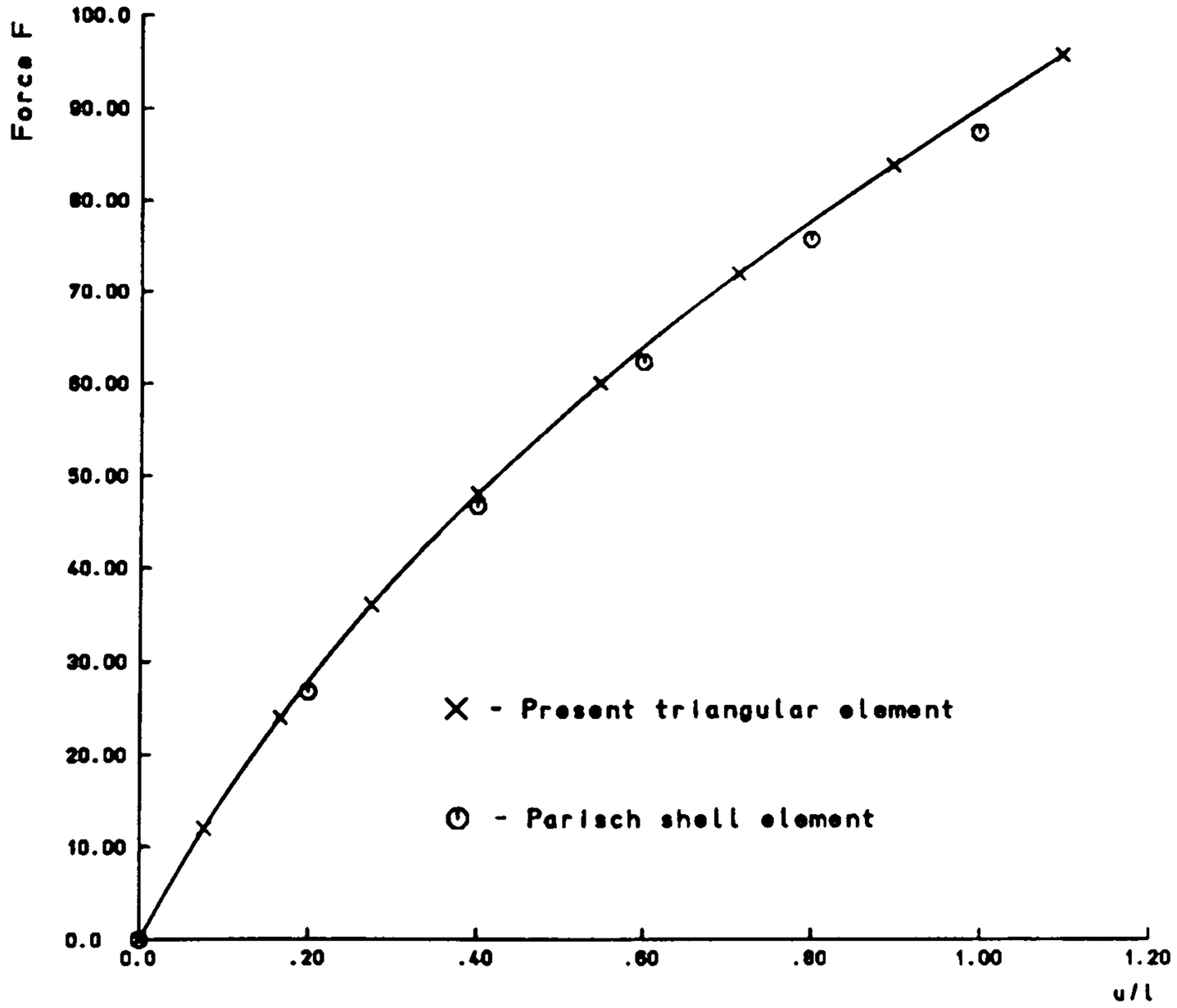


Figure 3.14: Sheet with a circular hole - force versus displacement

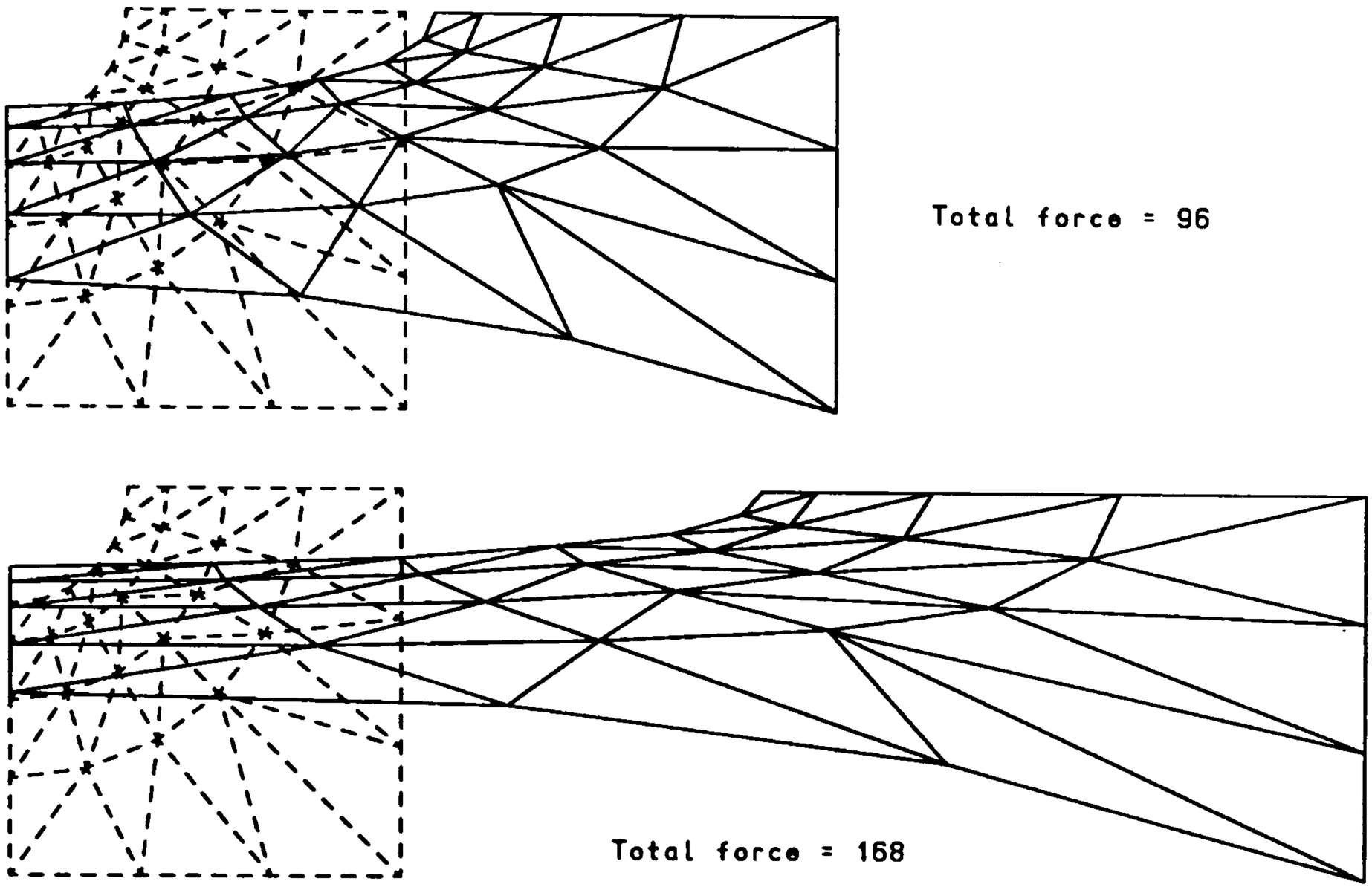


Figure 3.15: Sheet with a circular hole - Original and deformed meshes

3.5 Final remarks

In this chapter the formulation for an axisymmetric membrane element using the theory of hyperelasticity has been derived. In addition, a 3-noded triangular finite element for membranes with arbitrary geometry has also been formulated. The elements developed are applied to analyse problems which present very large strains and displacements. The formulation is based on the so-called total Lagrangian approach and to deal with hyperelastic response, strain energy functions are applied. The incompressibility condition is enforced by the use of the plane stress condition and introduces no special problems.

The use of a displacement-dependent pressure load (follower load) in the calculation of the external force vector and, consequently, the definition of an extra portion of the stiffness matrix coming from this vector proves to be accurate and effective because, besides producing very good results, it preserves the quadratic convergence rate of the Newton method.

The results shown by the examples ensure the consistency of the formulation. The

application of arc-length and Newton-Raphson methods together proved to be a very strong tool in the sort of analysis that has been studied. The quadratic rate of convergence in the iterative solution is again obtained.

Chapter 4

Plane–stress/Plane–strain Analysis - The use of Non–linear Incompatible Elements

4.1 Introduction

Plane-stress and plane-strain elements have been used for decades in the finite element context. In this chapter, these elements will be combined with a new set of tools intending to enhance their performance in linear and non-linear analysis. The advantages in these elements are obtained through the addition of incompatible modes that substantially improve the accuracy and efficiency of the original element.

In this chapter we will show the development of the incompatible displacement element for an ordinary elastic material. The formulation used is based on a total Lagrangian approach, employing Green's strains and second Piola-Kirchhoff stresses. The chapter will show all of the steps for the implementation of the element in a finite element code as well as the results of some tests. The formulation for displacement-dependent (follower) pressure load is also included in this chapter.

In the following stage, the development will take into consideration the use of the element for hyperelasticity. Again an Ogden type material will be used. For the plane-stress element the formulation closely follows the development adopted for the three-dimensional membrane element described in Chapter 3. The plane-strain element, however, is more complicated. The difficulty with this new plane-strain element is due to the incompressibility or near-incompressibility condition of almost all the hyperelastic materials, with special concern to rubber-like materials. The application of

the incompatible modes will make it possible for the element to overcome the problem of applying incompressible or near incompressible materials with plane-strain, especially with rubber.

Some problems with hyperelasticity arise and will be shown in the applications of the element.

4.2 Development

In this section we will present the development of the plane element. As already mentioned in the introduction, we will first consider the element as an ordinary elastic isotropic element; subsequently the element will be modified to incorporate large-strain elasticity. Unlike the element presented in the previous chapter, the element to be developed now is a four-noded quadrilateral finite element.

4.2.1 Linear elastic element

Before considering the non-linear developments, the standard linear element for plane-stress and plane-strain is reviewed. For the isoparametric bi-linear element presented in this chapter (figure 4.1) the geometry and displacement field are defined by

$$\begin{aligned} X &= \mathbf{h}^{\mathbf{T}}\,\mathbf{X} \\ Y &= \mathbf{h}^{\mathbf{T}}\,\mathbf{Y} \end{aligned}$$

$$\begin{aligned} u &= \mathbf{h}^{\mathbf{T}}\,\mathbf{u} \\ v &= \mathbf{h}^{\mathbf{T}}\,\mathbf{v} \end{aligned} \tag{4.1}$$

where the shape functions $\mathbf{h}$ for the element can be written as

$$\mathbf{h} = \frac{1}{4}\begin{Bmatrix} (1-\xi)(1-\eta) \\ (1+\xi)(1-\eta) \\ (1+\xi)(1+\eta) \\ (1-\xi)(1+\eta) \end{Bmatrix} \tag{4.2}$$

Having defined the geometry and the displacements in terms of the non-dimensional co-ordinates ξ and η, we need to relate the strains to the nodal displacements. In order to obtain this relationship, the Jacobian which relates variations with respect to the non-dimensional co-ordinates ξ and η to variations with respect to the co-ordinates X and Y is expressed via

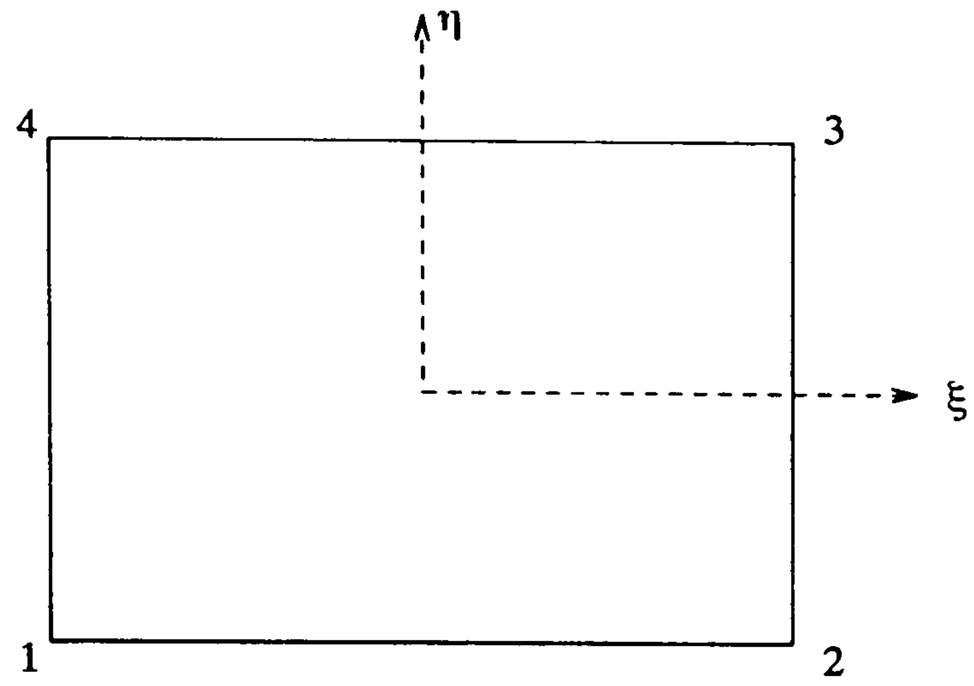


Figure 4.1: Isoparametric bi-linear element

$$\left\{ \begin{array}{c} \frac{\partial}{\partial \xi} \\ \frac{\partial}{\partial \eta} \end{array} \right\} = \left[\begin{array}{cc} \frac{\partial X}{\partial \xi} & \frac{\partial Y}{\partial \xi} \\ \frac{\partial X}{\partial \eta} & \frac{\partial Y}{\partial \eta} \end{array} \right] \left\{ \begin{array}{c} \frac{\partial}{\partial X} \\ \frac{\partial}{\partial Y} \end{array} \right\} = \mathbf{J} \left\{ \begin{array}{c} \frac{\partial}{\partial X} \\ \frac{\partial}{\partial Y} \end{array} \right\} \tag{4.3}$$

At this point the strains at a specific point can be expressed in terms of the nodal displacements via the inverse form of (4.3). Hence, following the notation of Crisfield [18], for this plane element we have

$$\boldsymbol{\epsilon} = \left\{ \begin{array}{c} \frac{\partial u}{\partial X} \\ \frac{\partial u}{\partial Y} \\ \frac{\partial u}{\partial Y} + \frac{\partial v}{\partial X} \end{array} \right\} =$$

$$\left[\begin{array}{cc} \mathbf{J}^{-1}(1,1)\mathbf{h}_\xi^T + \mathbf{J}^{-1}(1,2)\mathbf{h}_\eta^T & \mathbf{0}^T \\ \mathbf{0}^T & \mathbf{J}^{-1}(2,1)\mathbf{h}_\xi^T + \mathbf{J}^{-1}(2,2)\mathbf{h}_\eta^T \\ \mathbf{J}^{-1}(2,1)\mathbf{h}_\xi^T + \mathbf{J}^{-1}(2,2)\mathbf{h}_\eta^T & \mathbf{J}^{-1}(1,1)\mathbf{h}_\xi^T + \mathbf{J}^{-1}(1,2)\mathbf{h}_\eta^T \end{array} \right] \left\{ \begin{array}{c} \mathbf{u} \\ \mathbf{v} \end{array} \right\} = \mathbf{B}\,\mathbf{p} \tag{4.4}$$

where $\mathbf{h}_\xi$ and $\mathbf{h}_\eta$ are the partial differentials of the shape functions of (4.2) with respect to the non-dimensional co-ordinates ξ and η, respectively, and $\mathbf{p}$ is the displacement vector[§]. The terms $\mathbf{J}^{-1}(i,j)$ correspond to the i,j terms in the inverse matrix $\mathbf{J}^{-1}$.

By applying the principle of the virtual work, as in (3.12) for a linear case, and the variation of the strain from equation (4.4), the linear stiffness matrix $\mathbf{K}$ is obtained as

$$\mathbf{K} = \int_{V_o} \mathbf{B}^T\,\mathbf{D}\,\mathbf{B}\,dV_o \tag{4.5}$$

[§]$\mathbf{p}$ is now ordered as $(u_1, u_2, u_3, u_4, v_1, v_2, v_3, v_4)$ for convenience. This order is altered before the element assembly process.

where **D**, for an isotropic elastic material, is given by

$$\mathbf{D} = \frac{E}{(1-\nu^2)} \begin{bmatrix} 1 & \nu & 0 \\ \nu & 1 & 0 \\ 0 & 0 & \frac{(1-\nu)}{2} \end{bmatrix} \tag{4.6}$$

and

$$\mathbf{D} = \frac{E}{(1+\nu)(1-2\nu)} \begin{bmatrix} (1-\nu) & \nu & 0 \\ \nu & (1-\nu) & 0 \\ 0 & 0 & \frac{(1-2\nu)}{2} \end{bmatrix} \tag{4.7}$$

for plane-stress and plane-strain conditions, respectively. The term dV_o is expressed by

$$dV_o = t\, det\mathbf{J}\, d\xi d\eta \tag{4.8}$$

where t is the thickness and $det\mathbf{J}$ is the determinant of the Jacobian. Note that t is equal to 1 for a plane-strain case.

However, the element shown above suffers from severe locking in bending dominated situations. The element tends to be over-stiff and a process to 'soften' the element is necessary. The poor behaviour of the element under a pure bending mode is depicted in figure 4.2 where shear locking prevents the element from deforming in the expected way. This undesirable drawback can be avoided by under-integrating the shear term, that means, the shear energy is only considered at the centroid. This constant shear approach can be seen in details in references [15, 18, 44]. Another process to overcome the problem was proposed by Wilson *et al* [96]. They introduced a way of obtaining the correct response by the addition of quadratic incompatible displacement modes that would more accurately represent the exact bending solution (see figure 4.2). The incompatible modes are "nodeless" degrees of freedom that can be regarded as internal variable which have to be eliminated at the element level via a static condensation process. These incompatible modes act as a softening and the overall performance of the element is greatly improved.

Although the original idea produces accurate results, it fails to pass the *patch test* for non-rectangular elements. Taylor *et al.* [86] modified Wilson's element in such a manner that when the element is submitted to a constant stress state, the incompatible modes are not activated and do not affect the final solution. The technique involves the computation of the Jacobian for the incompatible modes at the centroid of the element,

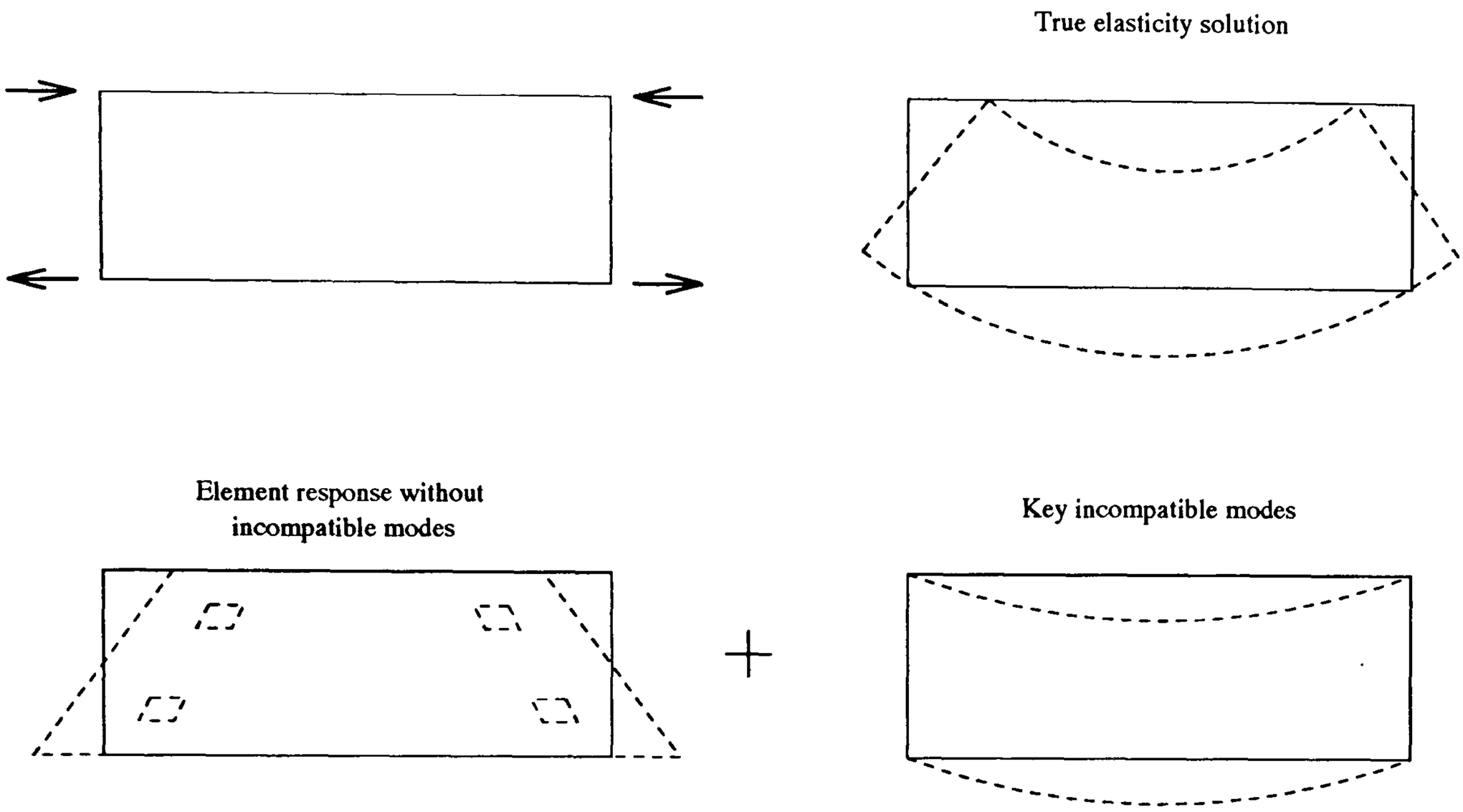


Figure 4.2: Pure bending problem

as will be presented subsequently. Consequently, the modified element successfully passes the patch test.

Besides the bending problems, the standard element cannot adequately treat incompressible or near-incompressible problems for plane-strain and solid analysis. This can be illustrated by the two-dimensional element shown in figure 4.3 where the nodes a, b and c are kept fixed. If the element is incompressible (no volume change) and we apply a force F at node d, the element will lock unless the additional incompatible displacement modes are incorporated whereby the final deformed shape can be more closely achieved. This is one example that demonstrates the need for the incompatible modes when the element is used with incompressibility or near-incompressibility.

So, if we add the incompatible modes (figure 4.4), the displacement field for the enhanced element will become

$$\begin{aligned} u &= \mathbf{h}^T \mathbf{u} + \mathbf{h}^{*T} \mathbf{u}^* \\ v &= \mathbf{h}^T \mathbf{v} + \mathbf{h}^{*T} \mathbf{v}^* \end{aligned} \tag{4.9}$$

where the shape functions for the incompatible modes are given by [96]

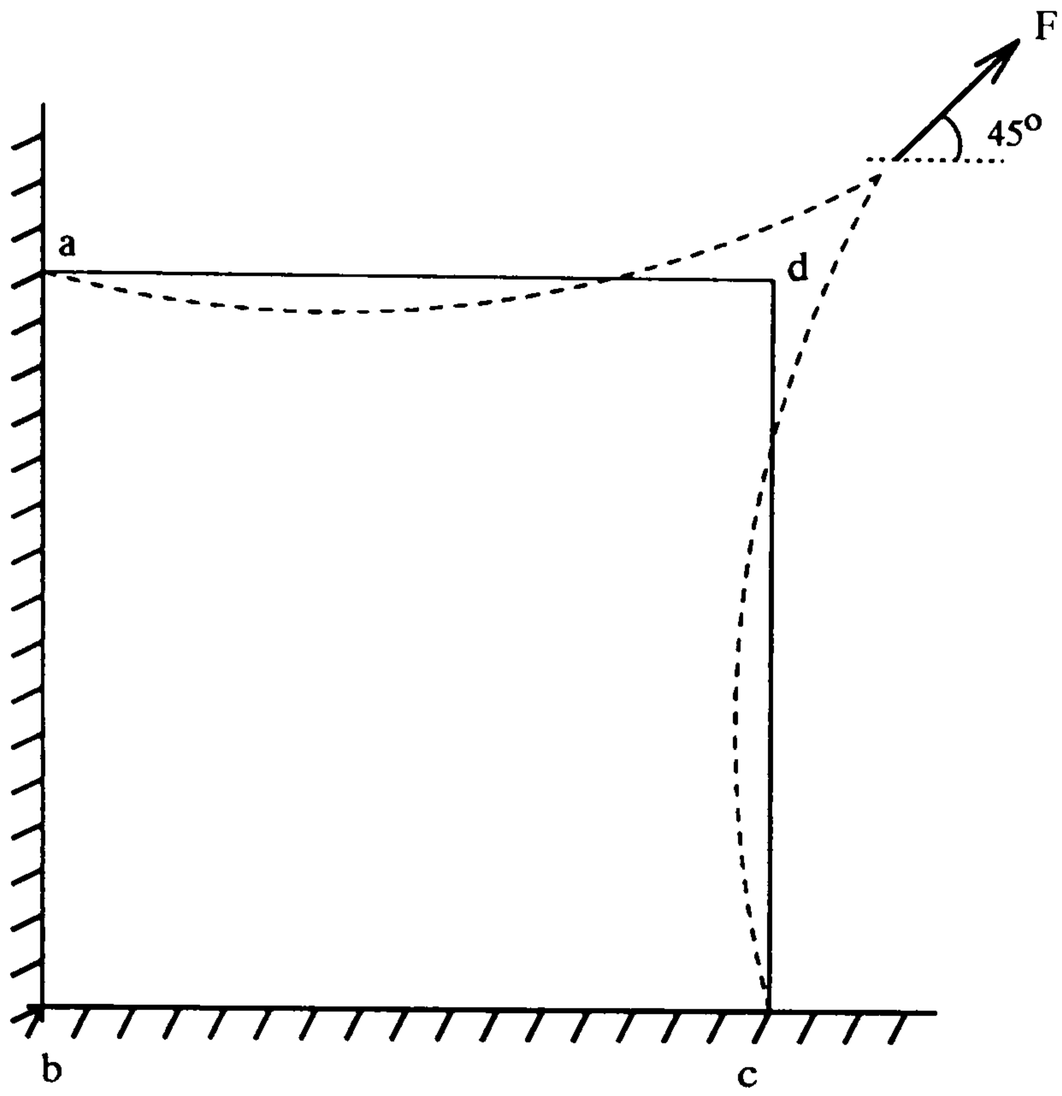


Figure 4.3: Incompressible element - original and deformed configuration

$$\mathbf{h}^* = \begin{Bmatrix} 1-\xi^2 \\ 1-\eta^2 \end{Bmatrix} \tag{4.10}$$

and

$$\mathbf{u}^* = \begin{Bmatrix} \alpha_1 \\ \alpha_3 \end{Bmatrix}$$

$$\mathbf{v}^* = \begin{Bmatrix} \alpha_2 \\ \alpha_4 \end{Bmatrix} \tag{4.11}$$

are the nodeless degrees of freedom.

To continue the development we will need to find the Jacobian for the incompatible modes. Hence, we can proceed using the Jacobian by just replacing its values by values calculated at the centroid, i.e., $\xi = \eta = 0$. This strategy is used to pass the patch test, as described below.

In the original incompatible element by Wilson *et al* [96], the classical idea of convergence of the element was not achieved unless the element had a square geometry. This means that the element could only pass the *patch test* for this particular geometry

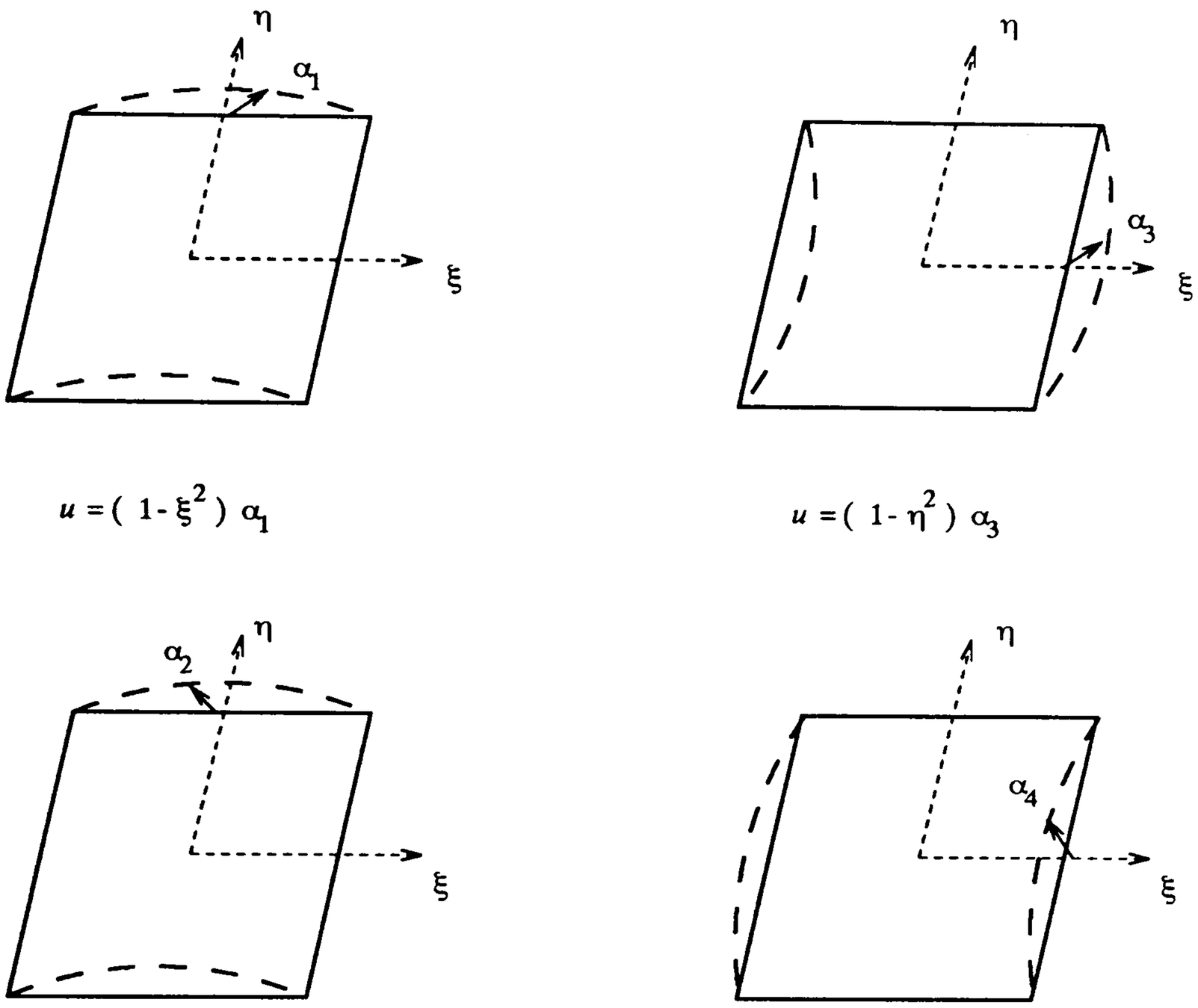


Figure 4.4: Incompatible displacement modes

and could not be use in a general context. Taylor *et al* [86] proposed a new strategy that overcomes the problem. All it is necessary to do is to guarantee that under constant stress state the extra virtual work produced by the incompatible mode vanishes. Hence,

$$\int_{V_o} \mathbf{B}^{*T}\, \boldsymbol{\sigma}\, dV_o = 0 \tag{4.12}$$

The basic idea is to use the Jacobian computed at the centroid of the element instead of at the Gauss points. To this end, the **B** matrix for the incompatible modes, here called $\mathbf{B}^*$, is as **B** in (4.4) but with $\mathbf{J}_o$ instead of **J** and $\mathbf{h}^*$ instead of **h**. This new $\mathbf{B}^*$ matrix also includes a term $\frac{det\,\mathbf{J}_o}{det\,\mathbf{J}}$ multiplying itself. This leads to an expression of the form

$$\mathbf{B}^* = \frac{det\mathbf{J}_o}{det\mathbf{J}}\ \bar{\mathbf{B}}^* =$$

$$\frac{det\mathbf{J}_o}{det\mathbf{J}} \begin{bmatrix} \mathbf{J}_o^{-1}(1,1)\mathbf{h}_\xi^{*T} + \mathbf{J}_o^{-1}(1,2)\mathbf{h}_\eta^{*T} & \mathbf{0}^T \\ \mathbf{0}^T & \mathbf{J}_o^{-1}(2,1)\mathbf{h}_\xi^{*T} + \mathbf{J}_o^{-1}(2,2)\mathbf{h}_\eta^{*T} \\ \mathbf{J}_o^{-1}(2,1)\mathbf{h}_\xi^{*T} + \mathbf{J}_o^{-1}(2,2)\mathbf{h}_\eta^{*T} & \mathbf{J}_o^{-1}(1,1)\mathbf{h}_\xi^{*T} + \mathbf{J}_o^{-1}(1,2)\mathbf{h}_\eta^{*T} \end{bmatrix} \tag{4.13}$$

where $\mathbf{h}_\xi^*$ and $\mathbf{h}_\eta^*$ are the partial derivatives with respect to ξ and η of (4.10) and the nodeless incompatible variables are ordered as

$$\mathbf{p}^* = \begin{Bmatrix} \mathbf{u}^* \\ \mathbf{v}^* \end{Bmatrix} \tag{4.14}$$

From this new $\mathbf{B}^*$ matrix and the Jacobian at the centroid, we have

$$\int\int \mathbf{B}^{*T}\,\boldsymbol{\sigma}\ det\mathbf{J}\ d\xi\ d\eta = \int\int \frac{det\mathbf{J}_o}{det\mathbf{J}}\ \bar{\mathbf{B}}^*\boldsymbol{\sigma}\ det\mathbf{J}\ d\xi\ d\eta = \int\int det\mathbf{J}_o\ \bar{\mathbf{B}}^*\boldsymbol{\sigma}\ d\xi\ d\eta \tag{4.15}$$

Because $\bar{\mathbf{B}}^*$ and $det\mathbf{J}_o$ are both constant, for a constant stress state (i.e. $\boldsymbol{\sigma}$ = constant) equation (4.15) leads to the requirement that

$$\int\int \mathbf{h}_\xi^* d\xi\ d\eta = 0 \quad ; \quad \int\int \mathbf{h}_\eta^* d\xi\ d\eta = 0 \tag{4.16}$$

which is true from (4.10).

Now we add the incompatible modes to the existing strain expression of (4.4). Hence,

$$\boldsymbol{\epsilon} = \mathbf{B}\,\mathbf{p} + \mathbf{B}^*\,\mathbf{p}^* \tag{4.17}$$

where $\mathbf{p}^*$ are the incompatible displacements as in (4.11) and (4.14).

From the variation of the (4.17) and the principle of virtual work, we obtain the total stiffness matrix for the element as given below:

$$\begin{Bmatrix} \mathbf{q}_i \\ \mathbf{q}_i^* \end{Bmatrix} = \begin{bmatrix} \mathbf{K}_{11} & \mathbf{K}_{12} \\ \mathbf{K}_{12}^T & \mathbf{K}_{22} \end{bmatrix} \begin{Bmatrix} \mathbf{p} \\ \mathbf{p}^* \end{Bmatrix} \tag{4.18}$$

with,

$$\mathbf{K}_{11} = \int_{V_o} (\mathbf{B}^T\,\mathbf{D}\,\mathbf{B})\,dV_o \tag{4.19}$$

$$\mathbf{K}_{12} = \int_{V_o} (\mathbf{B}^T\,\mathbf{D}\,\mathbf{B}^*)\,dV_o \tag{4.20}$$

$$\mathbf{K}_{22} = \int_{V_o} (\mathbf{B}^{*^T}\, \mathbf{D}\, \mathbf{B}^*)\, dV_o \tag{4.21}$$

Note that $\mathbf{K}_{11}$ corresponds to $\mathbf{K}$ of (4.5).

However, before the assembly of the element matrix into the global matrix, the incompatible displacements modes have to be eliminated at the element level and a static condensation has to be used. This is presented in details for the non-linear version of the element described in the next section.

4.2.2 Geometrical non-linearity using incompatible modes

In the section above we have described the classic incompatible element formulated by Wilson *et al.* and later modified by Taylor *et al.*. In a non-linear environment, the original approach has been applied by Simo and co-workers [76, 79] to introduce the formulation known by "mixed assumed strain method". The enhanced strain element developed utilises the first Piola-Kirchhoff stress formulation and the crucial idea of the method is to decompose the deformation gradient into a multiplication between a conforming part and an enhanced part [79]. The intention here, however, is to develop a simpler approach directly involving the Green's strain and the total Lagrangian formulation. It should be emphasised at this stage that the method proposed by Simo *et al.* cannot be regarded as the incompatible modes method but rather as a broader class of enhanced strain interpolations that encompass the original incompatible elements as a special case (details about this affirmation can be seen in [1] and [2]).

To extend the linear element of the previous section into a geometric non-linear approximation we begin with the definition of the displacement derivative tensor in a vector form as in equation (3.59) for the membrane element. In the vector shown here, only the contributions of the incompatible modes are involved. Therefore, employing equation (4.3), now with the Jacobian calculated at the centroid of the element, i.e., $\mathbf{J}_o$, we can write

$$\boldsymbol{\theta}^* = \left\{ \begin{array}{c} \frac{\partial u^*}{\partial X} \\ \frac{\partial u^*}{\partial Y} \\ \frac{\partial v^*}{\partial X} \\ \frac{\partial v^*}{\partial Y} \end{array} \right\} = \tag{4.22}$$

$$\frac{detJ_o}{detJ}\begin{bmatrix} \mathbf{J}_o^{-1}(1,1)\mathbf{h}_\xi^{*T} + \mathbf{J}_o^{-1}(1,2)\mathbf{h}_\eta^{*T} & \mathbf{0}^T \\ \mathbf{J}_o^{-1}(2,1)\mathbf{h}_\xi^{*T} + \mathbf{J}_o^{-1}(2,2)\mathbf{h}_\eta^{*T} & \mathbf{0}^T \\ \mathbf{0}^T & \mathbf{J}_o^{-1}(1,1)\mathbf{h}_\xi^{*T} + \mathbf{J}_o^{-1}(1,2)\mathbf{h}_\eta^{*T} \\ \mathbf{0}^T & \mathbf{J}_o^{-1}(2,1)\mathbf{h}_\xi^{*T} + \mathbf{J}_o^{-1}(2,2)\mathbf{h}_\eta^{*T} \end{bmatrix} \begin{Bmatrix} \mathbf{u}^* \\ \mathbf{v}^* \end{Bmatrix} = \mathbf{G}^*\,\mathbf{p}^*$$

As mentioned, the above vector $\boldsymbol{\theta}^*$ only involves the values coming from the incompatible modes. To obtain the complete vector, we have to add the contribution from the well established compatible modes, i.e.,

$$\boldsymbol{\theta}_{total} = \boldsymbol{\theta} + \boldsymbol{\theta}^* = \mathbf{G}\,\mathbf{p} + \mathbf{G}^*\,\mathbf{p}^* \tag{4.23}$$

From the above, the variation of $\boldsymbol{\theta}_{total}$ is simply,

$$\delta\boldsymbol{\theta}_{total} = \delta\boldsymbol{\theta} + \delta\boldsymbol{\theta}^* \tag{4.24}$$

In a similar manner to that of the linear case, here again we have to enforce the virtual work produced by the incompatible modes under a constant stress state to be zero and therefore the incompatible strain will be a linear variation of the displacements. This allows the element to recover the linear solution for these stress states.

It is easy now to compute the strain (Green's strain) as (see reference [20])

$$\mathbf{E} = \mathbf{E}_l + \mathbf{E}_{nl} + \mathbf{E}_l^* = \tag{4.25}$$

$$[\mathbf{H} + \tfrac{1}{2}\mathbf{A}(\boldsymbol{\theta})]\,\boldsymbol{\theta} + \mathbf{H}\,\boldsymbol{\theta}^* = [\mathbf{HG} + \tfrac{1}{2}\mathbf{A}(\boldsymbol{\theta})\mathbf{G}]\,\mathbf{p} + \mathbf{HG}^*\,\mathbf{p}^*$$

where

$$\mathbf{H} = \begin{bmatrix} 1 & 0 & 0 & 0 \\ 0 & 0 & 0 & 1 \\ 0 & 1 & 1 & 0 \end{bmatrix}$$

Observe that for a linear case $\mathbf{A}(\boldsymbol{\theta}) = 0$ and, as already mentioned, we recover

$$\int_{V_o} \mathbf{B}_{(total)}^T\,\mathbf{S}dV_o = 0$$

where now we use the 2nd Piola-Kirchhoff stress $\mathbf{S}$. Accordingly,

$$\mathbf{E} = \mathbf{E}_l + \mathbf{E}_l^* = \mathbf{HG}\,\mathbf{p} + \mathbf{HG}^*\,\mathbf{p}^* = \mathbf{B}\,\mathbf{p} + \mathbf{B}^*\,\mathbf{p}^* = \boldsymbol{\epsilon} \tag{4.26}$$

as in (4.17).

From virtual work we have,

$$V = \int_{V_o} \mathbf{S}^T \, \delta\mathbf{E}_v \, dV_o - V_e \tag{4.27}$$

where $\mathbf{S}$ is the second Piola-Kirchhoff stress vector and $\delta\mathbf{E}_v$ is the virtual change in Green's strain.

At this point we need the change in Green's strain that, with the help of (4.25) is given by

$$\delta\mathbf{E} = \underbrace{\mathbf{H}\mathbf{G}\,\delta\mathbf{p} + \mathbf{H}\mathbf{G}^*\,\delta\mathbf{p}^*}_{\delta\mathbf{E}_l + \delta\mathbf{E}_l^*} + \underbrace{\mathbf{A}(\boldsymbol{\theta})\mathbf{G}\,\delta\mathbf{p}}_{\delta\mathbf{E}_{nl}} \tag{4.28}$$

Finally,

$$\delta\mathbf{E} = \mathbf{B}\,\delta\mathbf{p} + \mathbf{B}^*\,\delta\mathbf{p}^* \tag{4.29}$$

where,

$$\begin{aligned} \mathbf{B} &= [\mathbf{H} + \mathbf{A}(\boldsymbol{\theta})]\,\mathbf{G} \\ \mathbf{B}^* &= \mathbf{H}\mathbf{G}^* \end{aligned} \tag{4.30}$$

Comparing (4.27) and

$$V = \delta\mathbf{p}^T\mathbf{q}_i + \delta\mathbf{p}^{*^T}\mathbf{q}_i^* - V_e \tag{4.31}$$

we can get the internal force vectors, for compatible and incompatible modes respectively, as

$$\begin{aligned} \mathbf{q}_i &= \textstyle\int_{V_o} \mathbf{B}^T\mathbf{S}\,dV_o \\ \mathbf{q}_i^* &= \textstyle\int_{V_o} \mathbf{B}^{*^T}\mathbf{S}\,dV_o \end{aligned} \tag{4.32}$$

The stiffness matrices can be obtained by the change of these internal force vectors. This leads to

$$\begin{Bmatrix} \delta\mathbf{q}_i \\ \delta\mathbf{q}_i^* \end{Bmatrix} = \begin{bmatrix} \mathbf{K}_{11} & \mathbf{K}_{12} \\ \mathbf{K}_{12}^T & \mathbf{K}_{22} \end{bmatrix} \begin{Bmatrix} \delta\mathbf{p} \\ \delta\mathbf{p}^* \end{Bmatrix} \tag{4.33}$$

with,

$$\mathbf{K}_{11} = \int_{V_o} (\mathbf{B}^T\,\mathbf{D}\,\mathbf{B} + \mathbf{G}^T\,\hat{\mathbf{S}}\,\mathbf{G})\,dV_o \tag{4.34}$$

and $\mathbf{K}_{12}$ and $\mathbf{K}_{22}$ from (4.20) and (4.21), respectively. $\hat{\mathbf{S}}$ is a two-dimensional form of (3.73), i.e.,

$$\hat{\mathbf{S}}_i = \begin{bmatrix} \begin{bmatrix} S_{11} & S_{12} \\ S_{12} & S_{22} \end{bmatrix} & \mathbf{0} \\ \mathbf{0} & \begin{bmatrix} S_{11} & S_{12} \\ S_{12} & S_{22} \end{bmatrix} \end{bmatrix}$$

A static condensation must now be used in order to eliminate the incompatible modes in the element level and produce a reduced element formulation.

For the non-linear analysis, a Newton-Raphson iteration procedure is applied. This will result in a solution procedure as described below:

Non-Linear Solution Process:

- Compute $\mathbf{K}_{11}$, $\mathbf{K}_{12}$ and $\mathbf{K}_{22}$.
- For a load step i, the iterative loop can be written as

1. Given $\delta\mathbf{p}$ from the solution of the Newton-Raphson equation (see below), update displacements $\rightarrow \mathbf{p}_n = \mathbf{p}_o + \delta\mathbf{p}$
2. Update incompatible modes $\rightarrow \mathbf{p}^*_n = \mathbf{p}^*_o + \delta\mathbf{p}^*$

$$\delta\mathbf{p}^* = \mathbf{K}_{22}^{-1}(\mathbf{q}^*_i - \mathbf{K}^T_{12}\delta\mathbf{p})$$

3. Total strain

$$\mathbf{E} = \mathbf{B}\,\mathbf{p}_n + \mathbf{B}^*\,\mathbf{p}^*_n$$

4. Compute stress

$$\mathbf{S} = \mathbf{D}\,\mathbf{E}$$

5. Compute new matrices $\mathbf{K}_{11}$, $\mathbf{K}_{12}$ and $\mathbf{K}_{22}$ (equations 4.34, 4.20 and 4.21) and 'internal force vectors'

$$\mathbf{q}_i = \int_{V_o} \mathbf{B}^T \mathbf{S}\, dV_o$$

$$\mathbf{q}^*_i = \int_{V_o} \mathbf{B}^{*^T} \mathbf{S}\, dV_o$$

6. Compute modified internal force vector and tangent stiffness matrix (static condensation)

$$\mathbf{q}_{i_{(tot)}} = \mathbf{q}_i - \mathbf{K}_{12}\mathbf{K}_{22}^{-1}\mathbf{q}^*_i$$

$$\mathbf{K}_{(tot)} = \mathbf{K}_{11} - \mathbf{K}_{12}\mathbf{K}_{22}^{-1}\mathbf{K}^T_{12}$$

7. Assemble and compute new residual from

$$\mathbf{g} = \mathbf{q}_e - \mathbf{q}_{i_{(tot)}}$$

8. a. if $|\mathbf{g}| < tolerance \rightarrow$ end increment;

   b. if not $\rightarrow \delta\mathbf{p} = \mathbf{K}^{-1}_{(tot)}\,\mathbf{g}$ and go back to 1.

4.3 Displacement-dependent (follower) pressure load

For an analysis involving large displacement and strains such as those with rubber-like materials, an applied pressure load, for instance, will be dependent on the current geometry of the structure, therefore the concept of follower load must be applied. This merely means that the load vector (magnitude and direction) has to be update within the non-linear process.

Consider the element as shown figure 4.5. It is loaded at the side $i-j$ with a pressure p^*. From virtual work,

$$\delta\mathbf{p}_v^T\,\mathbf{q}_e^{i-j} = \int_{S_{i-j}} {p^*}^{i-j}\,\delta {e'}_v^{i-j}\,dS_{i-j} \tag{4.35}$$

where: $\delta\mathbf{p}_v$ are the virtual displacements;

$\mathbf{q}_e^{i-j}$ is the external load vector applied at the side $i-j$;

${\delta e'}_v^{i-j}$ is the change of displacement in the direction of the normal to the surface on the area dS_{i-j};

S_{i-j} is the current area of the side in which the pressure is been applied (for plane-strain it is in fact the current length l_{i-j} since the thickness is 1.)

The variation of displacement in the normal direction of S_{i-j} can be calculated as

$$\delta {e'}_v^{i-j} = \delta\mathbf{u}_v^T\,\mathbf{n}_n^{i-j} \tag{4.36}$$

where

$$\delta\mathbf{u}_v = \mathbf{L}^{i-j}\,\delta\mathbf{p}_v \tag{4.37}$$

and the unit normal vector $\mathbf{n}_n^{i-j}$ is given by

$$\mathbf{n}_n^{i-j} = \frac{1}{l_{i-j}}\left(\begin{Bmatrix} -Y_{ji} \\ X_{ji} \end{Bmatrix} + \mathbf{M}^{i-j}\,\mathbf{p}\right) \tag{4.38}$$

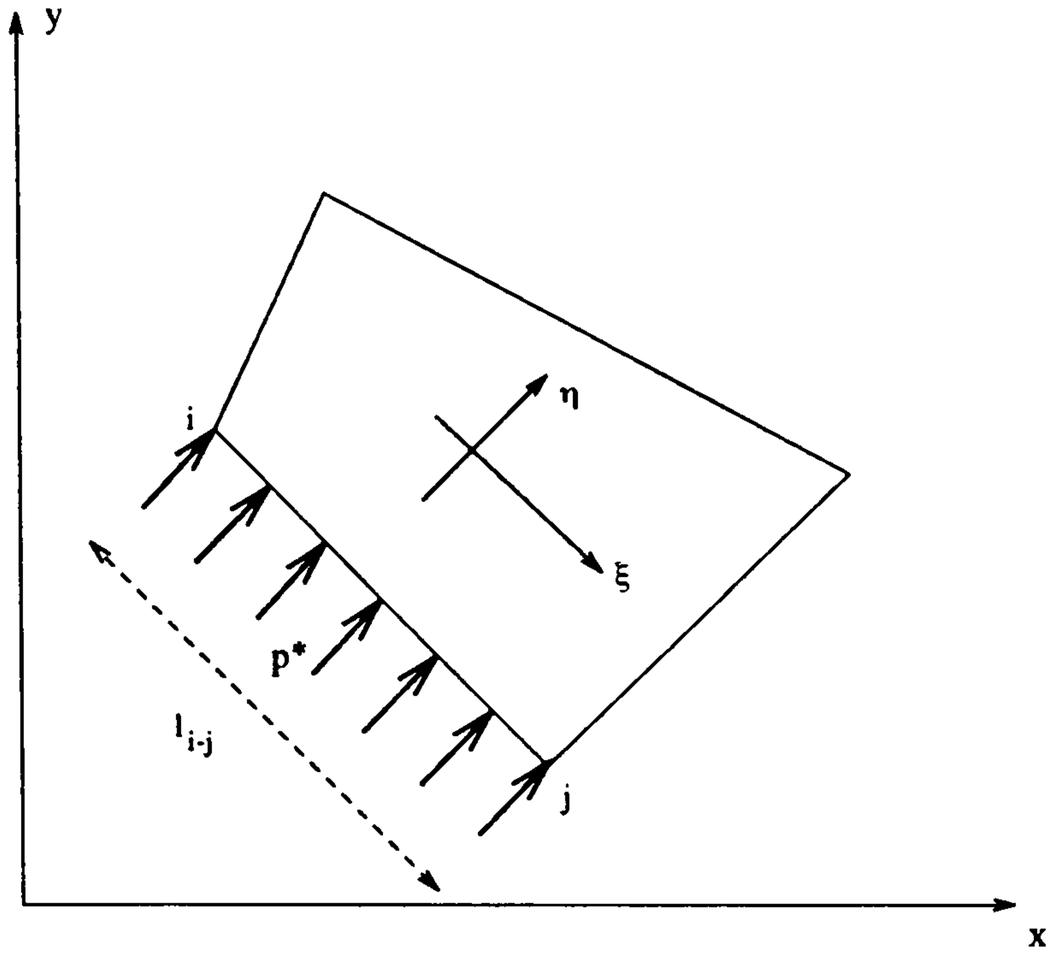


Figure 4.5: Displacement-dependent load pressure

where $X_{ji} = X_j - X_i$, for example, and $\mathbf{L}^{i-j}$ and $\mathbf{M}^{i-j}$ depend on the side the load is been applied. If we take the side $1-2$ as an example, we have

$$\mathbf{L}^{1-2} = \frac{1}{2}\begin{bmatrix} (1-\xi) & 0 & (1+\xi) & 0 & 0 & 0 & 0 & 0 \\ 0 & (1-\xi) & 0 & (1+\xi) & 0 & 0 & 0 & 0 \end{bmatrix} \tag{4.39}$$

$$\mathbf{M}^{1-2} = \begin{bmatrix} 0 & 1 & 0 & -1 & 0 & 0 & 0 & 0 \\ -1 & 0 & 1 & 0 & 0 & 0 & 0 & 0 \end{bmatrix} \tag{4.40}$$

After some calculations, we have the external force vector written as

$$\mathbf{q}_e^{T^{i-j}} = \frac{{p^*}^{i-j}}{2}\left(\begin{Bmatrix} -Y_{ji} \\ X_{ji} \end{Bmatrix}^T + \mathbf{p}^T \mathbf{M}^{i-j^T}\right)\mathbf{A}^{i-j} \tag{4.41}$$

where $\mathbf{A}^{i-j}$ is also dependent on the side where the load is been applied. For side $1-2$, for example, we have

$$\mathbf{A}^{1-2} = \begin{bmatrix} 1 & 0 & 1 & 0 & 0 & 0 & 0 & 0 \\ 0 & 1 & 0 & 1 & 0 & 0 & 0 & 0 \end{bmatrix} \tag{4.42}$$

Now $\mathbf{q}_e$ is not constant as before, thus a new portion should be added to the previous stiffness matrix established. This new part comes from the differentiation of $\mathbf{q}_e$ with respect to the displacements.

$$\mathbf{K}_p^{i-j} = \frac{{p^*}^{i-j}}{2} \mathbf{A}^{i-j^T} \mathbf{M}^{i-j} \tag{4.43}$$

4.4 Incompatible elements with hyperelastic materials

After the development of the formulation above, we will present the modifications needed to work with hyperelasticity. Some of the changes have already been shown in the previous chapter, although they will be presented here again to ease the understanding of the whole development. This section, however, will concentrate on the new formulation for plane-strain with rubber-like materials.

4.4.1 Plane stress

As was said before, the formulation for plane-stress has already been developed in the previous chapter. The main modifications are the replacement of the modulus matrix and the calculation of the new second Piola-Kirchhoff stresses. Having computed these modifications, as in Chapter 3, we just have to supersede them in the formulation for the ordinary elastic element of the previous section.

4.4.2 Plane strain

Although rubber is frequently regarded as incompressible, depending on the manufacturing process used, it can present a reasonable compressibility. Therefore, we need to modify the Ogden's strain energy function in order to use it for a compressible or near-incompressible rubber-like material. This modified energy function will be also applied in the development of a plane-strain element.

Following the work presented in Chapter 2, the strain-energy function of (2.41) is re-expressed here. Hence,

$$\varphi = \sum_p \frac{\mu_p}{\alpha_p} (\overline{\lambda}_1^{\alpha_p} + \overline{\lambda}_2^{\alpha_p} + \overline{\lambda}_3^{\alpha_p} - 3) + \frac{1}{2} k (J-1)^2 \tag{4.44}$$

where,

$$\overline{\lambda}_i = J^{-\frac{1}{3}} \lambda_i \tag{4.45}$$

These modified stretches $\overline{\lambda}_i$ are volume preserving and the deviatoric and volumetric terms can be separated [21]. The introduction of the bulk modulus k is due to the compressibility mentioned above.

At this point, we impose the plane-strain condition $\lambda_3 = 1$, so that

$$\varphi = \sum_p \frac{\mu_p}{\alpha_p}[J^{-\frac{\alpha_p}{3}}(\lambda_1^{\alpha_p} + \lambda_2^{\alpha_p} + 1) - 3] + \frac{1}{2}k(J-1)^2 \tag{4.46}$$

To obtain the principal stretches, we can use the right Cauchy-Green tensor $\mathbf{C}$ that comes from the displacement-derivative matrix (or displacement gradient matrix) $\mathbf{D}$. From (4.23), $\mathbf{D}$ is given by

$$\mathbf{D} = \begin{bmatrix} \frac{\partial u}{\partial X} & \frac{\partial u}{\partial Y} \\ \frac{\partial v}{\partial X} & \frac{\partial v}{\partial Y} \end{bmatrix} \tag{4.47}$$

From (4.47) above we can set

$$\mathbf{F} = \mathbf{I} + \mathbf{D} \tag{4.48}$$

as the deformation gradient.

The right Cauchy-Green tensor $\mathbf{C}$ can now be computed as

$$\mathbf{C} = \mathbf{F}^T\mathbf{F} \tag{4.49}$$

It is important to note that the expression for $\mathbf{C}$ can also be presented using the principal stretches and their directions, i.e.,

$$\mathbf{C} = \lambda_1^2\mathbf{N}_1\mathbf{N}_1^T + \lambda_2^2\mathbf{N}_2\mathbf{N}_2^T \tag{4.50}$$

where the values for λ_i^2 and $\mathbf{N}_i$ can be computed through an eigenproblem, where λ_i^2 =eigenvalues and $\mathbf{N}_i$ =eigenvectors [21]. Alternatively we can just compute the principal Green's strains and directions (using Mohr's circle [88]) and then compute the stretches from

$$\lambda_i = \sqrt{2E_i + 1} \tag{4.51}$$

Now, the stresses can easily be determined as

$$S_i = \frac{\partial \varphi}{\partial E_i} \tag{4.52}$$

Using the chain rule for the calculations, the second Piola-Kirchhoff stresses in the principal directions are

$$S_1 = \frac{1}{3\lambda_1^2}\sum_p \mu_p J^{-\frac{\alpha_p}{3}}(2\lambda_1^{\alpha_p} - \lambda_2^{\alpha_p} - 1) + \frac{kJ}{\lambda_1^2}(J-1) \tag{4.53}$$

$$S_2 = \frac{1}{3\lambda_2^2}\sum_p \mu_p J^{-\frac{\alpha_p}{3}}(2\lambda_2^{\alpha_p} - \lambda_1^{\alpha_p} - 1) + \frac{kJ}{\lambda_2^2}(J-1) \tag{4.54}$$

Noting that $\lambda_3 = 1$, the third stress S_3 can also be computed although it is not necessary for the formulation of the plane-strain element.

$$S_3 = \frac{1}{3}\sum_p \mu_p J^{-\frac{\alpha_p}{3}}(2 - \lambda_1^{\alpha_p} - \lambda_2^{\alpha_p}) + kJ(J-1) \tag{4.55}$$

Having computed S_1 and S_2 using the principal directions $\mathbf{N}_1$, $\mathbf{N}_2$, we can define the stresses in the original system as

$$\mathbf{S} = \mathbf{Q}(\mathbf{N})[\mathbf{diag}\, S_i]\mathbf{Q}^T(\mathbf{N}) \tag{4.56}$$

Next, to complete the formulation it only necessary to find the constitutive or modulus matrix for a hyperelastic material in plane strain. This $\mathbf{D}$ matrix comes from the variation of the stress and strain vectors in the Lagrangian triad. To this end, we have

$$\delta\mathbf{S}^L = \mathbf{D}\,\delta\mathbf{E}^L \tag{4.57}$$

which gives

$$\mathbf{D} = \begin{bmatrix} D_{11} & D_{12} & 0 \\ D_{21} & D_{22} & 0 \\ 0 & 0 & D_{33} \end{bmatrix} \tag{4.58}$$

where,

$$\begin{aligned}
D_{11} &= \frac{\partial S_1}{\partial E_1} = \frac{1}{3\lambda_1^4}\sum_p \mu_p J^{-\frac{\alpha_p}{3}}[(\frac{4}{3}\alpha_p - 4)\lambda_1^{\alpha_p} + (\frac{\alpha_p}{3} + 2)(\lambda_2^{\alpha_p} + 1)] + k\frac{\lambda_2}{\lambda_1^3} \\
D_{12} &= \frac{\partial S_1}{\partial E_2} = D_{21} = \frac{\partial S_2}{\partial E_1} = \frac{1}{9\lambda_1^2\lambda_2^2}\sum_p \mu_p \alpha_p J^{-\frac{\alpha_p}{3}}[1 - 2(\lambda_1^{\alpha_p} + \lambda_2^{\alpha_p})] + k(2 - \frac{1}{\lambda_1\lambda_2}) \\
D_{22} &= \frac{\partial S_2}{\partial E_2} = \frac{1}{3\lambda_2^4}\sum_p \mu_p J^{-\frac{\alpha_p}{3}}[(\frac{4}{3}\alpha_p - 4)\lambda_2^{\alpha_p} + (\frac{\alpha_p}{3} + 2)(\lambda_1^{\alpha_p} + 1)] + k\frac{\lambda_1}{\lambda_2^3} \\
D_{33} &= \frac{(S_1 - S_2)}{2(E_1 - E_2)}
\end{aligned} \tag{4.59}$$

Note that the last term in (4.59) comes from the isotropic condition that the directions of principal strain (Green's) and stress (second Piola-Kirchhoff) coincide. It must be replace by $\frac{1}{2}\sum_p \mu_p \alpha_p$ when $E_1 = E_2$. (See previous chapter for more details.)

This matrix is also defined in the principal directions. To place it back into x, y directions, we have to use the transformation matrix define in (3.90) , i.e.,

$$\mathbf{R} = \begin{bmatrix} c^2 & s^2 & sc \\ s^2 & c^2 & -sc \\ -2sc & 2sc & (c^2 - s^2) \end{bmatrix} \tag{4.60}$$

with $c = cos\theta$, $s = sin\theta$ and θ being the angle between the original and principal directions.

Hence,

$$\mathbf{D}_t = \mathbf{R}^T \mathbf{D} \mathbf{R} \tag{4.61}$$

The new stresses and modulus matrix should now be applied in the previous incompatible element formulation producing the complete plane-strain incompatible element for analysis of rubber-like materials.

4.5 Numerical tests

In this section, some examples will be given to confirm the good performance of the element for a range of problems. The section is divided in three parts to cover basis linear tests with the element, non-linear elastic tests and finally hyperelastic examples. In the latter, in spite of presenting some satisfactory results, the element fails to converge for a particular problem in this context. This was the motivation for the study of the new class of elements described in the subsequent chapters.

4.5.1 Linear elasticity

This tests directly relate to the "Wilson-Taylor" element described in the begin of this chapter. They are included here to demonstrate the good performance of this element and hence to justify its later use in a non-linear context.

Test of mesh sensitivity to distortion

This problem is widely used as a test for the sensitivity of the element to mesh distortion. A beam subject to a bending moment is modelled with two elements. It is kept fixed

on one end and the interface between the two element is rotated to distort the mesh. The results are then compared with those produced by Li [51] with the so-called mixed assumed strain element and by the compatible quadrilateral element (figure 4.6). Similar results were also obtained by Simo and Rifai [76] and Pian and Sumihara [71].

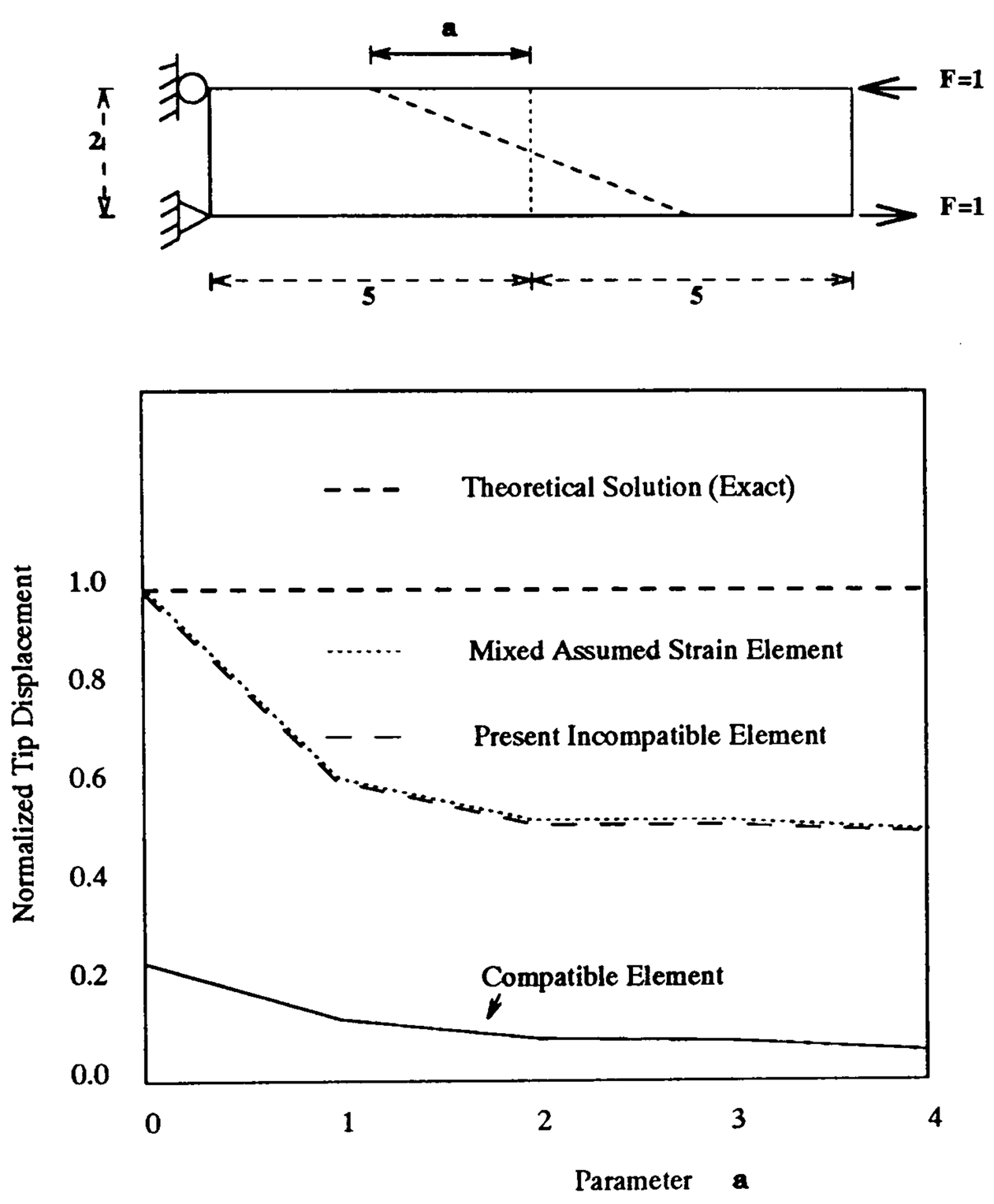


Figure 4.6: Mesh sensitivity to distortion

Thick-Walled Cylinder with Internal Pressure

The second example is a thick cylinder in plane strain as shown in figure 4.7. In this case, the problem is used to demonstrate the good performance and the accuracy in results, especially for stresses, for a elastic nearly incompressible material. The cylinder is analysed using Poisson's ratio of $\nu = 0.3$ (normal compressible material) and $\nu = 0.49$ (nearly incompressible material) and three values of stress in three different points through the thickness are compared with the exact solution, the compatible 4-noded element and the compatible 9-noded element shown in [97]. As can be seen in the table 4.1 below, the nearly incompressible material causes problem for both compatible

Stress	*Radial*			*Hoop*			*Axial*		
Radius	3.00	5.20	9.00	3.00	5.20	9.00	3.00	5.20	9.00
Poisson's ratio $\nu = 0.30$									
Compatible 4-Noded	-0.87	-0.25	-0.03	1.29	0.49	0.24	0.125	0.074	0.062
Compatible 9-Noded	-0.98	-0.24	0.01	1.26	0.50	0.25	0.075	0.075	0.075
Present Incomp.	-0.92	-0.25	-0.02	1.27	0.49	0.24	0.103	0.074	0.067
Exact	-1.00	-0.25	0.00	1.25	0.50	0.25	0.075	0.075	0.075
Poisson's ratio $\nu = 0.49$									
Compatible 4-Noded	0.69	-0.26	-0.43	2.77	0.44	-0.18	1.70	0.085	-0.299
Compatible 9-Noded	-0.79	-0.07	0.10	1.45	0.67	0.35	0.32	0.29	0.22
Present Incomp.	-0.92	-0.25	-0.02	1.30	0.49	0.23	0.186	0.121	0.105
Exact	-1.00	-0.25	0.00	1.25	0.50	0.25	0.123	0.123	0.123

Table 4.1: Thick cylinder

elements as the solution accuracy falls, with large errors in the computed stress values. The present incompatible element loses little accuracy due to the incompressibility.

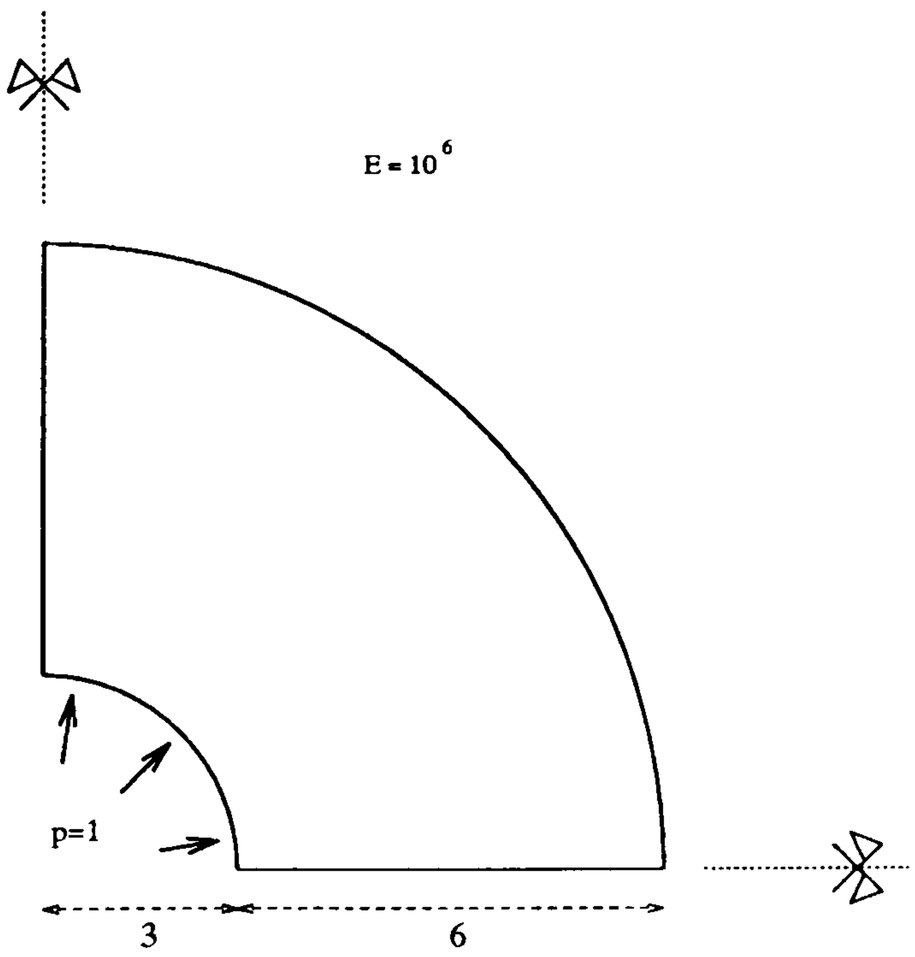


Figure 4.7: Thick-walled cylinder

4.5.2 Non-Linear Elasticity

Large deflection of a cantilever beam

This example involves a cantilever beam subject to a shear load at the tip and clamped at the opposite end. The structure is analysed using a 10×1 element mesh for the plane-stress condition. The beam has the length of $L = 20$ and the moment of inertia of $I = \frac{1}{12}$ (thickness $t = 1$ and width $h = 1$). The material properties are: Young's modulus $E = 4.8 \times 10^8$ and Poisson's ratio $\nu = 0.0$. The solutions for the present incompatible element, the standard compatible element and the analytical analysis (see [52]) are given in figure 4.8 where the normalised load ($\frac{PL}{EI}$) is plotted against the normalised tip deflection ($\frac{w}{L}$). The agreement between the present element and the analytical solution is excellent despite the relatively course mesh employed in the example. However, the compatible element exhibits an over-stiff response as already expected. The large deflection of the cantilever beam can more easily be seen from figure 4.9 where the deformed configuration for different load increments is presented (the total load applied is $F_{total} = 10 \times 100000$).

Shallow arch subject to a point load

A shallow arch structure is loaded with a concentrate load applied on the centre. This is a very usual test problem and it is analysed with a 5 element mesh, modelling only half of the arch due to the symmetry. The geometry of the arch is defined by its medium radius ($R = 100$) and a subtended angle ($\theta = 28.04^o$) as shown in figure 4.10. The thickness of the arch is $t = 1$ and its width is $h = 2$. The material properties used in this examples are: $E = 10^7$ and $\nu = 0.0$.

The concentrate load is plotted against the centre deflection and the solution is compared with the mixed assumed strain element [51] and the analytical solution [52] (figure 4.11). The performance of the present element is excellent and a very good agreement is obtained. Figure 4.12 depicts the deformed mesh for different load levels.

Cook's Membrane Problem

This classical problem is analysed in a non-linear environment. The tapered panel is kept fixed (clamped) on one edge and is subjected to a shear load on the opposite end as shown in figure 4.13. This example gives a very good indication of how the element behaves with distorted meshes. The material used in this example is nearly incompressible ($\nu = 0.49$) and its Young's modulus is $E = 70$. A plane strain analysis is

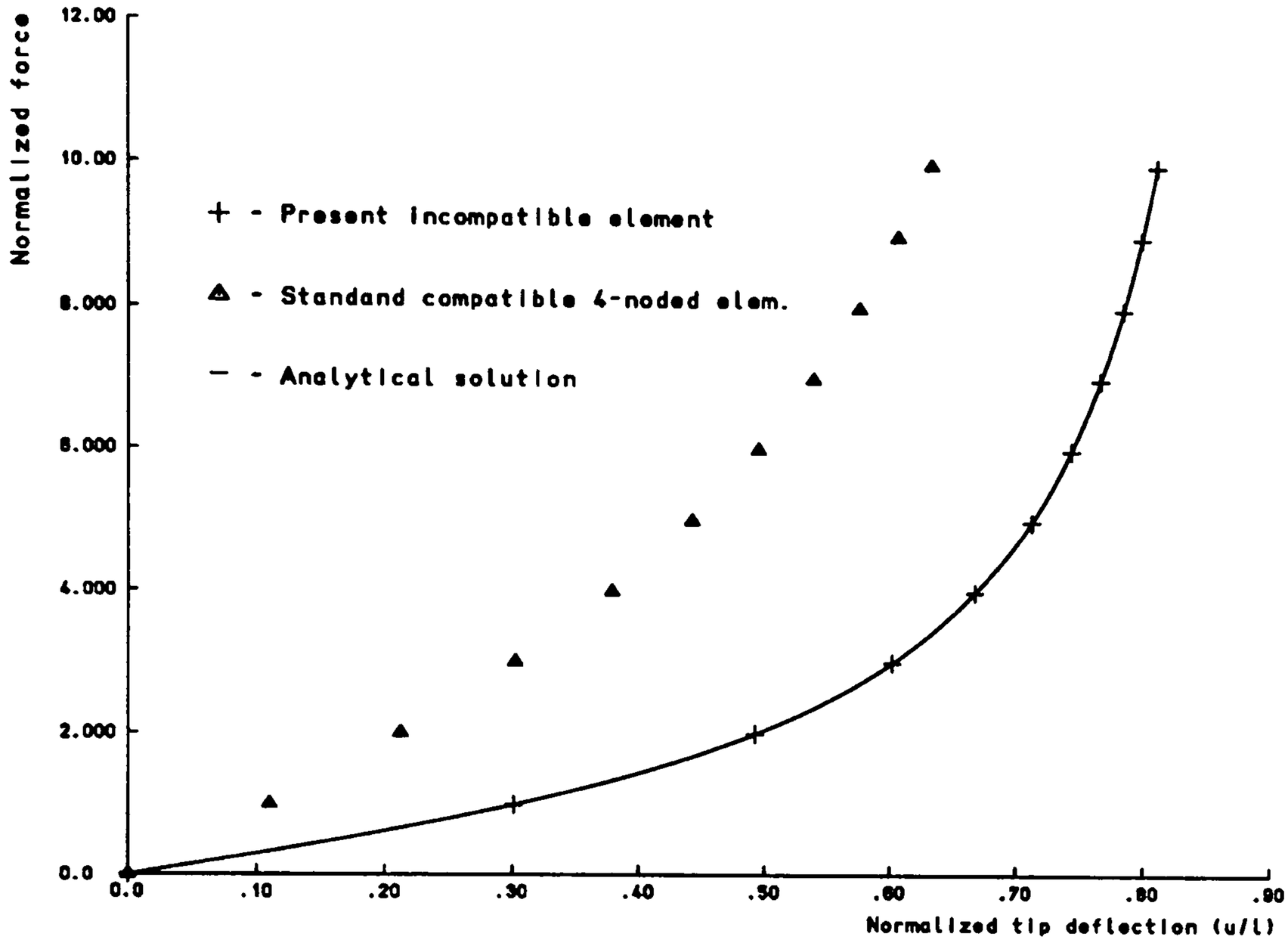


Figure 4.8: Large deflection of a cantilever beam

then performed with three different elements: a mixed assumed strain element [51], the quadratic 8-noded compatible element and the present incompatible element. Five load steps of $\Delta F = 16$ are imposed and the results for the stress σ_{xx} for the mixed assumed strain and the present elements is shown in figure 4.14. As can be noted, the present element produces a much more uniform stress distribution along the panel. As far as displacements are concerned, table 4.2 shows the final vertical and horizontal deflections for the three elements used. The three elements produce very similar results.

	Mixed assumed		*Present*		*8-noded*	
	u	v	u	v	u	v
Top corner A	-12.9872	13.1151	-12.9066	13.0296	-13.1678	13.0947
Bottom corner B	-5.6179	14.3518	-5.4762	14.3099	-5.7938	14.1827

Table 4.2: Displacement at points A and B for Cook's membrane

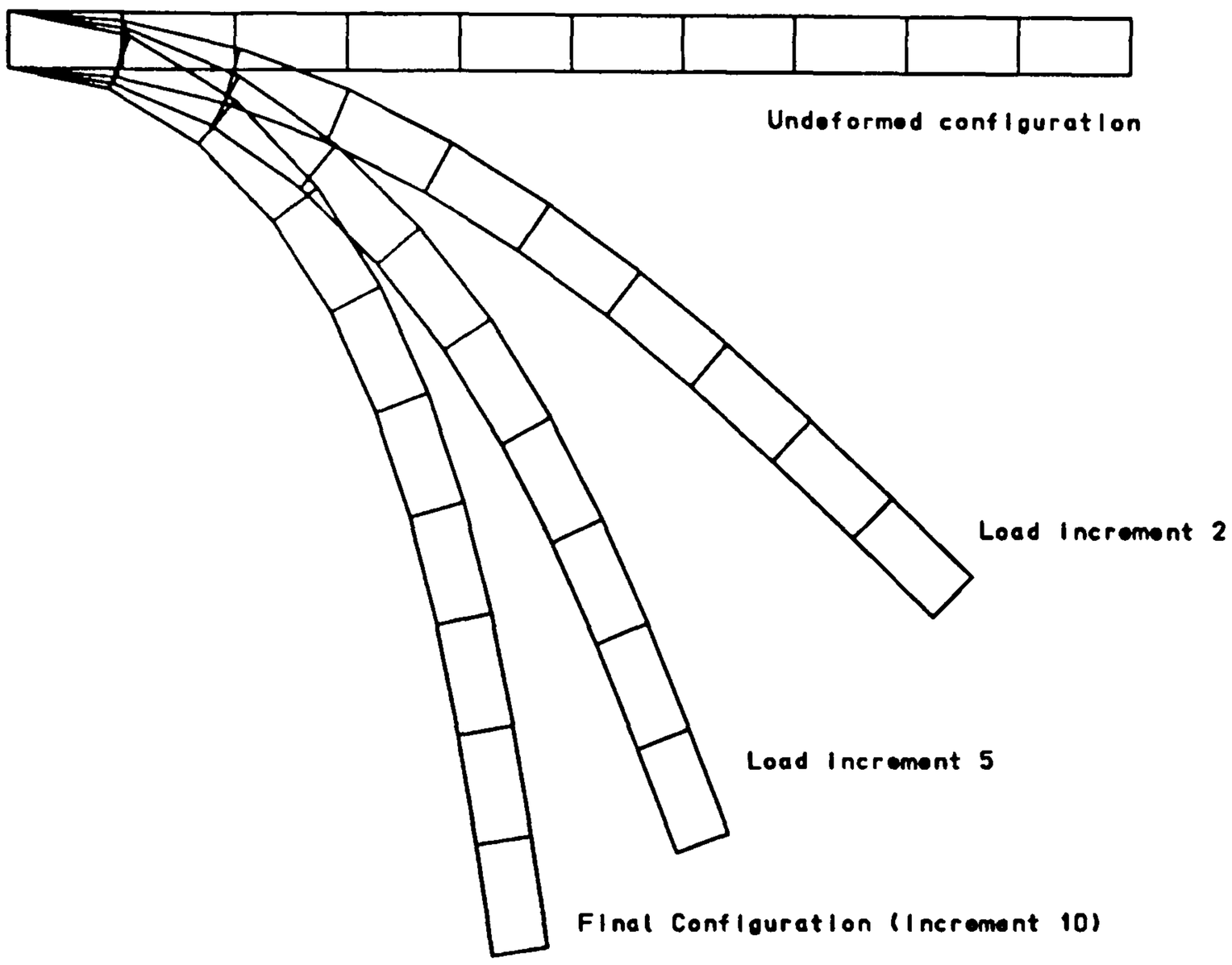


Figure 4.9: Deformation of the beam

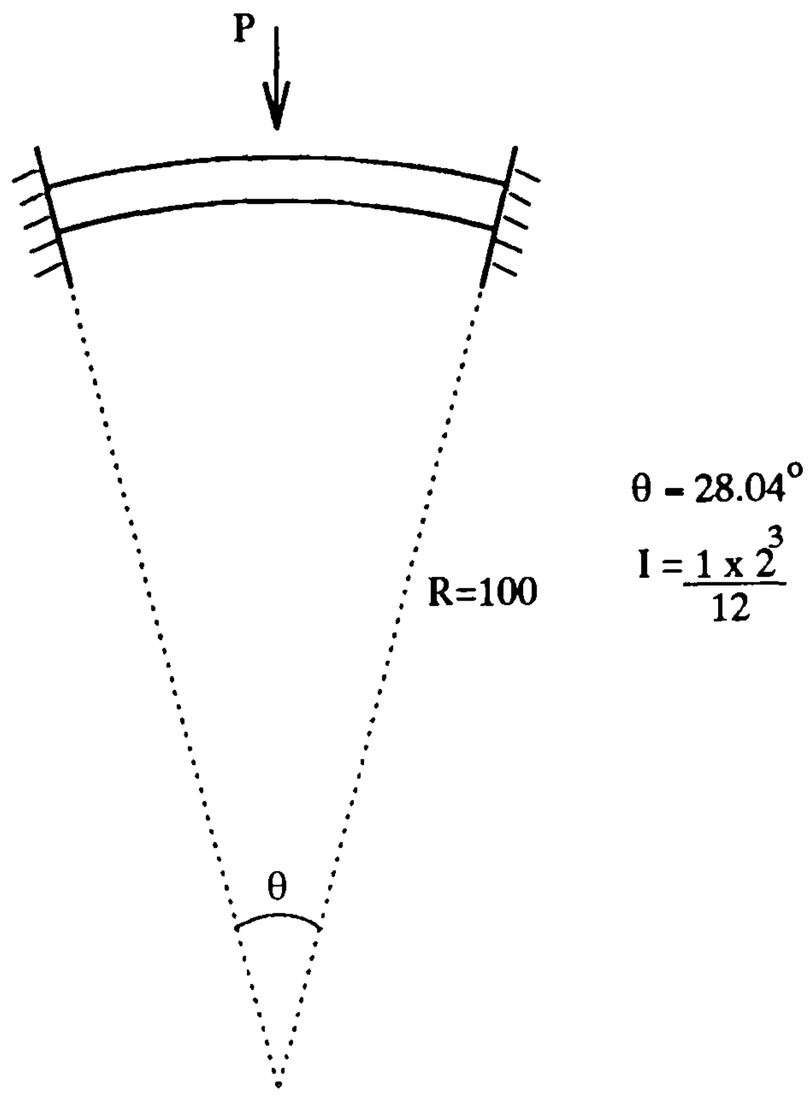


Figure 4.10: Shallow arch subject to a concentrated load

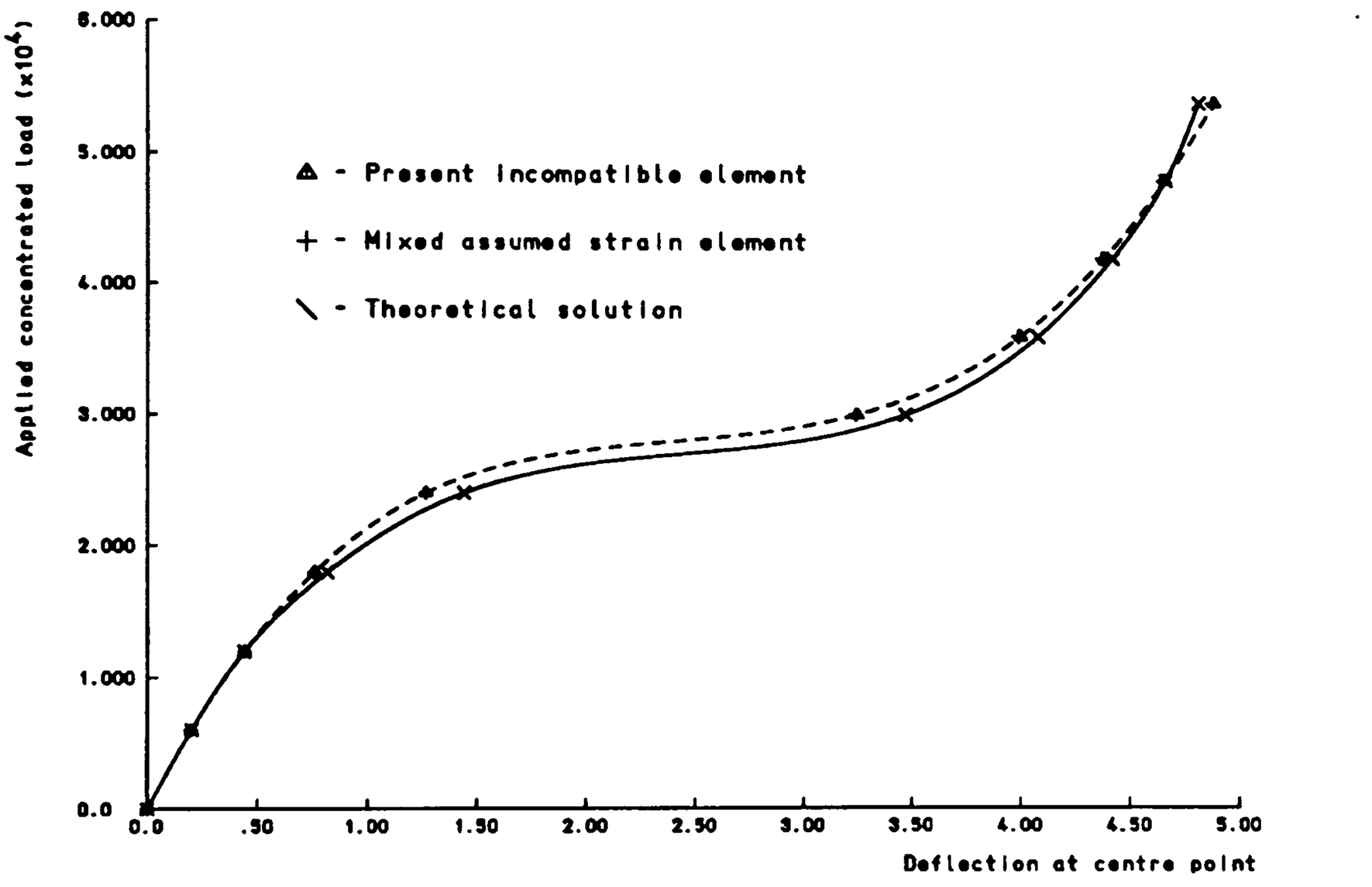


Figure 4.11: Load-deflection curve for the shallow arch problem

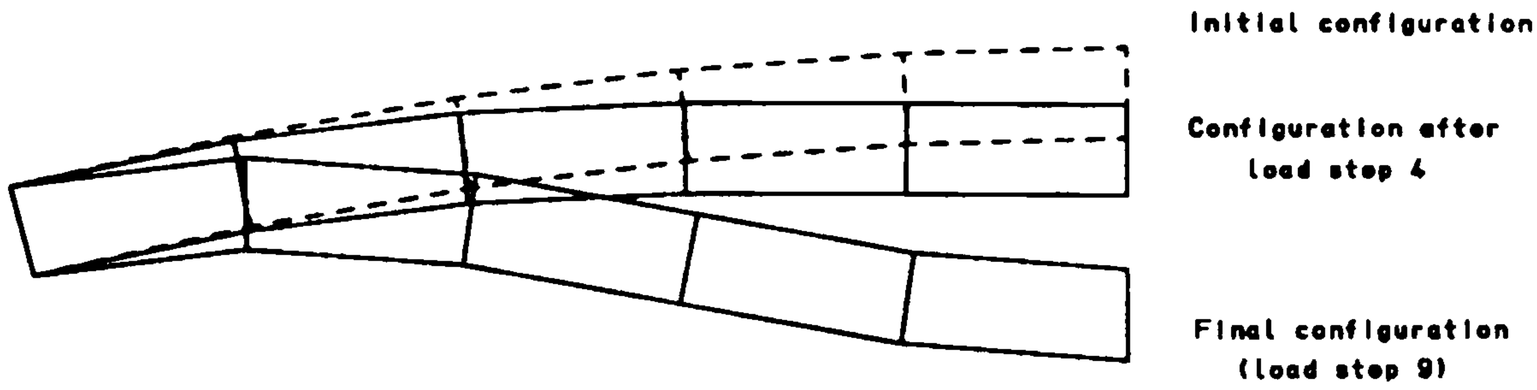


Figure 4.12: Shallow arch - original and deformed configuration

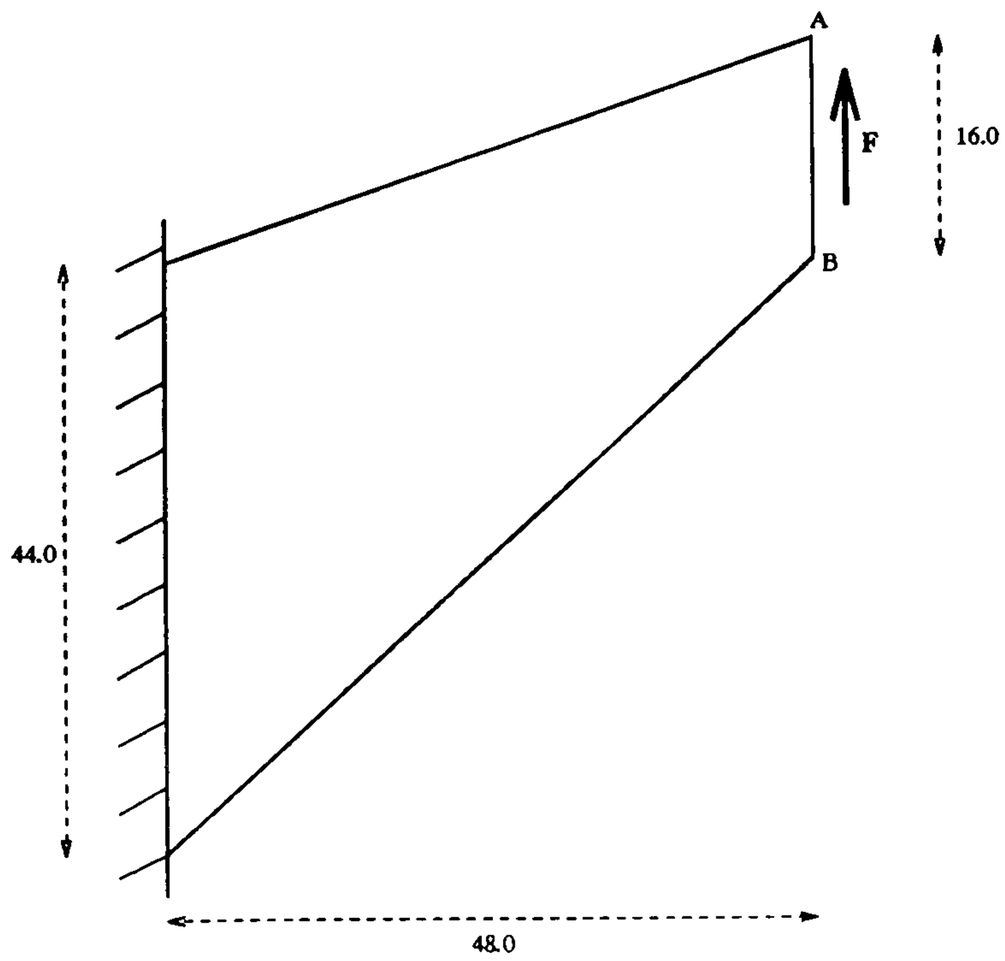


Figure 4.13: Cook's membrane problem

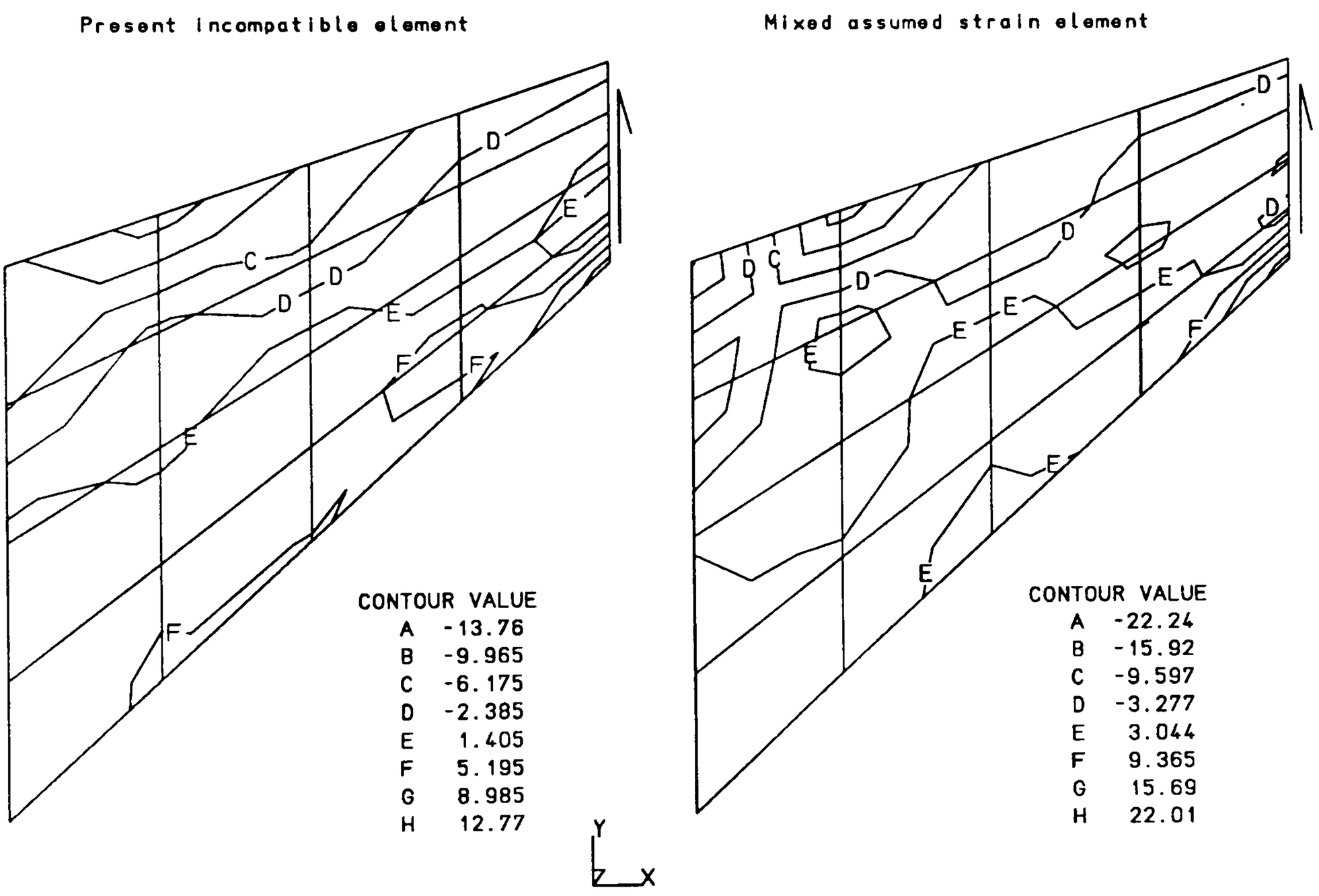


Figure 4.14: Cook's Membrane - Contour for σ_{xx} stress

4.5.3 Hyperelasticity

Cook's membrane problem using a neo-Hookean material

The next example to be presented is the same Cook's membrane studied in the non-linear elastic case (figure 4.13). This second analysis introduces the use of hyperelasticity with the present element. It uses a neo-Hookean material to model the (almost) incompressible rubberlike panel subject to a plane strain condition. The characteristics of the material are as the following:

Bulk Modulus $k = 40.0942 \times 10^4$

Shear Modulus $\mu = 80.1938$

A shear load of $F = 100$ is applied in 40 load steps to perform the analysis. The panel is idealised using two types of elements: the present non-linear incompatible element and the well known 'u-p' or constant pressure (where the volumetric and the deviatoric portions are separated) described in appendix B. The results with the two different elements are then compared with those produced by Simo and Armero [79] with 100 increments. In figure 4.15 the vertical displacement of top right corner is plotted against the number of elements per side for the simulations applied. Although it is clearly seen that the various formulations converge to the same correct value, the present element and the element by Simo and Armero demonstrate a superior accuracy for course meshes than the 'u-p' element. Finally, figure 4.16 depicts a plot of the original undeformed mesh and the final deformed mesh after 40 increments that qualitatively looks very similar to those produced by Simo and Armero.

Mooney-Rivlin cylinder

A cylindrical cylinder is analysed using a Mooney-Rivlin hyperelastic constitutive model. A quarter of the cylinder is modelled by a 10×1 non-linear incompatible element mesh. The geometric data for this plane strain structure can be summarised as: initial internal radius $R_1 = 20.$, thickness $t = 1.57$. The material constant are $C_1 = 1835.$ and $C_2 = 146.8$. The theoretical solution for the internal pressure can be written as [52]

$$P(r) = (C_1 + C_2)[\frac{(r^2 - R_1^2)(R_2^2 - R_1^2)}{r^2(r^2 + R_2^2 - R_1^2)} + \ln \frac{r^2}{r^2(r^2 + R_2^2 - R_1^2)} + \ln \frac{R_2^2}{R_1^2}] \qquad (4.62)$$

where r is the final internal radius of the cylinder and R_1 and R_2 are the initial internal and the initial external radii, respectively.

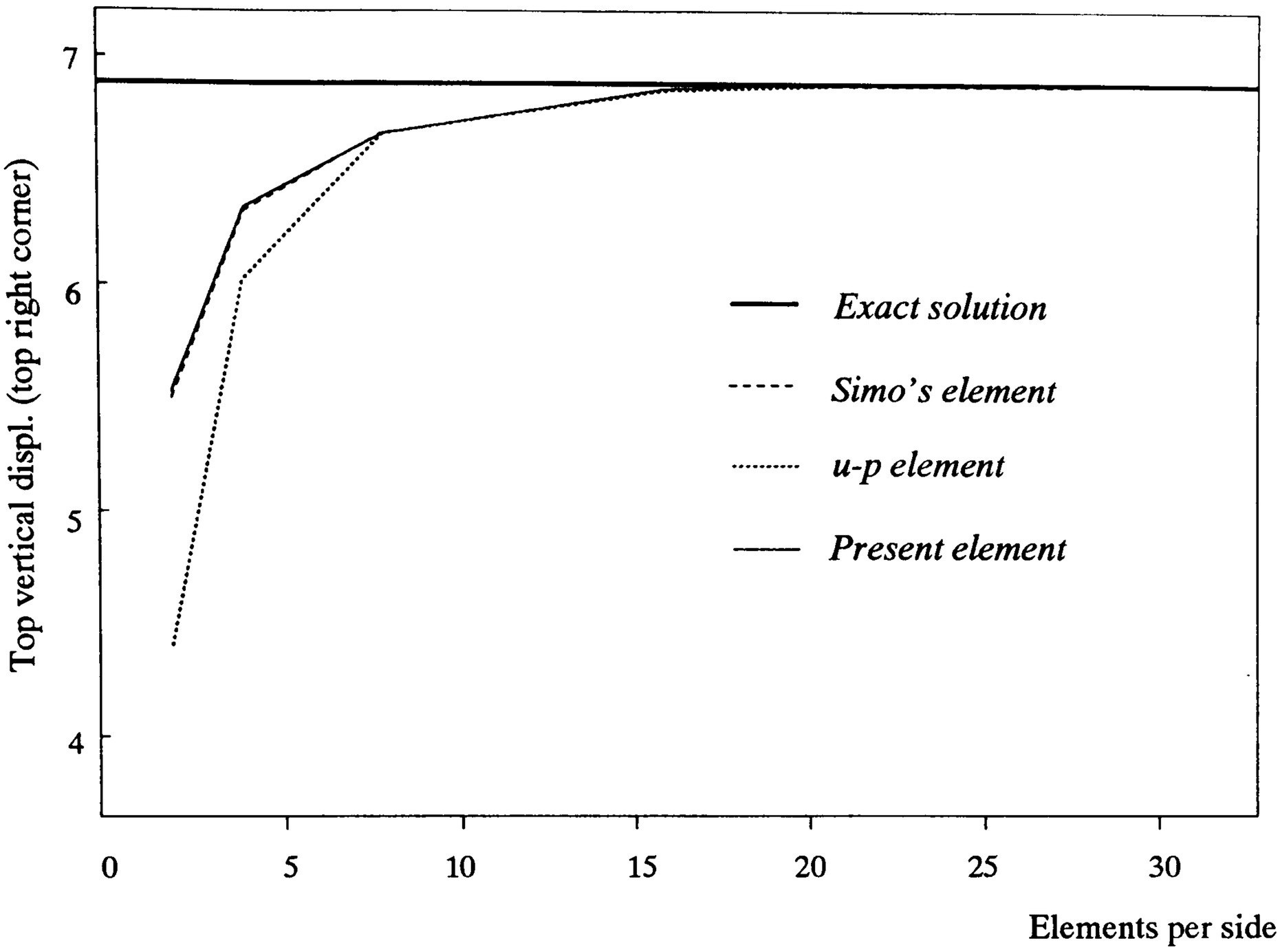


Figure 4.15: Cook's membrane - Neo-Hookean model

Figure 4.17 depicts the pressure-displacement curve for the 'u-p' element, the present incompatible element and the analytical solution.

Second cylinder with internal pressure

The last example of this chapter illustrates the problem where the non-linear incompatible element developed fails to provide a satisfactory response. A cylinder with internal pressure is analysed using the three-term Ogden model of example 3.4.1. The geometrical configuration of the cylinder is shown in figure 4.18 for a plane-strain problem. The test is performed using both the present incompatible element and the 'u-p' element defined in appendix B. The results given in figures 4.19 and 4.20 represent the analysis of the structure for a non-follower (non-conservative) and a follower (conservative) pressure load, respectively. The curves show the dimensionless pressure ($p^* = \frac{P}{\mu}$, where P is the total internal pressure and μ is the ground state of the shear modulus computed as in 3.91) plotted against the displacement of the inner circumference. In both cases the incompatible element fails to converge after a certain number of load increments. In the non-conservative problem it occurs after 36 increments. The element no longer

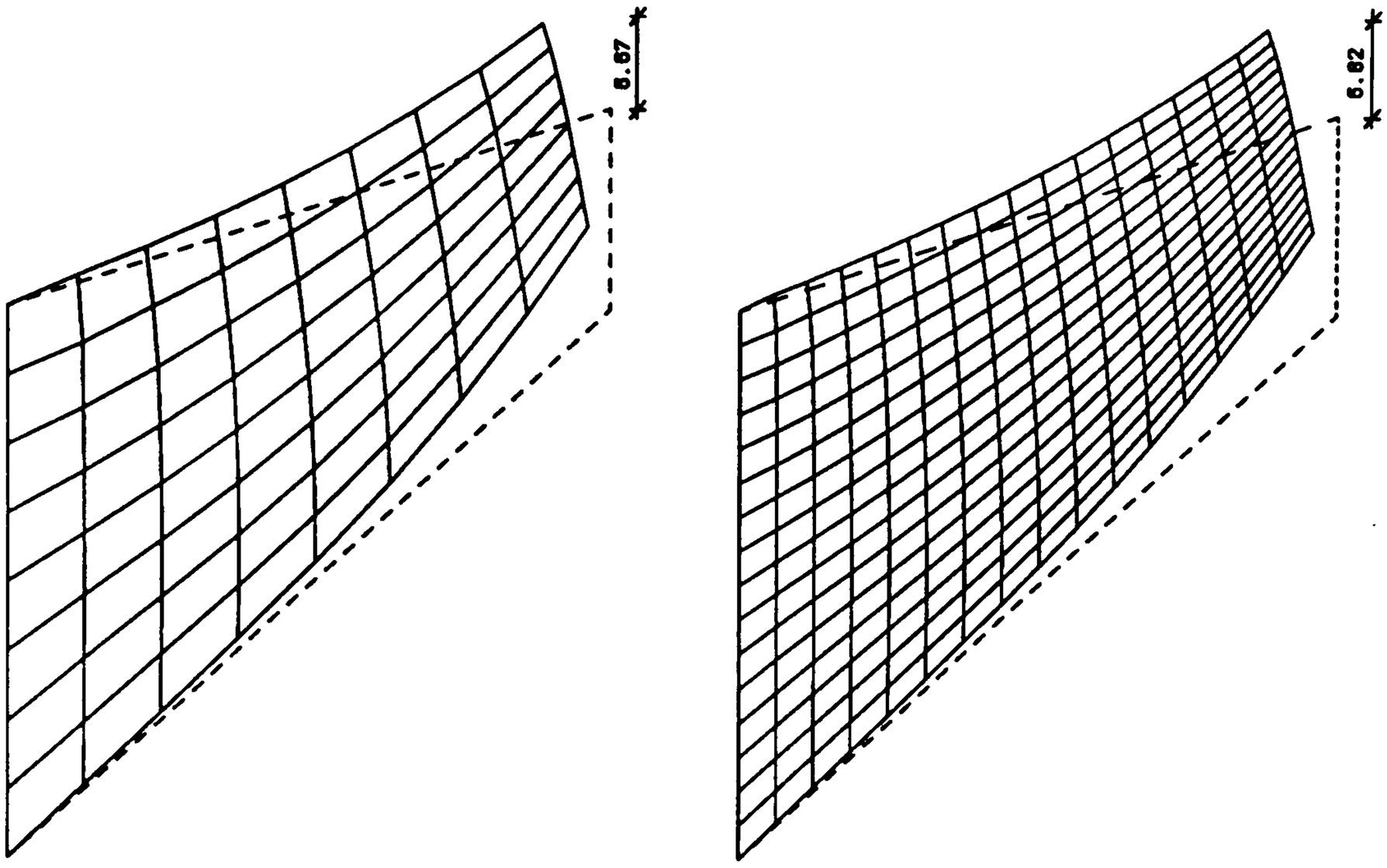


Figure 4.16: Cook's membrane - original undeformed and final deformed meshes

converges within the number of pre-established iterations and an increment size reduction has to be used. The element then converges but with two negative pivots in the factorised tangent stiffness matrix. This condition should not appear. The element cannot go beyond 38 increments. A similar problem occurs when a follower pressure load is applied. The element also fails after 35 increments when 5 negative pivots are encountered.

The problem seems to be due to spurious mechanisms that affect the element. Some of the incompatible modes are activated when the element is highly deformed. The incompatible modes that are supposed to lighten the problems caused by the incompressibility actually lead to the ill behaviour of the structure. If some of the incompatible modes are eliminated from the element for this particular problem, the complete deformation path can be evaluated and no negative pivot occur. The possible way forward is to generalise this concept but instead we decided to investigate a new formulation.

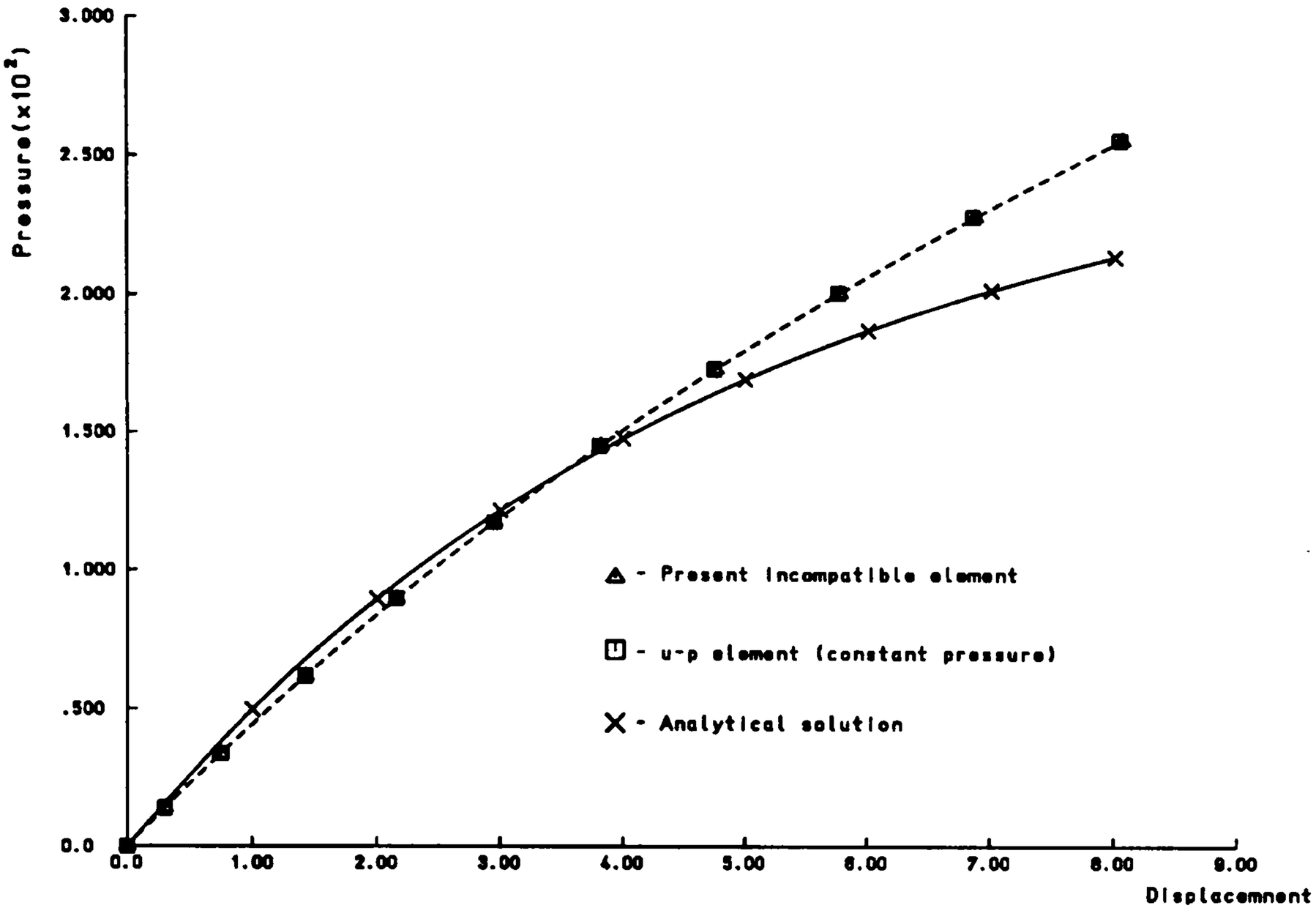


Figure 4.17: Mooney-Rivlin cylinder - load vs. displacement curve

This cylinder is re-analysed using the co-rotational element reported in the next chapter and the problem affecting the present element does not occur.

4.6 Final remarks

A 4-noded quadrilateral element has been presented. The element is coded for a non-linear analysis, considering both elastic and hyperelastic materials. Four quadratic incompatible displacements have been added to the element formulation mainly to cope with situations where this element produces a poor behaviour such as bending dominated problems and problems with irregular meshes. The other important characteristic of the formulation is the fact that in nearly incompressible problems the element is able to give very accurate solutions. For rubber-like materials, where the incompressibility appears in most of the problems, the element generated excellent results, especially in

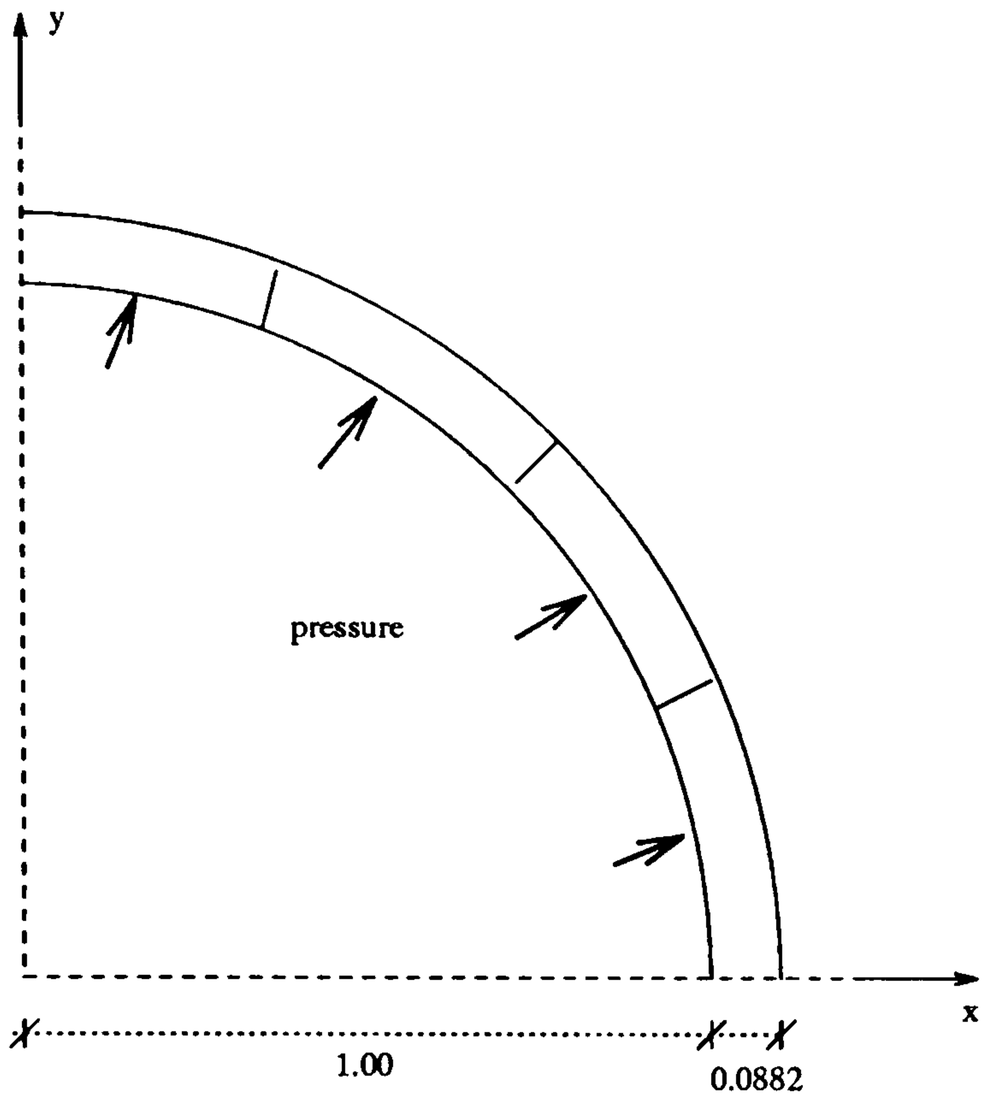


Figure 4.18: Cylinder under internal pressure

plane strain analysis, in which incompressible materials tend to have a very inaccurate performance.

From the series of examples shown, it can clearly be seen the good agreement of solutions demonstrated by the present incompatible element. Classical as well as other cases were presented, confirming the efficiency of approach adopted for most of the cases studied.

However, the element presents difficulties when analysing certain hyperelastic structures, as shown for the last example of this chapter. This is connected to the spurious mechanisms exhibited by the element for some kinds of problems. This drawback motivates the consideration of a new class of elements, known as co-rotational, which will be considered in the next chapters.

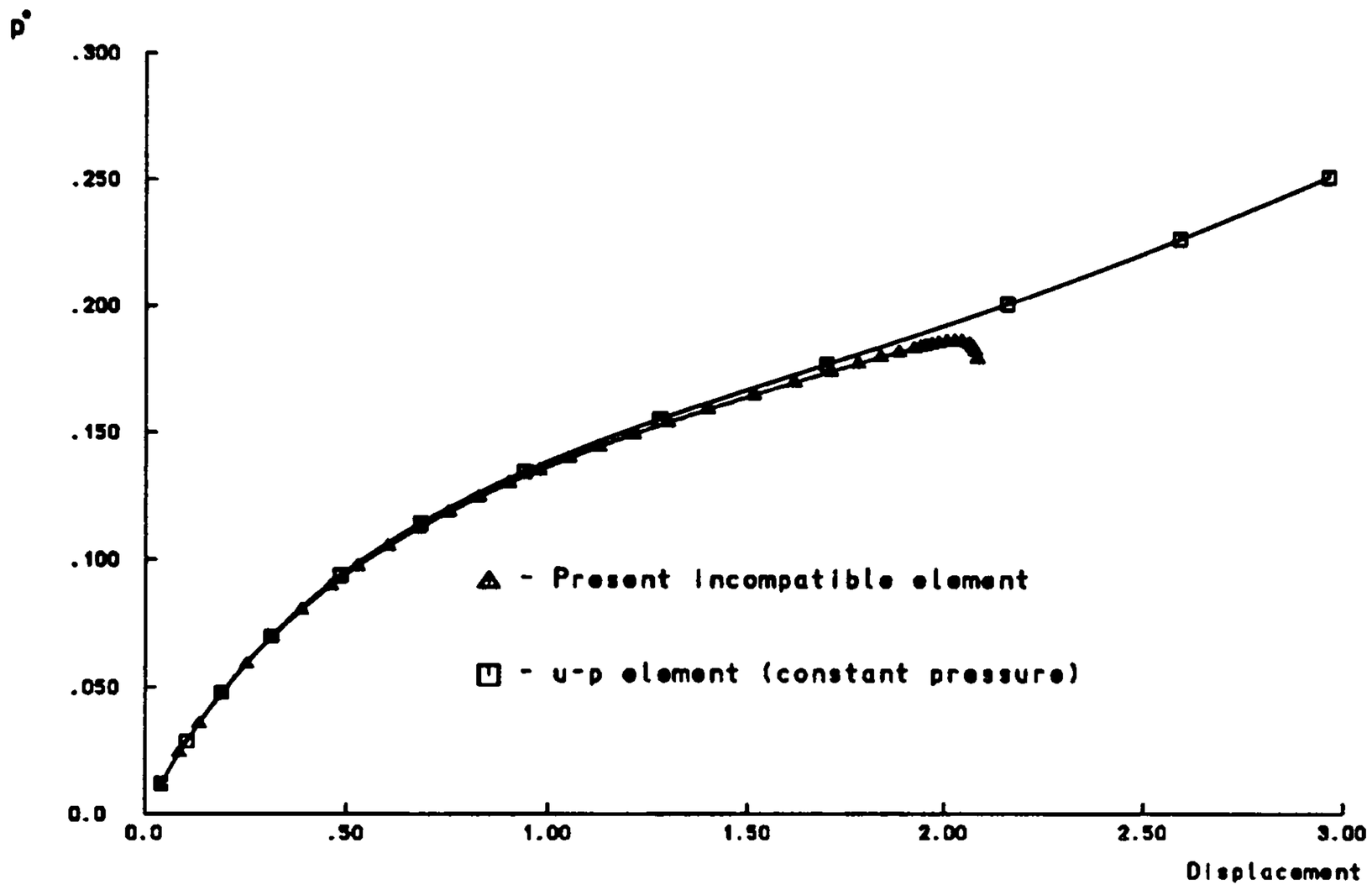


Figure 4.19: Cylinder under internal pressure - Dimensionless non-follower pressure vs. displacement

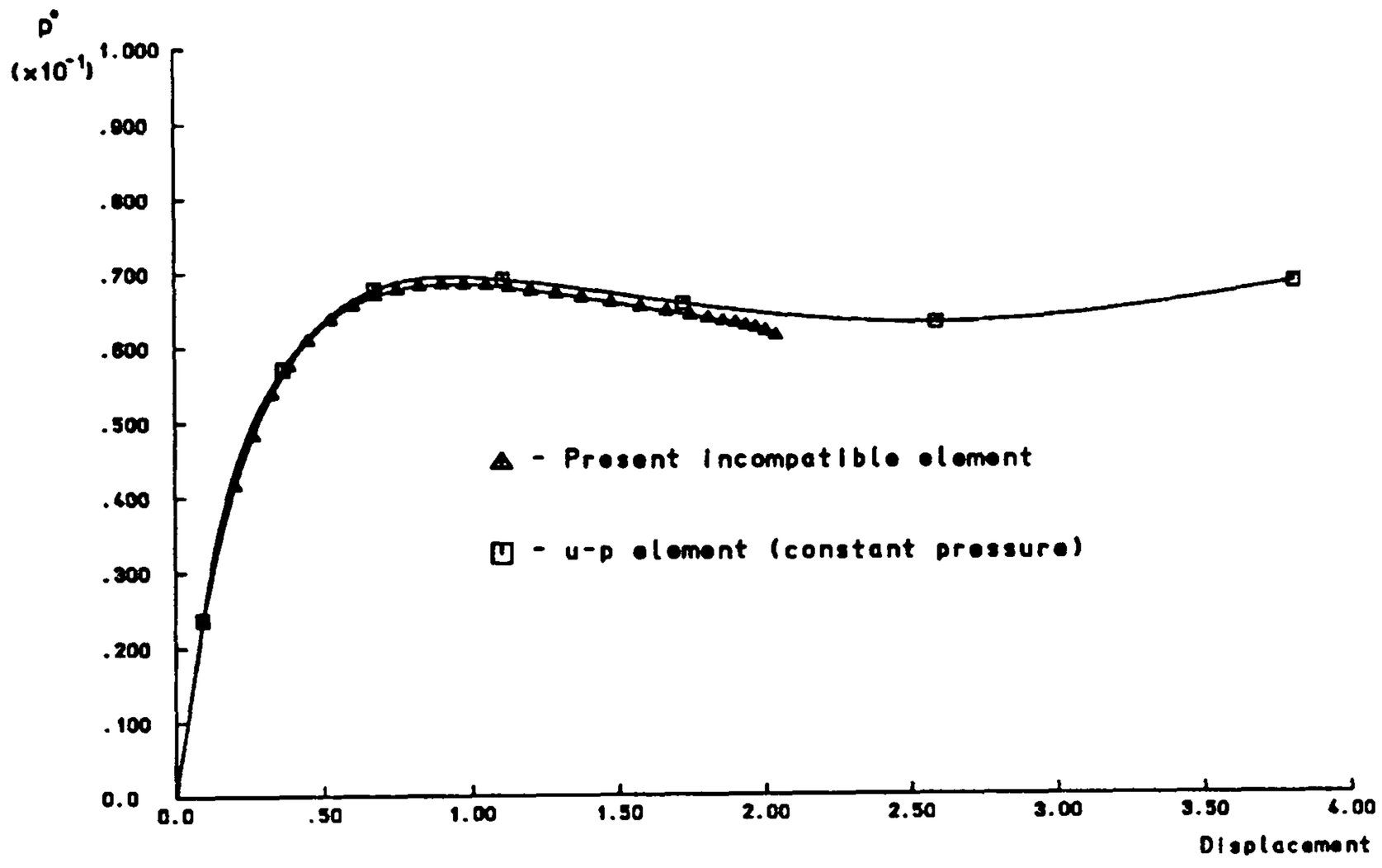


Figure 4.20: Cylinder under internal pressure - Dimensionless follower pressure vs. displacement

Chapter 5

Co-rotational Formulation for Two-dimensional Continua

5.1 Introduction

The co-rotational technique defines a procedure from which the standard linear engineering formulation is used with respect to a co-ordinate system that is attached to the element and continuously rotates with this element. It is usually applied for beams and shells where the local frame can be easily defined through two end nodes for beams and three corner nodes for shells [72, 19, 20, 69]. The non-linearity is introduced by the rotation of this local co-ordinate system.

The aim of this chapter is to devise a procedure to allow the use of the linear formulation for plane-stress and plane-strain at the element level and apply it together with the co-rotational technique. With this formulation the incompatible displacement modes, for a linear analysis, can be incorporated without any additional complexities. Since the elements here are considered as linear, the non-linear approximations come from applying transformation matrices to the linear tangent stiffness matrix. Consistent derivations for the out-of-balance force vector and the initial stress or geometric stiffness matrix are also addressed in this context.

The main difficult is how to define the co-rotating frame for this element. Two approaches were tried to solve the problem. Both of them are shown although the first one is not used because it fails to pass 'the large strain patch test'.

Another noteworthy point concerns the determination of the initial local co-ordinate system. There are number of ways of choosing this system but this issue is not important since the final solution will not depend on this initial system. Therefore, the approach

used here, i.e., initial local system equal to global system could be modified and a different local system could be used instead.

5.2 Development

5.2.1 Usual co-rotational procedure

The procedure applied in the co-rotational formulation is similar to that used in [19, 20, 69] but also influenced by the approach of Rankin and Brogan [72] in which the co-rotational aspects are kept totally separated from the local linear element formulation. However, in the latter the authors did not address the issue of consistent derivation of the stiffness matrix.

The general technique is usually applied for beams and shells where it is a simple matter to define the co-rotating base frame using the current configuration of the nodes. If we assume that a given element for continua (as illustrated in figure 5.1) has the local co-ordinate system previously defined, the local displacements $\mathbf{p}_l$ would be a function of the global displacements $\mathbf{p}_g$ via a certain transformation rule. Consequently,

$$\mathbf{p}_l = \mathrm{fn}(\mathbf{p}_g) \tag{5.1}$$

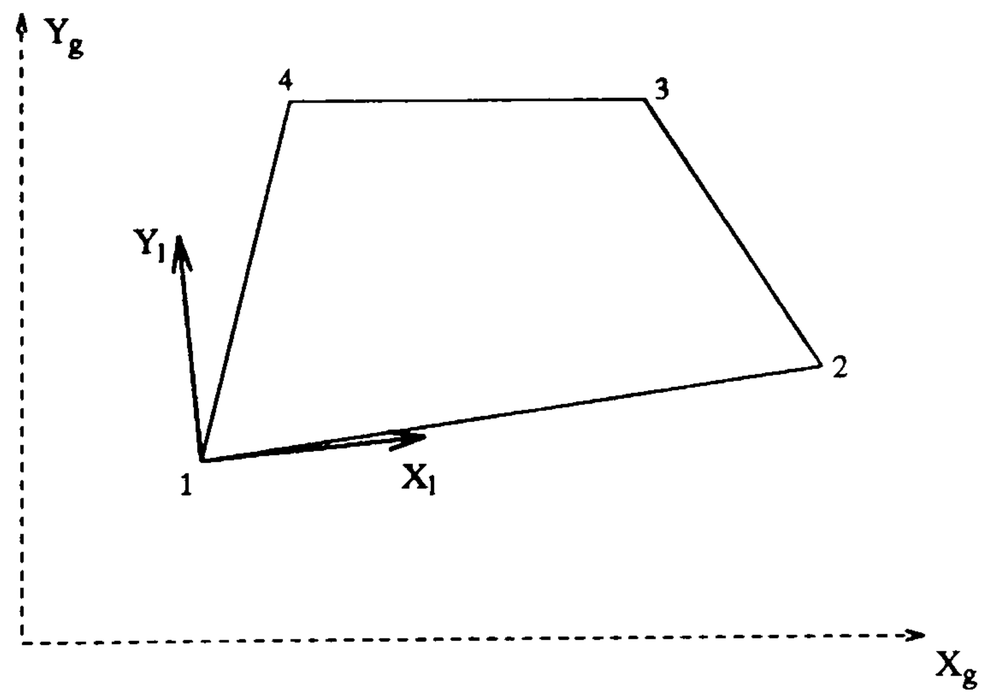


Figure 5.1: Element local triad

From the variation of (5.1) we obtain the transformation matrix $\mathbf{T}$ that relates changes of local displacements to changes of global displacements. This can be expressed as

$$\delta\mathbf{p}_l = \mathbf{T}(\mathbf{p}_g)\,\delta\mathbf{p}_g \tag{5.2}$$

Now we equate the virtual work in the local and global systems. This yields a relationship such as

$$\delta \mathbf{p}_l^T \, \mathbf{q}_{il} = \delta \mathbf{p}_g^T \, \mathbf{q}_{ig} \tag{5.3}$$

where $\mathbf{q}_{il}$ and $\mathbf{q}_{ig}$ are the internal nodal force vectors for the local and global configurations, respectively.

Substitution of (5.2) into (5.3) leads to

$$\mathbf{q}_{ig} = \mathbf{T}^T \, \mathbf{q}_{il} \tag{5.4}$$

On the other hand, if we know the local displacements, the variation of the local internal force vectors can be written in a standard manner, i.e.,

$$\delta \mathbf{q}_{il} = \mathbf{K}_{ll} \, \delta \mathbf{p}_l \tag{5.5}$$

or, if at the local level the system is entirely linear, we can write

$$\mathbf{q}_{il} = \mathbf{K}_{ll} \, \mathbf{p}_l \tag{5.6}$$

where $\mathbf{K}_{ll}$ is the conventional small-strain linear tangent stiffness matrix for the element in relation to the local axes. To obtain the global tangential stiffness matrix, we require the variation of (5.4) which gives

$$\delta \mathbf{q}_{ig} = \mathbf{T}^T \, \delta \mathbf{q}_{il} + \delta \mathbf{T}^T \, \mathbf{q}_{il} \tag{5.7}$$

If now we substitute (5.2) into (5.5) and replace the result into the first part of (5.7), the resulting expression is

$$\delta \mathbf{q}_{ig} = \underbrace{\mathbf{T}^T \, \mathbf{K}_{ll} \, \mathbf{T}}_{\mathbf{K}_{tg}} \, \delta \mathbf{p}_g + \delta \mathbf{T}^T \, \mathbf{q}_{il} \tag{5.8}$$

with $\mathbf{K}_{tg}$ being the standard tangent stiffness matrix. The second part of (5.8) results in the initial stress matrix $\mathbf{K}_{t\sigma}$, that means,

$$\delta \mathbf{T}^T \, \mathbf{q}_{il} = \mathbf{K}_{t\sigma} \, \delta \mathbf{p}_g \tag{5.9}$$

5.2.2 Co-rotational formulation for continua

The above derivation shows in a general manner how the co-rotational formulation can be obtained when the local axes have already being defined. At this point the question is how to establish this local system for a continuum?

We firstly need to determine the element to be studied. The plane-stress/plane-strain element used in this formulation presents the same geometry as the element of the previous chapter. This four-noded element has the nodal variables represented by the standard global nodal displacements, as written below.

$$\mathbf{p}_g^T = \begin{pmatrix} u^1 & v^1 & u^2 & v^2 & u^3 & v^3 & u^4 & v^4 \end{pmatrix} \tag{5.10}$$

Assuming that the initial local frame coincides in direction with the global frame [§], the initial geometry of the element can be established. The local X and Y co-ordinates of a node i are defined as

$$\begin{aligned} X_l^i &= X_g^i - X_g^1 \\ Y_l^i &= Y_g^i - Y_g^1 \end{aligned} \tag{5.11}$$

where X_l^i and Y_l^i are the local initial co-ordinates of the node i and X_g^i and Y_g^i are the global initial co-ordinates for the same node i. The vector of local initial co-ordinates for the element will be collectively referred as $\mathbf{X}_l$.

The next step is to obtain the angle θ which defines the local system for the non-linear procedure, i.e., for the rotating frame. In another words, θ defines the co-rotating base vectors $\mathbf{e}_1$ and $\mathbf{e}_2$ (figure 5.2) such that

$$\mathbf{e}_1 = \begin{Bmatrix} cos\theta \\ sin\theta \end{Bmatrix} \tag{5.12}$$

$$\mathbf{e}_2 = \begin{Bmatrix} -sin\theta \\ cos\theta \end{Bmatrix} \tag{5.13}$$

This allows the initial configuration of the element to be mapped onto the final configuration so that the resulting strains are local produced by the local nodal displacements $\mathbf{p}_l$.

Having obtained $\mathbf{e}_1$ and $\mathbf{e}_2$ (details later), from figure 5.2 we can write for each node i

[§]In the approach initially adopted, the initial co-ordinate system was defined by the unit vectors $\mathbf{E}_1$ and $\mathbf{E}_2$ which were determined via the co-ordinates of nodes 1 and 2 (see figure 5.1) of the element. Later it was observed that the approach could be modified and the current and much simpler choice of initial local co-ordinate frame equal to the global frame actually gives the same results.

$$\mathbf{x}_g^i - \mathbf{x}_g^1 = (\mathbf{X}_g^i + \mathbf{p}_g^i) - (\mathbf{X}_g^1 + \mathbf{p}_g^1) = \left[\begin{array}{cc} \mathbf{e}_1 & \mathbf{e}_2 \end{array} \right] (\mathbf{X}_l^i + \mathbf{p}_l^i) \tag{5.14}$$

where, for example,

$$\mathbf{X}_l^i = \left\{ \begin{array}{c} X_l^i \\ Y_l^i \end{array} \right\}$$

and

$$\mathbf{p}_g^i = \left\{ \begin{array}{c} u_g^i \\ v_g^i \end{array} \right\}$$

Here again the lower case letters relate to the current and the upper case letters relate to the initial configurations.

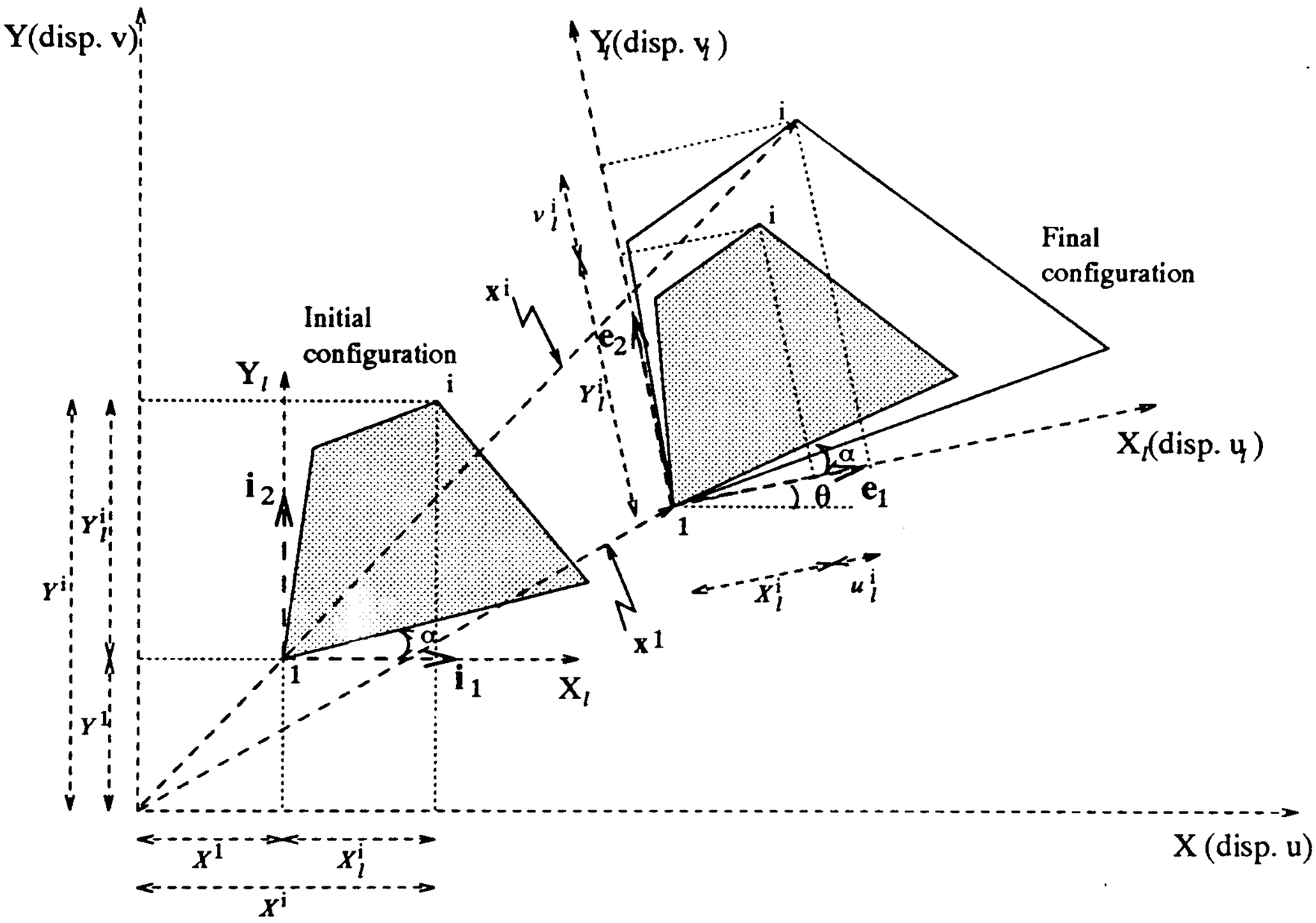


Figure 5.2: Initial and final element configuration

From the above, we have

$$\mathbf{p}_l^i = \left[\begin{array}{c} \mathbf{e}_1^T \\ \mathbf{e}_2^T \end{array} \right] (\mathbf{x}_g^i - \mathbf{x}_g^1) - \mathbf{X}_l^i \tag{5.15}$$

We have not yet defined the local axes. The first attempt was to try to work from mid-side nodes for each side of the element and then to obtain a co-ordinate system to represent this element. This can be achieved geometrically if we calculate two vectors that connect the mid-sides of the opposite sides of the element as shown in figure 5.3.a

(vectors $\mathbf{f}_m$ and $\mathbf{e}_m$). We then define two orthogonal unit vectors, $\mathbf{e}_1$ and $\mathbf{e}_2$, that have the origin coinciding with the origin of the vectors $\mathbf{f}_m$ and $\mathbf{e}_m$ and form equal angle γ with the two first vectors, respectively. From this angle the value of θ could be calculated.

This procedure can be evaluated algebraically as follows: From figure 5.3 the mid-side nodes for the sides $1-4$ and $2-3$ could be found respectively as

$$\mathbf{x}_8 = \tfrac{1}{2}(\mathbf{x}_1 + \mathbf{x}_4)$$
$$\mathbf{x}_6 = \tfrac{1}{2}(\mathbf{x}_2 + \mathbf{x}_3) \tag{5.16}$$

These two vectors are then used to obtain a unit vector such that

$$\mathbf{e}_m = \frac{1}{\|\mathbf{x}_{68}\|}\mathbf{x}_{68} \tag{5.17}$$

with $\mathbf{x}_{68} = \mathbf{x}_6 - \mathbf{x}_8$. Likewise for the vector $\mathbf{f}_m$ defined by the two other sides.

$$\mathbf{f}_m = \frac{1}{\|\mathbf{x}_{75}\|}\mathbf{x}_{75} \tag{5.18}$$

From the vectors $\mathbf{e}_m$ and $\mathbf{f}_m$ we can find a set of local axes chosen is such a manner that they make equal angles with these vectors.

Let α be the angle between the global x and the vector $\mathbf{e}_m$ and β be the angle between the global y and the vector $\mathbf{f}_m$ (figure 5.3). Therefore,

$$tan\alpha = \tfrac{e_{m2}}{e_{m1}}$$
$$tan(\beta - \tfrac{\pi}{2}) = -\tfrac{f_{m1}}{f_{m2}} \tag{5.19}$$

where e_{m1} and e_{m2} and f_{m1} and f_{m2} are the components of $\mathbf{e}_m$ and $\mathbf{f}_m$, respectively.

Now, let γ_1 and γ_2 be the angles between $\mathbf{e}_m$ and $\mathbf{e}_1$ and $\mathbf{f}_m$ and $\mathbf{e}_2$, respectively. If we equal the two angles, we have

$$\gamma = \frac{\alpha + \beta}{2} - \frac{\pi}{4} \tag{5.20}$$

which is used to compute θ.

This value of θ could be used for the rest of the calculations. However, as first noted by Jetteur and Cescotto [50], although the element passes the linear patch test, it does not pass the "large strain patch test". The test can be illustrated via the element of figure 5.4 which is subjected to a direct tension deformation in large strain. For this example, if we impose a displacement Δl as indicated below, the element should be able

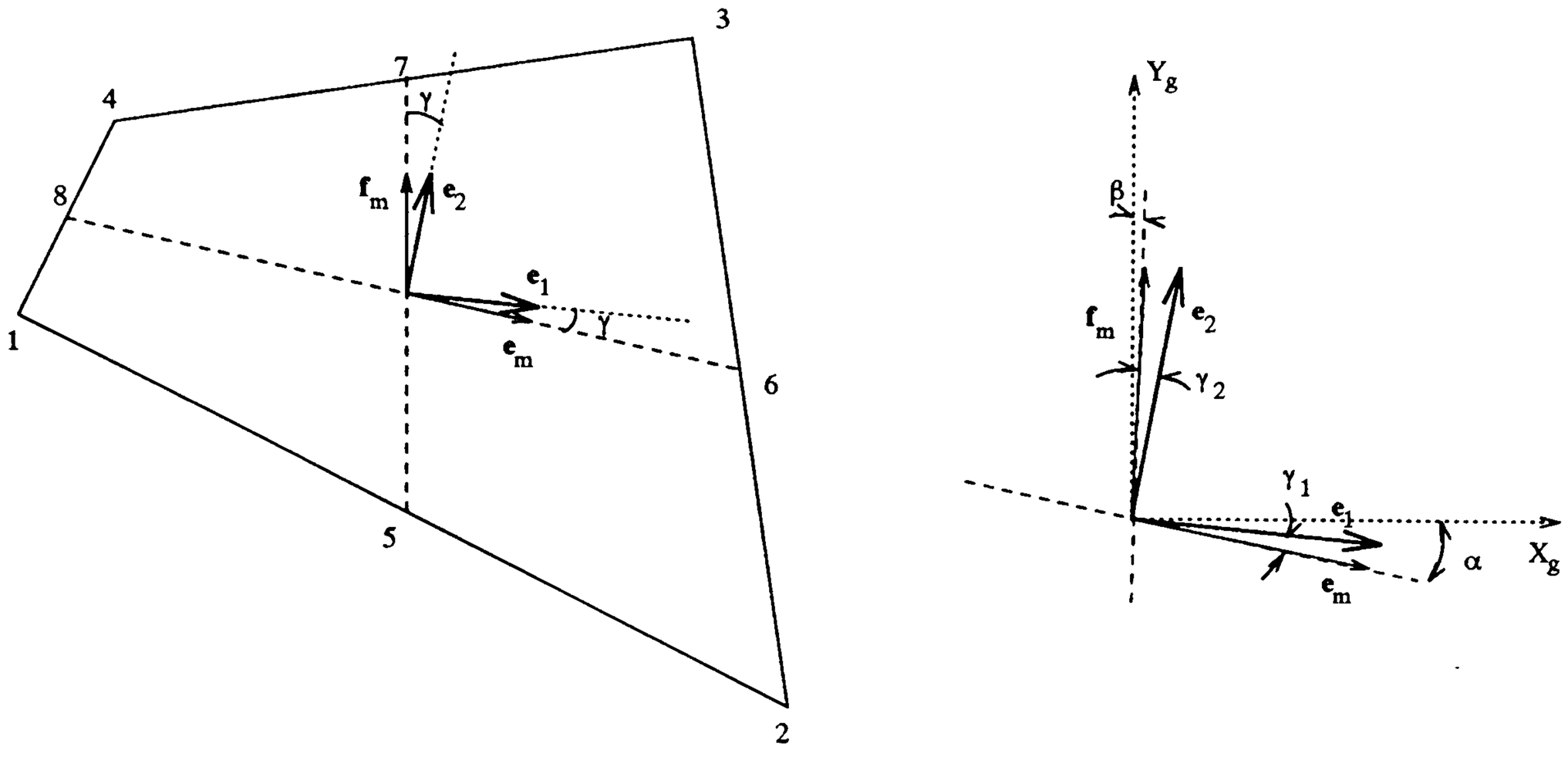


Figure 5.3: Determination of γ

to recover the constant stress state at all of the Gauss points, regardless of the strain measure being used. For instance, if we use an "engineering-type strain", $\epsilon_l = \Delta l / l_o$, a stress $\sigma_l = E\,\epsilon_l$ must be acting constantly over each element. Using θ obtained through the approach given above, this does not occur. If the test is now applied for a shear mode, since the "exact" solution for large strain is not straightforward, we can follow the definition of Simo *et al.* [81] in which the satisfaction of the patch test is ensured if the results reproduce the exact solution for the homogeneous deformations, that means, the deformations are such that the deformation gradient $\mathbf{F}$ is constant. For such a shear deformation, we require a hyperelastic formulation. Details will be given in Chapter 7.

We have to come up with a new procedure to compute the angle θ. To this end, following the suggestion of Jetteur and Cescotto (although here the approach adopted relates to the total instead of the incremental displacements) we assume that the local spin at the centroid of the element in the current configuration should be zero, i.e.,

$$\Omega_l = \frac{\partial u_l}{\partial Y_l} - \frac{\partial v_l}{\partial X_l} = 0 \tag{5.21}$$

This technique allows the computation of the angle θ that can be differentiated later. To compute θ we begin with the relationship coming from (5.21) as shown below.

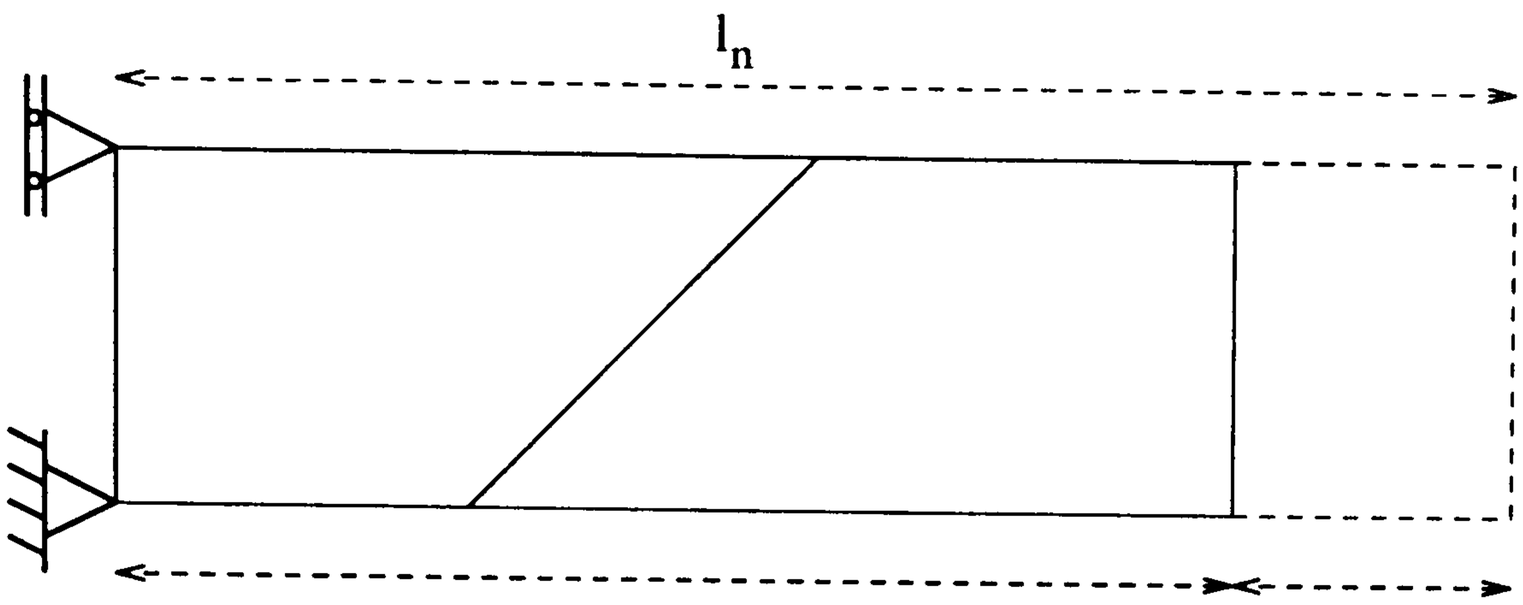


Figure 5.4: Large strain patch test

$$\Omega_l = \mathbf{A}_l^T \mathbf{p}_l = 0 \tag{5.22}$$

where $\mathbf{A}_l$ is found from the shape functions [20] as

$$\mathbf{A}_l = \left\{ \begin{array}{c} (\mathbf{J}_o^{-1}(2,1)\mathbf{h}_\xi^1 + \mathbf{J}_o^{-1}(2,2)\mathbf{h}_\eta^1) \\ -(\mathbf{J}_o^{-1}(1,1)\mathbf{h}_\xi^1 + \mathbf{J}_o^{-1}(1,2)\mathbf{h}_\eta^1) \\ (\mathbf{J}_o^{-1}(2,1)\mathbf{h}_\xi^2 + \mathbf{J}_o^{-1}(2,2)\mathbf{h}_\eta^2) \\ -(\mathbf{J}_o^{-1}(1,1)\mathbf{h}_\xi^2 + \mathbf{J}_o^{-1}(1,2)\mathbf{h}_\eta^2) \\ (\mathbf{J}_o^{-1}(2,1)\mathbf{h}_\xi^3 + \mathbf{J}_o^{-1}(2,2)\mathbf{h}_\eta^3) \\ -(\mathbf{J}_o^{-1}(1,1)\mathbf{h}_\xi^3 + \mathbf{J}_o^{-1}(1,2)\mathbf{h}_\eta^3) \\ (\mathbf{J}_o^{-1}(2,1)\mathbf{h}_\xi^4 + \mathbf{J}_o^{-1}(2,2)\mathbf{h}_\eta^4) \\ -(\mathbf{J}_o^{-1}(1,1)\mathbf{h}_\xi^4 + \mathbf{J}_o^{-1}(1,2)\mathbf{h}_\eta^4) \end{array} \right\} \tag{5.23}$$

where the Jacobian, $\mathbf{J}_o$, is computed at the centroid. $\mathbf{h}_\xi^i$ and $\mathbf{h}_\eta^i$ are simply the derivatives of the shape functions with respect to the non-dimensional co-ordinates ξ and η again at the centroid, respectively, with the i superscript relating to the node numbering. The vector $\mathbf{A}_l$ is (via $\mathbf{J}_o$) a function of $\mathbf{X}_l$ and is therefore fixed. Knowing the total global displacements $\mathbf{p}_g$, from (5.15) the local displacements $\mathbf{p}_l$ can be computed with θ, which defines $\mathbf{e}_1$ and $\mathbf{e}_2$, as the only unknown. Hence, substitution of (5.23) into (5.22) gives an equation for θ. After some algebraic manipulations, the equation becomes

$$\Omega_l = a\,sin\theta + b\,cos\theta - c = 0 \tag{5.24}$$

with

$$a = \mathbf{c}^T \mathbf{x}_g \tag{5.25}$$

$$b = \mathbf{d}^T \mathbf{x}_g \tag{5.26}$$

$$c = \mathbf{A}_l^T \mathbf{X}_l \tag{5.27}$$

But we can demonstrate that $c = 0$. To this end, from (5.23) we write c as

$$c = \sum h_y^i \, X_l^i - \sum h_x^i \, Y_l^i \tag{5.28}$$

which actually can be expressed as

$$c = \frac{\partial X_l}{\partial Y_l} - \frac{\partial Y_l}{\partial X_l} \tag{5.29}$$

and $\frac{\partial X_l}{\partial Y_l} = 0$ and $\frac{\partial Y_l}{\partial X_l} = 0$. Therefore, $c = 0$ as above.

Observe that $\mathbf{C}$ can be written as

$$\mathbf{C} = \begin{bmatrix} 0 & -1 & 0 & 0 & 0 & 0 & 0 & 0 \\ 1 & 0 & 0 & 0 & 0 & 0 & 0 & 0 \\ 0 & 0 & 0 & -1 & 0 & 0 & 0 & 0 \\ 0 & 0 & 1 & 0 & 0 & 0 & 0 & 0 \\ 0 & 0 & 0 & 0 & 0 & -1 & 0 & 0 \\ 0 & 0 & 0 & 0 & 1 & 0 & 0 & 0 \\ 0 & 0 & 0 & 0 & 0 & 0 & 0 & -1 \\ 0 & 0 & 0 & 0 & 0 & 0 & 1 & 0 \end{bmatrix} \mathbf{A}_l \tag{5.30}$$

and $\mathbf{d}$ is in fact equal to $\mathbf{A}_l$, i.e., $\mathbf{d} = \mathbf{A}_l$.

Working from (5.24) we obtain

$$\theta = arctan(\frac{-b}{a}) \tag{5.31}$$

Using this new θ the element satisfactorily passes the large strain patch test.

After computing the local displacements, the local stresses, local internal force vector and local tangent stiffness matrix are computed in the standard linear way (note that any linear element formulation can be adopted and in particular the linear incompatible element of section 4.2). If we apply the formulation for a linear plane-stress/plane-strain element, similar to that of Chapter 4 but initially excluding the incompatible modes, one could write

$$\boldsymbol{\epsilon}_l = \mathbf{B}_l \, \mathbf{p}_l \tag{5.32}$$

The variation of $\boldsymbol{\epsilon}_l$ is then given by

$$\delta\boldsymbol{\epsilon}_l = \mathbf{B}_l \, \delta\mathbf{p}_l \tag{5.33}$$

with the local strain-displacement matrix $\mathbf{B}_l$ unchanged since it is only a function of the initial geometry of the element.

Having found the strains, if we assume that the material is linear isotropic, the stresses are simply

$$\boldsymbol{\sigma}_l = \mathbf{D} \, \boldsymbol{\epsilon}_l \tag{5.34}$$

Before computing the internal force vector and the tangent stiffness matrix for the element from virtual work, it is necessary to find the relationship between the local and global small changes of displacement to ensure the consistency of the formulation. This process will eventually lead to the $\mathbf{T}$ matrix of (5.4). Therefore, if we re-write (5.14) as

$$(\mathbf{x}_g^i - \mathbf{x}_g^1) = \left[\begin{array}{cc} \mathbf{e}_1 & \mathbf{e}_2 \end{array} \right] \mathbf{x}_l^i \tag{5.35}$$

the differentiation of (5.35) above yields

$$\delta\mathbf{p}_g^i = \left[\begin{array}{cc} \mathbf{e}_1 & \mathbf{e}_2 \end{array} \right] \delta\mathbf{p}_l^i + x_l^i \delta\mathbf{e}_1 + y_l^i \delta\mathbf{e}_2 \tag{5.36}$$

In order to find an expression for the change of local displacement with respect to the change of global displacement, we need to determine the variation of $\mathbf{e}_1$ and $\mathbf{e}_2$. This could be given from (5.12) and (5.13) as

$$\delta\mathbf{e}_1 = \left\{ \begin{array}{c} -sin\theta \\ cos\theta \end{array} \right\} \delta\theta = \mathbf{e}_2 \delta\theta \tag{5.37}$$

$$\delta\mathbf{e}_2 = \left\{ \begin{array}{c} -cos\theta \\ -sin\theta \end{array} \right\} \delta\theta = -\mathbf{e}_1 \delta\theta \tag{5.38}$$

Now the variation of θ has to be derived. To this end, we need the variation of (5.25) and (5.26). Since the vector $\mathbf{c}$ and $\mathbf{d}$ are only functions of the initial geometry, we have

$$\delta a = \mathbf{c}^T \, \delta\mathbf{p}_g \tag{5.39}$$

$$\delta b = \mathbf{d}^T \, \delta \mathbf{p}_g \tag{5.40}$$

The differentiation of (5.31) leads to

$$\delta\theta = \frac{1}{(a^2+b^2)}(b\,\delta a - a\,\delta b) = \frac{1}{(a^2+b^2)}(b\mathbf{c}^T - a\mathbf{d}^T)\delta\mathbf{p}_g = \mathbf{v}^T\delta\mathbf{p}_g \tag{5.41}$$

Substituting equation (5.41) into (5.37) and (5.38) and replacing them in (5.36) we have

$$\delta\mathbf{p}_g^i = \left[\begin{array}{cc} \mathbf{e}_1 & \mathbf{e}_2 \end{array}\right] \delta\mathbf{p}_l^i + x_l^i \mathbf{e}_2 \mathbf{v}^T \delta\mathbf{p}_g - y_l^i \mathbf{e}_1 \mathbf{v}^T \delta\mathbf{p}_g \tag{5.42}$$

The re-organisation of (5.42) yields

$$\delta\mathbf{p}_l^i = \left[\begin{array}{c} \mathbf{e}_1^T \\ \mathbf{e}_2^T \end{array}\right] \delta\mathbf{p}_g^i - x_l^i \mathbf{v}^T \delta\mathbf{p}_g \left[\begin{array}{c} \mathbf{e}_1^T \\ \mathbf{e}_2^T \end{array}\right] \mathbf{e}_2 + y_l^i \mathbf{v}^T \delta\mathbf{p}_g \left[\begin{array}{c} \mathbf{e}_1^T \\ \mathbf{e}_2^T \end{array}\right] \mathbf{e}_1 \tag{5.43}$$

Therefore, for one element, equation (5.43) can be written as

$$\delta\mathbf{p}_l = (\mathbf{E} + \bar{\mathbf{x}}_l \, \mathbf{v}^T)\delta\mathbf{p}_g = \mathbf{T}\,\delta\mathbf{p}_g \tag{5.44}$$

T represents the transformation matrix for the co-rotational formulation and is fundamental in this development. The matrix **E** and the vector $\bar{\mathbf{x}}_l$ are given by

$$\mathbf{E} = \mathbf{diag}\left[\begin{array}{c} \mathbf{e}_1^T \\ \mathbf{e}_2^T \end{array}\right] = \left[\begin{array}{cccc} \left[\begin{array}{c} \mathbf{e}_1^T \\ \mathbf{e}_2^T \end{array}\right] & \mathbf{0} & \mathbf{0} & \mathbf{0} \\ \mathbf{0} & \left[\begin{array}{c} \mathbf{e}_1^T \\ \mathbf{e}_2^T \end{array}\right] & \mathbf{0} & \mathbf{0} \\ \mathbf{0} & \mathbf{0} & \left[\begin{array}{c} \mathbf{e}_1^T \\ \mathbf{e}_2^T \end{array}\right] & \mathbf{0} \\ \mathbf{0} & \mathbf{0} & \mathbf{0} & \left[\begin{array}{c} \mathbf{e}_1^T \\ \mathbf{e}_2^T \end{array}\right] \end{array}\right] \tag{5.45}$$

and

$$\bar{\mathbf{x}}_l^T = \{y_l^1, -x_l^1, y_l^2, -x_l^2, y_l^3, -x_l^3, y_l^4, -x_l^4\} \tag{5.46}$$

From the principle of virtual work (see (5.3)), it is required that

$$W = \mathbf{q}_{i_l}^T \delta\mathbf{p}_l = \mathbf{q}_{i_g}^T \delta\mathbf{p}_g \tag{5.47}$$

where $\mathbf{q}_{i_l}$ and $\mathbf{q}_{i_g}$ are the local and the global internal force vectors, respectively. $\mathbf{q}_{i_l}$ is obtained from

$$\mathbf{q}_{i_l} = \int_V \mathbf{B}^T \boldsymbol{\sigma}_l \, dV \tag{5.48}$$

or from (5.6) if the system is completely linear at the local level.

Inserting (5.44) into (5.47), we come up with a relationship between the local and global internal force vectors of the form:

$$\mathbf{q}_{i_g} = \mathbf{T}^T \mathbf{q}_{i_l} \tag{5.49}$$

Following a similar procedure to that used in the previous two chapters, we need to consider the variation of (5.49) which leads to the stiffness matrix. This can be achieved through

$$\delta\mathbf{q}_{i_g} = \mathbf{T}^T \delta\mathbf{q}_{i_l} + \delta\mathbf{T}^T \mathbf{q}_{i_l} \tag{5.50}$$

The first part of (5.50) can be obtained from the variation of $\mathbf{q}_{i_l}$, i.e.,

$$\delta\mathbf{q}_{i_l} = \int_{V_o} \mathbf{B}^T \, \mathbf{d} \, \mathbf{B} \, dV_o \delta\mathbf{p}_l = \mathbf{K}_{ll} \, \delta\mathbf{p}_l \tag{5.51}$$

Replacing (5.44) into (5.51) and substituting the results into (5.50), we can obtain the first contribution for the stiffness matrix of the element. Note that if the system is entirely linear at the local level $\mathbf{K}_{ll}$ is the standard linear matrix in relation to the local co-ordinate frame. The combination of (5.50) and (5.51) gives

$$\delta\mathbf{q}_{i_g} = \underbrace{\mathbf{T}^T \mathbf{K}_{ll} \, \mathbf{T}}_{\mathbf{K}_{t_g}} \delta\mathbf{p}_g + \delta\mathbf{T}^T \mathbf{q}_{i_l} \tag{5.52}$$

To complete to derivation of the global stiffness matrix, it is necessary to calculate the second term in (5.52). This involves the differentiation of the transformation matrix $\mathbf{T}$. The departure point is equation (5.44) which is reproduced here as

$$\mathbf{T}^T = \mathbf{E}^T + \mathbf{v} \, \bar{\mathbf{x}}_l^T \tag{5.53}$$

We will compute the change of (5.53) in two parts but first it is better to represent the second term of (5.52) as

$$\delta\mathbf{T}^T \mathbf{q}_{i_l} = \delta\mathbf{T}^1 \, q_{i_l}^1 + \delta\mathbf{T}^2 \, q_{i_l}^2 + \delta\mathbf{T}^3 \, q_{i_l}^3 + \ldots = \sum_{j=1}^{8} \delta\mathbf{T}^j \, q_{i_l}^j \tag{5.54}$$

where $\mathbf{T}^j$ is the jth column of $\mathbf{T}^T$ and q_{il}^j is the jth component of $\mathbf{q}_{il}$.

Suppose we work with the first term of (5.54). In this case, we have

$$\delta \mathbf{T}^1 \, q_{il}^1 = q_{il}^1 \, \delta \left\{ \left\{ \begin{array}{c} \mathbf{e}_1 \\ \mathbf{0} \\ \mathbf{0} \\ \mathbf{0} \end{array} \right\} + y_l^1 \, \mathbf{v} \right\} = q_{il}^1 \, \mathbf{G}^1 \, \delta \mathbf{p}_g \tag{5.55}$$

All we need is to calculate $\mathbf{G}^1 \, \delta \mathbf{p}_g$ from (5.55). This is given by

$$\mathbf{G}^1 \, \delta \mathbf{p}_g = \delta \left\{ \left\{ \begin{array}{c} \mathbf{e}_1 \\ \mathbf{0} \\ \mathbf{0} \\ \mathbf{0} \end{array} \right\} + y_l^1 \, \mathbf{v} \right\} = \left\{ \begin{array}{c} \mathbf{e}_2 \\ \mathbf{0} \\ \mathbf{0} \\ \mathbf{0} \end{array} \right\} \delta\theta + \delta y_l^1 \, \mathbf{v} + y_l^1 \, \delta \mathbf{v} \tag{5.56}$$

Note that δy_l^1 is derived from (5.44) which produces

$$\delta y_l^1 = \{ \left[\begin{array}{cccc} \mathbf{e}_2^T & \mathbf{0} & \mathbf{0} & \mathbf{0} \end{array} \right] - x_l^1 \, \mathbf{v}^T \} \, \delta \mathbf{p}_g \tag{5.57}$$

If the last term of (5.56) is not included now, from (5.41) and (5.57) $\mathbf{G}^{1,a}$ can be written as

$$\mathbf{G}^{1,a} = \left\{ \begin{array}{c} \mathbf{e}_2 \\ \mathbf{0} \\ \mathbf{0} \\ \mathbf{0} \end{array} \right\} \mathbf{v}^T + \mathbf{v} \left\{ \begin{array}{c} \mathbf{e}_2 \\ \mathbf{0} \\ \mathbf{0} \\ \mathbf{0} \end{array} \right\}^T - x_l^1 \, \mathbf{v} \, \mathbf{v}^T \tag{5.58}$$

which is symmetric. The complete form of the matrix $\mathbf{G}^1$ is achieved by also computing $\delta \mathbf{v}$.

The first step to differentiate $\mathbf{v}$ is to re-write equation (5.41) as

$$\mathbf{v} = \frac{1}{(a^2 + b^2)} b \, \mathbf{c} - a \, \mathbf{d} = \frac{1}{(a^2 + b^2)} [\mathbf{c} \, \mathbf{d}^T - \mathbf{d} \, \mathbf{c}^T] \, \mathbf{x}_g \tag{5.59}$$

where $\mathbf{x}_g$ is the vector containing the current (up-dated) co-ordinates in the global system. The differentiation of $\mathbf{v}$ leads to

$$\delta \mathbf{v} = \frac{-2}{(a^2 + b^2)} [ab\mathbf{c}\mathbf{c}^T - a^2 \mathbf{d}\mathbf{c}^T + b^2 \mathbf{c}\mathbf{d}^T - ab\mathbf{d}\mathbf{d}^T] \, \delta \mathbf{p}_g \tag{5.60}$$

As the results of manipulations on (5.60), the final relationship for $\delta \mathbf{v}$ is obtained, so that,

$$\delta\mathbf{v} = \frac{1}{(a^2+b^2)}[2ab(\mathbf{d}\mathbf{d}^T - \mathbf{c}\mathbf{c}^T) + (a^2-b^2)(\mathbf{c}\mathbf{d}^T + \mathbf{d}\mathbf{c}^T)]\,\delta\mathbf{p}_g = \mathbf{V}^T\,\delta\mathbf{p}_g \tag{5.61}$$

which is also symmetric. Therefore, the second part of $\mathbf{G}^1$ is obtained as

$$\mathbf{G}^{1,b} = y_l^1\,\mathbf{V}^T \tag{5.62}$$

From (5.56), in conjunction with (5.58) and (5.62), we can retrieve the final form of $\mathbf{G}^1$ that can be expressed as

$$\mathbf{G}^1 = \mathbf{G}^{1,a} + \mathbf{G}^{1,b} \tag{5.63}$$

However, it should be noted that the matrix $\mathbf{G}^1$ represents only the contribution of the first term of (5.54). The other matrices $\mathbf{G}^j$'s are determined in the same manner as that used for the first component just by using the variation of the different columns of $\mathbf{T}$ and their correspondent components of $\mathbf{q}_{il}$. This simply means that in equation (5.55) if we have, for example, the variation of the second column of $\mathbf{T}$ we will obtain the matrix $\mathbf{G}^2$ and so on. Finally, having obtained the remaining $\mathbf{G}^j$'s, the final form of the full stiffness matrix for the element will include the initial stress matrix calculated above. Hence, we have

$$\delta\mathbf{q}_{i_g} = \mathbf{K}_{tg}\,\delta\mathbf{p}_g + \mathbf{K}_{\sigma g}\,\delta\mathbf{p}_g \tag{5.64}$$

with $\mathbf{K}_{tg}$ given by (5.52) and

$$\mathbf{K}_{\sigma g} = \sum_{j=1}^{8} q_{il}^j\,\mathbf{G}^j \tag{5.65}$$

The full tangent stiffness matrix is symmetric since both portions of (5.64) are symmetric.

Although in the calculation of the initial stress stiffness equations we have incorporated the variation $\delta\mathbf{v}$, numerical results have shown that its contribution is not very important and that it produces little effect even in the quadratic convergence rate of the Newton method. Therefore, for future developments, including that of the next chapter for a solid element, the inclusion or not of this variation cause little or no difference at all in the convergence rate, as it will be shown in some examples. Naturally, this term does effect the final converged results.

The above formulation can very elegantly handle large rotations using the element co-ordinate frame but it is limited to small strains since the issue of hyperelasticity will

not be addressed at this stage (this will be presented in Chapter 7). However, it is important to examine carefully the question of incompressibility before turning our study into a hyperelastic approach. In the previous chapter we introduced the technique of incorporating incompatible displacement modes into the elements' shape functions and applied the linear and non-linear formulations. Besides improving the bending related performance of the element, the incompatible modes provided the element with a very good response to incompressible or near-incompressible problems. As mentioned earlier, the idea is to incorporate the linear incompatible displacement elements formulated in Chapter 4 within the co-rotational frame suggested above. To this end, the conventional element is replaced by the incompatible element without any modifications in the previously established co-rotational formulation. The result is a very neat formulation that can actually cope with the problem of incompressibility.

One of the main advantages of the co-rotational technique shown in this chapter is its flexibility of use. The linear element is not altered and the formulation can be placed "around" it. One can observe in the development that no consideration is made upon the 4-noded linear element employed. No special concern is also given to any displacement-dependent load that may be imposed into the system. It also can be used as defined for the previous element.

5.3 Numerical tests

In this section the new co-rotational formulation is tested and some examples will be given to confirm the good performance of the element. Three test cases are reported for this element where the different capabilities of the element are demonstrated. The behaviour of the formulation for distorted meshes, bending-dominated problems and incompressible conditions are examined for cases when large displacements and large rotations are involved. However, the tests involve only small strains and the subject of large strain and hyperelasticity is postponed until Chapter 7.

5.3.1 Convergence tests

In this first example a cantilever beam is subject to a bending moment in one of the edges and is fixed at the other edge, as shown in the figures below. The idea is to establish the accuracy of the several formulations for a bending-like problem. It can be seen from the results (figures 5.5, 5.6 and 5.7) that, as expected, the standard bilinear element does not perform well due to the poor bending response characteristic of this element. The

other responses can also be seen in figures 5.5, 5.6 and 5.7 . The materials used in this example have Poisson's ratios of $\nu = 0.3$ (figure 5.5 and 5.6) and $\nu = 0.49$ (figure 5.7). The main point to be stressed here is the fact that for a (*quasi*-)incompressible material ($\nu = 0.49$) subject to a bending load the u-p (displacements and constant pressure) formulation that can overcome the problem with incompressibility performs poorly in bending problems, whereas the co-rotational formulation and also the complete non-linear incompatible element of the previous chapter give a very reasonable solution for this bending-incompressibility combination. The problem above is also tested using a slightly irregular mesh to demonstrate the good results the new formulation produces for this class of problems.

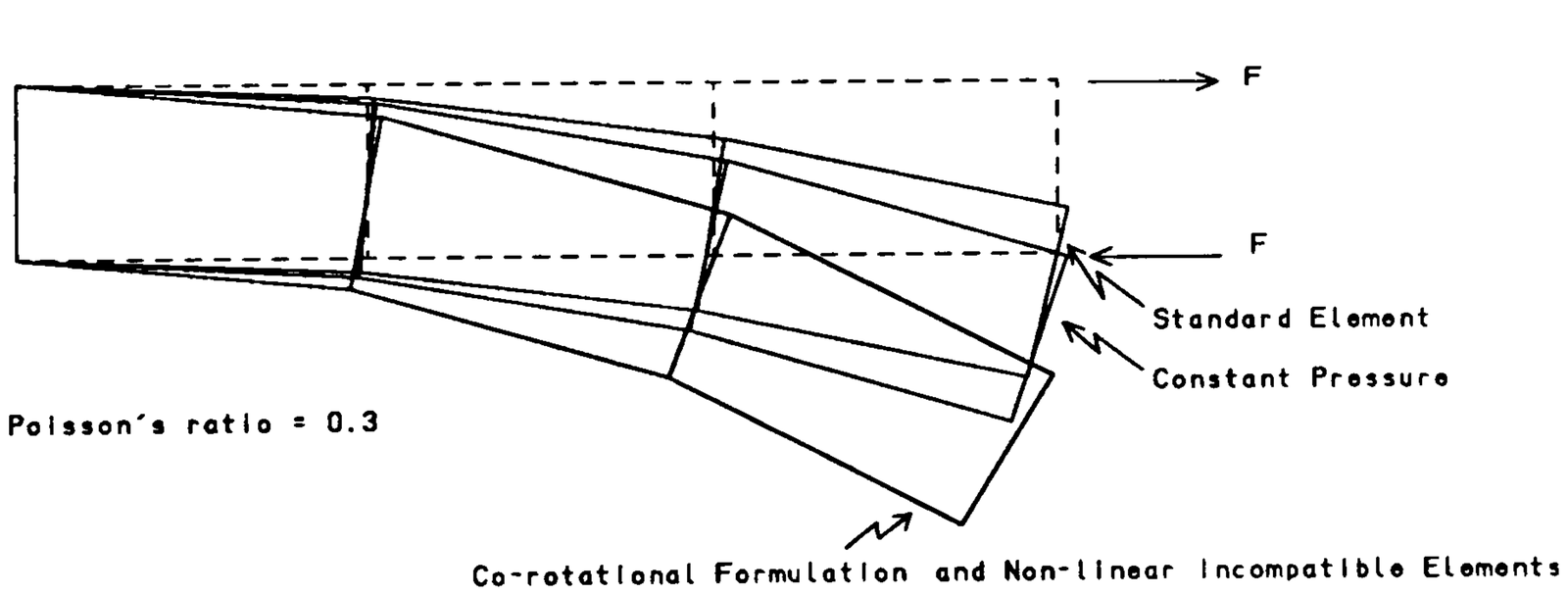


Figure 5.5: Cantilever Beam - $\nu = 0.3$

5.3.2 Cantilever beam subject to large deflections

This examples shows a cantilever beam subject to a large rotation. The objective of the example is to examine the behaviour of the element with large deflections and large load-step size. In this problem the transverse load is applied in one step and the problem iterates until convergence. The cantilever beam is modelled by a 6×1 element mesh

¶It is important to mention that higher values for ν (to simulate incompressibility) were also used with the formulation and the same very satisfactory performance was achieved

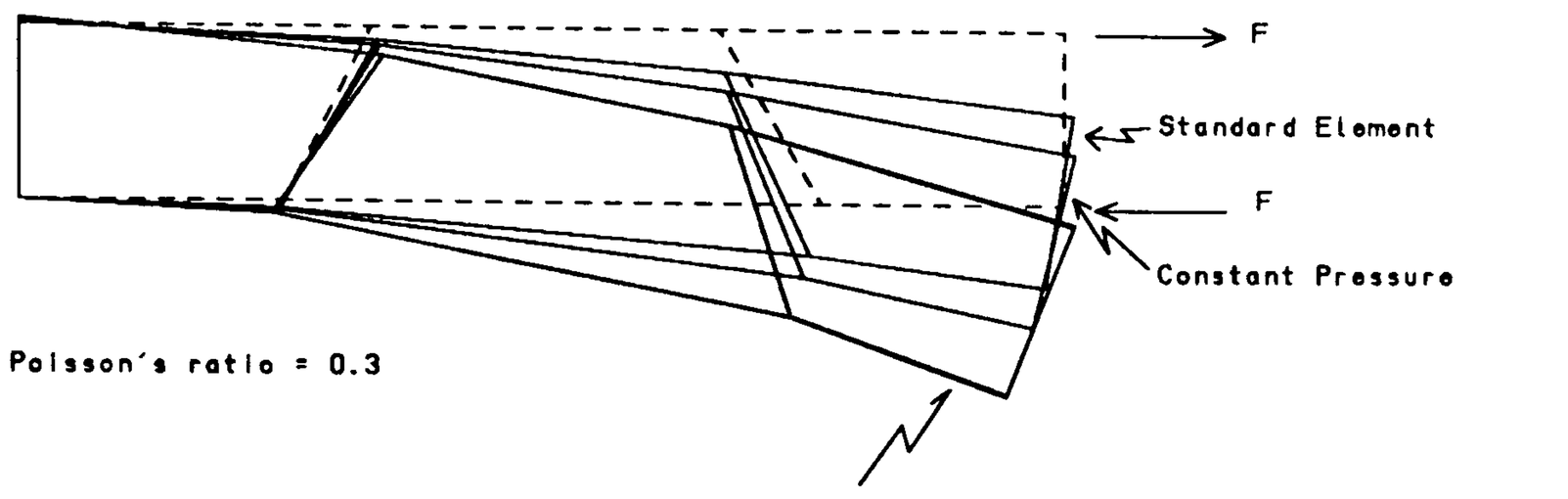


Figure 5.6: Cantilever Beam (irregular mesh) - $\nu = 0.3$

using irregular elements. Besides testing the co-rotational element for bending problems, we use a near-incompressible material (Poisson's ratio $\nu = 0.499$). The Young's modulus is $E = 1000$. The total shear load F is equal to 20. Figure 5.8 shows the original and deflected configuration of the cantilever. The problem was analysed using the present co-rotational element and the enhanced strain element developed by Li [51]. The former converges to the final deformed configuration with one load step whereas the latter needs 5 load step to reach convergence at the same load level. The final results are the same but the developed element allows larger load steps to be applied. We also compared the results with those obtained, more expensively, using 8-noded elements with a total Lagrangian formulation. The agreement is very good although in the latter case 17 iterations were required for the convergence.

In addition to the features tested above, we employ this problem to confirm the affirmation that the inclusion or not of the variation $\delta \mathbf{v}$ presented in equation (5.61) does not affect the overall performance of the element. The final result (displacements, stresses, etc.) is not modified and table 5.1 indicates that the contribution of this term has no effect even for the rate of convergence of the Newton-Raphson method.

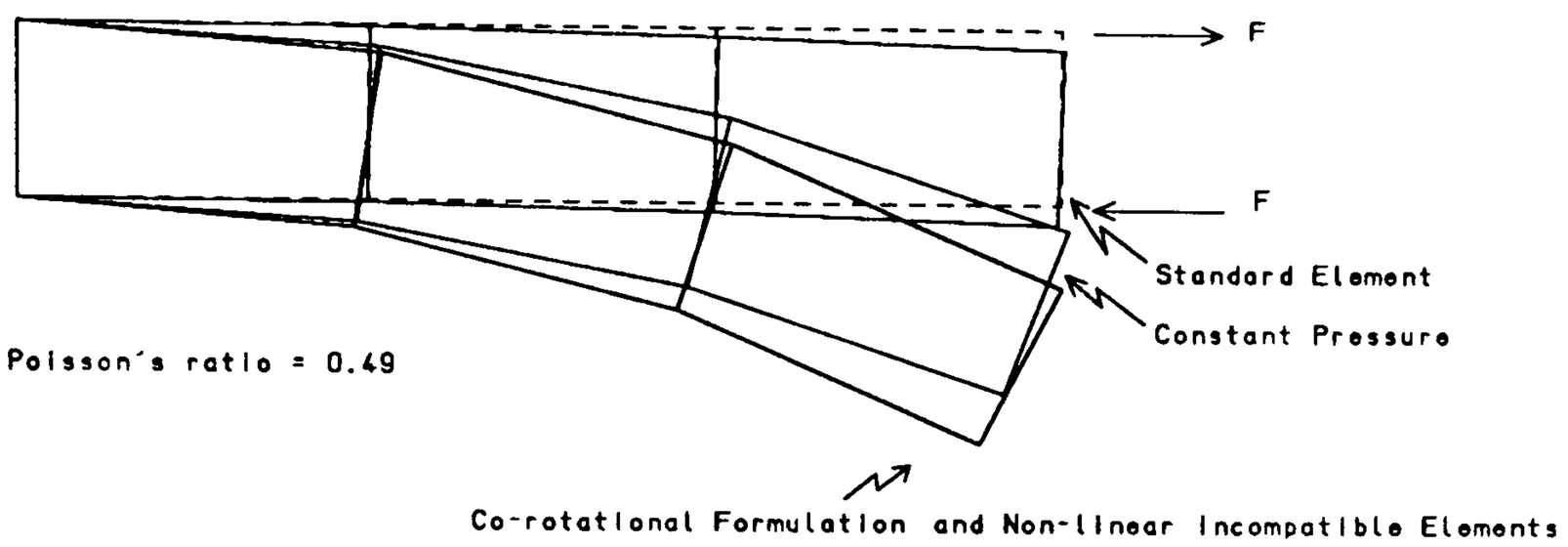


Figure 5.7: Cantilever Beam - $\nu = 0.49$

5.3.3 Shallow arch under central load

The last example of this chapter analyses the shallow arch presented in section 4.5.2. The geometrical properties are the same as those given in the previous analysis but with the present element we examine the problem assuming two different situations: first the same plane-stress analysis is used and the results are compared with the theoretical solution as for the first test; second the structure is studied in a plane-strain analysis with a near-incompressible material ($\nu = 0.49$) and the results are compared with the response obtained from the enhanced strain element of reference [51]. The good agreement achieved in the comparisons can be seen in figures 5.9 and 5.10 for both the plane-stress and plain-strain cases.

5.4 Final remarks

In this chapter we have shown that it is possible to apply a co-rotational formulation with a consistent derivation of the tangent stiffness matrix to study geometric non-linearities of two-dimensional continua. The formulation allows the use of conventional

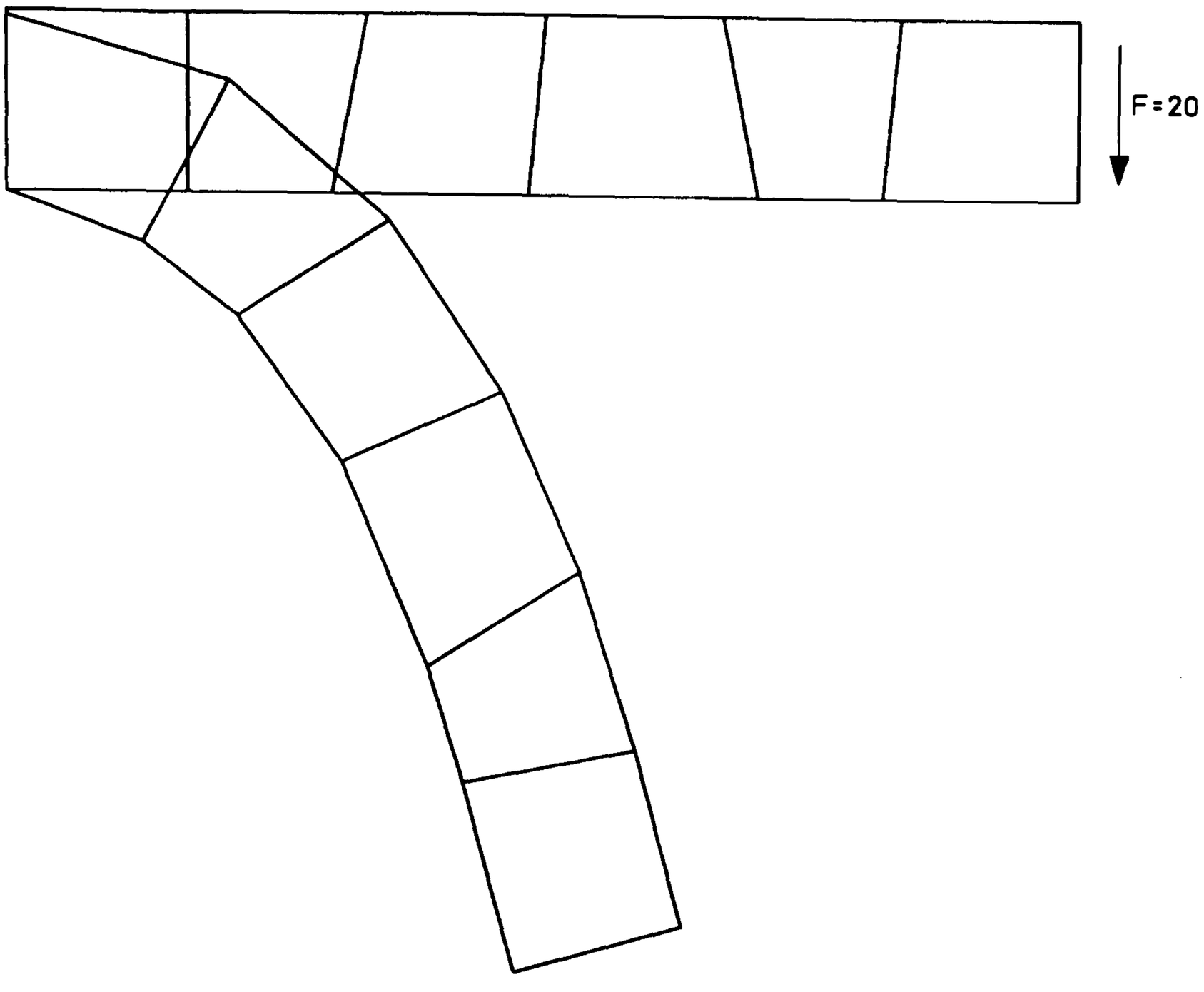


Figure 5.8: Cantilever beam under large deflection

linear elements that have been exhaustively investigated and very effective formulations have been developed. The technique then produces a formulation that incorporates linear elements into a co-rotating framework whereby non-linearities are introduced via the rotation of the system.

In the present development we included the linear incompatible element described in the previous chapter within the co-rotational procedure. The resulting formulation is able to analyse accurately problems involving large rotations and displacements, as well as bending and near-incompressible behaviour. Later in Chapter 7 we will extend the formulation to include large-strain analysis (hyperelasticity).

The examples presented here demonstrates the striking results obtained with the new formulation. The load increment size can be considerably large without any compromise as far as the final results are concerned. Due to this excellent results, the next step is to expand the formulation for three-dimensional analysis. This is shown in the next chapter.

Iteration	*Convergence factor*	
	considering $\delta\mathbf{v}$	without $\delta\mathbf{v}$
0	5993.7	5993.7
1	19.491	19.490
2	324.97	324.96
3	9.1360	9.1367
4	48.513	48.532
5	9.7291×10^{-3}	9.5997×10^{-3}
6	2.1052×10^{-3}	2.0017×10^{-3}
7	1.8354×10^{-10}	6.4750×10^{-9}

Table 5.1: Euclidean residual norm as a percentage of total reactions

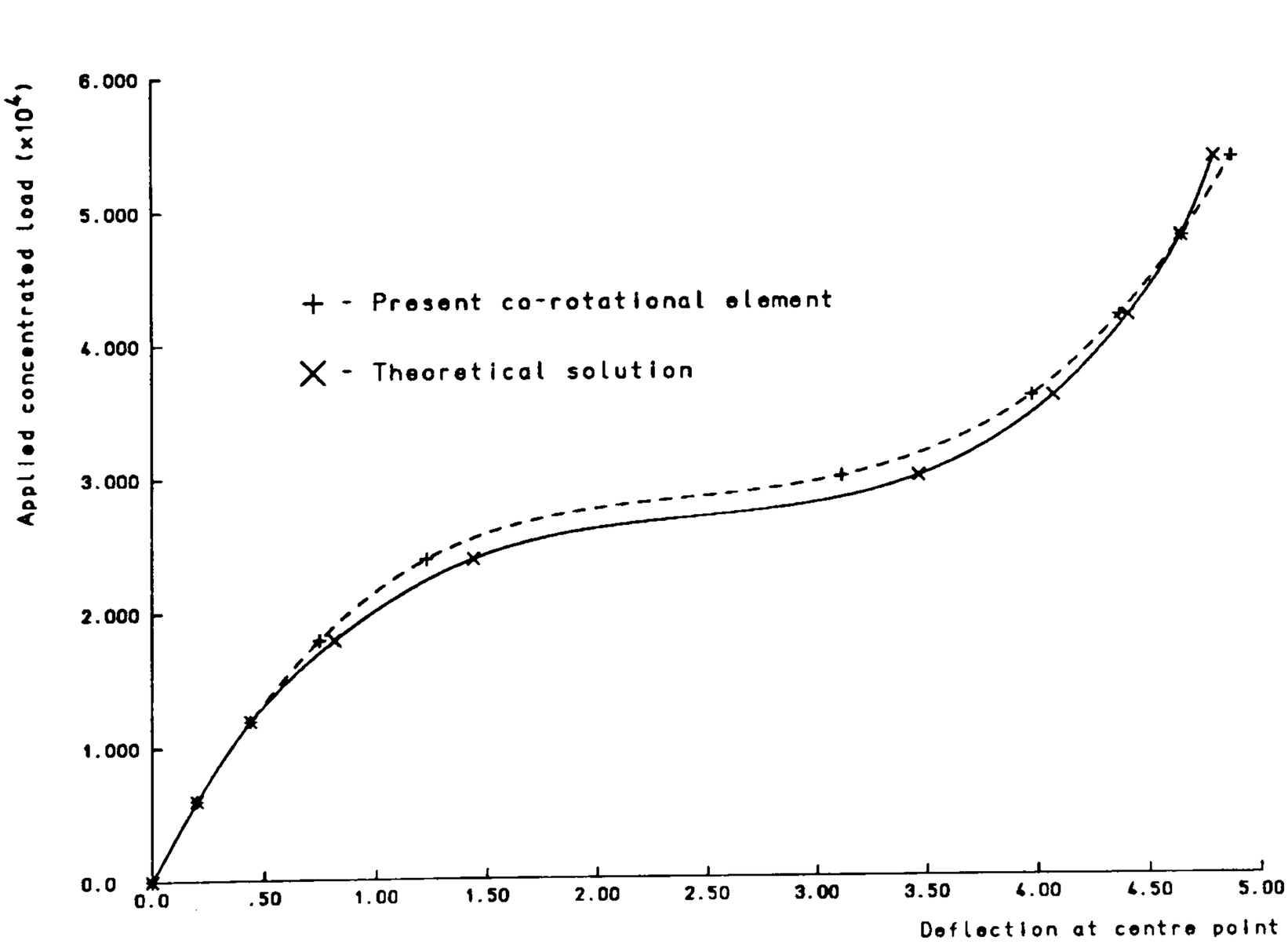


Figure 5.9: Shallow arch under central load - Load-deflection curve for the plane-stress analysis

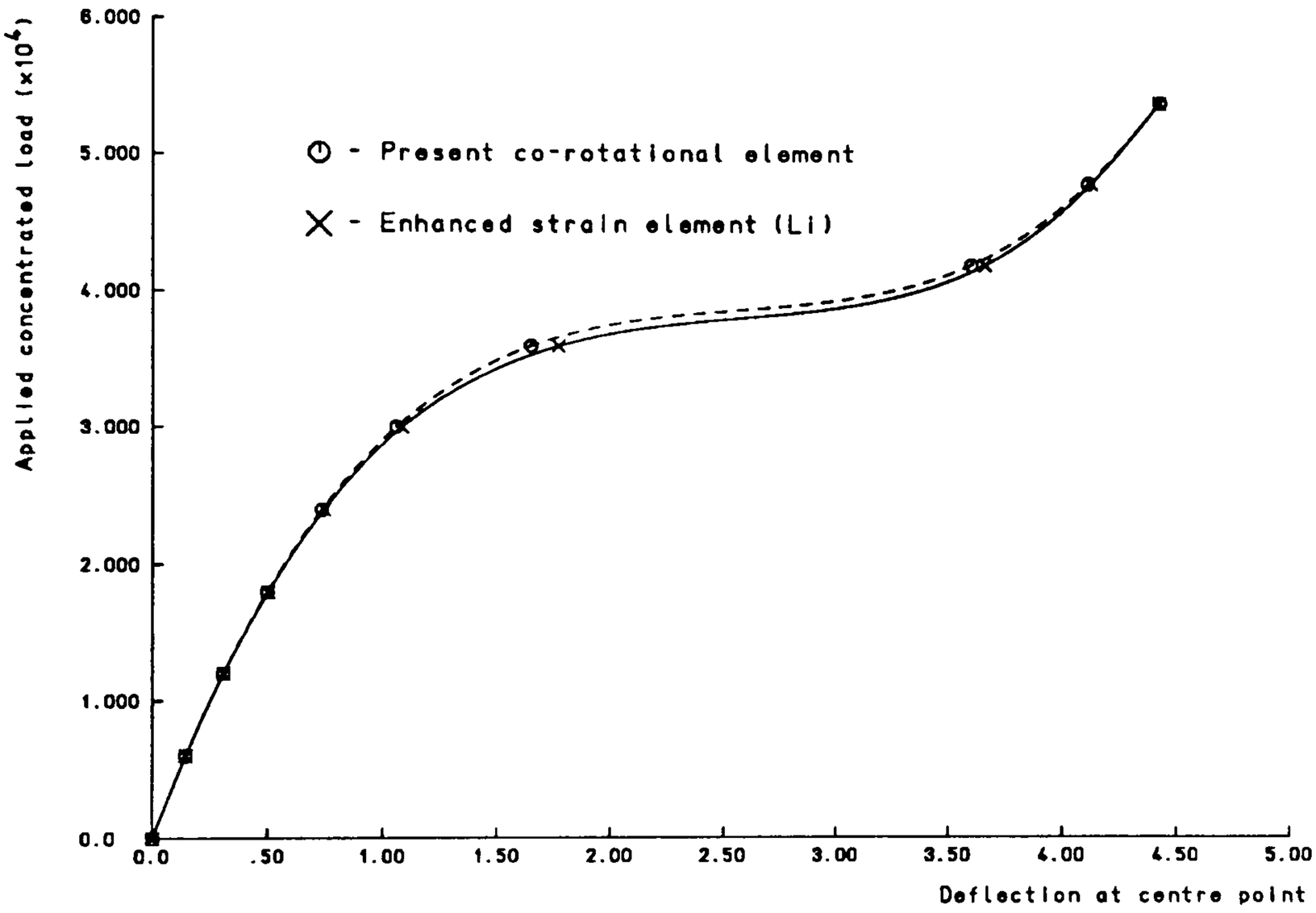


Figure 5.10: Shallow arch under central load - Load-deflection curve for the plane-strain analysis ($\nu = 0.49$)

Chapter 6

Co-rotational Formulation for Three-dimensional Continua

6.1 Introduction

The present chapter considers the extension of the two-dimensional work of the previous chapter to three dimensions. As with the previous formulation, the simplicity of a standard linear element is exploited whereby the element is used with respect to a local co-ordinate frame connected to the body which rotates with the element. The non-linear effects are incorporated via the rotation of the local frame.

The principal idea of the current co-rotational formulation is to separate the rotations from the stretches by the use of the polar decomposition theorem. In this way, rotations (mainly emanating from rigid body movements) and stretches can be disconnected and therefore treated independently. However, instead of using a conventional continuum approach in which the decomposition is applied at each Gauss point, it is here only applied at the centroid of the element. Nevertheless, if we use this approach for a two-dimensional case, the procedure leads to a formulation that is entirely equivalent with that of the previous chapter.

A consistent formulation is derived for the three-dimensional co-rotational procedure. The adopted technique involves a general process in which the variations of local strains are related to the variations of the global displacements. The virtual work expression is then applied to define the out-of-balance force vector that is differentiated to produce the consistent tangent stiffness matrix. The variation of the out-of-balance vector must include the differentiation of the transformation matrix that accounts for the local/global transformations. The final consistent stiffness matrix yields a quadratic

convergence rate when the Newton-Raphson method is used for solving the non-linear equations.

The element presented in this chapter also includes the application of incompatible displacement modes to enhance the performance of this 'tri-linear' element for bending situations and incompressibility problems.

6.2 Development

6.2.1 Conventional linear three-dimensional element

The initial development incorporates the conventional eight-noded linear brick element which we will now be briefly describing. The standard global nodal displacements of the element are given by the nodal degrees of freedom u, v and w at each node for the nodal configuration shown in figure 6.1. We adopt isoparametric elements in which displacements and geometry utilise the same shape functions to be interpolated. Therefore, if we have a non-dimensional co-ordinate system and ξ_i, η_i, ζ_i representing the nodal co-ordinates, the "Serendipity" shape function can be presented in a neat form as [101]:

$$h_i = \frac{1}{8}(1+\xi\xi_i)(1+\eta\eta_i)(1+\zeta\zeta_i) \tag{6.1}$$

with $i = 1$ to 8. The interpolation for the local displacement, which is similar to that of (4.1), is given by

$$\begin{aligned} u &= \mathbf{h}(\xi,\eta,\zeta)^T\mathbf{u} \\ v &= \mathbf{h}(\xi,\eta,\zeta)^T\mathbf{v} \\ w &= \mathbf{h}(\xi,\eta,\zeta)^T\mathbf{w} \end{aligned} \tag{6.2}$$

The Jacobian of the isoparametric map is then obtained via

$$\begin{Bmatrix} \frac{\partial}{\partial\xi} \\ \frac{\partial}{\partial\eta} \\ \frac{\partial}{\partial\zeta} \end{Bmatrix} = \begin{bmatrix} \frac{\partial X}{\partial\xi} & \frac{\partial Y}{\partial\xi} & \frac{\partial Z}{\partial\xi} \\ \frac{\partial X}{\partial\eta} & \frac{\partial Y}{\partial\eta} & \frac{\partial Z}{\partial\eta} \\ \frac{\partial X}{\partial\zeta} & \frac{\partial Y}{\partial\zeta} & \frac{\partial Z}{\partial\zeta} \end{bmatrix} \begin{Bmatrix} \frac{\partial}{\partial X} \\ \frac{\partial}{\partial Y} \\ \frac{\partial}{\partial Z} \end{Bmatrix} = \mathbf{J} \begin{Bmatrix} \frac{\partial}{\partial X} \\ \frac{\partial}{\partial Y} \\ \frac{\partial}{\partial Z} \end{Bmatrix} \tag{6.3}$$

The local strains at any point can now be related to the local nodal displacements, $\mathbf{p}_l$, so that

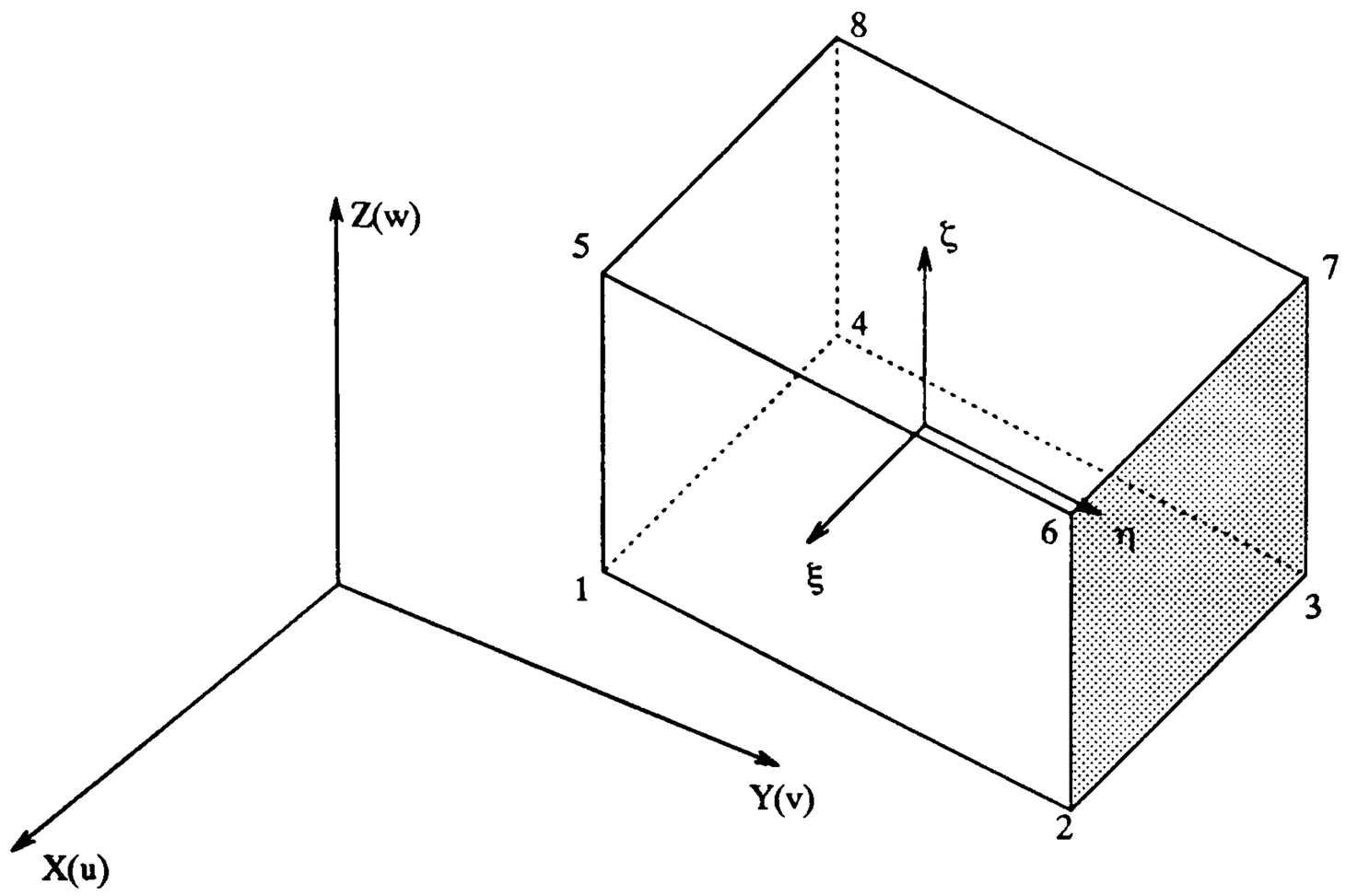


Figure 6.1: Eight-noded brick element

$$\epsilon_l = \left\{ \begin{array}{c} \frac{\partial u}{\partial X} \\ \frac{\partial u}{\partial Y} \\ \frac{\partial w}{\partial Z} \\ \frac{\partial u}{\partial Y} + \frac{\partial v}{\partial X} \\ \frac{\partial v}{\partial Z} + \frac{\partial w}{\partial Y} \\ \frac{\partial w}{\partial X} + \frac{\partial u}{\partial Z} \end{array} \right\} = \mathbf{B}_l \, \mathbf{p}_l \tag{6.4}$$

Using an appropriate three-dimensional constitutive matrix, $\mathbf{D}$, we produce the local element stiffness matrix as

$$\mathbf{K}_{ll} = \int_{V_o} \mathbf{B}_l^T \, \mathbf{D} \, \mathbf{B}_l \, dV_o \tag{6.5}$$

where $dV_o = \det\mathbf{J} \, d\xi \, d\eta \, d\zeta$.

6.2.2 Non-linear formulation

Having established the local element stiffness matrix, we can now include this element into a co-rotational framework. First we need to obtain the local nodal co-ordinates for the element. Following a similar approach as presented for the two-dimensional case, using the global co-ordinate system we can obtain the element local frame by translation of the origin of the global system to node 1 of the element of figure 6.1.

This procedure allows the determination of the local co-ordinates for the nodes just by addition or subtraction of the global co-ordinates, i.e.,

$$\mathbf{X}_l^i = \mathbf{X}_g^i - \mathbf{X}_g^1 \tag{6.6}$$

It is still necessary to compute local axes within the non-linear process. This local axes are used to map the initial configuration of the element onto its final configuration, as for the two-dimensional formulation. The hypothesis to be followed is demonstrated in two dimensions. It can be shown that the rotation matrix from the $\mathbf{F} = \mathbf{R}\,\mathbf{U}$ decomposition at the centroid of the element can be used to find the rotating base vectors which define the local system. To demonstrate the assumption, we begin with the deformations shown in figure 6.3. If we compare figure 6.2 with figure 6.3 we note that they are equivalent with the latter illustrating a process whereby the element is strained and later rotated while the former represents a rotation followed by a stretch. However, it is clear that the two systems are totally equivalent and therefore we can work with figure 6.3 which represents the $\mathbf{F} = \mathbf{R}\,\mathbf{U}$ decomposition. The latter process is known as a polar decomposition. In a more rigorous approach, the analogy given above should only be made for homogeneous deformations, i.e., deformations with constant deformation gradient $\mathbf{F}$. Nonetheless, we will apply the approach at the centroid for the current co-rotational procedure. We then can write $\mathbf{R} = [\mathbf{e}_1\mathbf{e}_2]$ and, according to figure 6.3, $\mathbf{R}$ rotates the base vectors $\mathbf{i}_1$ and $\mathbf{i}_2$ into the new configuration $\mathbf{e}_1$ and $\mathbf{e}_2$ that represents the local co-ordinates system or, in other words, the co-rotating base vectors.

Accordingly, for a three-dimensional formulation $\mathbf{R}$ is computed from $\mathbf{F}$ at the centroid and is given by

$$\mathbf{R} = \begin{bmatrix} \mathbf{e}_1 & \mathbf{e}_2 & \mathbf{e}_3 \end{bmatrix} \tag{6.7}$$

where $\mathbf{e}_1, \mathbf{e}_2, \mathbf{e}_3$ are the three unit vector of the transformation. Therefore, using the three-dimensional equivalent of (5.35), the current local co-ordinates values are

$$\mathbf{x}_l^i = \mathbf{X}_l^i + \mathbf{p}_l^i = \mathbf{R}^T\left(\mathbf{x}_g^i - \mathbf{x}_g^1\right) \tag{6.8}$$

where $\mathbf{x}_l^i$ and $\mathbf{x}_g^i$ are the current co-ordinates for the local and global configurations for the node i, respectively, and $\mathbf{p}_l^i$ is the local displacement vector for the node i.

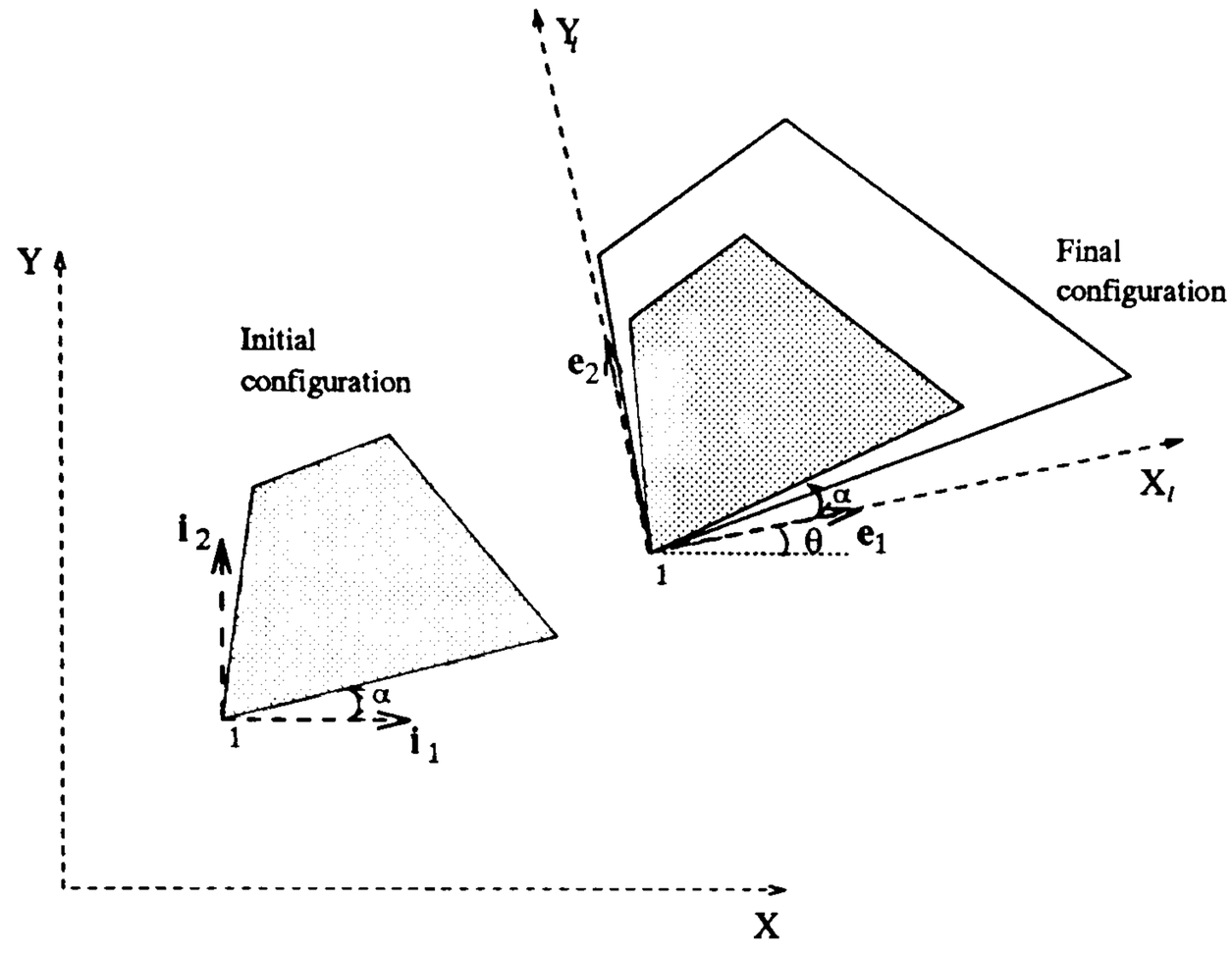


Figure 6.2: Initial and final configurations – rotation followed by stretch

Figure 6.3: Polar decomposition – stretching preceding the rotation

From figures 6.2 and 6.3, at the centroid of the element we can write

$$\mathbf{U} = \frac{\partial \mathbf{x}_l}{\partial \mathbf{X}_l} = [\mathbf{I} + \frac{\partial \mathbf{u}_l}{\partial \mathbf{X}_l}] = \mathbf{I} + \mathbf{D}_l \tag{6.9}$$

Here $\mathbf{x}_l = \mathbf{X}_l + \mathbf{u}_l$ corresponds to the current co-ordinates for the whole element and $\mathbf{D}_l$ is the local displacement-derivative matrix.

We also can write the local engineering strain (still at the centroid) as

$$\boldsymbol{\epsilon}_l = \frac{1}{2}(\mathbf{D}_l + \mathbf{D}_l^T) \tag{6.10}$$

Equations (6.9) and (6.10) above lead to an expression for the local engineering strain of the form

$$\boldsymbol{\epsilon}_l = \frac{1}{2}\mathbf{U} + \frac{1}{2}\mathbf{U}^T - \mathbf{I} = \mathbf{U} - \mathbf{I} \tag{6.11}$$

Note that in the above we have used the property of symmetry of the right stretch matrix $\mathbf{U}$ and that the relationships from (6.9) to (6.11) are also valid for a three-dimensional case. The latter equation represents an equivalent expression to the Biot strain.

In our development, however, the local strains are not obtained via the polar decomposition and the matrix $\mathbf{U}$ applying equation (6.11). Instead, the local strains are computed in a standard manner, as in equation (6.4), with the local displacements $\mathbf{p}_l$ being computed from (6.8).

It is worth mentioning that since the present formulation does not correspond to the pure polar decomposition which is implemented at the Gauss points, a direct link with a Biot-type formulation in fact only applies when we have homogeneous deformation over the element. Moreover, the procedure used here to determine the local axes actually agrees with that of Chapter 5 because it also produces zero spin at the centroid. This is true due to the fact that $\mathbf{D}_l = \mathbf{D}_l^T$ and $\Omega_l = \mathbf{D}_l - \mathbf{D}_l^T$.

To obtain the rotation matrix $\mathbf{R}$ it is necessary to begin by computing the deformation-gradient matrix $\mathbf{F}$. The latter can be calculated via the global displacement-gradient vector $\boldsymbol{\theta}_g$ which is given in a vector form by:

$$\boldsymbol{\theta}_g^T = \left(\begin{array}{ccccccccc} \frac{\partial u}{\partial X} & \frac{\partial u}{\partial Y} & \frac{\partial u}{\partial Z} & \frac{\partial v}{\partial X} & \frac{\partial v}{\partial Y} & \frac{\partial v}{\partial Z} & \frac{\partial w}{\partial X} & \frac{\partial w}{\partial Y} & \frac{\partial w}{\partial Z} \end{array} \right) \tag{6.12}$$

From $\boldsymbol{\theta}_g$ it is easy to form the global displacement-derivative matrix, here represented by $\mathbf{D}_g$. Hence, the matrix $\mathbf{F}$ comes from $\mathbf{D}_g$ as

$$\mathbf{F} = \mathbf{I} + \mathbf{D}_g \tag{6.13}$$

Considering that the right Cauchy-Green tensor can be written as

$$\begin{aligned} \mathbf{C} = \mathbf{F}^T\mathbf{F} &= \lambda_1^2\mathbf{N}_1\mathbf{N}_1^T + \lambda_2^2\mathbf{N}_2\mathbf{N}_2^T + \lambda_3^2\mathbf{N}_3\mathbf{N}_3^T \\ &= \mathbf{Q}(\mathbf{N})\,[\mathbf{diag}(\lambda_i^2)]\,\mathbf{Q}(\mathbf{N})^T \end{aligned} \tag{6.14}$$

the principal stretches and the principal directions can be obtained via the solution of the eigenproblem

$$[\mathbf{C} - \lambda^2\mathbf{I}]\,\mathbf{N} = \mathbf{0} \tag{6.15}$$

Before proceeding to find the matrix $\mathbf{R}$, we need to compute the right stretch matrix $\mathbf{U}$ that can be expressed by

$$\mathbf{U} = \lambda_1\mathbf{N}_1\mathbf{N}_1^T + \lambda_2\mathbf{N}_2\mathbf{N}_2^T + \lambda_3\mathbf{N}_3\mathbf{N}_3^T \tag{6.16}$$

Then, by applying the $\mathbf{F} = \mathbf{RU}$ decomposition, the rotation matrix is clearly found as

$$\mathbf{R} = \mathbf{F}\mathbf{U}^{-1} \tag{6.17}$$

The rotation matrix $\mathbf{R}$ defines the movement between the current configuration of the system and its initial configuration and can be also written as

$$\mathbf{R} = \mathbf{Q}(\mathbf{n})\,\mathbf{Q}(\mathbf{N})^T \tag{6.18}$$

where $\mathbf{n}$ is the equivalent of $\mathbf{N}$ in relation to the Eulerian triad [20].

From (6.8), the local nodal displacements, for a particular node i, are found as

$$\mathbf{p}_l^i = \mathbf{R}^T\,(\mathbf{x}_g^i - \mathbf{x}_g^1) - \mathbf{X}_l^i \tag{6.19}$$

In order to achieve a relationship between the variation of the local displacements and the variation of the global displacements it is required to calculate the differentiation of (6.19). Thus,

$$\delta\mathbf{p}_l^i = \delta\mathbf{R}^T\,\mathbf{x}_g^i + \mathbf{R}^T\,\delta\mathbf{p}_g^i \tag{6.20}$$

To continue the development of the theory it is useful to first consider some background information relating to large rotations. Using Rodrigues formula [21], we have

$$\mathbf{r}_n = \mathbf{R}\,\mathbf{r}_o = [\mathbf{I} + \frac{sin\theta}{\theta}\mathbf{S}(\boldsymbol{\theta}) + \frac{(1 - cos\theta)}{\theta^2}\mathbf{S}(\boldsymbol{\theta})\mathbf{S}(\boldsymbol{\theta})]\,\mathbf{r}_o \tag{6.21}$$

where $\mathbf{r}_o$ and $\mathbf{r}_n$ are the initial and final position of the $\mathbf{r}$ vector, respectively, and θ can be defined as

$$\theta = \sqrt{\theta_1^2 + \theta_2^2 + \theta_3^2} \tag{6.22}$$

The terms θ_1, θ_2 and θ_3 are the components of the *pseudo-vector* $\boldsymbol{\theta}$, that is,

$$\boldsymbol{\theta} = \left\{ \begin{array}{c} \theta_1 \\ \theta_2 \\ \theta_3 \end{array} \right\} \tag{6.23}$$

$\mathbf{S}(\boldsymbol{\theta})$ is the skew-symmetric matrix associated with the *pseudo-vector* $\boldsymbol{\theta}$ such as

$$\mathbf{S}(\boldsymbol{\theta}) = \left[\begin{array}{ccc} 0 & -\theta_3 & \theta_2 \\ \theta_3 & 0 & -\theta_1 \\ -\theta_2 & \theta_1 & 0 \end{array} \right] \tag{6.24}$$

The definition of $\boldsymbol{\theta}$ as a pseudo-vector is due to the fact that $\boldsymbol{\theta}$ cannot be treated as a vector. The rotation are non-vectorial quantities and, as it can be seen in figure 6.4, the final results of a given set of large rotation is dependent upon the order in which the rotations have been applied.

To evaluate the variation of the Rodrigues formula, equation (6.21) can be expanded in terms of exponential series. Firstly we write $sin\theta$ and $cos\theta$ as

$$\begin{aligned} sin\theta &= \theta - \frac{\theta^3}{3!} + \frac{\theta^5}{5!} + \ldots \\ cos\theta &= 1 - \frac{\theta^2}{2!} + \frac{\theta^4}{4!} + \ldots \end{aligned} \tag{6.25}$$

If we write $\delta\mathbf{r}_o$ as the infinitesimal rotation from $\mathbf{r}_o$ to $\mathbf{r}_n$, it is possible to have,

$$\mathbf{r}_n = \mathbf{r}_o + \delta\mathbf{r}_o = [\mathbf{I} + \frac{sin(\delta\theta)}{\delta\theta}\mathbf{S}(\delta\boldsymbol{\theta}) + \frac{(1 - cos(\delta\theta))}{\delta\theta^2}\mathbf{S}(\delta\boldsymbol{\theta})\mathbf{S}(\delta\boldsymbol{\theta})]\,\mathbf{r}_o \tag{6.26}$$

Hence,

$$\delta\mathbf{r}_o = [\frac{sin(\delta\theta)}{\delta\theta}\mathbf{S}(\delta\boldsymbol{\theta}) + \frac{(1 - cos(\delta\theta))}{\delta\theta^2}\mathbf{S}(\delta\boldsymbol{\theta})\mathbf{S}(\delta\boldsymbol{\theta})]\,\mathbf{r}_o \tag{6.27}$$

From (6.25), neglecting the higher order terms, it follows that

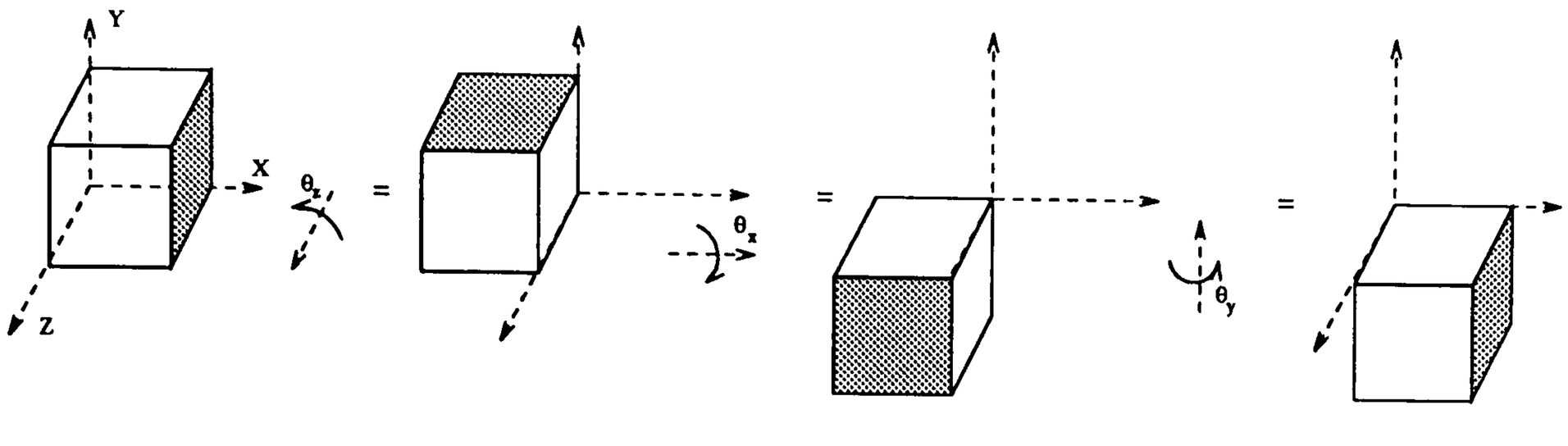


Figure 6.4: Pseudo-vector $\boldsymbol{\theta}$ - Order-dependence of the rotations

$$\delta \mathbf{r}_o = \mathbf{S}(\delta\boldsymbol{\theta})\mathbf{r}_o \tag{6.28}$$

The expression (6.28) above can also be written for a matrix $\mathbf{R}$. Therefore,

$$\delta \mathbf{R} = \mathbf{S}(\delta\boldsymbol{\theta})\,\mathbf{R} \tag{6.29}$$

It is relevant to show that the composition of the skew-symmetric matrix $\mathbf{S}(\boldsymbol{\theta})$ allows for the relationship given by

$$\mathbf{S}(\boldsymbol{\theta})^T = -\mathbf{S}(\boldsymbol{\theta}) \tag{6.30}$$

Another important relationship that is used throughout the development of this work comes from the vector (or cross) product $\boldsymbol{\theta} \times \mathbf{r}_o$, so that

$$\mathbf{S}(\boldsymbol{\theta})\,\mathbf{r}_o = \boldsymbol{\theta} \times \mathbf{r}_o = -\mathbf{r}_o \times \boldsymbol{\theta} = -\mathbf{S}(\mathbf{r}_o)\,\boldsymbol{\theta} \tag{6.31}$$

The variation (6.20) can now be obtained. From (6.29) and (6.30), we have

$$\delta\mathbf{R}^T = -\mathbf{R}^T\,\mathbf{S}(\delta\boldsymbol{\theta}) \tag{6.32}$$

Consequently, by using (6.31) it follows that

$$\delta\mathbf{p}_l^i = \mathbf{R}^T\,\mathbf{S}(\mathbf{x}_g^i)\,\delta\boldsymbol{\theta} + \mathbf{R}^T\,\delta\mathbf{p}_g^i = \mathbf{z}^i\,\delta\boldsymbol{\theta} + \mathbf{R}^T\,\delta\mathbf{p}_g^i \tag{6.33}$$

The variation of the total element local displacement vector is obtained by re-arranging (6.33) to produce

$$\delta\mathbf{p}_l = \underbrace{[\mathbf{col}\,\mathbf{z}^i]}_{\mathbf{z}}\,\delta\boldsymbol{\theta} + [\mathbf{diag}\,\mathbf{R}^T]\,\delta\mathbf{p}_g \tag{6.34}$$

where $[\mathbf{col}\,\mathbf{z}^i]$ is the 24×3 matrix formed by placing each nodal 3×3 $\mathbf{z}^i$ matrix into a column matrix $\mathbf{z}$.

The next step of the development is to evaluate the change of $\boldsymbol{\theta}$ to be used in (6.34). This can be achieved by a similar procedure as the one employed for the two-dimensional co-rotational element of last chapter. If we define a "spin" vector based on the local spin of (5.22), we have an expression such as

$$\boldsymbol{\Omega}_l = \mathbf{A}_l^T\,\mathbf{p}_l \tag{6.35}$$

Now the term $\mathbf{A}_l$ is a 24×3 matrix and $\boldsymbol{\Omega}_l$ is a 3×1 *pseudo-vector* of local rotations. The values of $\mathbf{A}_l$, consequently the local rotations, are computed at the centroid of the element. Hence, with no rotation being produced at the centroid, we assume that

$$\boldsymbol{\Omega}_l = \mathbf{0} \tag{6.36}$$

Differentiating (6.35), we obtain

$$\delta\boldsymbol{\Omega}_l = \mathbf{A}_l^T\,\delta\mathbf{p}_l = \mathbf{A}_l^T\,[\mathbf{diag}\,\mathbf{R}^T]\,\delta\mathbf{p}_g + \mathbf{A}_l^T\,\mathbf{z}\delta\boldsymbol{\theta} = \mathbf{0} \tag{6.37}$$

From which,

$$\delta\boldsymbol{\theta} = -[\mathbf{A}_l^T\,\mathbf{z}]^{-1}\,\mathbf{A}_l^T\,[\mathbf{diag}\,\mathbf{R}^T]\,\delta\mathbf{p}_g \tag{6.38}$$

or, by analogy with (5.41), we can write

$$\delta\boldsymbol{\theta} = \mathbf{v}^T \, \delta\mathbf{p}_g \tag{6.39}$$

Note that now $\mathbf{v}$ is a 24×3 matrix. The substitution of equation (6.39) into (6.34) leads to the transformation matrix $\mathbf{T}$.

$$\delta\mathbf{p}_l = [[\mathbf{diag}\,\mathbf{R}^T] + \mathbf{z}\,\mathbf{v}^T]\delta\mathbf{p}_g = \mathbf{T}\,\delta\mathbf{p}_g \tag{6.40}$$

It can be noticed that (6.40) is the three-dimensional equivalent of (5.44).

Having defined the relationship between local and global change of the displacements, one would have to apply the principle of virtual work to establish the relationship between local and global internal force vectors. This follows exactly the same development shown for the two-dimensional element, leading to (5.49) that is re-expressed here.

$$\mathbf{q}_{i_g} = \mathbf{T}^T \, \mathbf{q}_{i_l} \tag{6.41}$$

The differentiation of (6.41) results in the consistent tangent stiffness matrix. Continuing with the development, we reach

$$\delta\mathbf{q}_{i_g} = \mathbf{T}^T \, \mathbf{K}_{ll} \, \mathbf{T} \, \delta\mathbf{p}_g + \delta\mathbf{T}^T \, \mathbf{q}_{i_l} \tag{6.42}$$

as previously presented. $\mathbf{K}_{ll}$ is the element local stiffness matrix of (6.5).

In the same way as derived for the two-dimensional case, we need the variation of the transformation matrix $\mathbf{T}$ in order to obtain the initial stress or geometric stiffness matrix. Working with a typical node j, it can be written:

$$\delta\mathbf{T}^j \, \mathbf{q}_{i_l}^j = \delta[\mathbf{R} + \mathbf{v}\,\mathbf{z}^{T^j}] \, \mathbf{q}_{i_l}^j \tag{6.43}$$

In this moment, it is more suitable to split the r.h.s. of (6.43) into two terms. The differentiation of the first term leads to

$$\delta\mathbf{R}\,\mathbf{q}_{i_l}^j = \delta\mathbf{R}\,\mathbf{R}^T\,\mathbf{R}\,\mathbf{q}_{i_l}^j = \mathbf{S}(\delta\boldsymbol{\theta})\bar{\mathbf{q}}_{i,l}^j \tag{6.44}$$

where the identity $\mathbf{R}^T\mathbf{R} = \mathbf{I}$ is used in the first part of (6.44) and $\bar{\mathbf{q}}_{i,l}^j = \mathbf{R}\mathbf{q}_{i_l}^j$.

Using the relationship (6.31), we have

$$\delta\mathbf{R}\,\mathbf{q}_{i_l}^j = -\mathbf{S}(\bar{\mathbf{q}}_{i,l}^j)\,\delta\boldsymbol{\theta} = \mathbf{S}(\bar{\mathbf{q}}_{i,l}^j)^T \, \mathbf{v}^T \, \delta\mathbf{p}_g^j \tag{6.45}$$

where (6.30) is applied to obtain the last part of (6.45).

Now we can work with the second term of (6.43). The differentiation of this term becomes

$$\delta[\mathbf{v}\,\mathbf{z}^{Tj}]\,\mathbf{q}_{il}^{j} = \mathbf{v}\,\delta\mathbf{z}^{Tj}\,\mathbf{q}_{il}^{j} + \delta\mathbf{v}\,\mathbf{z}^{Tj}\,\mathbf{q}_{il}^{j} \tag{6.46}$$

Neglecting the variation of $\mathbf{v}$ based on the same argument given in the previous chapter whereby the terms generated by this differentiation would not affect the final results nor the convergence rate, we concentrate on the first term of (6.46). It leads to the variation of $\mathbf{z}^j$ as

$$\mathbf{v}\,\delta\mathbf{z}^{Tj}\,\mathbf{q}_{il}^{j} = \mathbf{v}\,\delta[\mathbf{R}^T\mathbf{S}(\mathbf{x}_g^j)]^T\,\mathbf{q}_{il}^{j} \tag{6.47}$$

Again it is better to isolate and work with each part of (6.47) separately, this means,

$$\mathbf{v}\,\delta[\mathbf{R}^T\mathbf{S}(\mathbf{x}_g^j)]^T\,\mathbf{q}_{il}^{j} = -\mathbf{v}\delta[\mathbf{S}(\mathbf{x}_g^j)\,\mathbf{R}]\,\mathbf{q}_{il}^{j} = -\mathbf{v}\delta\mathbf{S}(\mathbf{x}_g^j)\,\mathbf{R}\,\mathbf{q}_{il}^{j} - \mathbf{v}\,\mathbf{S}(\mathbf{x}_g^j)\,\delta\mathbf{R}\,\mathbf{q}_{il}^{j} \tag{6.48}$$

The first term of (6.48) gives

$$\mathbf{v}[-\delta\mathbf{S}(\mathbf{x}_g^j)\,\mathbf{R}]\,\mathbf{q}_{il}^{j} = -\mathbf{v}\mathbf{S}(\delta\mathbf{p}_g^j)\,\mathbf{R}\,\mathbf{q}_{il}^{j} = \mathbf{v}\mathbf{S}(\bar{\mathbf{q}}_{i,l}^{j})\,\delta\mathbf{p}_g^j \tag{6.49}$$

For the equation above we used (6.30), (6.31) and $\bar{\mathbf{q}}_{i,l}^{j} = \mathbf{R}\mathbf{q}_{il}^{j}$.

The second portion of (6.48) involves the variation of $\mathbf{R}$ and after some manipulations it leads to

$$\mathbf{v}[\mathbf{S}(\mathbf{x}_g^j)\,\delta\mathbf{R}]\,\mathbf{q}_{il}^{j} = -\mathbf{v}\,\mathbf{S}(\mathbf{x}_g^j)\,\mathbf{S}(\delta\boldsymbol{\theta})\,\mathbf{R}\mathbf{q}_{il} = \mathbf{v}\,\mathbf{S}(\mathbf{x}_g^j)\,\mathbf{S}(\bar{\mathbf{q}}_{i,l}^{j})\,\delta\boldsymbol{\theta} = \mathbf{v}\,\mathbf{S}(\mathbf{x}_g^j)\,\mathbf{S}(\bar{\mathbf{q}}_{i,l}^{j})\,\mathbf{v}^T\,\delta\mathbf{p}_g \tag{6.50}$$

which is a symmetric term.

Associating (6.45), (6.49) and (6.50) and placing them back into (6.43), the final form for the initial stress stiffness matrix for a node j is represented by:

$$\delta\mathbf{T}^j\,\mathbf{q}_{il}^{j} = [\mathbf{S}(\bar{\mathbf{q}}_{i,l}^{j})^T\,\mathbf{v}^T + \mathbf{v}\,\mathbf{S}(\bar{\mathbf{q}}_{i,l}^{j})]\delta\mathbf{p}_g^j + [\mathbf{v}\,\mathbf{S}(\mathbf{x}_g^j)\,\mathbf{S}(\bar{\mathbf{q}}_{i,l}^{j})\,\mathbf{v}^T]\delta\mathbf{p}_g \tag{6.51}$$

By adding up all the contributions of the nodes j's into the final stiffness matrix for the element, we can obtain a symmetric matrix that can be expressed as

$$\mathbf{K}_T = \mathbf{K}_{tg} + \mathbf{K}_{\sigma g} \tag{6.52}$$

where,

$$\mathbf{K}_{tg} = \mathbf{T}^T \mathbf{K}_l \mathbf{T} \tag{6.53}$$

and

$$\mathbf{K}_{\sigma g} = \sum_{j=1}^{8} \delta \mathbf{T}^j \mathbf{q}_{il}^j \tag{6.54}$$

6.2.3 Adding the incompatible modes

The eight-noded brick element described at the first part of this chapter suffers similar drawbacks to the four-noded plane element of Chapter 4. It reveals a poor performance for bending dominated and near-incompressible problems. The same solution used for a plane element can be adapted for a solid one. The element can be improved by adding a set of incompatible displacement modes to its original interpolation function, as initially suggested by Wilson [96]. These modes are internal degrees of freedoms and should be eliminated at the element level before assembling into the total structure by a static condensation. The principle is the same applied for the plane four-noded element but not considering the non-linear stage included in that element.

The shape functions of equations (6.1) are improved as

$$\begin{aligned} u &= \mathbf{h}^T \mathbf{u} + \mathbf{h}^{*T} \mathbf{u}^* \\ v &= \mathbf{h}^T \mathbf{v} + \mathbf{h}^{*T} \mathbf{v}^* \\ w &= \mathbf{h}^T \mathbf{w} + \mathbf{h}^{*T} \mathbf{w}^* \end{aligned} \tag{6.55}$$

where the additional shape functions for the incompatible modes are similar to that of (4.10) and can be expressed by

$$\mathbf{h}^* = \begin{Bmatrix} 1-\xi^2 \\ 1-\eta^2 \\ 1-\zeta^2 \end{Bmatrix} \tag{6.56}$$

The vectors $\mathbf{u}^*$, $\mathbf{v}^*$ and $\mathbf{w}^*$ represent the nine incompatible modes.

The inclusion of the incompatible displacement modes into the formulation of an eight-noded three-dimensional element also helps to avoid problems caused by incompressibility. This is demonstrated in some examples shown later in this chapter and also in the next chapter in hyperelasticity. The final enhanced incompatible element often produces very accurate results. The problem of locking for bending problems tends to

disappear since the over-stiff characteristic of the element tend to be eliminated by the use of the 'softening', here represented by the additional incompatible modes.

The element needs a special treatment in order to pass the *patch test.* The approach is shown in Chapter 4 for the plane element and can be applied in a similar manner for the current element, therefore the demonstration will not be shown here.

Using the same technique introduced for the two-dimensional co-rotational element, this three-dimensional element can be incorporated into the formulation for the three-dimensional co-rotational element described above. The incompatible element does not change since its formulation is developed for linear analysis. The non-linear procedure is included as explained before.

6.3 Numerical tests

This section contains some results of numerical tests carried out using the three-dimensional co-rotational element described above. The examples involve solutions of problems presenting large displacements and large rotations although at this point only small strains are assumed. Large strain analyses are discussed in the next chapter.

The results for three problems are shown below and illustrate the accuracy and iterative performance of the element. They confirm the consistency and effectiveness of the formulation.

6.3.1 Large deflection and rotation analysis of a cantilever beam

A three-dimensional cantilever beam is considered. The beam is subjected to an end shear with loads applied as shown in figure 6.5. The support conditions and the dimensions for the beam are also shown in the figure below. The material characteristics are as follows: Young's modulus $E = 100$ and Poisson's ratio $\nu = 0.49999$. The beam is modelled by a mesh with highly distorted elements. The load is applied in one step and it converge to the final deformed configuration reproduced in figure 6.6. The example is used to confirm the excellent response of the element to large deflections and large rotations and to show that large load steps can be applied with the new element. Incidentally, the enhanced strain element [51] does not converge in one step but needs 5 increments to reach the same deformation.

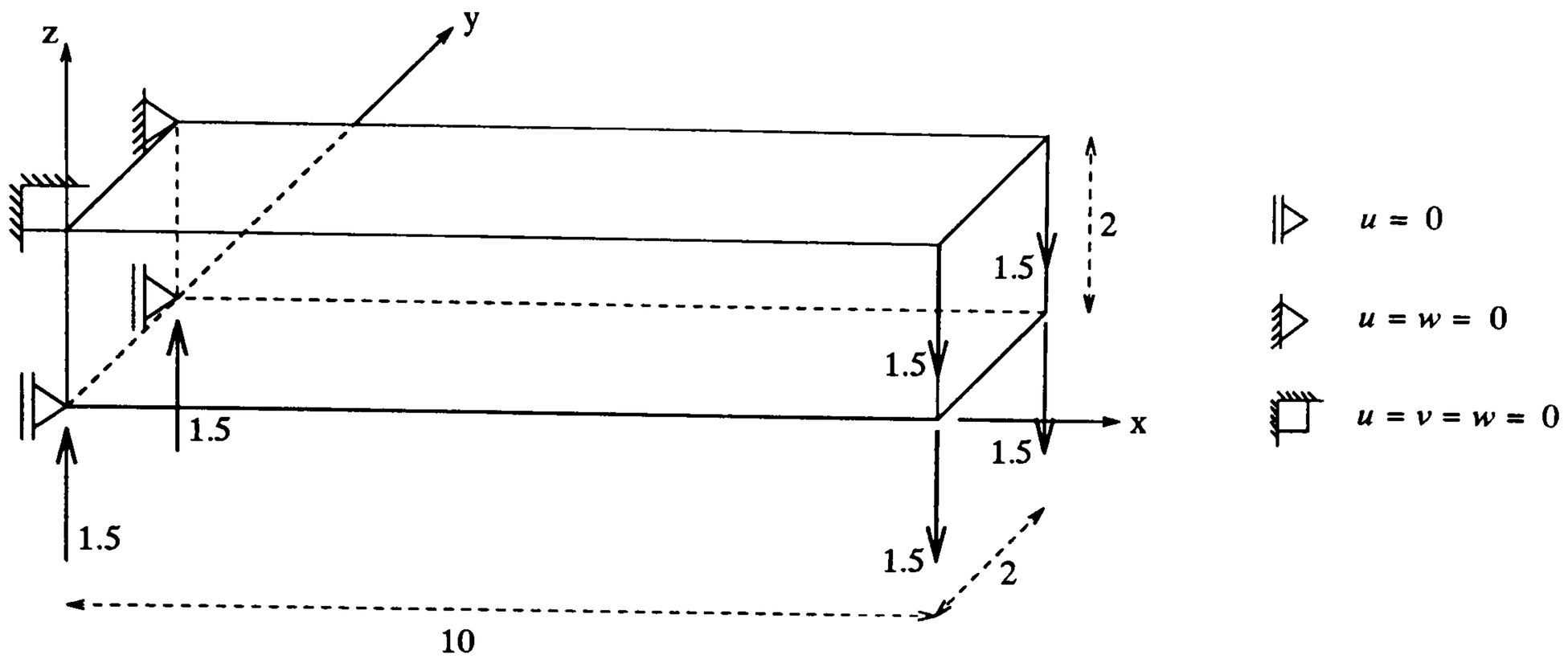


Figure 6.5: Three-dimensional cantilever beam under end shear

6.3.2 Three-dimensional curvilinear beam

In this example the large displacement response of a three-dimensional curvilinear cantilever beam subject to a concentrated end load is calculated. Due to the geometry and the applied load the cantilever undertakes both bending and twisting deformations. The beam lies in the X–Y plane and its cross-sectional area is $1in^2$. The cantilever bend has an average radius of $100in$ and an angle of 45^o, as figure 6.7 shows. The concentrated load is applied at one of the ends of the beam in the Z direction while the opposite end is kept fixed. The analysis is executed using Young's modulus of $E = 10^7 psi$ and Poisson's ratios of $\nu = 0.$ and $\nu = 0.499$. The problem is analysed using a $16 \times 1 \times 1$ element mesh. The load is applied in 12 increments up to a maximum of $P = 600lb$.

Figure 6.8 shows the deflected shapes of the cantilever at different load levels. The graph for the tip deflection plotted against the load parameter can be seen in figure 6.9. This figure relates to the analysis using $\nu = 0.$ and it is compared with the results given by the beam element of Bathe and Bolourchi [7]. The solutions are virtually the same. An excellent agreement is also obtained for the test with a near-incompressible material. This time, the comparison shown in figure 6.10 is taken against the solution predicted by the enhanced strain element of Li [51].

6.3.3 Hinged cylindrical shell subject to a point load

The cylindrical shell shown in figure 6.11 is studied in this last example. A quarter of the shell is idealised using a 32 element mesh ($4 \times 4 \times 2$). A concentrated load F is

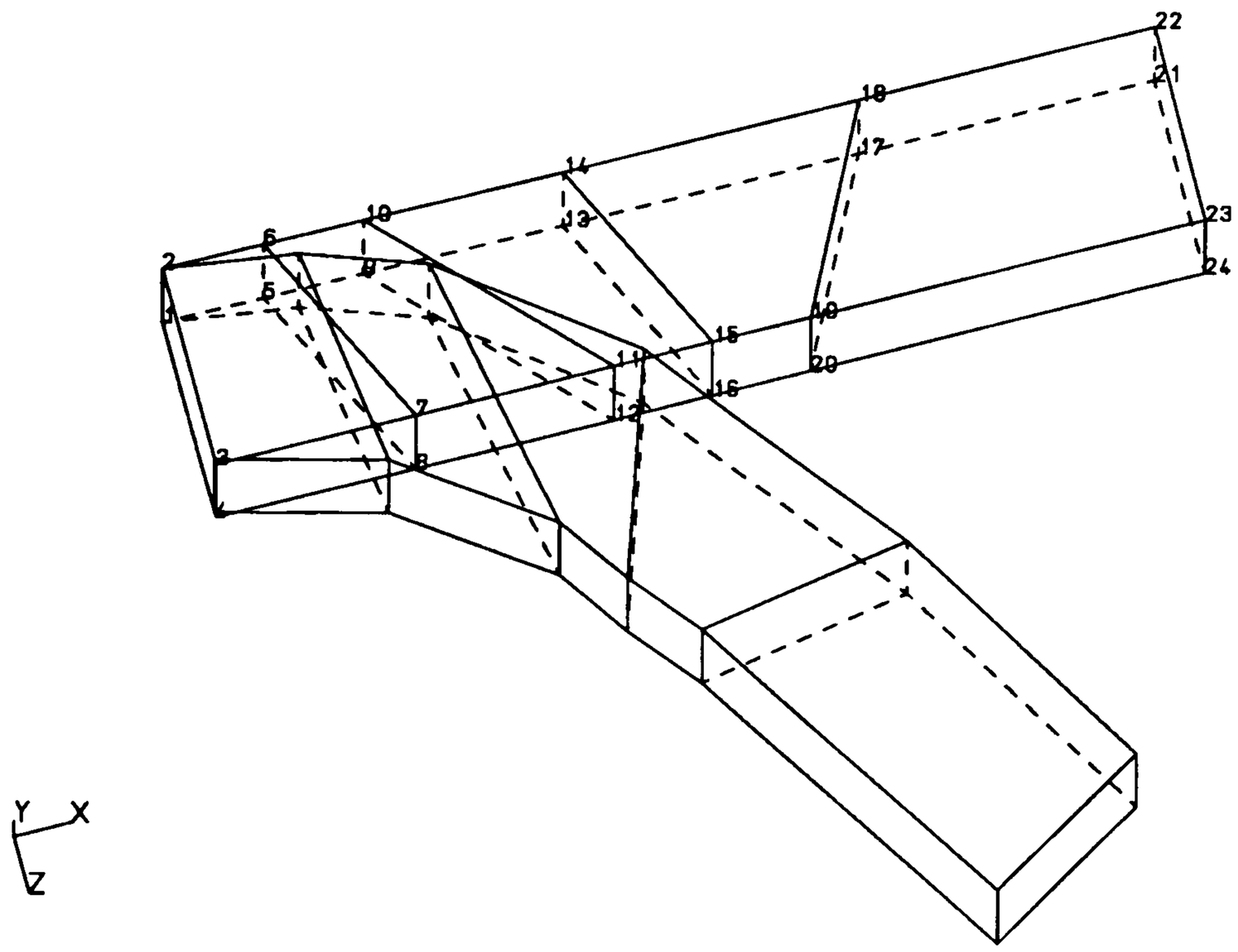


Figure 6.6: Large deflection and rotation of a cantilever beam

applied in the point A on the middle of the shell as seen in figure 6.11. The boundary condition are imposed such that the structure is simply supported on the straight edges and is free on the remain edges. The radius of the cylinder is $R = 2540mm$, the length is $l = 254mm$ and angle theta is $\theta = 0.1$radians. The analysis is performed using two distinct thicknesses: first the shell is studied with $t = 12.7mm$; the second analysis is executed with half of the first thickness, i.e., $t = 6.35mm$. The Young's modulus and Poisson's ratio are $E = 3105N/mm^2$ and $\nu = 0.3$.

The load-deflection curves for points A (middle of the shell) and B (mid-point of the curved edge) for the two analysis are compared with the results given by Oliver and Oñate [64] using a shell element. However, in their analysis they used displacement control to overcome limit points that occur in this problem. In figure 6.12, the paths for the load versus the displacement in w for the thickness of $t = 12.7mm$ are presented. It can be seen in both curves snap-throughs. We can easily follow the entire path

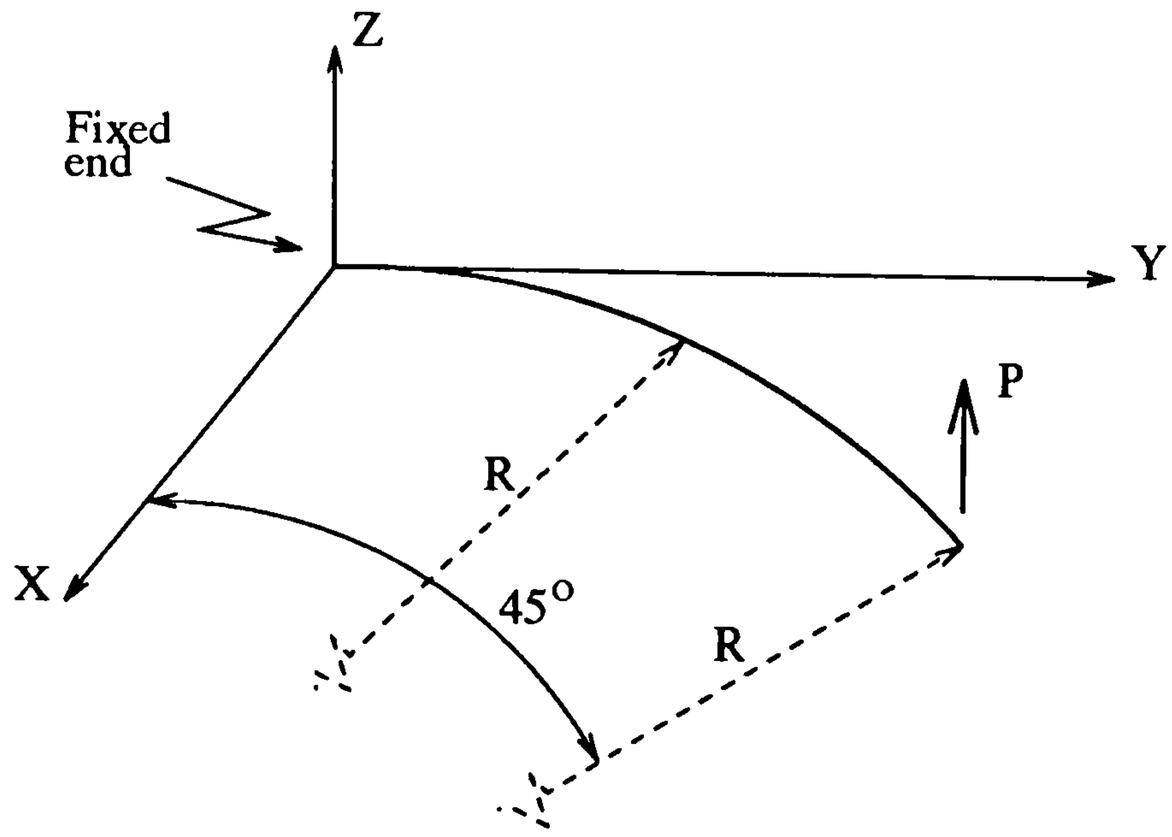


Figure 6.7: Three-dimensional curve cantilever beam

by using the arc-length method combined with the Newton-Raphson procedure. No problems with increment sizes is encountered. In the second figure (figure 6.13) the shell thickness is reduced to half its value. The point B presents a snap-through in its curve but the path for the point A involves both horizontal (snap-through) and vertical (snap-back) limit points. The latter relates to the snap-back depicted in the graph. The solution process used is the same combination as that described for the previous shell. Crisfield [16] displays the same results but only for the point A.

6.4 Final remarks

A three-dimensional version of the two-dimensional co-rotational element of Chapter 5 has been described in the present chapter. Although the procedure used in this chapter produces identical results for two dimensions as that of the previous chapter, an alternative technique has been employed in which the polar decomposition theorem has been used at the centroid of the element to find the co-rotating base frame for the element. This technique leads to a neat and attractive formulation that can handle a wide class of problems involving large rotations and deflections, however, at this stage, with only small-strain analysis.

The actual linear element used in the formulation is the eight-noded brick element incorporating the incompatible displacement modes. The final formulation can therefore analyse problems involving bending and near-incompressibility besides the large deformation mentioned above.

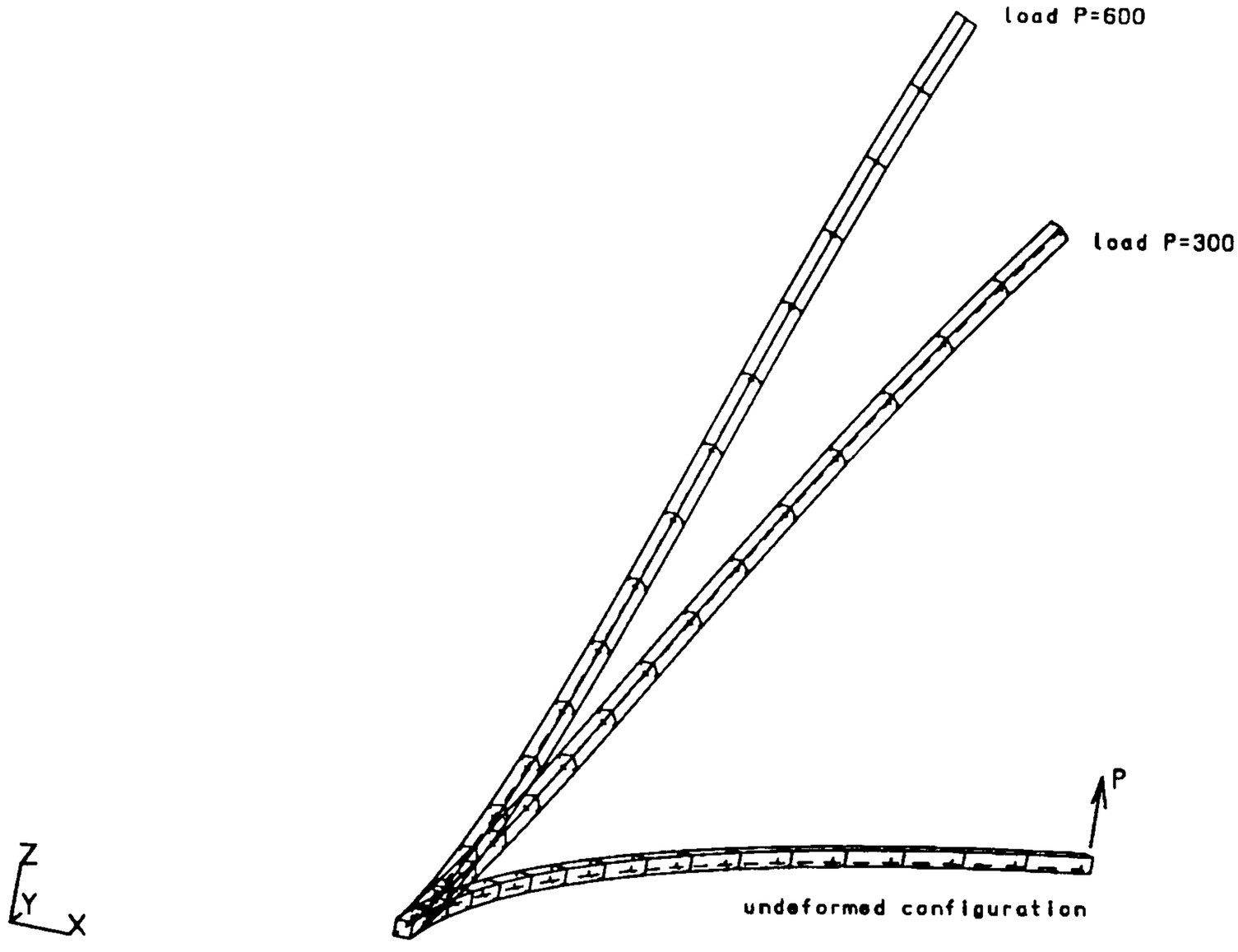


Figure 6.8: Three-dimensional curvilinear beam

It can be observed from the numerical applications the outstanding performance of the element, both related to the accuracy and also the increment size and number of iterations for the Newton-Raphson method. An interesting example tested was the thin shell presenting the snap-back. The element can correctly analyse the problem and good agreement can be obtained with previous works. The potentialities of the element are further explored in the hyperelastic approach to be shown in the next chapter.

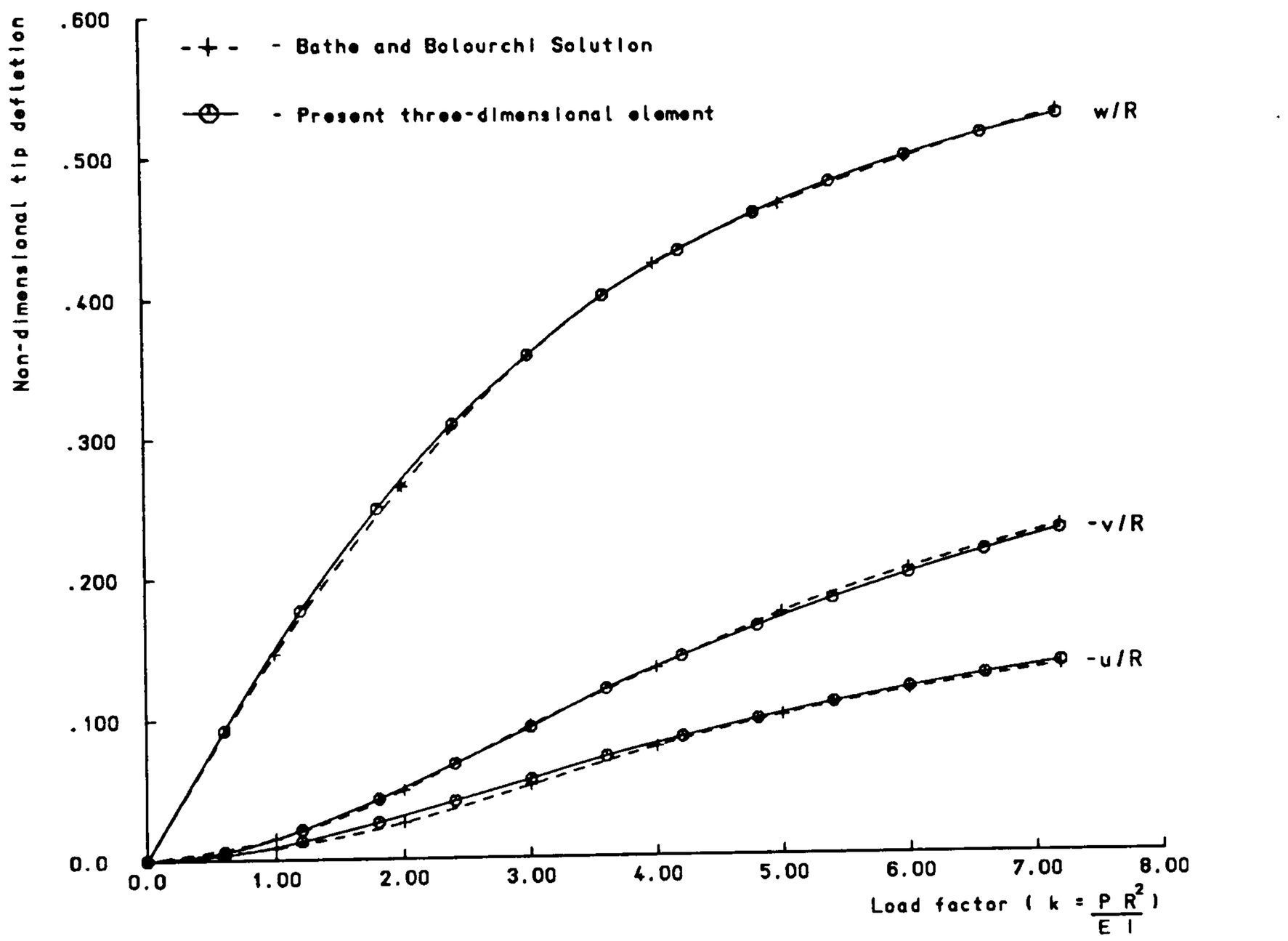


Figure 6.9: Three-dimensional curvilinea beam - Non-dimensional tip deflection vs. load factor ($\nu = 0.$)

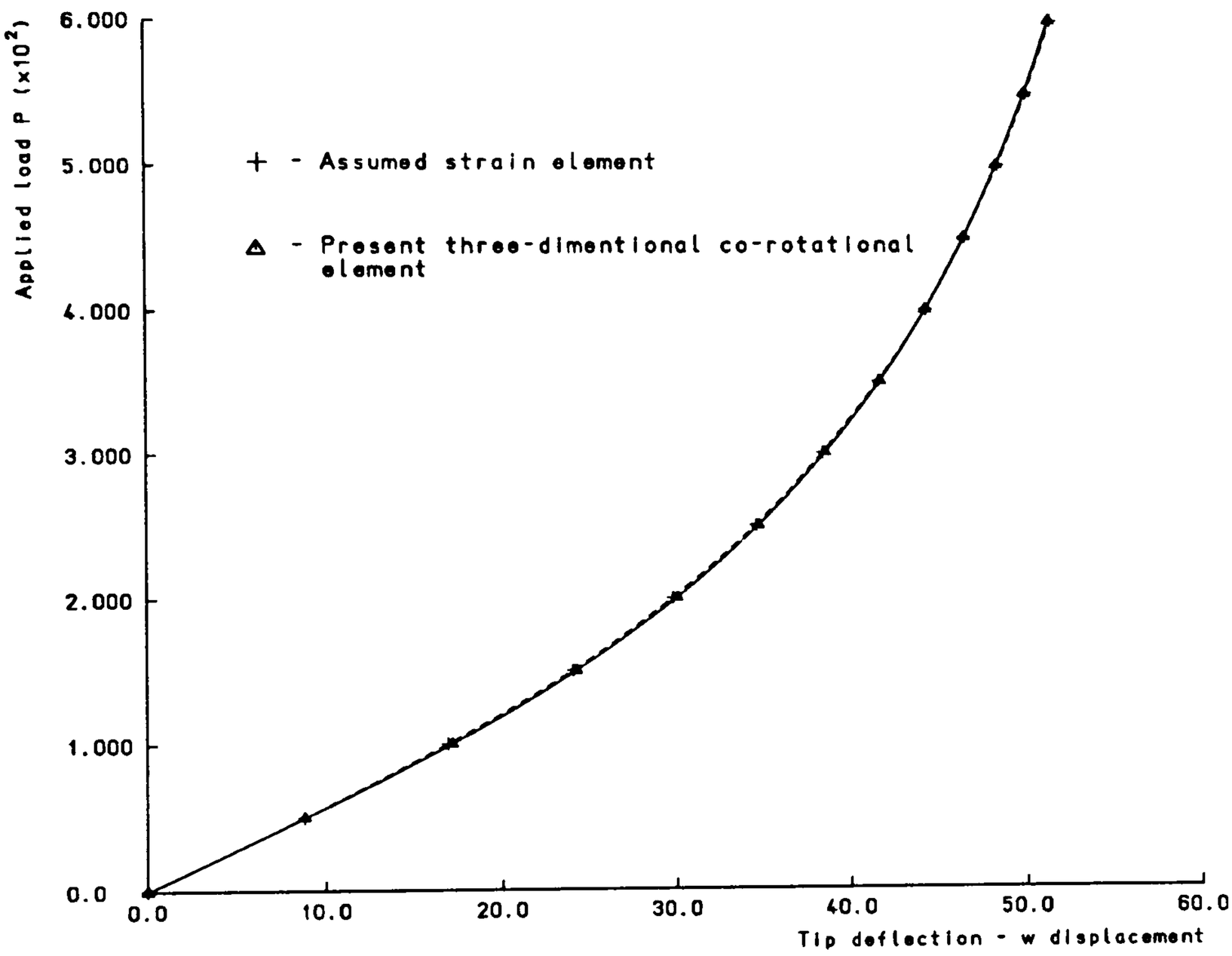


Figure 6.10: Three-dimensional curvilinea beam - Non-dimensional tip deflection vs. load factor ($\nu = 0.49$)

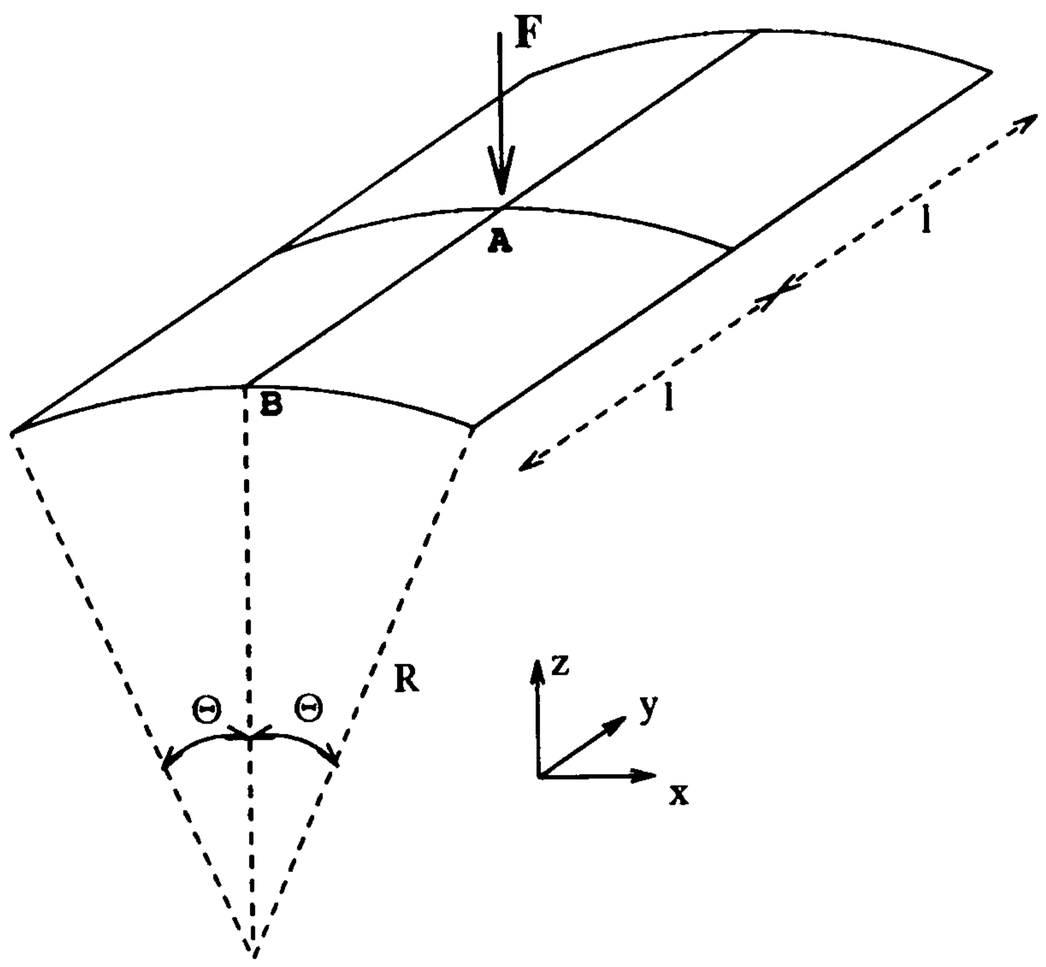


Figure 6.11: Cylindrical shell under a point load

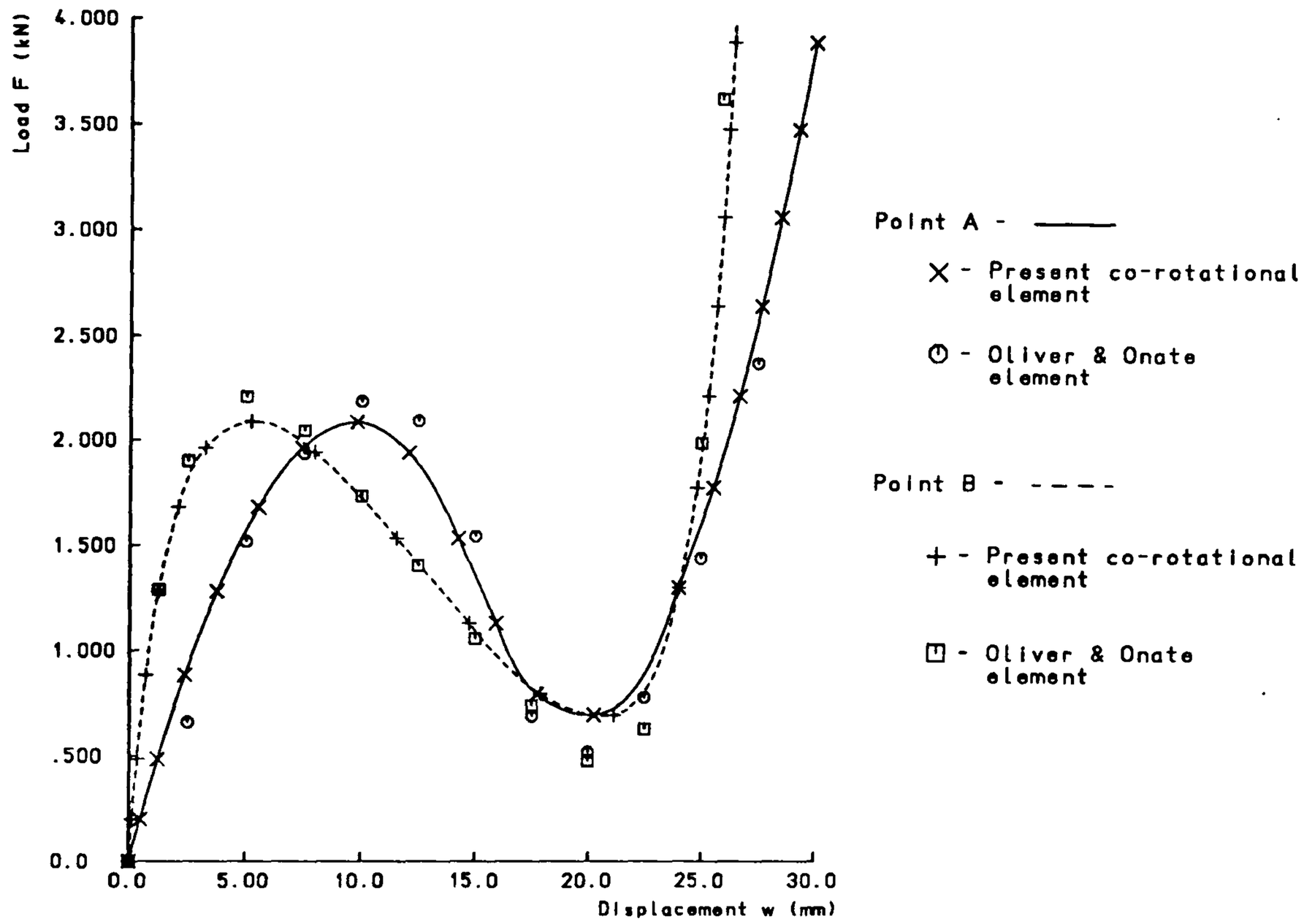


Figure 6.12: Cylindrical shell under a point load - Load vs. displacement curve (thickness $t = 12.7mm$)

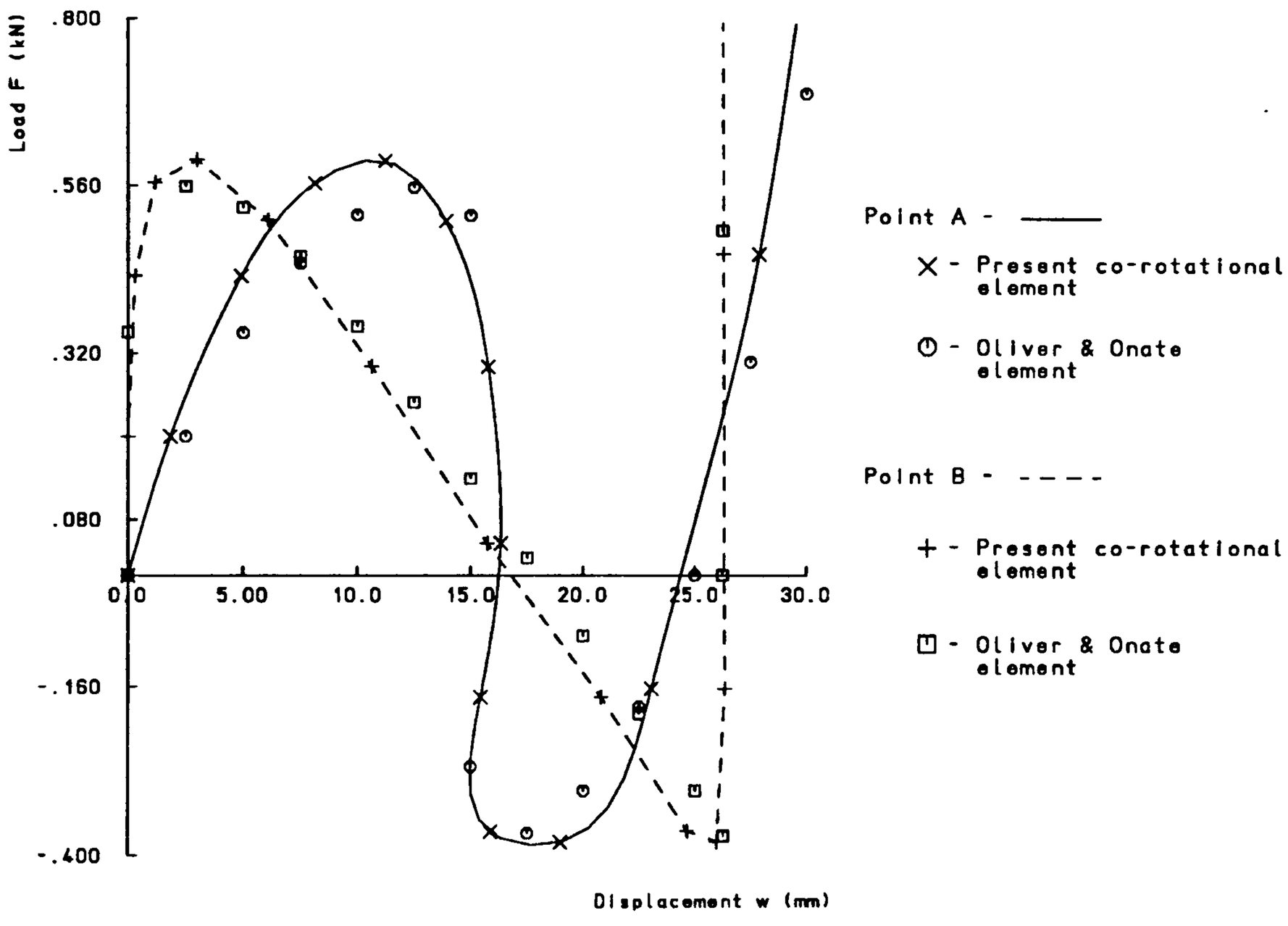


Figure 6.13: Cylindrical shell under a point load - Load vs. displacement curve (thickness $t = 6.35mm$)

Chapter 7

Co-rotational Formulation for Hyperelasticity

7.1 Introduction

In Chapter 2 of this thesis some of the kinematic relationships for hyperelasticity materials have been introduced. They involve the choice of strain measure (consequently, stress tensor) that is convenient to the non-linear procedure to be applied. This chapter is devoted to the application of the two- and three-dimensional elements to large-strain hyperelasticity using the appropriate type of strain/stress measure.

The developments in Chapter 6 were based on the close relationship that was established between the Biot strain and the "local engineering strain" related to the co-rotational formulation. As a consequence, the present hyperelastic work will be directly associated to the Biot stress and strain measures.

In this chapter the derivation of the stress tensors for two different hyperelastic models is described. The developments are presented for both two- and three-dimensions. The procedure used follows closely those introduced for the membrane and for the plane-strain elements of Chapters 3 and 4. The tangential constitutive tensors (or matrices) are also found from the expressions previously devised. These new stresses and tangential modular matrices are used in the co-rotational context and some interesting results are presented. The formulation presented here can be extended and used as the basis for a formulation involving large-strain plasticity.

7.2 Plane-strain analysis

In this chapter we start with the development of a formulation for plane-strain analysis. Due to the fact that for a plane-stress condition the incompressibility issue does not create any additional difficulty for the problem, this kind of analysis will not be addressed in this chapter. Plane-stress problems can be studied by using the formulation given in Chapters 3 and 4 and satisfactory results can be obtained.

If we bring our attention back to the incompressible (or nearly incompressible) behaviour exhibited by most of the hyperelastic or rubberlike materials, we have to face the special problem caused by such a characteristic. Pure incompressibility leads to serious numerical difficulties. This problem of element locking or instability can be partially solved if the relative compressibility of the hyperelastic materials is taken into account. However, the introduction of a volumetric term separated from the deviatoric term into a given material does not solve all of the problems and the convergence of the formulation may still be poor. The co-rotational element by itself cannot handle the incompressibility thus the need for combining the co-rotational formulation and a linear element that works reasonably well with near-incompressibility. In addition, the aim is to overcome the problem of non-convergence associated with the non-linear incompatible element of Chapter 4.

To be able to establish the stress values for the hyperelastic analysis illustrated here, it is necessary to choose a certain strain-energy function. To this end, before defining the hyperelastic model used in most of the developments here, namely the Ogden model, we firstly express the relationships for a simple and more direct "log-based" model. This model is also used to validate the co-rotational formulation for a large-strain analysis that can be regarded as a large-strain patch test for shear deformation, as indicated earlier in Chapter 5.

We will initially consider a pure continuum approach that will be modified later to incorporate the current co-rotational formulation. With this in mind, we adopt the strain-energy function of a hyperelastic model in terms of principal stretches that can be expressed as

$$\varphi = \mu[(\ln \lambda_1)^2 + (\ln \lambda_2)^2 + (\ln \lambda_3)^2] + \frac{1}{2}(k - \frac{2}{3}\mu)(\ln J)^2 \tag{7.1}$$

where $J = \det\mathbf{F} = \lambda_1\lambda_2\lambda_3$ and μ and k are the shear modulus and the bulk modulus, respectively. The approach of (7.1) is known as the Hencky strain-energy function [38]. The principal stretches λ_i can be obtained directly from the right Cauchy-Green tensor

of equation (2.4) which is defined in terms of principal directions of the Lagrangian triad.

The principal stretches could also be obtained via the left Cauchy-Green tensor **B** which gives the stretches in terms of principal directions of the Eulerian triad $\mathbf{n}_1, \mathbf{n}_2, \mathbf{n}_3$, i.e.,

$$\mathbf{B} = \mathbf{F}\mathbf{F}^T = \lambda_1^2 \mathbf{n}_1 \mathbf{n}_1^T + \lambda_2^2 \mathbf{n}_2 \mathbf{n}_2^T + \lambda_3^2 \mathbf{n}_3 \mathbf{n}_3^T = \mathbf{Q}(\mathbf{n})[\mathbf{diag}(\lambda_i^2)]\mathbf{Q}^T(\mathbf{n}) \tag{7.2}$$

The above definition can be used if we want to find the Kirchhoff stress which is related to the current configuration, so that,

$$\boldsymbol{\tau} = \tau_1 \mathbf{n}_1 \mathbf{n}_1^T + \tau_2 \mathbf{n}_2 \mathbf{n}_2^T + \tau_3 \mathbf{n}_3 \mathbf{n}_3^T = \mathbf{Q}(\mathbf{n})[\mathbf{diag}(\tau_i)]\mathbf{Q}^T(\mathbf{n}) \tag{7.3}$$

Here τ_i are the principal components of the Kirchhoff tensor $\boldsymbol{\tau}$. This stress measure is relevant due to the necessity of expressing the final stresses in a more conventional way. This topic will be further investigated later. In this section, however, we will concentrate on obtaining the Biot stress tensor.

Following the developments of Chapter 2, we know that for isotropic conditions the principal directions of stress and strain coincide. Therefore, the Biot stress tensor can be written in the same manner as the Biot strain tensor of equation (2.21). Hence, we write

$$\begin{aligned} \boldsymbol{\sigma}_b &= \sigma_{b1}\, \mathbf{N}_1 \mathbf{N}_1^T + \sigma_{b2}\, \mathbf{N}_2 \mathbf{N}_2^T + \sigma_{b3}\, \mathbf{N}_3 \mathbf{N}_3^T \\ &= \mathbf{Q}(\mathbf{N})[\mathbf{diag}\, \sigma_{bi}]\mathbf{Q}^T(\mathbf{N}) \end{aligned} \tag{7.4}$$

where $[\mathbf{diag}\, \sigma_{bi}]$ is the diagonal matrix containing the principal values of σ_{bi} which can be found from the differentiation of the strain-energy function with respect to the principal strains. In a straightforward manner (see equation (2.24)), we have

$$\sigma_{bi} = \frac{\partial \varphi}{\partial E_{bi}} \tag{7.5}$$

where E_{bi} are the principal values of the Biot strain.

Using continuum mechanics definitions, the principal Biot strains are expressed as in (2.21). Thus,

$$E_{bi} = \lambda_i - 1 \tag{7.6}$$

From the above, $\delta E_{bi} = \delta \lambda_i$. Therefore,

$$\sigma_{bi} = \frac{\partial \varphi}{\partial \lambda_i} = \frac{1}{\lambda_i}(k \ln J + 2\mu \ln \bar{\lambda}_i) \tag{7.7}$$

Here $\bar{\lambda}_i$ is given by the same expression as shown before in (2.34).

Following the developments of Chapter 4, from the principal values for stress and strain we can determine the relationship between the incremental stresses and the incremental strains leading to the tangential constitutive matrix for the material. Hence, an equivalent expression to (2.19) in terms of the strain/stress measure used here is

$$\delta \boldsymbol{\sigma}_b = \mathbf{D} : \delta \mathbf{E}_b \tag{7.8}$$

According to (2.20) and (7.8) above in relation to the principal directions, $\mathbf{N}_i$, the $\mathbf{D}$ matrix, for a two-dimensional case, becomes

$$\mathbf{D} = \begin{bmatrix} D_{11} & D_{12} & 0 \\ D_{21} & D_{22} & 0 \\ 0 & 0 & D_{33} \end{bmatrix} \tag{7.9}$$

where,

$$\begin{aligned} D_{11} &= \frac{\partial \sigma_{b1}}{\partial \lambda_1} = \frac{1}{\lambda_1^2}[k(1 - \ln J) + \frac{4}{3}\mu(1 - \frac{3}{2}\ln \bar{\lambda}_1)] \\ D_{22} &= \frac{\partial \sigma_{b2}}{\partial \lambda_2} = \frac{1}{\lambda_2^2}[k(1 - \ln J) + \frac{4}{3}\mu(1 - \frac{3}{2}\ln \bar{\lambda}_2)] \\ D_{12} &= \frac{\partial \sigma_{b1}}{\partial \lambda_2} = D_{21} = \frac{\partial \sigma_{b2}}{\partial \lambda_1} = \frac{1}{J}(k - \frac{2}{3}\mu) \end{aligned} \tag{7.10}$$

$$D_{33} = \frac{(\sigma_{b1} - \sigma_{b2})}{2(E_{b1} - E_{b2})} \tag{7.11}$$

Note that once more the ground state of the shear modulus μ is used when $E_{b1} = E_{b2}$, as for the plain-strain element previously described. This is obtained from the limit

$$\lim_{E_{b1} \to E_{b2}} \frac{(\sigma_{b1} - \sigma_{b2})}{2(E_{b1} - E_{b2})} = \frac{1}{2}(\frac{\partial \sigma_{b1}}{\partial E_{b1}} - \frac{\partial \sigma_{b2}}{\partial E_{b1}}) = \mu \tag{7.12}$$

The final form of the tangential constitutive matrix is obtained by transforming (7.9) back to the global axes using the same transformation matrix of (4.60) and the transformation relation of (4.61). The remaining procedure is equivalent to that already given for the elastic element developed in Chapter 5.

Now we modify the formulation described above in order to include it in the previously defined co-rotational technique. Observe that we have been using the Biot strain tensor that is work-conjugate to the Biot stress. Prior to this computation, it is essential to highlight the fact that because the co-rotational formulation is "Biot-like", although now the formulation does not represent a "pure" Biot approach, from the results of Chapter 6 we should recover a "pure" Biot formulation in the limit as the mesh is refined or, in other words, when the element tend to behave as subjected to a constant stress state.

For the co-rotational approach used here the polar decomposition is only performed at the centroid of the element. Therefore, the stretches obtained at the Gauss point will not exactly in general correspond to those produced by a 'proper' $\mathbf{F} = \mathbf{RU}$ decomposition. However, for a general case reasonable results are still achieved. The aforementioned affirmation is endorsed via some of the problems analysed. A direct comparison for a plane-strain analysis between the co-rotational technique and the non-linear total Lagrangian formulation of Chapter 4 shows that in spite of not following a Gauss point by Gauss point procedure, the former results in a much more robust approach, especially owing to the fact that the latter fails to converge for the majority of the hyperelastic examples tested here. Nevertheless, before the element of Chapter 4 fails, both formulations give comparable responses.

From the developments of Chapter 6, the principal directions to be used here are obtained via the local engineering strain that can be computed in a standard way from the local displacements as indicated earlier in this thesis. This leads to an expression of the form

$$\boldsymbol{\epsilon}_l = \epsilon_{l1}\, \mathbf{a}_1\mathbf{a}_1^T + \epsilon_{l2}\, \mathbf{a}_2\mathbf{a}_2^T + \epsilon_{l3}\, \mathbf{a}_3\mathbf{a}_3^T \tag{7.13}$$

where $\epsilon_{li} \simeq E_{bi}$ and E_{bi} is given by (7.6) while $\mathbf{a}_i \simeq \mathbf{N}_i$. The strain tensor $\boldsymbol{\epsilon}_l$ has been defined in (5.32). Equation (7.13) is evaluated using an eigensolver to obtain the principal strains and the principal directions $\mathbf{a}_1, \mathbf{a}_2, \mathbf{a}_3$. The principal local stretches are computed directly from (7.6). Accordingly, the local stresses σ_{li} can then be calculated using (7.7) with $\sigma_{li} \simeq \sigma_{bi}$ and the tensor $\boldsymbol{\sigma}_l \simeq \boldsymbol{\sigma}_b$ comes from (7.4) with $\mathbf{a}_i$ instead of $\mathbf{N}_i$.

At this stage we re-visit Ogden's strain-energy function introduced in the second chapter. Equation (2.41) represents the compressible approximation for the Ogden model.

The differentiation of φ of (2.41) with respect to the principal stretches yields

$$\sigma_{b1} = \frac{1}{3\lambda_1}\sum_p \mu_p J^{-\frac{\alpha_p}{3}}(2\lambda_1^{\alpha_p} - \lambda_2^{\alpha_p} - 1) + k(J-1)\lambda_2 \tag{7.14}$$

$$\sigma_{b2} = \frac{1}{3\lambda_2}\sum_p \mu_p J^{-\frac{\alpha_p}{3}}(2\lambda_2^{\alpha_p} - \lambda_1^{\alpha_p} - 1) + k(J-1)\lambda_1 \tag{7.15}$$

Again here we need to place the stresses in the system directions using (7.4) with $\mathbf{a}_i$ replacing $\mathbf{N}_i$.

It should be emphasised at this point that, for output purpose, because the local Biot-type stresses calculated in the above are not easy to be visualised, they should be converted into a more conventional "global" stress measure. One possibility is to employ the Kirchhoff stresses defined in (2.8) or in (7.3). They can be obtained through the following approximation: from a pure continuum mechanics point of view the Kirchhoff stress can be evaluated via (7.3). Using the definitions $\tau_i = \lambda_i\,\sigma_{bi}$ and $\mathbf{R} = \mathbf{Q}(\mathrm{n})\mathbf{Q}^T(\mathrm{N})$, we can write

$$\begin{aligned}\boldsymbol{\tau} &= \mathbf{Q}(\mathrm{n})\mathbf{Q}^T(\mathrm{N})\mathbf{Q}(\mathrm{N})[\mathbf{diag}\,\tau_i]\mathbf{Q}^T(\mathrm{N})\mathbf{Q}(\mathrm{N})\mathbf{Q}^T(\mathrm{n}) \\ &= \mathbf{R}\mathbf{Q}(\mathrm{N})[\mathbf{diag}\,(\lambda_i\,\sigma_{bi})]\mathbf{Q}^T(\mathrm{N})\mathbf{R}^T = \mathbf{R}\,[\sigma_b\mathbf{U}]\,\mathbf{R}^T\end{aligned} \tag{7.16}$$

The last part of (7.16) is obtained from

$$\mathbf{U} = \mathbf{Q}(\mathrm{N})[\mathbf{diag}\,\lambda_i]\mathbf{Q}^T(\mathrm{N}) \tag{7.17}$$

and (7.4).

If we recall equation (2.21) (using the approximation for the local engineering strain which gives $\mathbf{U} = \mathbf{I} + \boldsymbol{\epsilon}_l$) and the rotation matrix $\mathbf{R}$ at the centroid, we can finally reach an approximation for the value of $\boldsymbol{\tau}$, that is,

$$\boldsymbol{\tau} = \mathbf{R}_c[\boldsymbol{\sigma}_l(\mathbf{I} + \boldsymbol{\epsilon}_l)]\mathbf{R}_c^T \tag{7.18}$$

The Kirchhoff stress computed in this manner recovers its exact solution when a homogeneous stress state is imposed upon the element.

From the differentiation of the principal stress, we can compute the components of the tangential constitutive matrix for the Ogden model. Hence, in relation to the principal directions,

$$D_{11} = \frac{\partial\sigma_{b1}}{\partial\lambda_1} = \frac{1}{3\lambda_1^2}\sum_p \mu_p J^{-\frac{\alpha_p}{3}}[(\frac{4}{3}\alpha_p - 2)\lambda_1^{\alpha_p} + (\frac{\alpha_p}{3} + 1)(\lambda_2^{\alpha_p} + 1)] + k\lambda_2^2$$

$$
\begin{aligned}
D_{22} &= \frac{\partial \sigma_{b2}}{\partial \lambda_2} = \frac{1}{3\lambda_2^2} \sum_p \mu_p J^{-\frac{\alpha_p}{3}} [(\frac{4}{3}\alpha_p - 2)\lambda_2^{\alpha_p} + (\frac{\alpha_p}{3} + 1)(\lambda_1^{\alpha_p} + 1)] + k\lambda_1^2 \\
D_{12} &= \frac{\partial \sigma_{b1}}{\partial \lambda_2} = D_{21} = \frac{\partial \sigma_{b2}}{\partial \lambda_1} = \\
&= \frac{1}{9\lambda_1\lambda_2} \sum_p \mu_p \alpha_p J^{-\frac{\alpha_p}{3}} [1 - 2(\lambda_1^{\alpha_p} + \lambda_2^{\alpha_p})] + k(2J - 1)
\end{aligned}
\tag{7.19}
$$

D_{33} is the same as given for the Hencky model in equation (7.10.d). It is again necessary here to place the tangential modular matrix related to the principal directions back into the original system via (4.61).

7.3 Three-dimensional analysis

In this section we explore the three-dimensional element with hyperelasticity. Only the Ogden model will be used here although the Hencky model could be utilised for the element.

The incompressible behaviour of most hyperelastic materials also deserves considerable attention when a three-dimensional study is taking place. The same problems encountered under plane-strain conditions will occur for a solid-type analysis. In Chapter 6 we have shown that the three-dimensional incompatible modes element performs very well for near-incompressibility ($\nu \rightarrow 0.5$). We now apply the same element to extend the formulation to encompass non-linear hyperelasticity via a co-rotational technique. More recent developments (e.g. Andelfinger and Ramm in [5]) bring even more efficient elements to treat near-incompressibility which could be easily incorporated into the current formulation by simply replacing the existing linear element by its new counterpart. However, in the present work we will restrict ourselves to the incompatible modes element described earlier.

It has already been observed that the full incompressibility, besides leading to bad response, causes locking of the elements, especially in problems where significant compression is being imposed. The introduction of a strict separation in the stress field where the volumetric part is independent from the deviatoric part have been used and good predictions of the deformations in a given structure have been achieved. Nonetheless, it is still a difficult task to precisely choose an appropriate value for the bulk modulus for a hyperelastic body that correctly represents its near-incompressibility.

This bulk modulus strongly influences the whole analysis due to numerical difficulties it can impose. This problem does not only affect the three-dimensional solutions but it is also very important for the plane-strain case studied earlier. The effects originated by the use of different rates for bulk modulus and shear modulus can be seen in a more comprehensive way in the examples shown subsequently.

To begin the derivations, the principal stresses computed via (7.5) are given for a general three-dimensional case in a neater form as

$$\sigma_{bi} = \frac{1}{3\lambda_i}\sum_p \mu_p J^{-\frac{\alpha_p}{3}}(2\lambda_i^{\alpha_p} - \lambda_j^{\alpha_p} - \lambda_k^{\alpha_p}) + \frac{1}{\lambda_i}kJ(J-1) \tag{7.20}$$

with cyclic permutation of 1, 2 and 3 for the subscript i, j and k. The principal stresses for a plane-strain condition (as in (7.14) and (7.15)) can be easily recovered from (7.20) by setting $\lambda_3 = 1$. Once more the principal stresses have to be transformed through (7.4) to be placed back into the element base frame using the principal directions obtained for the principal strains (isotropic material).

The stress-strain relation can be established. We return to equation (7.8) to define the three-dimensional **D** matrix which can be expressed as

$$\mathbf{D} = \begin{bmatrix} D_{11} & D_{12} & D_{13} & 0 & 0 & 0 \\ D_{21} & D_{22} & D_{23} & 0 & 0 & 0 \\ D_{31} & D_{32} & D_{33} & 0 & 0 & 0 \\ 0 & 0 & 0 & D_{44} & 0 & 0 \\ 0 & 0 & 0 & 0 & D_{55} & 0 \\ 0 & 0 & 0 & 0 & 0 & D_{66} \end{bmatrix} \tag{7.21}$$

where the upper 3×3 matrix can be written compactly as

$$D_{ii} = \frac{\partial \sigma_{bi}}{\partial \lambda_i} = \frac{1}{3\lambda_i^2}\sum_p \mu_p J^{-\frac{\alpha_p}{3}}[(\frac{4}{3}\alpha_p - 2)\lambda_i^{\alpha_p} + (\frac{\alpha_p}{3}+1)(\lambda_j^{\alpha_p} + \lambda_k^{\alpha_p})] + \frac{1}{\lambda_i^2}kJ^2 \tag{7.22}$$

$$D_{ij} = \frac{\partial \sigma_{bi}}{\partial \lambda_j} = \frac{1}{9\lambda_i\lambda_j}\sum_p \mu_p \alpha_p J^{-\frac{\alpha_p}{3}}[\lambda_k^{\alpha_p} - 2(\lambda_i^{\alpha_p} + \lambda_j^{\alpha_p})] + \frac{1}{\lambda_i\lambda_j}kJ(2J-1)$$

and $D_{ji} = D_{ij}$. The subscript i, j and k are a cyclic permutation of 1, 2 and 3. For the shear components, we have

$$D_{44} = \frac{(\sigma_{b1} - \sigma_{b2})}{2(E_{b1} - E_{b2})}$$

$$D_{55} = \frac{(\sigma_{b1} - \sigma_{b3})}{2(E_{b1} - E_{b3})} \tag{7.23}$$

$$D_{66} = \frac{(\sigma_{b2} - \sigma_{b3})}{2(E_{b2} - E_{b3})}$$

Each component of shear in the **D** matrix should be replaced by the ground state of the shear modulus for the material when the value for the denominator of (7.23.a), (7.23.b) or (7.23.c) is zero, as in equation (7.12).

If we rewrite the expression for the tangential constitutive relation in a tensor form, we have

$$\sigma_{bij} = D_{ijkl} E_{bkl} \tag{7.24}$$

Now, by transforming **D** back to the system frame using the standard tensor transformation of co-ordinates [21] we obtain

$$D^t_{ijkl} = Q_{ia} Q_{jb} Q_{kc} Q_{ld} D_{abcd} \tag{7.25}$$

The tensor D^t_{ijkl} corresponds to the 6×6 matrix **D** to be used in the co-rotational calculations.

The tensor transformation above corresponds to the more conventional matrix transformation shown for the two-dimensional case using the principal directions $\mathbf{N}_1$, $\mathbf{N}_2$ in the matrix form **R** with components *sin* and *cos* (see (4.60)) via (4.61).

Note: Towards the end of this work the author became aware of a paper by Wriggers and Reese [99] indicating possible difficulties for the incompatible element when used in large-strains analysis. They pointed out that the problems were associated with rank deficiency for a given class of problems. Although the problem seems not to be affecting the examples shown here, for completeness and awareness an outline of the phenomenon is given in appendix C of this thesis.

7.4 Numerical tests

This section presents a series of tests performed using the two and three-dimensional co-rotational elements with hyperelasticity. They are employed here to verify the suitability of the elements to handle the large strain behaviour of a given structure. Comparisons with the non-linear incompatible formulation of Chapter 4 shows the improvement

obtained and the capabilities of the new approach. The three-dimensional tests also demonstrate the satisfactory results that can be achieved using the new brick element.

7.4.1 Hyperelastic shear deformation of a rectangular block

The first example to be tested here is a rectangular block subjected to a shear deformation. The block is actually analysed using the plane-strain co-rotational element. The idea is to validate the formulation using the concept of the large-strain patch test described in Chapter 5. For such a test we can obtain an analytical solution that will be shown here. Subsequently the finite element results are compared against the results obtained analytically.

Let the element under shear deformation be given by figure 7.1. The displacements in this case are defined as

$$u = Y\,e \quad ; \quad v = 0 \tag{7.26}$$

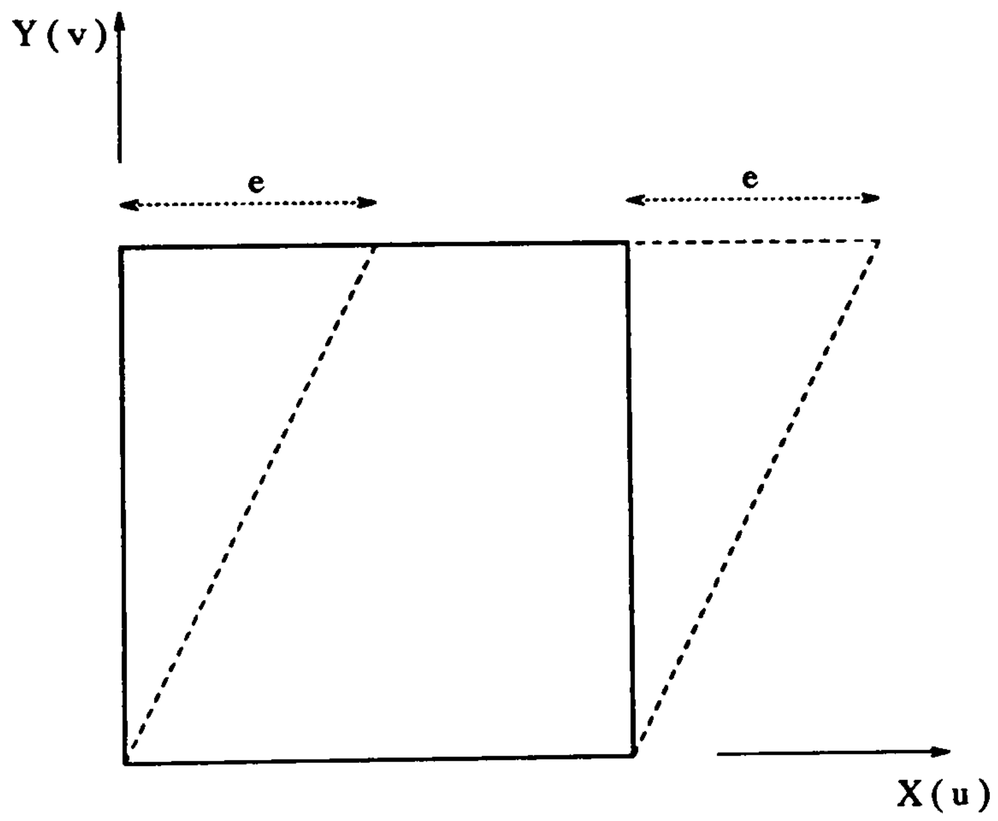


Figure 7.1: Shear deformation of a rectangular block

The displacement-derivative matrix $\mathbf{D}$ is then expressed as

$$\mathbf{D} = \begin{bmatrix} 0 & e \\ 0 & 0 \end{bmatrix} \tag{7.27}$$

Consequently, the deformation gradient is given by

$$\mathbf{F} = \mathbf{I} + \mathbf{D} = \begin{bmatrix} 1 & e \\ 0 & 1 \end{bmatrix} \tag{7.28}$$

From the above we can obtain the left Cauchy-Green tensor of (7.2) as

$$\mathbf{B} = \mathbf{F}\mathbf{F}^T = \begin{bmatrix} 1+e^2 & e \\ e & 1 \end{bmatrix} \tag{7.29}$$

Note that we are working under plane-strain conditions whereby $\lambda_3 = 1$.

The eigenvalues of (7.29) give the squares of the principal stretches. Accordingly,

$$\lambda_1 = \frac{e+\sqrt{e^2+4}}{2} \quad ; \quad \lambda_2 \frac{-e+\sqrt{e^2+4}}{2} \tag{7.30}$$

Using the strain-energy function of (7.1) and considering the material as incompressible ($j = 1$), we can compute the principal Kirchhoff stresses that corresponds, for this case, to the principal components of the Cauchy stress (see equation (2.8)). Hence,

$$\begin{aligned} \tau_1 = \sigma_1 = \lambda_1 \frac{\partial \varphi}{\partial \lambda_1} = 2\mu \ln \lambda_1 \\ \tau_2 = \sigma_2 = \lambda_2 \frac{\partial \varphi}{\partial \lambda_2} = 2\mu \ln \lambda_2 = -2\mu \ln \lambda_1 \end{aligned} \tag{7.31}$$

The second expression can be derived simply by using $\lambda_2 = \lambda_1^{-1}$.

We now require the principal direction in the Eulerian triad to transform the Kirchhoff stress into the base co-ordinate system. To this end, if we define the displacement or the shear strain e as

$$e = 2\,tan\beta \tag{7.32}$$

we can obtain an equivalent expression for (7.29), therefore, the values for the principal stretches are expressed in the form

$$\lambda_1 = \frac{1+s}{c} \quad ; \quad \lambda_2 = \frac{1-s}{c} \tag{7.33}$$

where $s = sin\beta$ and $c = cos\beta$.

The principal directions of the Eulerian triad are the eigenvectors of this new representation of $\mathbf{B}$, i.e.,

$$\begin{aligned} \mathbf{n}_1^T &= \frac{1}{\sqrt{2(1+s)}} \begin{bmatrix} 1+s & c \end{bmatrix} \\ \mathbf{n}_2^T &= \frac{1}{\sqrt{2(1+s)}} \begin{bmatrix} -c & 1+s \end{bmatrix} \end{aligned} \tag{7.34}$$

The Kirchhoff stress tensor can be found directly from the principal directions given above via equation (7.3) for a two-dimensional situation which finally produces an expression:

$$\tau = 2\mu \ln \lambda_1 \begin{bmatrix} s & c \\ c & -s \end{bmatrix} \tag{7.35}$$

The final results entirely agree with those presented by Dienes [24].

For the sake of completeness, using the principal directions of the Lagrangian triad (obtained from (2.4)) and the Eulerian triad from (7.34), we can compute the rotation matrix as

$$\mathbf{R} = \mathbf{Q}(\mathbf{n})\,\mathbf{Q}^T(\mathbf{N}) = \begin{bmatrix} c & s \\ -s & c \end{bmatrix} \tag{7.36}$$

Having computed the analytical expression for the Kirchhoff stress under shear deformation, the normalised Kirchhoff stress (τ/μ) plotted against the displacement e is shown in figure 7.2. The figure illustrates the comparison between the closed-form solution and the current finite element formulation. The two solutions exactly agree which confirms the affirmation made in Chapter 5 that the element successfully passes the large-strain patch test.

7.4.2 Thick-walled cylinder with internal pressure

As a natural consequence of the non-convergence exhibited by the two-dimensional non-linear incompatible element with regard to the cylinder shown in the last example of section 4.5.3, the example is re-examined now using the new co-rotational technique. The characteristics of the cylinder are the same as those shown in figure 4.18 with the material being defined in example 3.4.1. Unlike the previous attempt, the problem does not suffers any drawback and the entire path can be followed. Figure 7.3 depicts the load-deflection curves for the formulation of Chapter 4 (which fails to converge), the results produced by the 'u-p' formulation and the new co-rotational approach. The agreement is perfect.

In the first analysis the material used is the classical Ogden's material with a three-term strain-energy function. Now we change slightly the problem and, besides using the material above, we also use a two-term and a single-term functions and a rubberlike material represented by a Mooney-Rivlin approximation for comparison with the solutions due to Duffett and Reddy [27]. In this case the thickness of the cylinder is

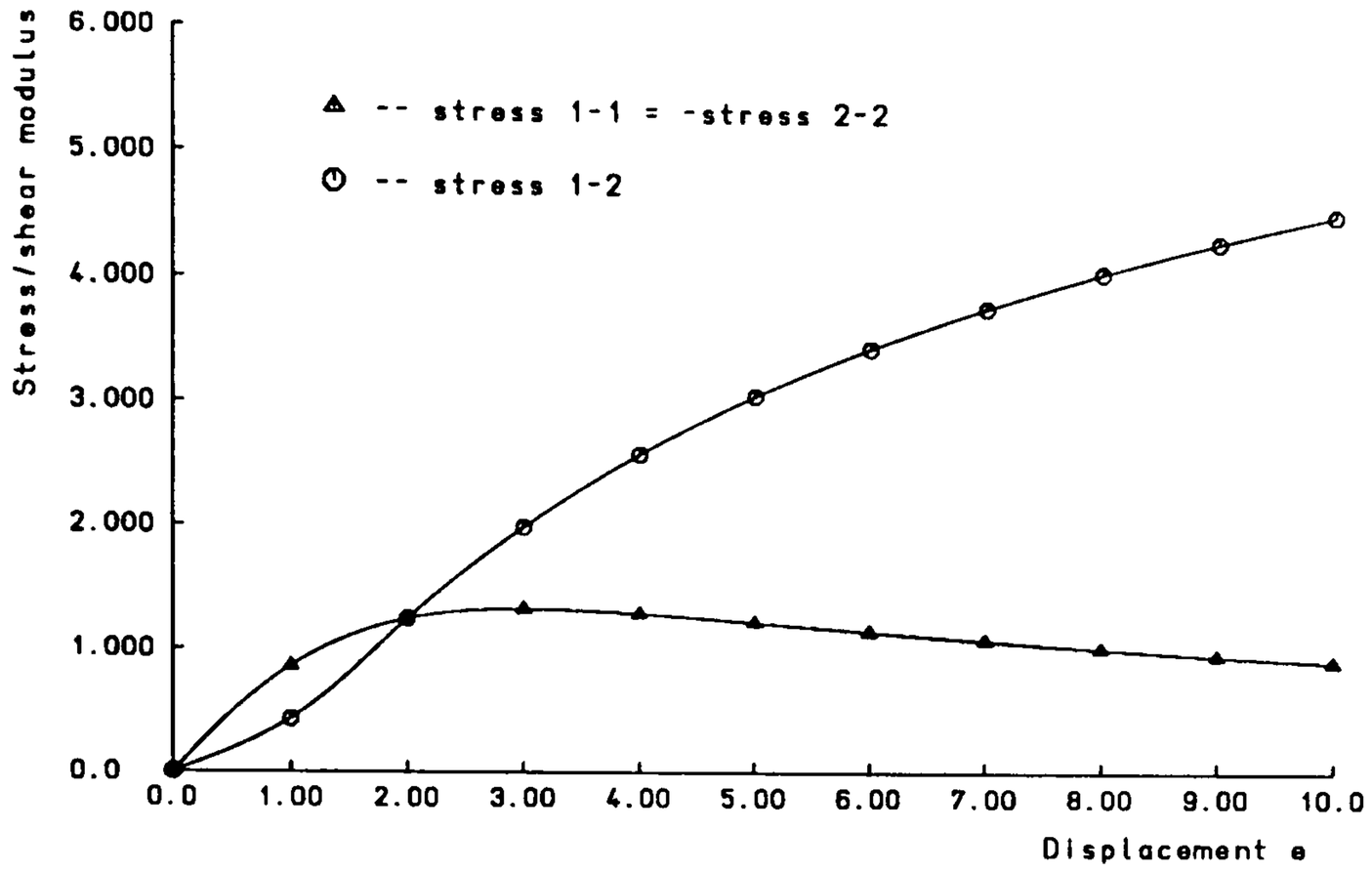


Figure 7.2: Shear deformation - Normalised stress vs. displacement e: ($\triangle$) and ($\bigcirc$) are the analytical solutions for $\tau_{11} = -\tau_{22}$ and τ_{12}, respectively

doubled, i.e., $t = 0.1764$. A follower internal pressure load is used in this example. The curves for the dimensionless pressure (total pressure/ground state of shear modulus) versus the stretch of the inner radius for the various approximations is shown in figure 7.4. Tests have shown that the previous non-linear incompatible formulation (Chapter 4) is not able to analyse this problem either.

Ogden's Material	three-term:	$\mu_1 = 6.3$	$\alpha_1 = 1.3$
		$\mu_2 = 0.012$	$\alpha_2 = 5.0$
		$\mu_3 = -0.1$	$\alpha_3 = -2.0$
	two-term:	$\mu_1 = 6.456$	$\alpha_1 = 1.3$
		$\mu_2 = 0.012$	$\alpha_2 = 5.0$
	one-term:	$\mu_1 = 7.043$	$\alpha_1 = 1.2$
Mooney-Rivlin		$\mu_1 = 4.153$	$\alpha_1 = 2.0$
		$\mu_2 = -0.072$	$\alpha_2 = -2.0$

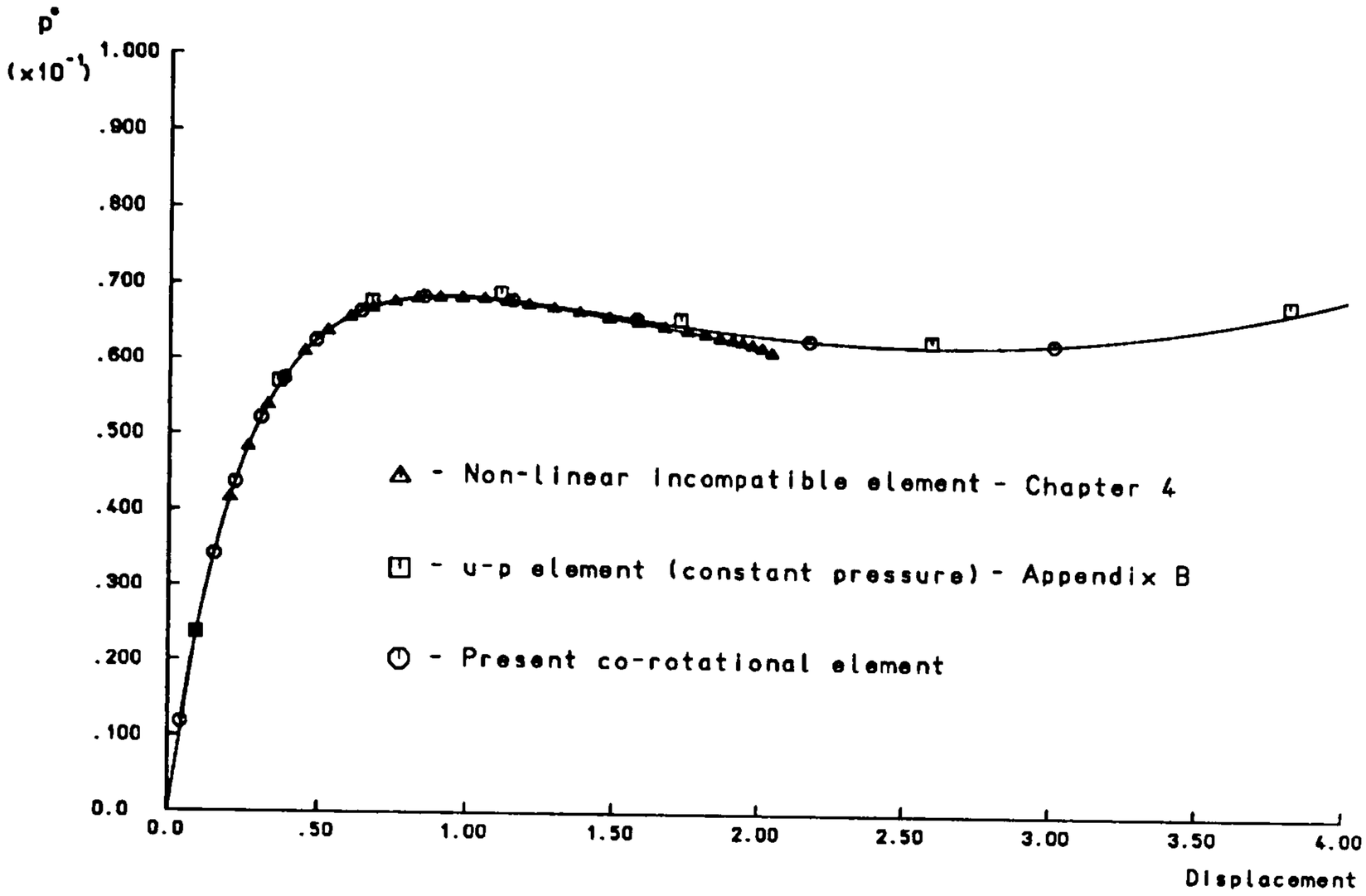


Figure 7.3: Cylinder under Internal Pressure - Load vs. Displacement

7.4.3 Indentation problem

The next example is the analysis of a plane strain block as shown in figure 7.5. This problem has been analysed by Yamada and Kikuchi [100] and presents a geometry with the displacements in the y direction on the bottom and the displacements in the x direction on the sides kept fixed. A uniform displacement representing a rigid plate is imposed on the left half of the free edge (top) as indicated in the figure. The analysis is executed using different formulations and it is terminated when the element fails to converge within the maximum number of iteration set. The problem is basically a compression problem and convergence can become very unstable when the elements are highly deformed. This is especially true when hyperelastic materials are involved. A Mooney-Rivlin model is used to describe the material constitutive model for this rubberlike structure. The constants are $C_1 = 1.5$ and $C_2 = 0.5$. A high value for the

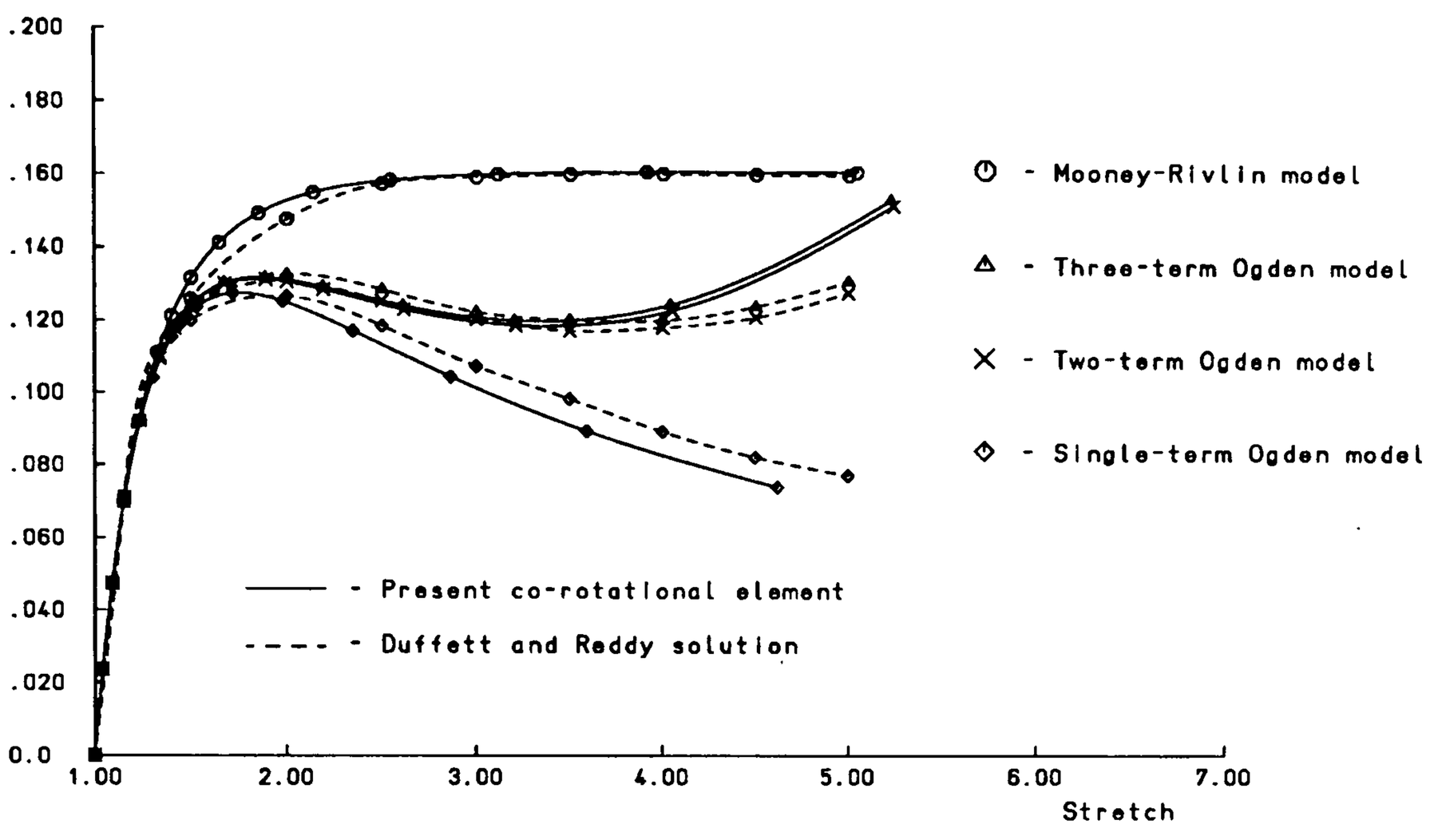


Figure 7.4: Cylinder under Internal Pressure - Load vs. Displacement (Different Materials)

bulk modulus is used to simulate in incompressibility of the problem ($k = 100000$). The model uses an 8×4 mesh but a 16×8 mesh is applied in some cases.

Using the new co-rotational formulation together with the full incompatible modes the problem fails to converge when the uniform displacement imposed is 0.255. This occurs after 51 increments. Although in the results of Yamada and Kikuchi using the so-called arbitrary Lagrangian-Eulerian (ALE) formulation (more details are given below) the deformation can reach 0.506, the present element performs fairly well, as can be seen in figure 7.6. In a second analysis, the problem is analysed employing a more traditional 'u-p' formulation (splitting the volumetric and deviatoric terms). In this case the maximum deformation is 0.24 after 48 increments. We also used the direct non-linear incompatible element developed in Chapter 4. The calculation for this element was terminated when the displacements were 0.164 (65 increments).

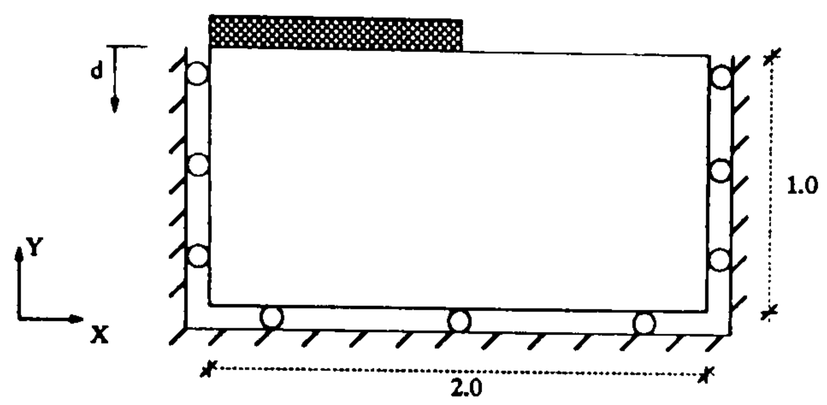


Figure 7.5: Indentation problem

The convergence problems in this sort of problem are closely connected to the ill-conditioning of the solution due to the high value for the bulk modulus. This behaviour can be observed because as we gradually decrease the value of the bulk modulus, the block can actually undergo larger deformations. One way of overcoming the problem is to use the so-called 'augmented Lagrangian technique' whereby the problem with convergence is eliminated by means of a procedure that starts as a penalty function and tends to a Lagrangian multiplier; the technique removes the ill-conditioning associated with the high bulk modulus and the incompressibility constraint. This procedure has successfully been applied by Simo and Taylor in [77].

An alternative solution for the problem is the introduction of the ALE formulation to deal with the incompressibility problem and especially with the strongly distorted mesh observed in some hyperelasticity simulations. The technique has been presented by Yamada and Kikuchi in the aforementioned paper. Their proposal is based on the variation of the geometric mappings for both the material and spatial configurations and on the mixed finite element to avoid the problems with incompressibility.

A plot with the deformed mesh for the co-rotational formulation with the incompatible elements is presented in figure 7.6. The highly deformed elements can be clearly seen in this figure.

In order to demonstrate that the current formulation can adequately analyse the problem if the ill-conditioning is minimised, we re-examine the example using lower bulk moduli, i.e., $k = 1000$ and $k = 100$. With such k values the maximum deflections reached are, respectively, 0.35 and 0.42. Figure 7.7 shows the deformed mesh for $k = 100$ at a displacement of 0.40.

The deformed configuration of figure 7.6 agrees well with the results presented by Yamada and Kikuchi. Even the second figure, with the reduced bulk modulus, also

indicates a reasonable agreement with the results given by the authors above.

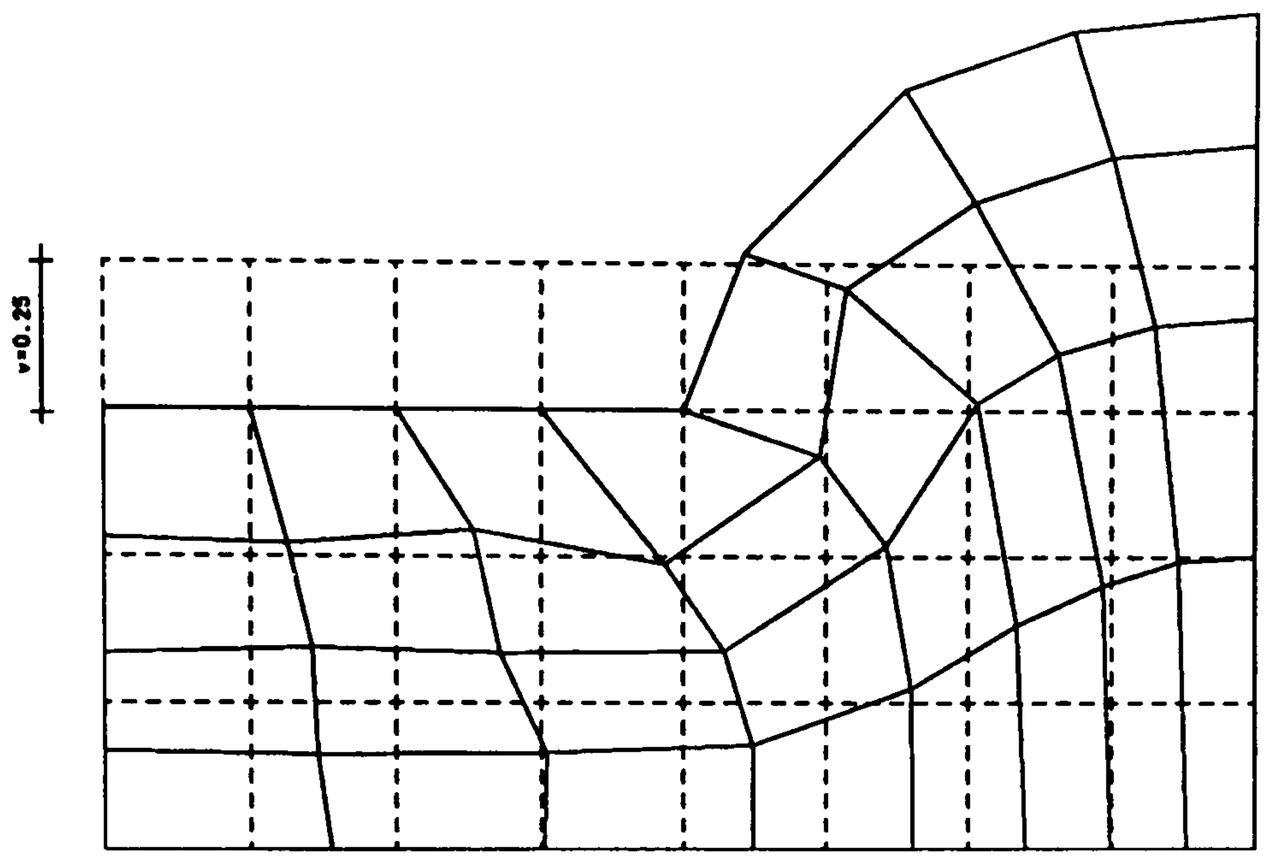


Figure 7.6: Indentation problem - Deformed mesh for Co-rotational formulation

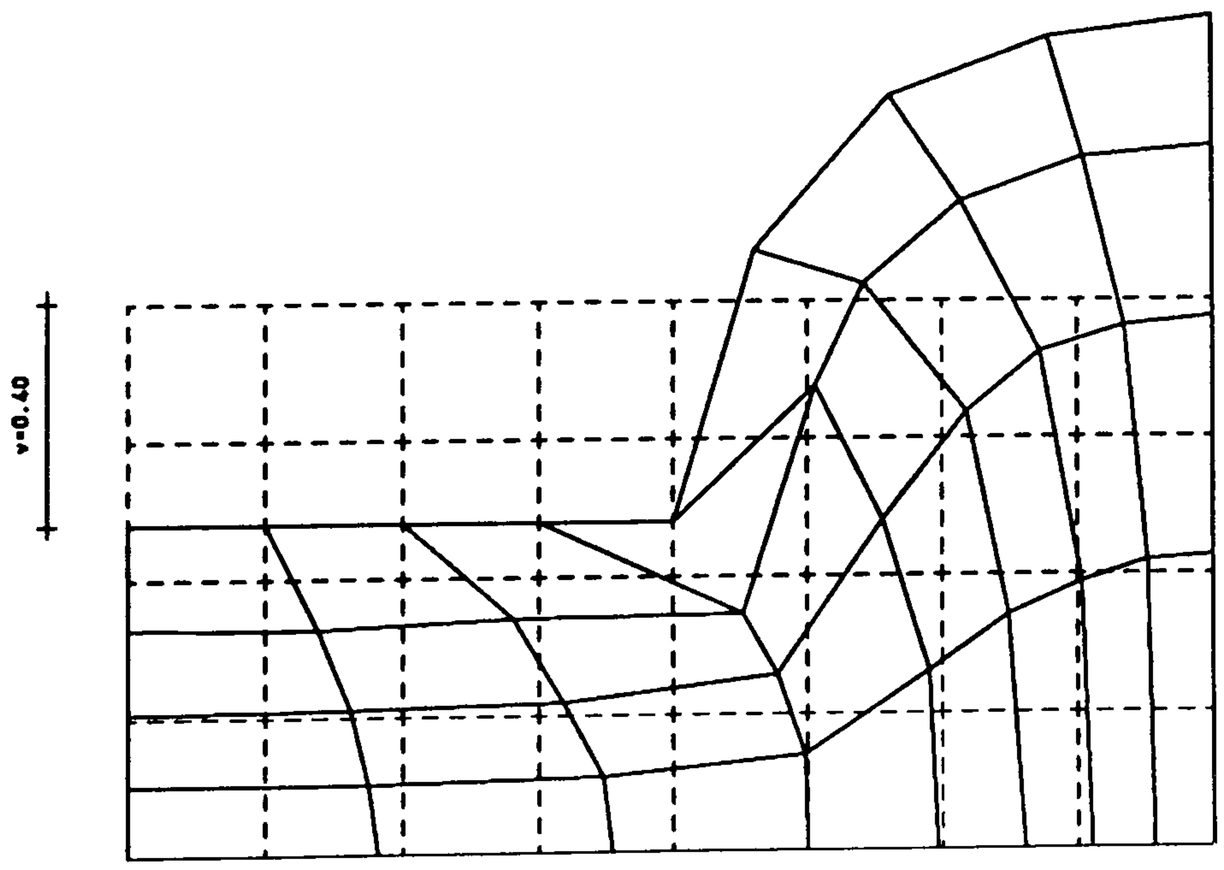


Figure 7.7: Indentation problem - Deformed mesh for Co-rotational formulation ($k = 100$)

[§]Although the formulation reaches a very high level of deformation, the results, particularly the stresses, might not be very accurate especially around the very distorted corner element. An alternative is to use different meshes or an ALE formulation.

7.4.4 Cracked rectangular bar

In this example we study the stretching in plane strain of a cracked square bar with an uniform distributed load applied at one of its end and a partial crack at the other end (figure 7.8). The bar is modelled with a 432-element mesh and uses the same three-term strain-energy function as in the thick cylinder problem above. Using the same technique of the previous example, the bar is loaded (in this case stretched) up to the point where the problem no longer converges. The bar is also analysed using different formulations. The problem is very useful to show the performance of the present formulation in very large stretch situations and particularly the difficulties arising from the incompressible materials.

The new co-rotational formulation applied with incompatible elements presents a maximum displacement of 8.7372 at point A. The stress contour for σ_{22} is shown in the deformed mesh in figure 7.9 which agrees qualitatively with the previous work of Simo and Taylor [77]. However, the maximum stretch obtained for their simulation seems to be larger than the one obtained here (they do not give details about load level in their example). This can be explained because in the strategy used by these authors the incompressible limit is enforced by the use of an augmented Lagrangian procedure, as mentioned in the previous example.

If the same analysis is performed (same load-step size) using the non-linear incompatible formulation developed in Chapter 4, the maximum displacement (before failing to converge) is 0.2275 at the same point A. If a smaller step-size is applied, the non-linear incompatible formulation produces a maximum displacement of 1.2996.

7.4.5 Suspension ring

This examples is concerned with the mechanical behaviour of a suspension ring under internal pressure. The suspension ring can be applied as a seal in certain machines (see reference [13] for more details). In this problem, the working load can be described as an internal gas pressure acting at side ABC of the seal. The ring is analysed using a mesh of 180 four-noded elements. Despite the fact that the ring is an axisymmetric structure, we have used plane-strain elements to model an unit strip of the seal and this appears to be a reasonable approximation. The plane-strain element incorporates the so-called incompatible modes in it formulation and uses the co-rotational technique for the non-linearity. As far as the boundary conditions are concerned, the displacements are prescribed to zero along the side ADE in both directions while the side CGF is fixed only in the horizontal direction. The bottom side CGF can move in the vertical direction

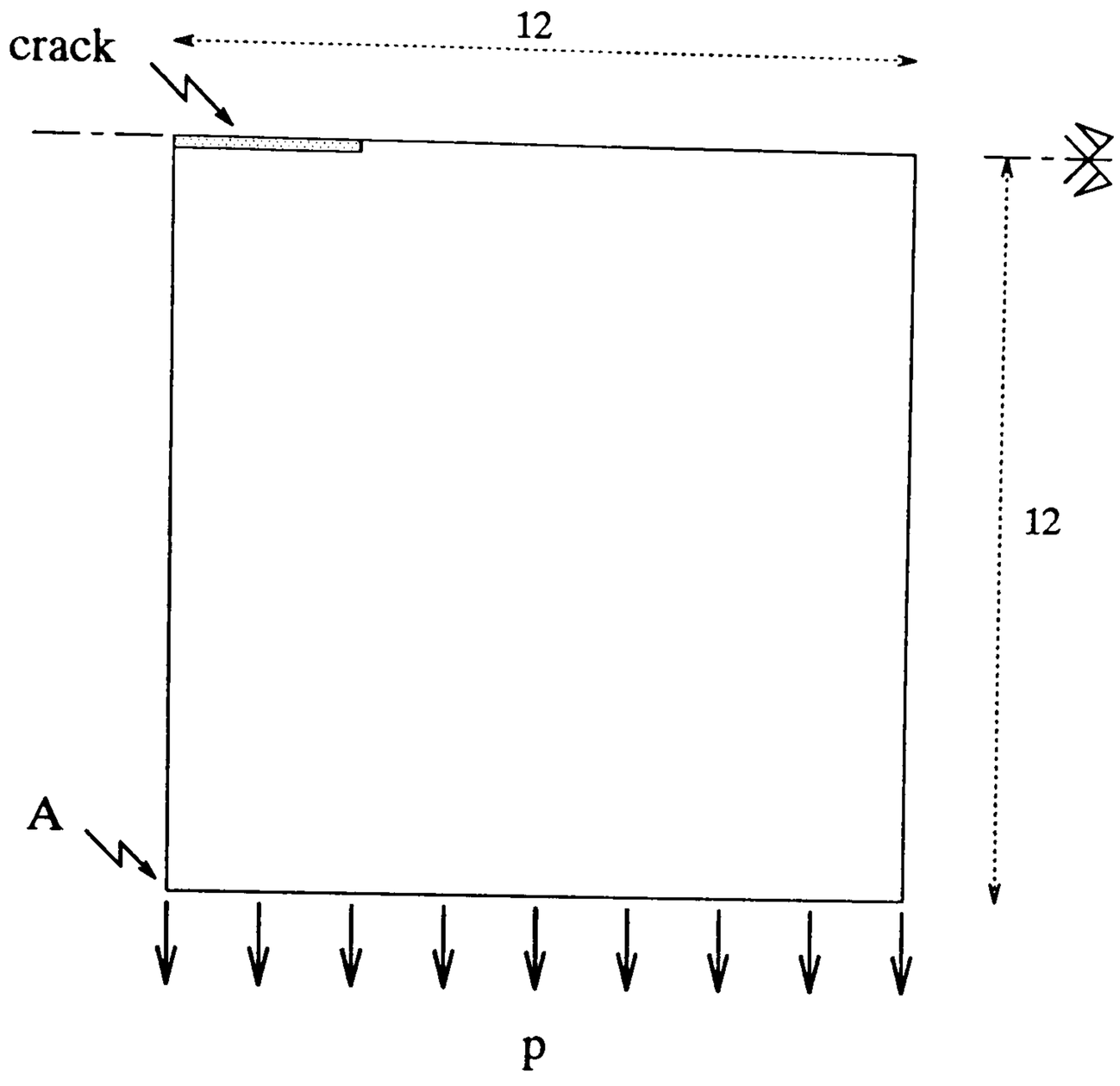


Figure 7.8: Cracked rectangular bar

but only in a rigid way. We use constraints equations to allow for this movement. Figure 7.10 shows the geometry for the structure.

The suspension ring is modelled using a Mooney-Rivlin material with constants $C_1 = 0.4896 N/mm^2$ and $C_2 = 0.1468 N/mm^2$ and to impose a near-impressible condition a bulk modulus of $k = 1000 N/mm^2$ is applied. The approach assumes that the pressure is displacement-dependent and a follower load vector is used. Figure 7.11 below depicts the mesh used and the deformed configuration after 20 increments resulting in a total pressure of $p = 1.12\, NPa$. Observe that the final deformed configuration maintains the circular shape of the inner part of the ring which would not occur if a non-follower load was applied. The shape of the deformed mesh agrees with the results reported by de Borst *et al.* [13] and Bogert [12]. In figure 7.12 the contour for the stress in the y-y direction can be seen. Both the deformed configuration and the stress contour illustrate the good performance of the element in real hyperelastic structures.

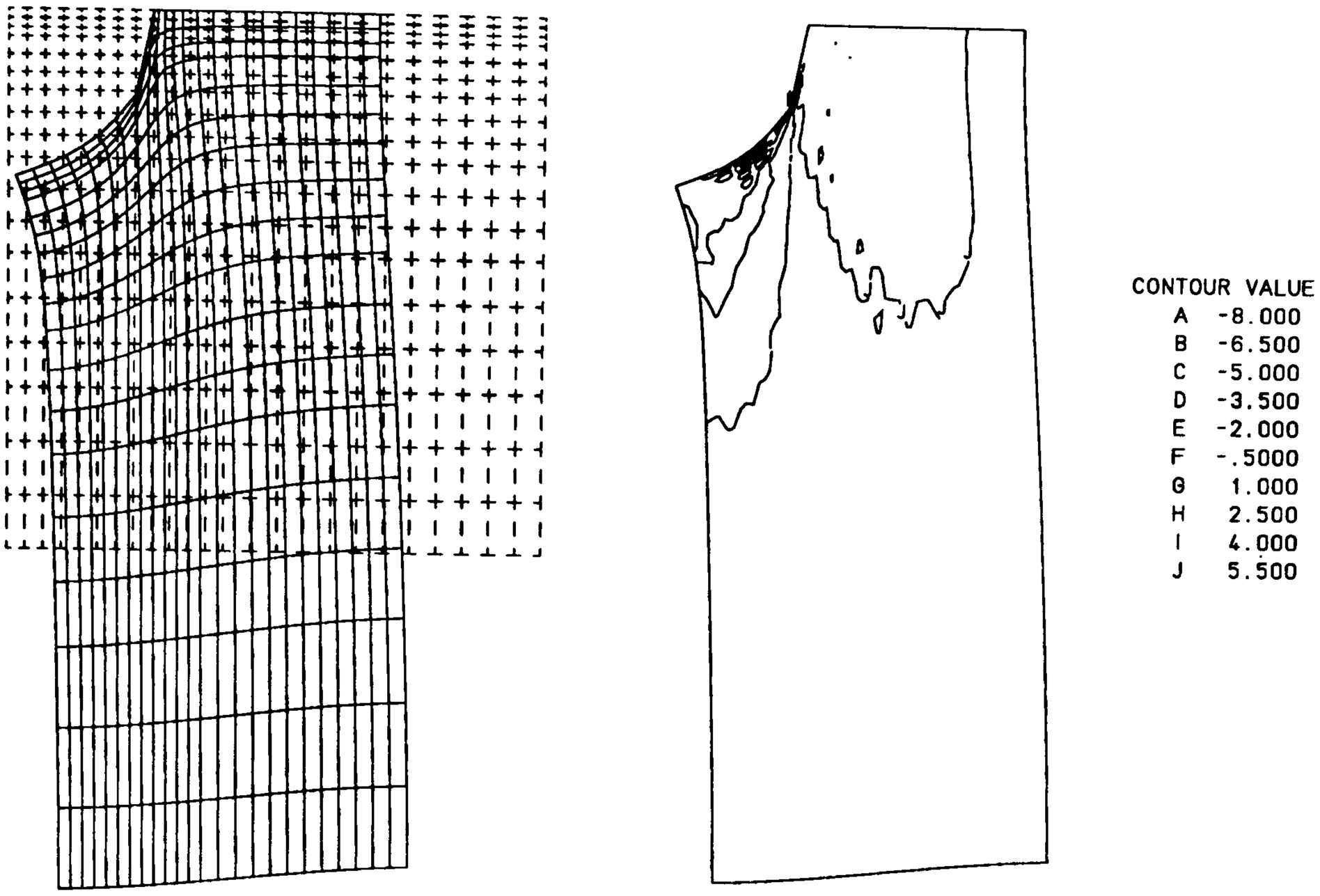


Figure 7.9: Cracked bar - Original and deformed mesh and σ_{22} contour

7.4.6 Thick-cylinder analysed with the three-dimensional element

The inflation of the cylinder presented earlier in example 7.4.2 is again considered. Now we use the problem to test the three-dimensional co-rotational element. The characteristics of the structure are preserved as in the original two-dimensional problem. We use the conventional three-term Ogden model to simulate the rubber-like behaviour. This example provides a verification of the new brick element in large-strain analysis. One and two elements are used to idealise the thickness of the cylinder and the final results are identical. They also accurately agree with the results obtained for the co-rotational 4-noded plane-strain element. The comparison is made with a non-conservative pressure load since the three-dimensional element cannot yet handle follower loads. Figure 7.13 depicts the results for the two-dimensional and three-dimensional elements where dimensionless pressure (normalised by the shear modulus) is plotted against the displacement

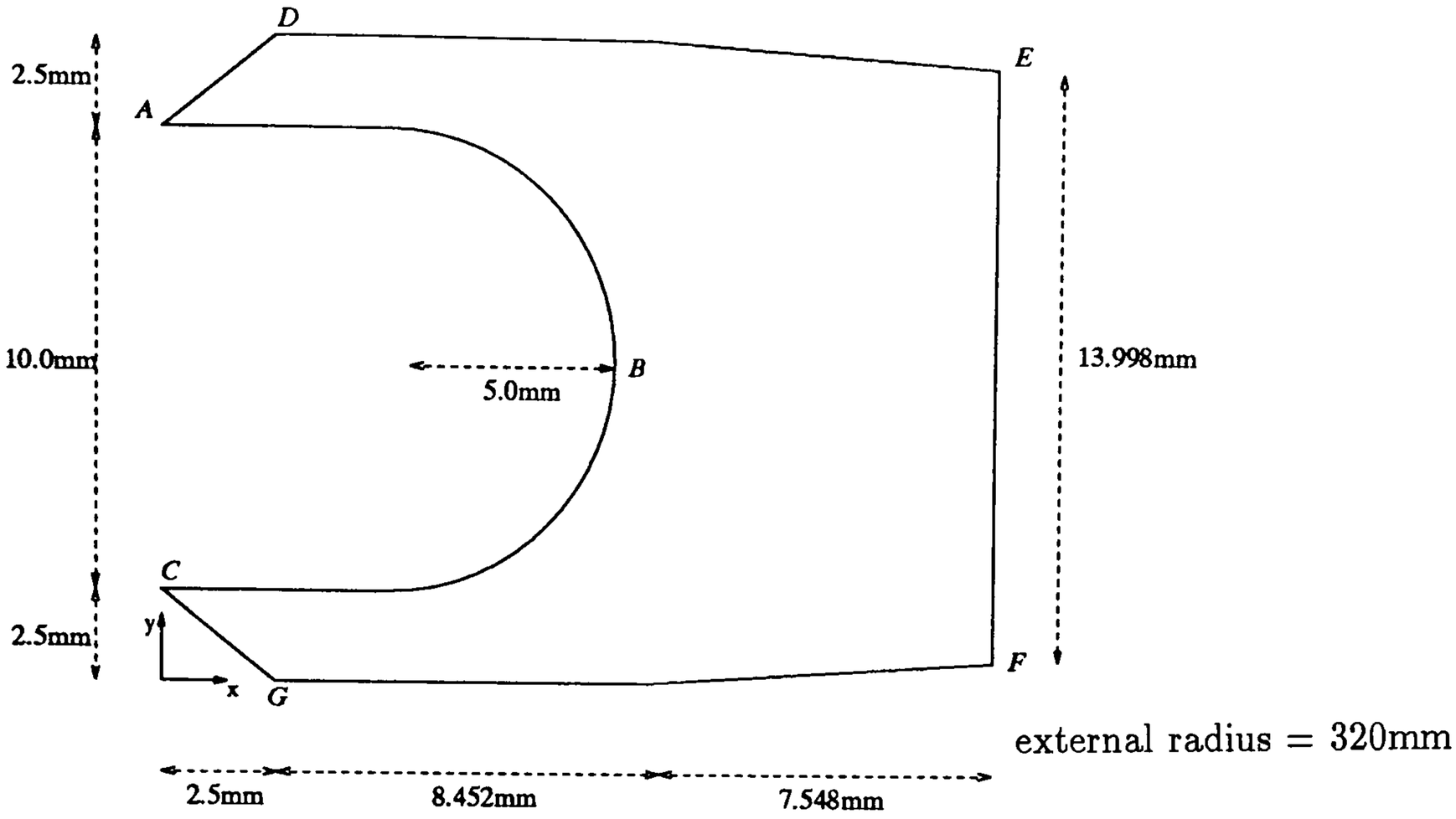


Figure 7.10: Suspension ring

of the internal radius.

7.4.7 Rubber block under compression

The last example to be discussed is a supporting rubber block under compression. This kind of structure is commonly employed as a support in bridges and other structures to avoid direct contact between two rigid parts (concrete and steel, for example) and to absorb impacts. The example uses a Mooney-Rivlin model to simulate the material behaviour. Different values of the bulk modulus have been applied to predict the deformations of the block. The aim of the example is to confirm the effectiveness of the co-rotational element in compressive problems. As already mentioned, converging solution for compression with incompressibility are difficult to obtain even for a low level of compression. Unlike the problems where extensions play the dominant rule and the convergence can be achieved relatively easily, special attention should be paid in order to obtain an adequately converged solution for problems where compression is the main deforming force.

The geometry of the structure can be described as a layered rubber-steel package with a surface area of $200 \times 100mm^2$. The thickness of one rubber layer is $33mm$ (here we will only study one layer). The block is analysed using a 30-element mesh to model one-eighth of the structure due to the symmetry. The block is compressed by applying prescribed uniform displacement on its top surface, while the sides are kept free. The

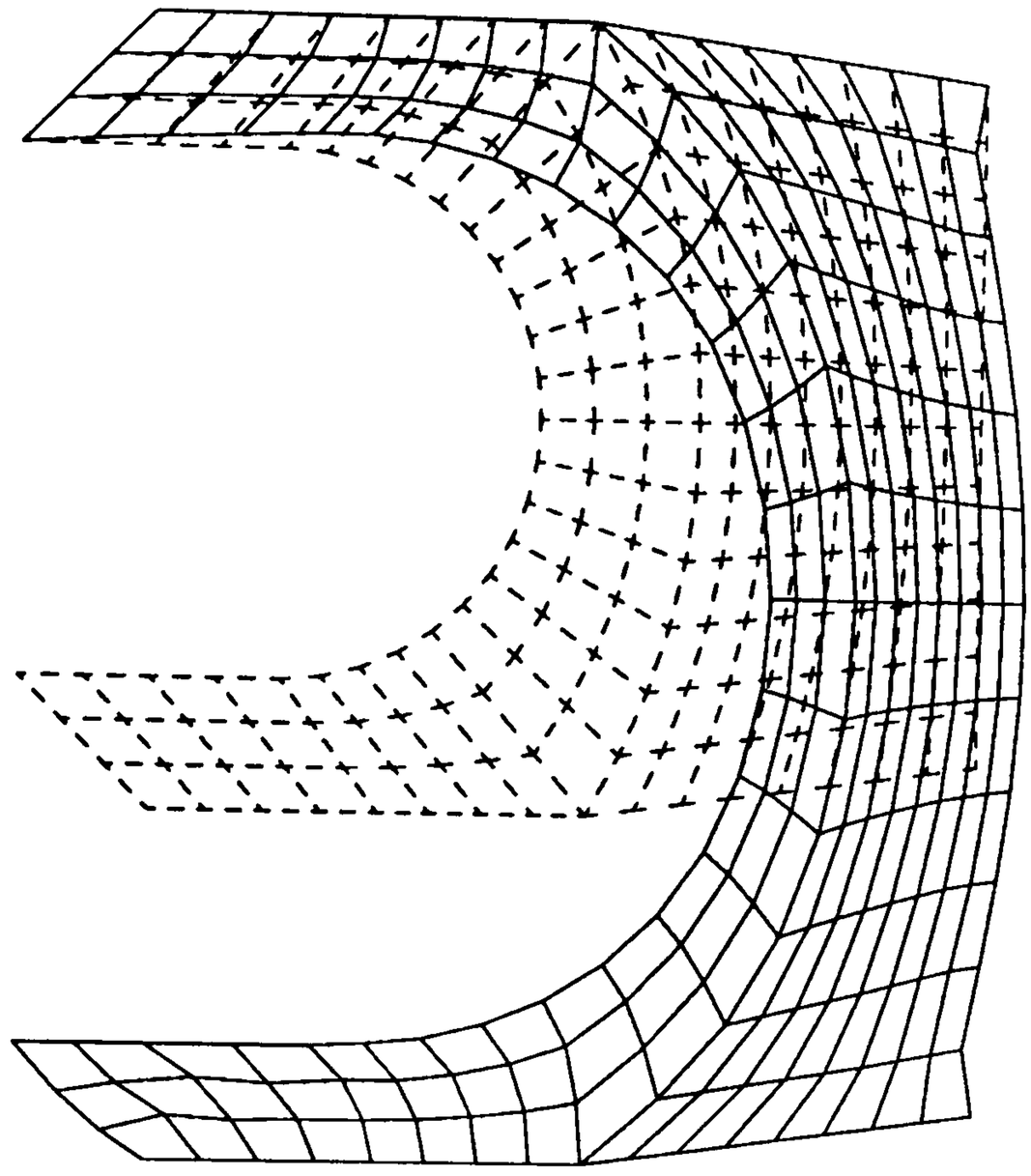


Figure 7.11: Suspension ring - Undeformed and deformed configurations

results are compared with those produced by the twenty-noded brick element with one internal pressure node given in [13]. The load-deflection curves for various values of bulk modulus are shown in figure 7.14 and compared with the results presented in [13]. The results do not agree very well but the analysis with the present co-rotational element shows that for bulk moduli of $k = 100N/mm^2$ and $k = 1000N/mm^2$ the curves obtained tend to the experimental curve, as expected.

In addition to the graph described above, figure 7.15 depicts the relation between the horizontal displacement perpendicular to the mid-point of the shorter side and the vertical displacement of the top surface. The difference between the experimental solution and the other solutions, including those from the present element is explained due to the compressibility of the specimen analysed. According to [13] the volume

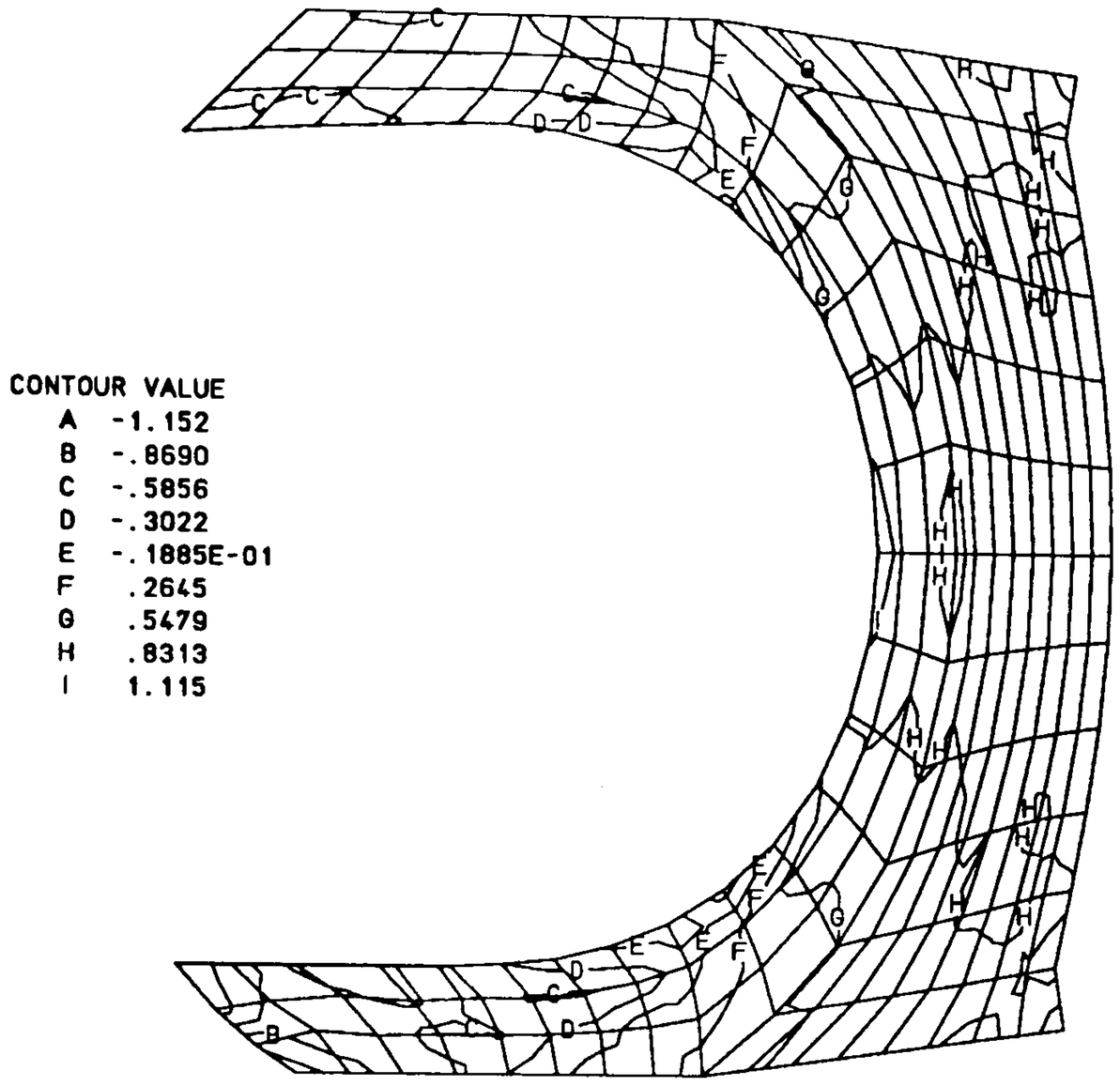


Figure 7.12: Suspension ring - Contour for y-y stress

decrease obtained from the experimental analysis is about 1.2%. To reach the same volume decrease from the analytical estimation we would need a bulk modulus smaller than $k = 100 N/mm^2$ which is consistent with the numerical results evaluated. However, to obtained the combination of a better approximation of the lateral displacement and accurate load/vertical deflection curve it would be necessary to use very low value for the bulk modulus and at the same time very high values for the Mooney-Rivlin constants which, as stated by de Borst *et al.*, are unrealistic. Nevertheless, the example emphasizes the importance of an accurate measurement when an incompressible or near-incompressible material is being studied.

The final results obtained using the new co-rotational element can be regard as

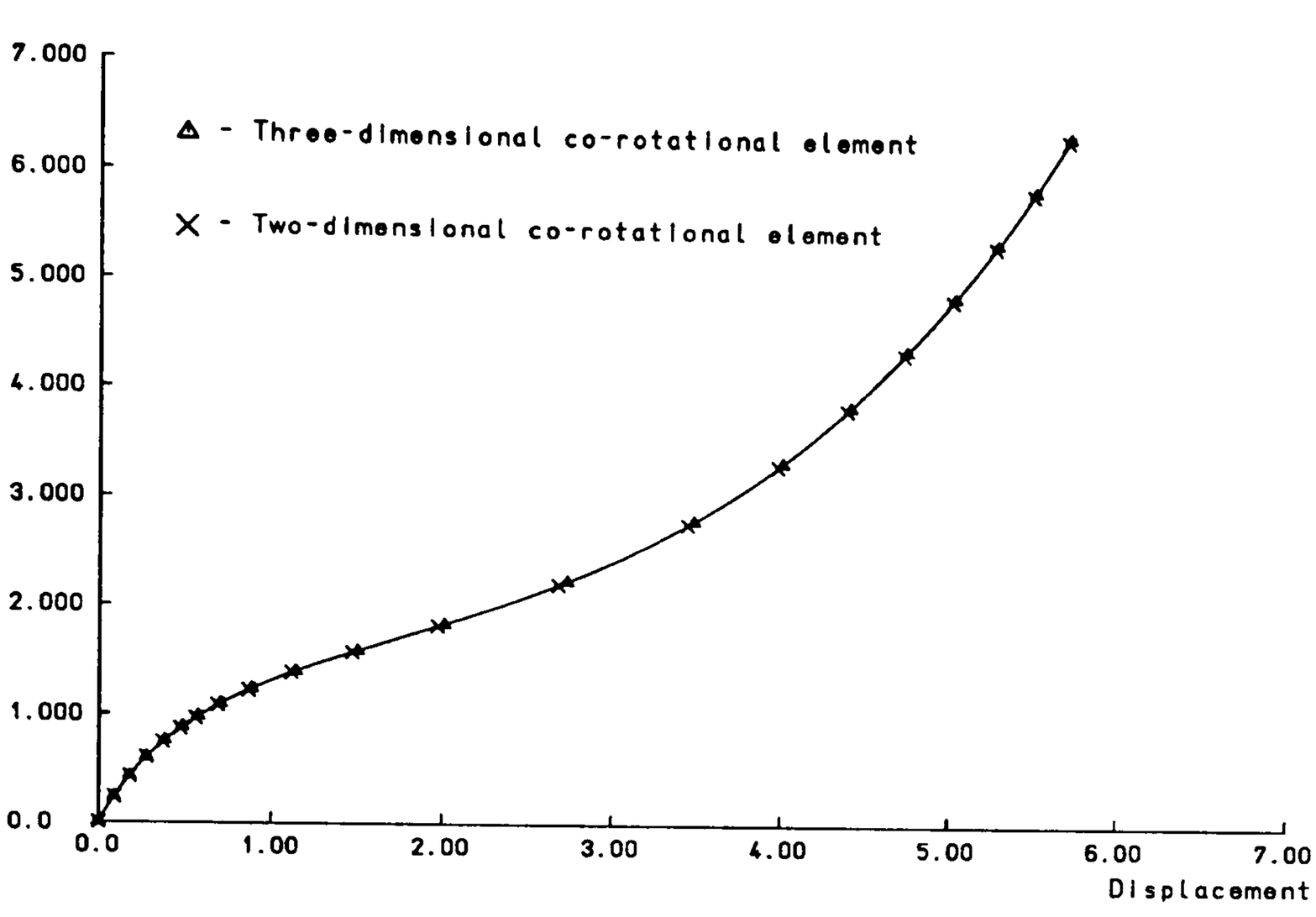


Figure 7.13: Cylinder analysed with three-dimensional elements - dimensionless pressure vs. displacement

satisfactory and agree reasonably with those produced by de Borst *et al.*. However, problems of convergence still affects the present formulation and the maximum displacement the element can handle in this compression test is $4.5mm$ or 13.6% of the total thickness for a bulk modulus of $k = 1000N/mm^2$. Again, the difficulty could be eased by using one of the techniques mentioned earlier in this chapter. Unlike the problems usually present in this sort of analysis, i.e., locking and spurious mechanisms, the current techniques appears to be free of these difficulties, despite the rather coarse mesh used to idealise the block. This smooth response can be observed in figure 7.16 where the original and final mesh at 13.6% deformation are plotted. The termination of the analysis is more due to numerical problems in the iterative process than to the appearance of spurious mechanisms and locking, although the occurrence of locking leads to a poor iterative performance.

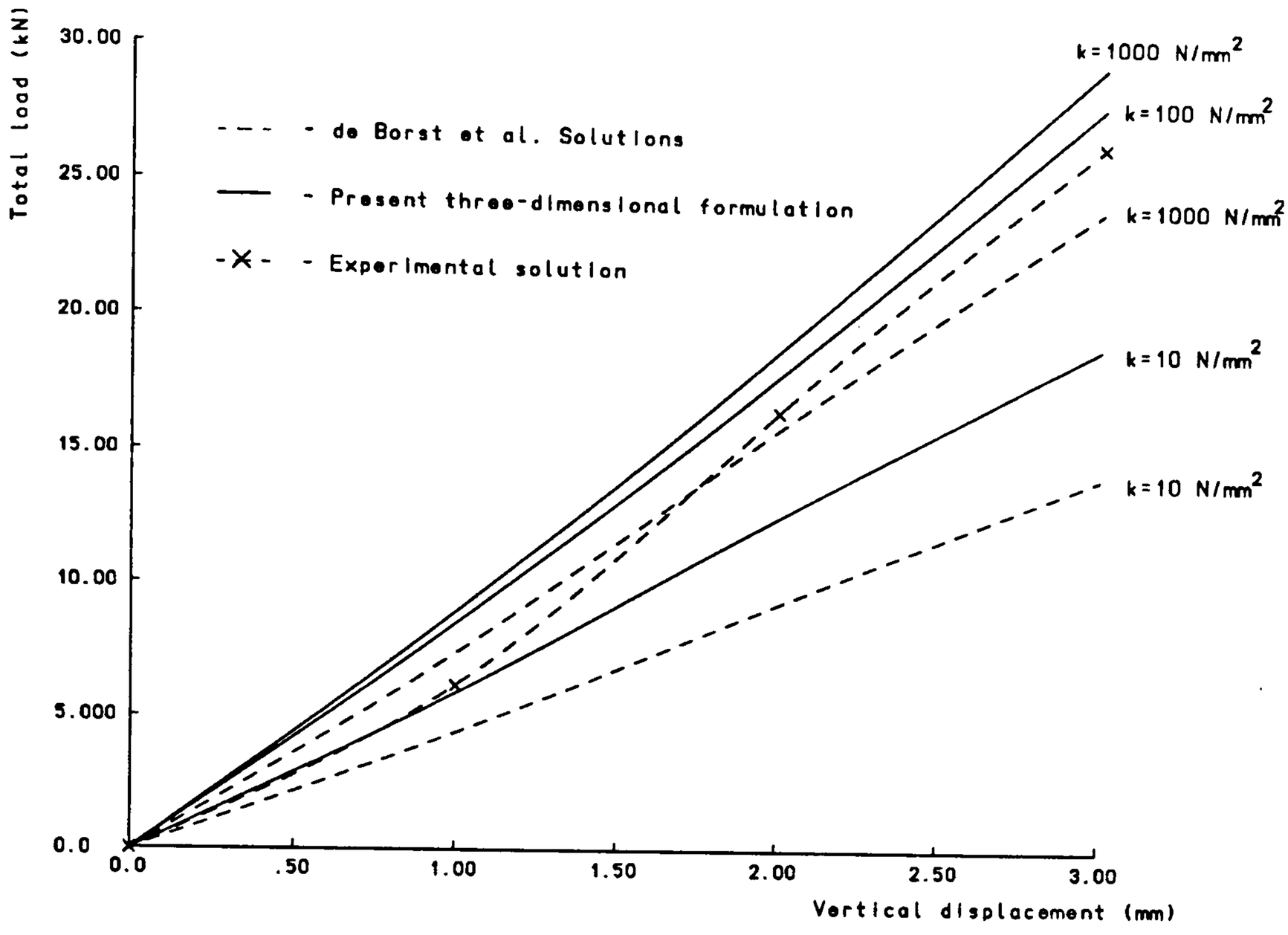


Figure 7.14: Block under compression - total force vs. vertical displacement

7.5 Final remarks

The inclusion of hyperelastic simulations into the co-rotational framework of the previous two chapters has been presented in this chapter. It is demonstrated from the numerical analysis performed here that the problems affecting the large-strain analysis encountered with the formulation of Chapter 4 have been eliminated with this new approach. However, problems with ill-conditioning are still a major concern and failures when a very high bulk modulus is being used still occur. Alternative solutions for the problem include the use of the augmented Lagrangian method and the use of ALE formulation. Despite this, the series of examples shown disclose an accurate and reliable formulation that is relatively free from incompressible locking which is the main difficulty with rubberlike materials.

The hyperelastic approach given here can be used later as the first step towards the development of a formulation for large-strain plasticity.

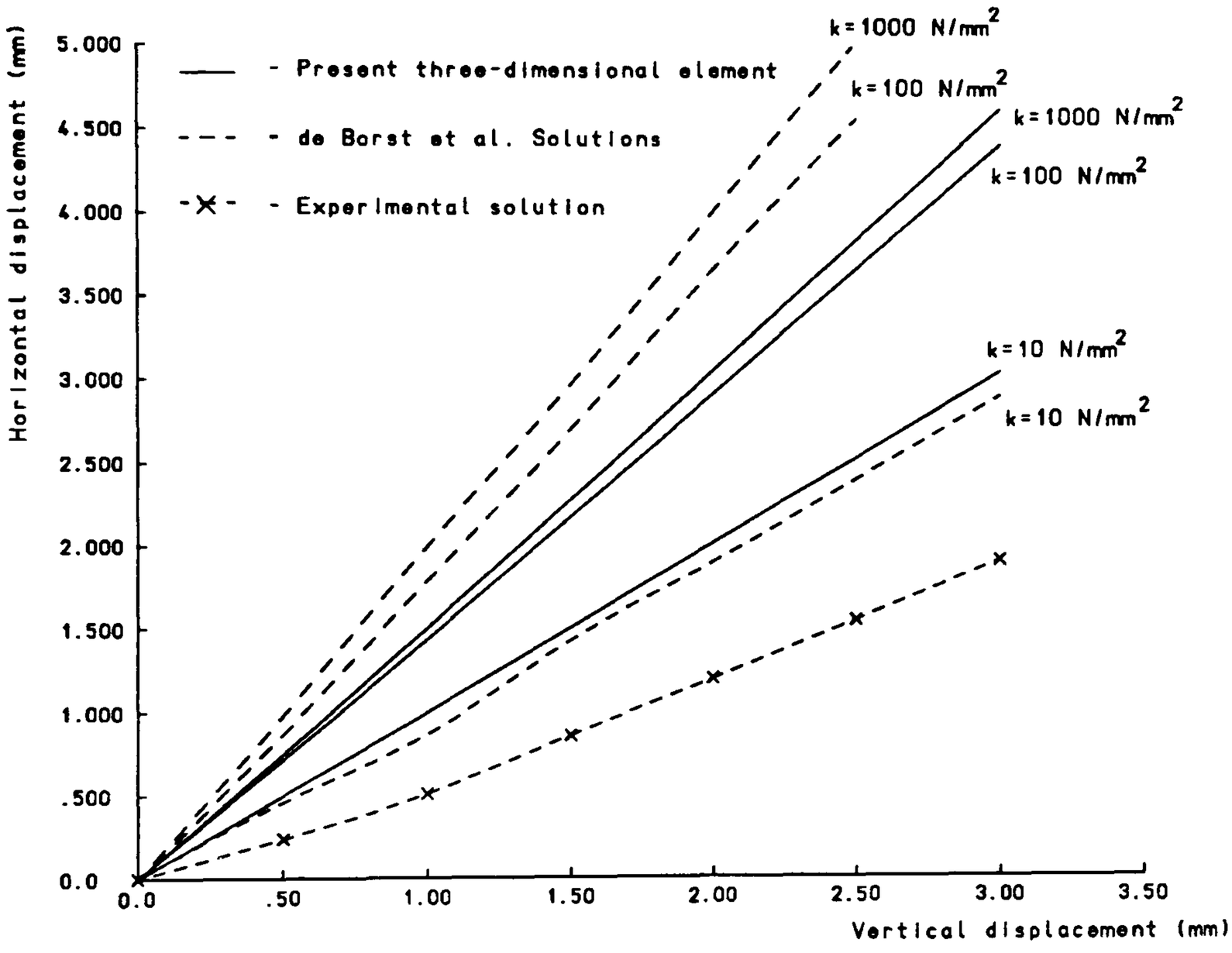


Figure 7.15: Block under compression - horizontal displacement vs. vertical displacement

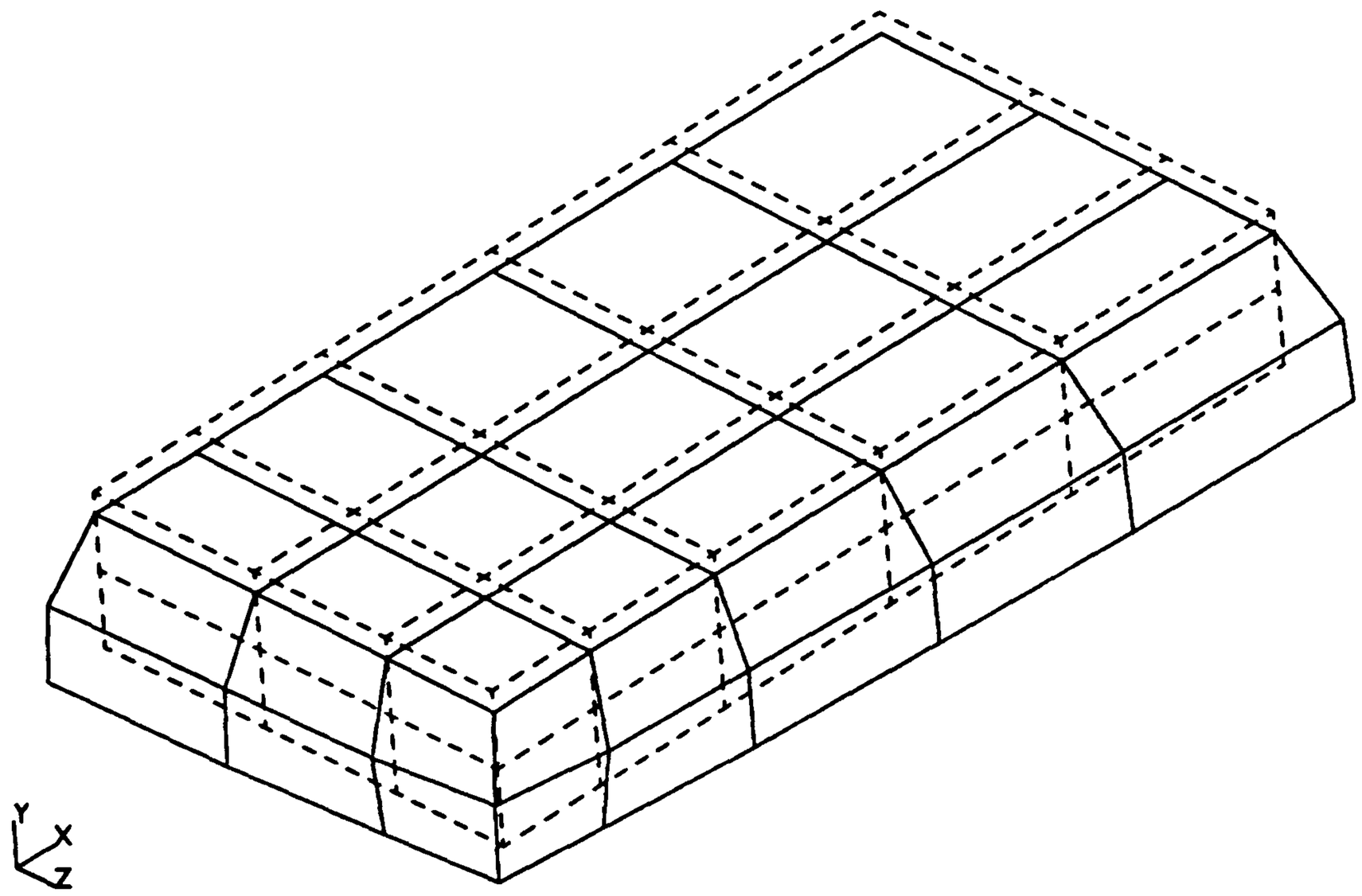


Figure 7.16: Block under compression - Undeformed and deformed meshes at 13.6% compression

Chapter 8

Final Remarks and Conclusions

8.1 General conclusions

This research concentrated on the investigation of efficient finite element algorithms which are suited for analysis concerning large strains in addition to large displacements and rotations. The ultimate goal is to formulate elements capable of adequately studying the well known hyperelastic or rubberlike materials. The principal difficulty with such materials comes from their inherent incompressible or near-incompressible behaviour. This characteristic tends to cause instability within the finite element leading to locking and failures in convergence when the element is not devised to cope with these problems. The elements proposed in this work can satisfactory circumvent the difficulties arising from the incompressibility issue. Furthermore, in spite of applying linear interpolation, the elements, especially the plane and the three-dimensional ones, display an outstanding performance even for bending dominated problems.

The work began with the study of simple membrane elements for hyperelastic analysis. The first element formulated was a two-noded axisymmetric membrane. This study can be regarded as an initial approach for the understanding of the methodology employed to examine large elastic strains. Important features were included for this basic element such as the displacement-dependent load force (follower load) and the use of arc-length to overcome problems in the solution procedure. These tools were also used in the subsequent elements studied apart from the brick element which did not incorporate the follower conservative load.

Hyperelastic constitutive models due to Ogden and Mooney-Rivlin were considered for the axisymmetric membrane and no problem was observed. To enable a wider class of membranes to be analysed, the extension to a general three-dimensional three-noded

triangular element was developed. Henceforth, we only used Ogden's material model for the rubber-like materials. The element performs well although some problems related to coarse meshes were encountered. In the development of the membrane elements the total Lagrangian approach was used and excellent results were achieved.

The next step was to enter a "more" continuum mechanics approach, again using the total Lagrangian formulation. We chose a four-noded element for plane analysis. The element is enhanced to handle incompressibility and bending problems by using quadratic incompatible displacement modes that are eliminated at the element level. Our main consideration was with the plane-strain element since this element is particularly affected by the incompressible characteristic of the material. In a linear environment it was clearly demonstrated that the incompatible mode element gives much better answers than both the conventional bi-linear element and a constant pressure (u-p) element, particularly as $\nu \rightarrow 0.5$. A total Lagrangian formulation was presented to extend the approach to handle geometric non-linearity. The results obtained for the element in a small strain (but large rotations and deflections) environment, even for near-incompressible situations, were very satisfactory. However, for some problems the large-strain analysis was not successful. This is due to mechanisms appearing in the analysis when some of the incompatible modes were not activated. A solution could be to switch off certain modes for a pre-defined kind of analysis. Of course this technique would be far from be reasonable for a general case. Nevertheless, the excellent results obtained for the standard non-linear elastic case were very encouraging and the technique has further possibilities.

A co-rotational procedure was then applied for the four-noded plane and the eight-noded three-dimensional elements for continua. The technique is more directly and widely used for beams and shells due to the suitability of using the current configuration of the nodes in order to define the co-rotating base frame for each element. The main benefit of the formulation is based on the concept of making use of the linear element embedded within the co-rotating framework. The non-linearities are introduced via the transformation (rotation) of the co-rotational frame system. Such an idea can also be inserted into the continua framework whereby the continuously effort invested in the development of effective linear elements can simply be used in a non-linear process. In this work we have used the four-noded plane element with incompatible modes as well as the eight-noded brick element again incorporating the incompatible modes to demonstrate the validity of the development.

The most complex part in attempting to use the above formulation for continua

comes from the definition of the local rotating system. We adopted the technique in which the local spin is set to zero. This results in good solutions for both the two- and three-dimensional cases. The resulting formulation is clear and neat and its derivation is relatively straightforward. We also addressed the issue of the consistent derivation of the tangent stiffness matrix. A series of examples illustrates the potential of the technique.

At that stage we turned out attention back to the problem that motivated the use of the co-rotational technique: the large-strain analysis. The hyperelasticity is now treated via a "Biot-like formulation". The formulation presented is similar to a co-rotated engineering type formulation. Once more, excellent results were obtained and the previous problem with mechanisms did not occur for the several test cases presented here. The overall performance obtained indicated that the approach results in a very efficient and robust formulation for the general analysis of continua. Some problems with convergence due to the incompressibility, especially for structures undergoing compression, still have to be overcome. However, the effect is only relevant when these compressive strains are very large. This drawback by no means invalidates the methodology proposed in this work and some solutions are suggested in the next section.

Towards the end of this research the author came across a new problem again related to spurious mechanisms and instability of the element. This issue is discussed in Appendix C. Although no spurious instabilities were encountered in the wide range of problems tackled in this thesis, the problem clearly requires further investigation.

8.2 Future works

The need for further work in relation to spurious mechanisms was indicated at the end of the previous section.

Another natural and evident step in the continuation of this work is to strengthen the formulation of the co-rotational elements to be able to handle more properly the incompressibility problem, notably in structures subjected to compression. This could be accomplished by replacing the technique used here in which, for the case of incompressibility, the bulk modulus k effectively represents a penalty function by a formulation in which the incompressibility constraint is treated via Lagrangian multipliers which would be solved for at the element level. As an alternative, the current formulation (with only displacements as structural variables) could be preserved and then an augmented Lagrangian procedure [77, 93] could be applied. In this approach the Lagrangian multi-

pliers are iteratively up-dated at the Gauss-point level while the penalty term gradually becomes less important.

The general techniques used in this work could be clearly extended to adapt the element to include large-strain elasto-plasticity. Many current large-strain elasto-plastic formulations are based on the use of a hyperelastic relationship for the elasticity [28, 70, 80, 22].

A further improvement in the performance of the formulation can be achieved, especially with respect to the volumetric locking, by using different linear elements such as those proposed by Andelfinger and Ramm [5] and Simo and co-workers [81]. These elements could be easily incorporated into the existing co-rotational formulation described in this thesis.

Another detail that is not deeply investigated in this thesis is why the inclusion of variation of the vector $\mathbf{v}$, defined in equations (5.41) and (6.39), into the initial stress stiffness matrix can be negleted. This issue is relevant and further examination is required.

Appendix A

Arc-Length Method with a Displacement-Dependent Load

The Out-of-balance Force Vector of the equation (3.29) can be re-written as (see [20] for details)

$$\mathbf{g}(\mathbf{p}, \lambda) = \mathbf{q}_i(\mathbf{p}) - \lambda(\mathbf{s})\mathbf{q}_e(\mathbf{p}) \tag{A.1}$$

with a new incremental factor λ now function of the arc-length s.

From Newton-Raphson, a truncated Taylor Series is used to produce

$$\mathbf{g}_n = \mathbf{g}_o + \frac{\partial \mathbf{g}}{\partial \mathbf{p}}\delta\mathbf{p} + \frac{\partial \mathbf{g}}{\partial \lambda}\delta\lambda + O(\delta\mathbf{p}^2) \tag{A.2}$$

where the subscripts n and o mean new and old, respectively.

The series then becomes

$$\mathbf{g}_n = \mathbf{g}_o + (\frac{\partial \mathbf{q}_i}{\partial \mathbf{p}} - \lambda\frac{\partial \mathbf{q}_e}{\partial \mathbf{p}})\delta\mathbf{p} - \mathbf{q}_e\delta\lambda + O(\delta\mathbf{p}^2) \tag{A.3}$$

In the expression above, $\frac{\partial \mathbf{q}_i}{\partial \mathbf{p}}$ is the matrix K_t and $\frac{\partial \mathbf{q}_e}{\partial \mathbf{p}}$ is the matrix K_p defined previously in (3.30) and (3.31), respectively. Adding both matrices to obtain the total matrix K_T, (A.3) can be expressed as

$$\mathbf{g}_n = \mathbf{g}_o + K_T\delta\mathbf{p} - \mathbf{q}_e\delta\lambda + O(\delta\mathbf{p}^2) \tag{A.4}$$

The Newton step is taken from (A.4) with the higher-order ($O(\delta\mathbf{p}^2)$) term neglected. The form of the resulting equation is unaltered by the presence of displacement-dependent loads. The quadratic convergence rate expected is then obtained indepen-

dently from the kind of analysis it has been used. The Newton-Raphson iteration is obtained by setting $\mathbf{g}_n = 0$ in (A.4). The general development of the Arc-Length Method is given by Crisfield [20].

Appendix B

Pressure as a Separated Variable

We consider a four-noded finite element for plane-strain analysis of a hyperelastic material (rubberlike material). The material definition is based on an Ogden-type Model. The element is analysed using two different approaches, both intended to overcome the problems caused by the incompressibility that is a characteristic of a rubberlike material.

The first approach, described in chapter 4, incorporates incompatible displacement modes to the original element. The second method can be stated as the separation of the volumetric and the deviatoric terms in the stress definition, resulting in a pressure term (hydrostatic) independent that is eliminated at the element level. This formulation is also known as the so-called $u-p$ approach. This appendix shows briefly the formulation related to the second method.

Splitting into Volumetric and Deviatoric Terms

a. Displacement and pressure variable

$$\begin{aligned} u &= \mathbf{h}^T \mathbf{u} \\ v &= \mathbf{h}^T \mathbf{v} \end{aligned} \tag{B.1}$$

$$p_e = \mathbf{h}_p^T \mathbf{p}_e \tag{B.2}$$

where $\mathbf{h}_p$ is the shape function for the pressure degree-of-freedom and $\mathbf{p}_e$ are the pressure nodes. Note that for the current case, we only use one pressure node and, therefore, $\mathbf{h}_p$ is a unit constant. Hence, p_e is an scalar.

b. 2nd Piola-Kirchhoff stress definition

The Strain Energy Function of (4.41) can be represented as

$$\varphi = \underbrace{\sum_p \frac{\mu_p}{\alpha_p}[J^{-\frac{1}{3}}(\lambda_1^{\alpha_p} + \lambda_2^{\alpha_p} + 1) - 3]}_{\varphi_d} - \underbrace{p_e(J-1)}_{\varphi_b} \tag{B.3}$$

from which we get

$$S_1 = \frac{1}{3\lambda_1^2}\sum_p \mu_p J^{-\frac{\alpha_p}{3}}(2\lambda_1^{\alpha_p} - \lambda_2^{\alpha_p} - 1) - p_e\frac{\lambda_2}{\lambda_1} \tag{B.4}$$

and

$$S_2 = \frac{1}{3\lambda_2^2}\sum_p \mu_p J^{-\frac{\alpha_p}{3}}(2\lambda_2^{\alpha_p} - \lambda_1^{\alpha_p} - 1) - p_e\frac{\lambda_1}{\lambda_2} \tag{B.5}$$

c. Compute $\mathbf{D}'$ and $\mathbf{A}$

$$\delta\mathbf{S} = \mathbf{D}'\delta\mathbf{E} + \mathbf{A}\delta p_e \tag{B.6}$$

where the matrix $\mathbf{D}'$ and the vector $\mathbf{A}$ are obtained via manipulations on (B.4) and (B.5). If we compute δp_e from

$$p_e = -k(J-1) \tag{B.7}$$

we have

$$\delta p_e = -k\left\{\begin{array}{c}\frac{\lambda_2}{\lambda_1}\\ \\ \frac{\lambda_1}{\lambda_2}\end{array}\right\}^T \delta\mathbf{E} \tag{B.8}$$

Hence, (B.6) can be re-written in the usual form $\delta\mathbf{S} = \mathbf{D}\delta\mathbf{E}$ where the terms of $\mathbf{D}$ were given in Chapter 4 (equations (4.59)).

d. Variation of the Green's strain

$$\delta\mathbf{E} = \mathbf{B}\,\delta\mathbf{p} \tag{B.9}$$

e. Using virtual work we obtain

$$\mathbf{g} = \mathbf{q}_i - \mathbf{q}_e = \int_{V_o} \mathbf{B}^T\,\mathbf{S}dV_o - \mathbf{q}_e \tag{B.10}$$

with the variation of the out-of-balance force vector **g** above giving:

$$\delta \mathbf{q}_i = \int_{V_o} \mathbf{B}_{nl}^T \delta \mathbf{S} dV_o + \int_{V_o} \delta \mathbf{B}_{nl}^T \mathbf{S} dV_o \tag{B.11}$$

From (B.9), (B.11) becomes

$$\delta \mathbf{q}_i = \underbrace{\int_{V_o} \mathbf{B}_{nl}^T \mathbf{D}' \mathbf{B}_{nl} dV_o}_{\mathbf{K}_t} \delta \mathbf{p} + \underbrace{\int_{V_o} \mathbf{G}^T \hat{\mathbf{S}} \mathbf{G} dV_o}_{\mathbf{K}_s} \delta \mathbf{p} + \underbrace{\int_{V_o} \mathbf{B}_{nl}^T \mathbf{A} \mathbf{h}_p^T dV_o}_{\mathbf{P}} \delta \mathbf{p}_e \tag{B.12}$$

f. Using the weak form of (B.7), we can write

$$\mathbf{f} = -\int_{V_o} \mathbf{h}_p [(J-1) + \frac{1}{k} p_e] dV_o \tag{B.13}$$

Differentiating **f**, we have

$$\delta \mathbf{f} = \underbrace{\int_{V_o} \mathbf{h}_p \mathbf{A}^T \mathbf{B}_{nl} dV_o}_{\mathbf{P}^T} \delta \mathbf{p} - \underbrace{\int_{V_o} \frac{1}{k} \mathbf{h}_p \mathbf{h}_p^T dV_o}_{\mathbf{H}} \delta \mathbf{p}_e \tag{B.14}$$

Observe that for the current case we use one pressure node. This means that **P** of (B.12) is a vector and **f** of (B.13) and **H** of (B.14) are scalars.

g. From (B.12) and (B.14) above, we can write

$$\begin{Bmatrix} \delta \mathbf{g} \\ \delta \mathbf{f} \end{Bmatrix} = \begin{bmatrix} \mathbf{K}_T & \mathbf{P} \\ \mathbf{P}^T & \mathbf{H} \end{bmatrix} \begin{Bmatrix} \delta \mathbf{p} \\ \delta \mathbf{p}_e \end{Bmatrix} \tag{B.15}$$

$$\mathbf{K}_T = \mathbf{K}_t + \mathbf{K}_s$$

Now we need a static condensation to eliminate the pressure terms at the element level.

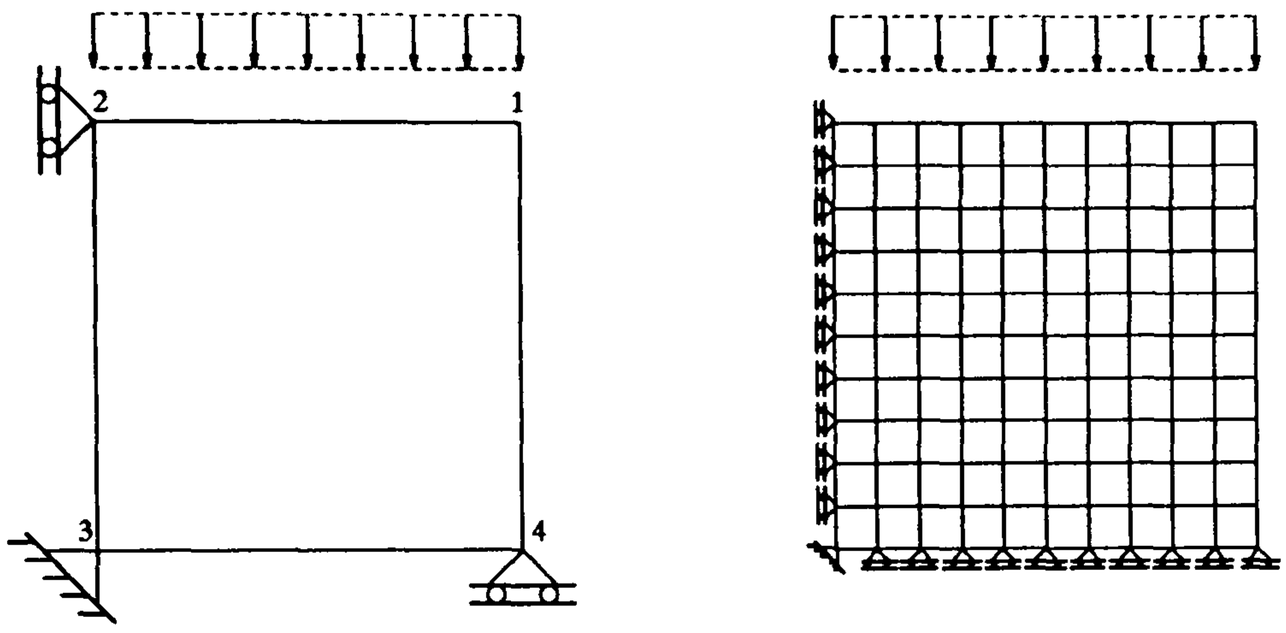
Appendix C

Problems with Rank Deficiency

The application of the new formulation to the test case recently proposed by Wriggers and Reese [99] seems to be a very interesting problem. As pointed out by the authors, even the case of a homogeneous stress state can lead to some difficulties when the incompatible element or 'enhanced strain element' are applied in conjunction with large-strain deformations. We used the present co-rotational formulation to analyse the rectangular block under compressive load as given in [99]. In this example, the block is modelled by plane-strain elements and subjected to finite elastic deformations imposed via a displacement-control procedure. The compressive neo-Hookean model utilised here differs from that originally used in [99] but an approximation is used to match the 'Lamé constants' ($\lambda = 100000$ and $\mu = 20$) for the original model to the constants of the present compressible neo-Hookean. Therefore, we can establish $k = 100013.33$ and $C_1 = 10$ that are employed in (2.35).

The analysis is accomplished using two different meshes. First we used a single element with the geometry and boundary conditions as shown in figure C.1.a. For this case, in contrast to the solution of Wriggers and Reese, the element did not display any problem and no rank deficiency seems to be present. We also release the horizontal displacement of the top corner (node 2) to allow the element to deformed as indicated in [99] but again the element performed well. Following the modelling used in [99], we analysed the same problem (same dimensions and support conditions) idealised with a 10×10 element mesh (figure C.1.b). For this second attempt, the problem indicated by the above authors can be observed around the same displacement level that they found; in other words, around 40% of the initial height. The tangent stiffness matrix reveals one negative pivot which denotes the occurrence of spurious mechanisms at this level.

Unfortunately, the version of the finite element package LUSAS used at this stage cannot trigger an eigenvalue analysis when this problems occurs thus the problem cannot (at present) be further investigated. The latest version of the program is able to execute such an analysis but it was not available when the work was completed. However, we tried to solve the problem by integrating the element using different numbers of Gauss points. The original element is integrated by a 2×2 Gauss points rule. We tried 5-point and 3×3 integrations rules but the problem still occurs.



a) Single element b) Multi-element

Figure C.1: Test problem - block under compression

It should be emphasised that the problem does not occur for small strain analyses and, even with large strains, only seems to exist for this particular homogeneous strain state. Also, it did not arise for any of the problems described previously in this thesis. Nevertheless, a technique to overcome the problem is necessary. Wriggers and Reese recommended the elimination of the incompatible modes when their contribution is zero but this procedure requires further investigation.

References

[1] Andelfinger,U., Ramm,E. and Roehl,D. 2D– and 3D–enhanced Assumed Strain Elements and Their Application in Plasticity, *Computational Plasticity, Fundamental and Applications*, edited by D.R.J.Owen, E.Oñate and E.Hinton, Proceedings of the Third International Conference, Pineridge Press, Barcelona, April, 1992.

[2] Andelfinger,U. and Ramm,E. EAS–elements for Two–dimensional, Three–dimensional, Plate and Shell Structures and Their Equivalence to HR–elements, *Int. J. Numer. Methods Engrg.*, Vol.36, 1311-1337, 1993.

[3] Argyris,J.H., Kersey,S. and Kamel,H. Matrix Methods of Structural Analysis, A Précis of Recent Developments, *Matrix Methods of Structural Analysis*, AGARDograph72, edited by F.de Veubeke, 1-164, Pergamon Press, London, 1964.

[4] Argyris,J.H., Balmer,H., Doltsinis,J.St., Dunne,P.C., Haase,M., Kleiber,M., Malejannakis,G.A., Mlejenek,H.P., Müller,M. and Scharpf,D.W. Finite Element Method – The Natural Approach, *Comp. Met. in App. Mech. and Engrg.*, Vol.17/18, 1-106, 1979.

[5] Argyris,J.H. and Symeonidis, Sp. Nonlinear Finite Element Analysis of Elastic Systems Under Nonconservative Loading – Natural Formulation. Part I. Quasistatic Problems, *Comp. Met. in App. Mech. and Engrg.*, Vol.26, 75-123, 1981.

[6] Bathe,K-J *Finite Element Procedures in Engineering Analysis*, Prentice-Hall, New Jersey, 1982.

[7] Bathe,K-J and Bolourchi,S. Large Displacement Analysis of Three-dimensional Beam Structures, *Int. J. for Num. Meth. in Engrg.*, Vol.14, 961-986, 1979.

[8] Belytschko,T. and Hsieh,B.J. Non–linear Transient Finite Element Analysis with Convected Co–ordinates, *Int. J. for Num. Meth. in Engrg.*, Vol.7, 255-271, 1973.

[9] Belytschko,T., Schwer,L. and Klein,M.J. Large Displacement, Transient Analysis of Space Frames, *Int. J. for Num. Meth. in Engrg.*, Vol.11, 65-84, 1977.

[10] Belytschko,T. and Glaum,L.W. Application of Higher Order Corotational Stretches Theories to Nonlinear Finite Element Analysis, *Computers and Structures*, Vol.10, 175-182, 1979.

[11] Blatz,P.J. and Ko,W.L. Application of Finite Elastic Theory to the Deformation of Rubbery Materials, *Transactions of the Society of Rheology*, VI, 223-251, 1962.

[12] Bogert,P.A.J. van den. *Computational Modelling of Rubberlike Materials*, Ph.D. Thesis, Delft University of Technology, October, 1991.

[13] de Borst,R., van den Bogert,P.A.J. and Zeilmaker,J. Modelling Analysis of Rubberlike Materials, *Heron*, Vol.33, No.1, 1988.

[14] Cole,G. *Co–rotational Beam Elements Consistently Formulated for Geometrically Nonlinear Problems Involving Large Rotation*, Ph.D. Thesis, Kingston Polytechnic, 1990.

[15] Cook,R.D., Malkus,D.S. and Plesha,M.E. *Concepts and Applications of Finite Element Analysis*, Third Edition, John Wiley, 1989.

[16] Crisfield,M.A. A Fast Incremental/Iterative Solution Procedure that Handles "Snap-Through", *Computers and Structures*, Vol.13, No.1-3, 55-62, 1981.

[17] Crisfield,M.A. An Arc–length Method Including Line–search and Accelerations, *Int. J. for Num. Meth. in Engrg.*, Vol.19, 1269-1289, 1983.

[18] Crisfield,M.A. *Finite Element and Solution Procedures for Structural analysis Vol.1: Linear Analysis*, Pineridge Press, Swansea, 1986.

[19] Crisfield,M.A. A Consistent Co–rotational Formulation for Non–linear, Three–dimensional, Beam–elements, *Comp. Met. in App. Mech. and Engrg.*, Vol.81, 131-150, 1990.

[20] Crisfield,M.A. *Non–linear Finite Element Analysis of Solids and Structures: Vol.1, Essentials*, John Wiley, 1991.

[21] Crisfield,M.A. *Non–linear Finite Element Analysis of Solids and Structures: Vol.2*, to be published.

[22] Cuitiño,A. and Ortiz,M. A Material–independent Method for Extending Stress Update Algorithms for Small–strain Plasticity to Finite Plasticity with Multiplicative Kinematics, *Eng Comput*, Vol.9, 437-451, 1992.

[23] Desai,C.S. and Siriwardane,H.J. *Constitutive Laws for Engineering Materials, with emphasis on geologic materials*, Prentice-Hall, 1984.

[24] Dienes,J.K. On the Analysis of Rotation and Stress Rates in Deforming Bodies, *ACTA Mech*, Vol.32, 217-232, 1979.

[25] Dobrowolski,M. A Mixed Finite Element Method for Approximating Incompressible Materials, *SIAM J. Numer. Anal.*, Vol.29, No.2, 365-389, April, 1992.

[26] Donea,J. and Belytschko,T. Advances in Computational Mechanics, *Nuclear Engineering and Design*, Vol.134, 1-22, 1992.

[27] Duffett,G. and Reddy,B.D. The Analysis of Incompressible Hyperelastic Bodies by Finite Element Method, *Comp. Met. in App. Mech. and Engrg.*, Vol.41, 105-120, 1983.

[28] Eterović,A.L. and Bathe,K-J. A Hyperelastic–based Large Strain Elasto–plastic Constitutive Formulation with Combined Isotropic–kinematic Hardening Using Logarithmic Stress and Strain Measures, *Int. J. Numer. Methods Engrg.*, Vol.30, 1099-1114, 1990.

[29] Freakley,P.K. and Payne,A.R. *Theory and Practice of Engineering with Rubber*, Applied Science Publishers LTD, London, 1978.

[30] Fried,I. Finite Element Computation of Large Rubber Membrane Deformations, *Int. J. Numer. Methods Engrg.*, Vol.18, 653-660, 1982.

[31] Fried,I. and Johnson,A.R. Nonlinear Computation of Axisymmetric Solid Rubber Deformation, *Comp. Met. in App. Mech. and Engrg.*, Vol.67, 241-253, 1988.

[32] Gadala,M.S The Use of Bubble Functions for the Solution of Problems with Incompressibility, *Constitutive Laws for Engineering Materials*, edited by C.S.Desai *et. al.*, ASME Press, 101-105, 1991.

[33] Gadala,M.S Alternative Methods for the Solution of Hyperelastics Problems with Incompressibility, *Computers and Structures*, Vol.42, No.1, 1-10, 1992.

[34] Gent,A.N. Rubber and Rubber Elasticity: A Review, *Rubber and Rubber Elasticity, Journal of Polymer Science: Polymer Symposia*, No.48, 1-17, edited by A.S.Dunn, Interscience, 1974.

[35] Gere,J.M. and Timoshenko,S.P. *Mechanics of Materials*, Second SI Edition, Van Nostrand Reinhold (International) Co. Ltd, London, 1987.

[36] Gruttmann,F. and Taylor,R.L. Theory and Finite Element Formulation of Rubber-like Membrane Shells Using Principal Stretches, *Int. J. for Num. Meth. in Engrg.*, Vol.35, 1111-1126, 1992.

[37] Häggblad,B. and Sundberg,J.A. Large Strain Solution of Rubber Components, *Computers and Structures*, Vol.17, No.5-6, 835-843, 1983.

[38] Hencky,H. The Elastic Behaviour of Vulcanized Rubber, *Journal of Applied Mechanics*, Vol.1, 45-53, 1933.

[39] Hibbitt,H.D. Some Follower Forces and Load Stiffness, *Int. J. Num. Met. Engrg.*, Vol.14, 937-941, 1979.

[40] Hinton,E.(ed.) *Introduction to Non-linear Finite Element Analysis*, NAFEMS, Glasgow, 1992.

[41] Hsiao,K.M. Nonlinear Analysis of General Shell Structures by Flat Triangular Shell Element, *Computers and Structures*, Vol.25, 665-675, 1987.

[42] Hsiao,K.M. and Hou,F.Y. Nonlinear Finite Element Analysis of Elastic Frames, *Computers and Structures*, Vol.26, 693-701, 1987.

[43] Hsiao,K.M., Horng,H.J. and Chen,Y.R. A Corotational Procedure that Handles Large Rotations of Spatial Beam Structures, *Computers and Structures*, Vol.27, 769-781, 1987.

[44] Hughes,T.J.R. *The Finite Element Method, Linear Static and Dynamic Finite Element Analysis*, Prentice-Hall International, 1987.

[45] Hunter,S.C. *Mechanics of Continuous Media*, 2nd edition, Ellis Horwood, Chischester, 1983.

[46] Ibrahimbegović, A. and Wilson,E.L., A Modified Method of Incompatible Modes, *Communications in Applied Numerical Methods*, Vol.7, 187-194, 1991.

[47] Ibrahimbegović,A. Plate Quadrilateral Finite Element with Incompatible Modes, *Communications in Applied Numerical Methods*, Vol.8, 497-504, 1992.

[48] Ibrahimbegović,A. and Frey,F. Geometrically Nonlinear Method of Incompatible Modes in Application to Finite Elasticity with Independent Rotations, LSC Internal Report 92/12, Department of Civil Engineering, Swiss Federal Institute of Technology, Lausanne, June, 1992.

[49] Ibrahimbegović,A. and Gruttmann,F. A Consistent Finite Element Formulation of Nonlinear Membrane Shell Theory with Particular Reference to Elastic Rubberlike Material, *Finite Elements in Analysis and Design*, Vol.12, 75-86, 1993.

[50] Jetteur,PH. and Cescotto,S. A Mixed Finite Element for the Analysis of Large Inelastic Strains, *Int. J. Numer. Methods Engrg.*, Vol.31, 229-239, 1991.

[51] Li,X. The Mixed Assumed Strain Elements for 2–D and 3–D Solid Mechanics, Software Development Report, SDR/LUSAS/030, FEA Ltd, 1991.

[52] Liu,W.K., Belytschko,T. and Chen,J-S. Nonlinear version of flexurally superconvergent elements, *Comp. Met. in App. Mech. and Engrg.*, Vol.71, 241-258, 1988.

[53] LUSAS User Manual, FEA, Version 10.0, October, 1990.

[54] Malvern,L.E. *Introduction to the Mechanics of a Continuous Medium*, Prentice-Hall, Englewood Cliffs, N.J., 1969.

[55] Mooney,M. A Theory of Large Elastic Deformations, *Journal of Applied Mechanics*, Vol.11, 582-592, 1940.

[56] Mullins,L. and Thomas,A.G. Theory of Rubber–like Elasticity, Chapter 7 in *The Chemistry and Physics of Rubber–like Substances*, edited by L.Bateman, Maclaren, London, 1963.

[57] Needleman,A. Inflation of Spherical Rubber Balloons, *Int. J. Solids Struct.*, Vol.13, 409-421, 1977.

[58] Nygård,M.K. The Free Formulation for Nonlinear Finite Elements with Applications to Shells, Report No.86-2, Division of Structural Mechanics, The University of Trondheim, Norway, 1986.

[59] Ochi,M., Hato,S. and Abe,T. Numerical Analysis of Deformation of Rubber Composite Materials, *JSME International Journal, Series I*, Vol.35, No.4, 1992.

[60] Oden,J.T. *Finite Elements of Non–Linear Continua*, McGraw-Hill, New York, 1972.

[61] Ogden,R.W. Large Deformation Isotropic Elastic – On the Correlation of Theory and Experiment for Incompressible Rubberlike Solids, *Proc. R. Soc. Lond.*, Vol.A(326), 565-584, 1972.

[62] Ogden,R.W. Elastic Deformations of Rubberlike Solids, *Mechanics of Solids, The Rodney Hill 60th Anniversary Volume*, edited by H.G.Hopkins and M.J.Sewell, Pergamon, Oxford, 1982.

[63] Ogden,R.W. *Non–linear Elastic Deformations*, Ellis Horwood, Chichester, 1984.

[64] Oliver,J. and Oñate,E. A Total Lagrangian Formulation for the Geometrically Nonlinear Analysis of Structures Using Finite Elements. Part 1. Two–dimensional Problems: Shell and Plate Structures, *Int. J. Numer. Methods Engrg.*, Vol.20, 2253-2281, 1984.

[65] Oran,C. Tangent Stiffness in Plane Frames, J. of Structural Division, ASCE, ST6, Vol.99, 973-985, 1973.

[66] Oran,C. Tangent Stiffness in Space Frames, J. of Structural Division, ASCE, ST6, Vol.99, 987-1001, 1973.

[67] Oran,C. and Kassimali,A. Large Deformations of Framed Structures under Static and Dynamic Loads, *Computers and Structures*, Vol.6, 539-547, 1976.

[68] Parisch,H. Efficient Non–linear Finite Element Shell Formulation Involving Large Strains, *Eng Comput*, Vol.3, 121-128, 1986.

[69] Peng,X. and Crisfield,M.A. A Consistent Co–rotational Formulation for Shell Using the Constant Stress/Constant Moment Triangle, *Int. J. Numer. Methods Engrg.*, Vol.35, 1829-1847, 1992.

[70] Perić,D., Owen,D.R.J. and Honnor,M.E. A Model for Finite Strain Elasto–plasticity Based on Logarithmic Strains: Computational Issues, *Comp. Met. in App. Mech. and Engrg.*, Vol.94, 35-61, 1992.

[71] Pian,T.H.H. and Sumihara,K. Rational Approach for Assumed Stress Finite Elements,*Int. J. Numer. Methods Engrg.*, Vol.20, 1685-1695, 1985.

[72] Rankin,C.C. and Brogan,F.A. An Element Independent Corotational Procedure for the Treatment of Large Rotation, ASME *Journal of Pressure Vessel Technology*, Vol.108, 165-174, 1986.

[73] Rivlin,R.S. Large Deformations of Isotropic Materials IV. Further Developments of the General Theory, *Phil. Trans. Roy. Soc.*, Vol.A241, 379-397, 1948.

[74] Saleed,A.F., Chang,T.Y.P. and Arnold,S.M. On the Development of Explicit Robust Schemes for Implementation of a Class of Hyperelastic Models in Large–strain Analysis of Rubber, *Int. J. Numer. Methods Engrg.*, Vol.33, 1237-1249, 1992.

[75] Schweizerhof,K. and Ramm,E. Displacement Dependent Pressure Loads in Nonlinear Finite Element Analyses, *Computers and Structures*, Vol.18, 1099-1114, 1984.

[76] Simo,J.C. and Rifai,M.S., A Class of Mixed Assumed Strain Methods and The Method of Incompatible Modes, *Int. J. Numer. Methods Engrg.*, Vol.29, 1595-1638, 1990.

[77] Simo,J.C. and Taylor,R.L. Quasi–incompressible Finite Elasticity in Principal Stretches. Continuum Basis and Numerical Algorithms, *Comp. Met. in App. Mech. and Engrg.*, Vol.85, 273-310, 1991.

[78] Simo,J.C., Taylor,R.L. and Wriggers,P. A Note on Finite–Element Implementation of Pressure Boundary Loading, *Communications in Applied Numerical Methods*, Vol.7, 513-525, 1991.

[79] Simo,J.C. and Armero,F. Geometrically Non–Linear Enhanced Strain Mixed Methods and The Method of Incompatible Modes, *Int. J. Numer. Methods Engrg.*, Vol.33, 1413-1449, 1992.

[80] Simo,J.C. Algorithms for Static and Dynanic Multiplicative Plasticity that Preserve the Classical Return Mapping Schemes of the Infinitesimal Theory, *Comp. Met. in App. Mech. and Engrg.*, Vol.99, 61-112, 1992.

[81] Simo,J.C., Armero,F and Taylor,R.L. Improved Versions of Assumed Enhanced Strain Tri-linear Elements for 3D Finite Deformation Problems, *Comp. Met. in App. Mech. and Engrg.*, Vol.110, 359-386, 1993.

[82] Spencer,A.J.M. *Continuum Mechanics*, Longmans, Hong Kong, 1980.

[83] Stevenson,A. *Rubber in Offshore Engineering*, Proceedings of a conference held in London from April 13 to April 15 1983, Adam Hilger Ltd, Bristol, 1984.

[84] Sussman,T. and Bathe,K-J. A Finite Element Formulation for Nonlinear Incompressible Elastic and Inelastic Analysis, *Computers and Structures*, Vol.26, No.1/2, 357-409, 1987.

[85] Sze,K.Y. and Chow,C.L., An Incompatible Element for Axisymmetric Structure and Its Modification by Hybrid Method, *Int. J. Numer. Methods Engrg.*, Vol.31, 385-405, 1991.

[86] Taylor,R.L., Beresford,P.J. and Wilson,E.L. A Non–conforming Element for Stress Analysis, *Int. J. Numer. Methods Engrg.*, Vol.10, 1211-1219, 1976.

[87] Taylor,R.L., Simo,J.C., Zienkiewicz,O.C. and Chan,A.C. , The Patch Test: A Condition for Assessing Finite Element Convergence, *Int. J. Numer. Methods Engrg.*, Vol.22,39-62, 1986.

[88] Timoshenko,S.P. and Goodier,J.N. *Theory of Elasticity*, 3rd Edition, McGraw-Hill, 1970.

[89] Treloar,L.R.G. Stress–strain Data for Vulcanized Rubber Under Various Types of Deformation, *Trans Faraday Soc*, 40, 59-70, 1944.

[90] Treloar,L.R.G. The Mechanics of Rubber Elasticity, *Rubber and Rubber Elasticity, Journal of Polymer Science: Polymer Symposia*, No.48, 107-123, edited by A.S.Dunn, Interscience, 1974.

[91] Treloar,L.R.G. *The Physics of Rubber Elasticity*, 3rd Edition, Oxford, 1975.

[92] Valanis,K.C. and Landel,R.F. The Strain–energy Function of a Hyperelastic Material in Terms of the Extension Ratios, *Journal of Applied Physics*, Vol.38, No.7, 2997-3002, 1967.

[93] Vanderplaats,G.N. *Numerical Optimization Techniques for Engineering Design*, with Applications, McGraw-Hill, 1984.

[94] Weissman,S.L. A Mixed Formulation of Nonlinear–elastic Problems, *Computers and Structures*, Vol.44, No.4, 813-822, 1992.

[95] Wempner,G. Finite Elements, Finite Rotations and Small Strains of Flexible Shells, *Int. J. Solids Struct.*, Vol.5, 117-153, 1969.

[96] Wilson,E.L., Taylor,R.L., Doherty,W.P. and Ghaboussi, J. Incompatible Displacement Models, *Numerical and Computer Methods in Structural Mechanics*, edited by

S.J.Fenves, N.Perrone, A.R.Robinson and W.C.Schnobrich, Academic Press, New York, 1973.

[97] Wilson,E.L. and Ibrahimbegović, A., Use of Incompatible Displacement Modes for the Calculation of Element Stiffness or Stresses, *Finite Element in Analysis and Design*, 7, 229-241, 1990.

[98] Wriggers,P. and Taylor,R.L. A Fully Non–linear Axisymmetrical Membrane Element for Rubber–like Material, *Eng. Comput.*, Vol.7, 303-310, December, 1990.

[99] Wriggers,P. and Reese,S. A Note on Enhanced Strain Methods for Large Deformations, to be published.

[100] Yamada,T. and Kikuchi,F. An Arbitrary Lagrangian–eulerian Finite Element Method for Incompressible Hyperelasticity, *Comp. Met. in App. Mech. and Engrg.*, Vol.102, 149-177, 1993.

[101] Zienkiewicz,O.C. and Taylor,R.L. *The Finite Element Method, Fourth Edition, Vol.1, Basic Formulation and Linear Problems*, McGraw-Hill International Editions, 1989.

[102] Zienkiewicz,O.C. and Taylor,R.L. *The Finite Element Method, Fourth Edition, Vol.2, Solid and Fluid Mechanics, Dynamics and Non–linearity*, McGraw-Hill International Editions, 1991.